New Construction and Catalyst Support Materials for Water Electrolysis at Elevated Temperatures

Nikiforov, Aleksey Valerievich; Petrushina, Irina; Bjerrum, Niels J.; Jensen, Jens Oluf; Christensen, Erik

Publication date:
2011

Document Version
Publisher's PDF, also known as Version of record

Technical University of Denmark

Aleksey Nikiforov

New Construction and Catalyst Support Materials for Water Electrolysis at Elevated Temperatures

Ph.D. Thesis, June 2011

DTU Chemistry
Department of Chemistry

Aleksey Nikiforov

New Construction and Catalyst Support Materials for Water Electrolysis at Elevated Temperatures

Ph.D. Thesis, June 2011

New Construction and Catalyst Support Materials for Water Electrolysis at Elevated Temperatures

Author
Aleksey Nikiforov

Supervisors
Niels J.Bjerrum, Professor
Erik Christensen, Associate professor
Irina Petrushina, Associate professor

Department of Chemistry
Energy and Materials Science group
Technical University of Denmark
Kemitorvet building 207
DK-2800 Kgs. Lyngby
Denmark

www.energi.kemi.dtu.dk
Tel: (+45) 45 25 24 19
Fax: (+45) 45 88 31 36
E-mail: alnik@kemi.dtu.dk

Release date:	June 2011
Category:	1 (public)
Edition:	First
Comments:	This thesis is part of the requirements to achieve the Ph.D. in Chemistry degree at the Technical University of Denmark.

Preface

The present work was conducted at the Energy and Materials Science Group at the Department of Chemistry, DTU, during the period from June 2008 to June 2011.

I would like to express my high acknowledgement to all my supervisors. Firstly, to Professor Niels J. Bjerrum for the excellent and professional supervision, whose effective guidance helped to complete the Ph.D. program, fully covering all requirements for it. My co-supervisors, Drs. Irina Petrushina and Erik Christensen daily supported my research and writing, giving highly valuable feedback, providing challenging ideas and having constant availability to put work aside while having a busy schedule and help me with my problems.

I would also like to thank our current Ph.D. student Antonio, who helped me a lot during his master project, both with experimental and data analysis part.

I would like to express my sincere acknowledgements to Sinh Hy Nguyen, a principal technician at the Department of Enviromental Engineering at DTU, whose professional help with measurements can not be overestimated.

During February 2010 I had a pleasure of doing research at the Department of Materials Technology, NTNU. Professor Svein Sunde and Dr Mikhail Tsypkin are thanked for their cooperation in help with experimental work and providing worthwhile discussions. It was a very fruitful time with much inspiration and obtained experience in the field of catalyst characterisation.

I would also like to acknowledge Professor Karel Bouzek, who provided my stay at the Department of Inorganic Technology at the Institute of Chemical Technology in Prague during the summer 2010. He assured that my work at the group was interesting and worthwhile, while Drs. Milan Kouril and Martin Paidar showed interest in my efforts and provided ideas for further

investigations.

After all, I would like to thank my parents for sincere guiding and support thought all the time in spite of today's geographical distance between us.

This work was financially supported by the Center for renewable hydrogen cycling (HyCycle), Denmark, contract No. 2104-07-0041 and WELTEMP project under EU Seventh Framework Programme (FP7), grant agreement No. 212903 [1, 2].

Thanks

Aleksey Nikiforov, DTU, Lyngby, June 2011

Abstract

Proton exchange membrane (PEM) water electrolysis presents an attractive technology allowing to produce hydrogen for further use as a renewable energy source in the "Hydrogen cycle". Electrolysis of water steam at elevated temperatures has several advantages over the low temperature process. However, at the same time it involves increased demands to dimensional and chemical stability of components against corrosion environment.

Therefore, materials utilized in low temperature PEM electrolyzers cannot be used in systems operating above 100 °C and new candidates should be tested.

The materials in question are those for bipolar plates, gas diffusion layers (GDLs), catalysts and catalyst supports. This work is focused on developing bipolar plate, GDL and catalyst support materials for the anode compartment of PEM electrolyzers, operating at elevated temperatures.

The thesis starts with Chapter 1, which gives an introduction into the subject and Chapter 2 subsequently presents the theoretical background of the topic and describes techniques used to characterize catalysts and construction materials.

Chapter 3 presents general principles and overview of materials used for PEM water electrolysis.

Chapter 4 reports results of testing different types of commercially available stainless steels, Ni-based alloys as well as titanium and tantalum as possible metallic bipolar plates and construction materials for HTPEMEC. The corrosion resistance was measured under simulated conditions of high temperature PEM steam electrolyzer. Steady-state voltammetry was used in combination with scanning electron microscopy (SEM) and energy-dispersive X-ray spectroscopy (EDX) to evaluate the stability of the mentioned materials. It was found that stainless steels were the least resistant to corrosion

under strong anodic polarization. On the contrary, Ni-based alloys showed higher corrosion resistance in the simulated PEM electrolyzer medium. In particular, Inconel®625 was the most promising among the tested corrosion-resistant alloys for the anodic compartment of high-temperature steam electrolyzer. The tantalum coated stainless steel showed outstanding resistance to corrosion in selected media, while passivation of titanium was weak, and the highest rate of corrosion among all tested materials was observed for titanium at 120 °C.

Today, there is a high interest in the field towards investigation of new catalyst materials, which can make it possible to avoid noble metals. However, this work suggests a different approach of decreasing the loading of the active component at the oxygen electrode by using a catalyst support.

In order to achieve that, investigation of a novel SiC-Si compound was performed and is presented in Chapter 5. The active iridium oxide was deposited on the SiC-Si in-situ by the Adams fusion synthesis and characterized by different techniques. XRD and nitrogen adsorption experiments showed an influence of the support on surface properties of the IrO_2 particles, affecting IrO_2 particle size. The prepared catalysts were electrochemically characterized by cyclic voltammetry experiments at 25, 80, 120 and 150 °C. In accordance with the observed variation in particle size, a support loading of up to 80% improved the activity of the catalyst. Powder conductivity measurements were also performed, which showed the influence of the support on the packing of IrO_2 particles. Investigation showed that even a support material with poor electrical conductivity contributes beneficially to the electrocatalyst active surface area, increasing its utilization. Results demonstrated potential perspectives of using low conductive ceramics as a catalyst support which means that further research in this field is of high interest.

An essential part of the study was devoted to the development of a method of elevated temperature catalyst electrochemical characterization, which was implemented for the evaluation of the performance of the synthesised catalysts.

Chapter 6 consists of concluding remarks and proposals for the future research.

Chapter 7 contains two articles, which were published during the project period.

Dansk Resumé

Vandelektrolyse baseret på polymer elektrolyt membraner (PEM) er en lovende teknologi, som tillader at produktion af brint. Da brint muligvis kan blive en fremtidig energibærer i en "Brint cyklus". Elektrolyse af vanddamp ved forhøjede temperaturer har flere fordele i forhold til en lavtemperatur elektrolyse proces. Dog betyder den forøgede temperatur samtidig et øget krav til konstruktionsmaterialerne i cellen, f.eks. kommer der et øget krav til dimensionsstabiliteten og den kemiske stabilitet under de stærkt korrosive forhold som findes i systemet. Materialer der benyttes i lavtemperatur elektrolyse kan således ikke nødvendigvis anvendes i systemer, som virker ved temperaturer over 100 °C og nye materialer skal derfor undersøges.

I afhandlingens kapitel 1 gives en generel introduktion til emnet, medens Kapitel 2 gennemgår teoretiske aspekter vedrørende elektrokatalyse. Desuden beskrives de teknikker, der er blevet benyttet til karakterisering af katalysatorerne og kontruktionsmaterialerne.

I kapitel 3 gennemgås opbygningen af PEM elektrolysatorer, samt litteraturen vedrørende de forskellige materialer der indgår, dvs. membraner, katalysatorer og konstruktionsmaterialer.

I kapitel 4 fremlæggers resultaterne af korrosionstests af forskellige typer kommercielle rustfrie stålmaterialer, nikkel-baserede legeringer, samt titanium og tantal for anvendelse som mulige bipolare plader og konstruktionsmateriale for højtemperatur PEM elektrolyseceller (HTPEMEC). Korrosionsresistensen er blevet målt under betingelser som simulerer en højtemperatur PEM dampelektrolysecelle. Steady state voltammetri er blevet anvendt i kombination med skanning elektron mikroskopi (SEM), og energi dispersiv røntgen spektroskopi (EDX) er benyttet for at evaluere stabiliteten af ovenfor nævnte materialer. Det blev fundet at blandt legeringerne var de rustfri ståltyper mindst modstandsdygtige overfor korrosion under stærk anodisk polarisering. Af nikkel-legeringerne udviste Inconel 625 størst po-

tentiale som et muligt materiale i højtemperatur elektrolyse celler, da den var den mest korrosionsbestandig blandt de testede stålmaterialer og nikkellegeringer.

Tantal-belagt rustfrit stål viste fremragende korrosionsbestandighed ved de undersøgte betingelser, derimod var der ringe passivering af titanium, som da også havde den højeste korrosionshastighed blandt de undersøgte materialer ved 120 °C.

I dag er der stor interesse for nye katalysatormaterialer, som kan gøre det mulig at undgå ædelmetaller, men der mangler stadig et afgørende gennembrud. I dette arbejde er der benyttet en anden strategi, nemlig formindskelse af den anvendte katalysatormængde på anodesiden, ved brug af et bæremateriale.

Som mulig anodekatalysatorbærer er her undersøgt et SiC-Si-materiale. Udførelsen og præsentationen af dette findes i kapitel 5. Det katalytisk aktive IrO_2 er blevet påført på SiC-Si ved "Adams fusion synthesis", og karakteriseret med forskellige teknikker. XRD og BET målinger viste indflydelse af bærematerialet på egenskaberne af de dannede IrO_2 partikler. De fremstillede katalysatorer blev karakteriserede gennem cyklisk voltammetri og andre elektrokemiske metoder ved 25, 80, 120 og 150 °C. I overensstemmelse med den observerede variation i partikelstørrelsen, vil en 80 % loading af IrO_2 på bærematerialet give en maximal forbedring af aktivitet af katalysatoren. Målinger af elektrisk ledningsevne af pulverene viste en indflydelse af bærematerialet på pakningen af IrO_2 partiklerne. I dette tilfælde kunne det konkluderes, at et materiale med dårlig elektrisk ledningsevne godt kunne bidrage til en forøgelse af udnyttelsen af en elektrokatalysator. Resultaterne peger således på fremtidige perspektiver ved brug af lavt ledende keramiker som bærematerialer, og for videre forskning inden for dette emne.

En væsentlig del af arbejdet har været helliget udvikling af en metode til elektrokemisk karakterisering af katalysatorer ved forhøjede temperaturer.

Kapitel 6 består af afsluttende bemærkninger og forslag til fremtidigt arbejde.

Kapitel 7 udgøres af to artikler der er publicerede i løbet af projekt perioden.

Contents

List of Acronyms xi

List of Figures xiii

List of Tables xvii

1 Introduction 1

1.1 Hydrogen and modern society 1

1.2 Hydrogen production 2

1.3 Hydrogen and renewable energy 4

1.4 Targets of the project 6

1.4.1 Corrosion tests 6

1.4.2 Supported catalysts 7

1.5 List of publications 7

2 Theory and Background 9

2.1 Principles of water electrolysis 9

2.2 Thermodynamics and kinetics 10

2.2.1 Thermodynamics 10

2.2.2 Kinetics 11

2.3 Electrode reactions in PEM water electrolysis 19

2.3.1 Hydrogen evolution reaction (HER) 19
2.3.2 Oxygen evolution reaction (OER) 21
2.4 Electrochemical analysis techniques 26
2.4.1 Cyclic voltammetry 26
2.4.2 Steady state polarisation and corrosion studies 30
2.5 Physicochemical analysis techniques 33
2.5.1 X-Ray powder diffraction (XRD) 33
2.5.2 Scanning electron microscopy (SEM) 35
2.5.3 Energy dispersive X-ray spectroscopy (EDX) 37
2.5.4 Sample preparation for scanning electron microscopy (SEM) and energy dispersive X-ray spectroscopy (EDX) for catalyst powder analysis. 38
2.5.5 SediGraph particle size analysis 39
2.5.6 Brunauer-Emmett-Teller (BET) surface area 42
2.6 Electrocatalysts and their properties 43
2.6.1 Crystal structure of catalysts 43
2.6.2 Electrical conductivity 44
2.6.3 Catalyst support 46
2.6.4 Electrochemical behaviour of IrO_2 and RuO_2 47

3 High Temperature PEM Water Electrolysis 51

3.1 Principles of polymer electrolyte membrane (PEM) water electrolysis 51
3.2 High temperature PEM electrolysis. Advantages and drawbacks 54
3.3 Construction materials for high temperature PEM water electrolysis (bipolar plates and current collectors) 55
3.3.1 Metal coatings and a CVD technique 57
3.4 Oxygen evolution electrodes (OEEs) 58
3.5 Preparation of powder electrocatalysts and films for the OER 60
3.5.1 Adams fusion technique 60
3.5.2 Polyol method 61

3.5.3 Modified polyol method (colloid method) 61
3.5.4 Catalyst film preparation methods 62
3.6 DSA-type electrodes, their preparation and properties 62
3.7 Electrolytes for water electrolysis 66
3.7.1 Alkaline electrolyte 67
3.7.2 Solid oxide electrolyte 67
3.7.3 Acidic electrolyte and polymer electrolyte membranes 67
3.8 Catalyst supports in PEM systems and possibilities of use refractory ceramics 70

4 Construction Materials for High Temperature PEM Electrolyzers 73
4.1 Experimental part 73
4.1.1 Materials and reactants 73
4.1.2 Materials and sample preparation 74
4.1.3 Characterisation 74
4.2 Results and discussion 76
4.3 Conclusions 86

5 Preparation and Study of IrO_2/SiC−Si Supported Anode Catalyst for High Temperature PEM Steam Electrolyzers 87
5.1 Experimental part 87
5.1.1 Materials and reactants 87
5.1.2 SiC-Si/IrO_2 powder catalyst preparation 88
5.1.3 The electrochemical characterization 89
5.1.4 Physico-chemical characterization 93
5.2 Results and discussion 98
5.2.1 Structural and electrical properties 98
5.2.2 Electrochemical characterization 112
5.3 Conclusions 126

6 Concluding Remarks, Perspectives and Further Research 131

7 Papers **133**

References **158**

Appendix **184**

A Rietveld Treatment of the XRD Data for the SiC-Si Powder Catalyst Support **185**

B Optimisation of the SEM and EDX Sampling for Supported IrO_2/SiC-Si Catalyst **191**

B.1 Sample preparation 191

B.2 Results and discussion 192

B.2.1 SEM analysis 192

B.2.2 EDX analysis 192

B.3 Conclusion 197

List of Acronyms

AISI American Iron and Steel Institute

ASTM american society for testing and materials

BET Brunauer-Emmett-Teller

CR corrosion rate

CV cyclic voltammetry

CVD chemical vapour deposition

DSA dimensionally stable anode

EDX energy dispersive X-ray spectroscopy

EMF electromotive force

ESD equivalent spherical diameter

GDL gas diffusion layer

HER hydrogen evolution reaction

HHV higher heating value

HTPEMEC high temperature PEM electrolyzer cell

HTPEMFC high temperature PEM fuel cell

LHV lower heating value

MEA membrane electrode assembly

NIST National Institute of Standards and Technology

OEE oxygen evolution electrode

OER oxygen evolution reaction

ORR oxygen reduction reaction

PBI Poly[2,2'-(m-phenylene)-5,5'-bibenzimidazole

PEM polymer electrolyte membrane

PEMFC PEM fuel cell

PEMEC PEM electrolyzer cell

PTFE polytetrafluoroethylene

RF radio frequency

SCE standard calomel reference electrode

SCSI strong catalyst support interaction

SEM scanning electron microscopy

SHE standard hydrogen electrode

SOEC solid oxide electrolyzer cell

SOFC solid oxide fuel cell

SPE solid polymer electrolyte

SPEEK sulfonated polyetheretherketone

SPPQ sulfonated polyphenyl quinoxaline

TEM transmission electron microscopy

UPD underpotential deposited

URFC unitized regenerative fuel cell

XRD X-Ray powder diffraction

XRF X-ray fluorescence

List of Figures

1.1 A taste of 20th century: Smog over New York in 1988 [3]. . . 2

1.2 A possible application of hydrogen as an energy vector: the conversion of solar energy into fuel for transportation [4]. . . 5

2.1 The theoretical cell voltage [5] 12

2.2 Plot of the electrode current according to the Butler-Volmer equation. 17

2.3 Tafel behaviour at large η [6]. 19

2.4 Volcano plot of the HER for dirrerent metals [7]. 20

2.5 CV for Pt in 1.0 M H_2SO_4 solution [8]. 21

2.6 A Tafel plot for a Pt cathode in 5M H_2SO_4 [9]. 22

2.7 Schematic overpotential-*logi* curves for the OER on various oxides from acid solutions [10]. 24

2.8 Electrocatalytic activity in O_2 evolution at various oxide electrodes as a function of the enthalpy of the lower to higher oxide transition. (∘) Alkaline and (•) acid solutions [11]. . . . 25

2.9 Typical cyclic voltammogramm and its basic parameters [9]. . 27

2.10 Dependence of the peak potential one the log of potential sweep rate. 27

2.11 Dependence of the I_p on the v^2, showing the transition from reversible to irreversible regimes [9]. 27

2.12 A CV curve of the reversible electrochemical adsorbtion reaction [9]. 28
2.13 Hypothetical cathodic and anodic polarization diagram [12]. . 31
2.14 Illustration of Bragg's Law. 34
2.15 Scanning electron microscope schematic overview. 35
2.16 Interaction between an incident beam and a specimen [13]. . 37
2.17 The principle scheme of EDX spectroscopy. 38
2.18 Dependence of the components of the potential difference applied to an electrolysis cell on current flow [14]. 44
2.19 Rutile structure of IrO_2 45
2.20 The idealised structure of carbon-supported platinum catalyst for PEMFC [15]. 47
2.21 TEM image of a TiC-supported Ir catalyst [16]. The darkest zones are richer in Ir. 48
2.22 Cyclic voltammogram of $Ru_xIr_{1-x}O_2$ for x=1, 0.5 and 0 in 1 N H_2SO_4 [17]. 48
2.23 One-catalytic site model for the OER on Ir surface 50

3.1 The schematic diagram of a PEM electrolyzer cell [18]. 52
3.2 Commercial Hogen® PEM water electrolyzer unit [19]. 53
3.3 General structure of Poly[2,2'-(m-phenylene)-5,5'-bibenzimidazole (PBI) [20]. 68

4.1 The electrochemical cell. 75
4.2 Potential window for Pt and Au in 85% H_3PO_4, 120 °C, 1 mV/s (vs. SHE). 76
4.3 Tafel plot for AISI 316L in 85% H_3PO_4, 80 °C, 1 mV/s (vs. SHE). 77
4.4 Tafel plot for AISI 316L in 85% H_3PO_4, 120 °C, 1 mV/s (vs. SHE). 78
4.5 Tafel plot for AISI 321 in 85% H_3PO_4, 80 °C, 1 mV/s (vs. SHE). 79
4.6 Tafel plot for AISI 321 in 85% H_3PO_4, 120 °C, 1 mV/s (vs. SHE). 80

4.7 Tafel plot for titanium in 85% H_3PO_4, 120 °C, 1 mV/s (vs. SHE). 81

4.8 Tafel plot for tantalum in 85% H_3PO_4, 120 °C, 1 mV/s (vs. SHE). 82

4.9 SEM image of the CVD-tantalum coated stainless steel sample. Numbers refer to EDX points and areas measured. . . . 83

4.10 SEM of AISI 321 before(a) and after(b) the electrochemical tests. Numbers refer to EDX points and areas measured. . . . 84

4.11 SEM of Inconel®625 before(a) and after(b) the electrochemical tests. Numbers refer to EDX points and areas measured. 84

5.1 Three-electrode setup designed for controlled potential electrolysis study [9]. 89

5.2 A typical three-electrode cell (provided by Radiometer analytical [21]). 90

5.3 The electrochemical cell used in cyclic voltammetry (CV) experiments 95

5.4 A photograph of the electrochemical cell used in CV experiments. 96

5.5 The working electrode, designed for the CV experiments. . . 96

5.6 The electrical conductivity setup. The outermost rods are the anvil and spindle of a micrometer. 97

5.7 A photograph of the setup used for electrical conductivity measurements. 97

5.8 Cumulative mass percent finer vs. diameter of SiC-Si composite, ball milled during different time. 98

5.9 XRD spectrum for IrO_2. 99

5.10 Diffractogram of a ball milled SiC-Si support, showing peak assignations for corresponding phases. 100

5.11 XRD spectra for IrO_2, SiC-Si support, and a 50% composite. 101

5.12 XRD spectra for the prepared support powder. 102

5.13 Correlation of XRD relative phase signals with nominal powder composition. 104

5.14 Calculated average crystal sizes for different samples. 105

5.15 BET area trend with sample composition. 106

5.16 SEM micrograph of a sample with composition 60% IrO_2 and 40% SiC-Si support 107

5.17 SEM micrograph for EDX analysis at 5 kV on a gold plate. Sample composition: 60 wt.% IrO_2 and 40 wt.% SiC-Si support 108

5.18 Evolution of resistance with powder thickness for some samples. 109

5.19 Resistivities of all samples, calculated from conductivity values (the latter are presented in Figure 5.20). 110

5.20 Powder conductivities of all samples. 111

5.21 The Tafel plot for a SiC-Si plate. Scan rate 1 mV/s, electrolyte: 85% H_3PO_4, 120 °C. 112

5.22 Comparison of the voltammograms of the support and some samples. Scan rate 20 mV/s. 113

5.23 CV experiment of the SiC-Si support in H_3PO_4. Room temperature, 20 mV/s. 114

5.24 CV experiments in H_3PO_4 at room temperature. 20 mV/s. **a)** pure IrO_2. **b)** 90%. **c)** 80%. **d)** 70%. **e)** 60%. **f)** 50%. **g)** 40%. **h)** 30%. **i)** 20%. **j)** 10%. 115

5.25 CV experiment of pure IrO_2 at different scan speeds. Room temperature. 116

5.26 Calculated capacitance for different speeds. Pure IrO_2, room temperature. 117

5.27 CV experiments of several supported catalysts in 85% H_3PO_4 at room temperature. Scan rate 20 mV/s. 118

5.28 Capacitance calculated with charge integration. Same conditions as in Figure 5.26. 119

5.29 Peak current for the IrO_2 90% sample at different scan rates. 120

5.30 Integrated anodic peak charge for the IrO_2 90% sample at different speeds. H_3PO_4, room temperature. 121

5.31 Characteristic i-E curve for the reaction of adsorbed species [22]. 122

5.32 Integrated peak charge of all samples. 85% H_3PO_4, room temperature. Scan rate 20 mV/s. 123

5.33 Total capacitance for all sample compositions. 85 % H_3PO_4, room temperature. 123

5.34 CV experiments for the 90% IrO_2 sample at different temperatures in 85% H_3PO_4. Scan rate 20 mV/s. 124

5.35 CV experiments for some samples at 150 °C in 85% H_3PO_4. Scan rate 20 mV/s. 124

5.36 Evolution of capacitance with temperature for some samples in 85% H_3PO_4. Scan rate 20 mV/s. 125

A.1 Rietveld fitting for the X-Ray powder diffraction (XRD) data for SiC-Si support. 186

B.1 SEM images on carbon tape support, observed from two different detectors 192

B.2 SEM images on carbon support at two different voltages . . . 193

B.3 SEM images at low and high magnifications 194

B.4 SEM images at low voltage for different spot sizes 195

B.5 EDX analysis of the polished gold plate 197

List of Tables

2.1 Main components of scanning electron microscope and their functions. 36

2.2 Requisites for electrodes for technological applications 44

2.3 Factors of electrocatalysis at oxides 45

4.1 Alloys chemical composition. 74

4.2 The comparison of corrosion currents (approximate CRs) of different materials at T=30, 80 and 120 °C. 77

4.3 Measured corrosion potentials for forward and backward polarisation. 82

4.4 EDX data for the CVD-tantalum coated stainless steel sample, in wt.%. 82

4.5 The content of Ni and Ti in the tested alloys. 82

4.6 EDX analysis data of AISI 321 before(a) and after(b) the electrochemical tests. 83

4.7 EDX analysis data of Inconel®625 before(a) and after(b) the electrochemical tests. 85

5.1 Nominal composition of the samples 93

5.2 Quantitative analysis of the support by Rietveld treatment of the XRD data. 99

5.3 Relative intensity of XRD peaks for different powders with different composition. 103

5.4 Peak width and crystal size of selected peaks for the catalyst and the support. 103

5.5 BET area for all samples. 104

5.6 EDX data for SiC-Si/IrO_2 sample (SiC-Si:IrO_2 = 40:60). . . . 105

5.7 Comparison of properties of IrO_2 and SiC-Si compound. . . . 127

B.1 X-ray line energies for C, Si and Ir 193

B.2 EDX on carbon support 194

B.3 EDX data analysis at low and high magnifications 195

B.4 EDX data at low voltage and different spot sizes 196

B.5 EDX analysis of supported catalyst powder, dispersed in ethanol and applied on gold plate, 5 kV 196

Chapter 1

Introduction

"Water, taken in moderation, cannot hurt anybody."

(Mark Twain)

1.1 Hydrogen and modern society

Energy is a main aspect of modern life. Traditionally, the ever-increasing need for mechanical work in industrialised societies has led to an intense investment on energy-related research and development. In the last years, there has been an increasing focus on energy technologies. From energy sources, going through transformation and distribution, to energy system management, the prominence of energy in modern society has been reflected in its comprehensive flourishing.

However, in recent decades, the growing public awareness of the effects of man on the environment through the different forms of pollution, ecosystem alteration, and lastly, the alteration of climate, have shown the need for a different model of interaction with natural systems, where conservation and sustainability are central concepts. In this aspect, much of the responsibility for the degradation of environment and human health is attributed to pollution sources coming from the energy sector. This way, exhaust emissions from vehicles, as well as emissions from industries and power plants, contribute to most of the anthropogenic sources of greenhouse gases, CO_2, NO_x and other substances. This state of things requires, thus, the development of new energy technologies at all levels.

Figure 1.1: A taste of 20th century: Smog over New York in 1988 [3].

Hydrogen has been known as a fuel ever since its discovery. A main difference between hydrogen and other fuels is that, since the only combustion product is water, it is one of the cleanest fuels available. It is mostly because of this that hydrogen has been proposed as an alternative fuel in substitution of fossil fuels, most notably oil fractions like gasoline or diesel [23].

Although hydrogen is commonly mistaken as an energy source, there are no significant amounts of elemental hydrogen on the Earth surface. It is rather an energy carrier, which means that its generation is as important as its transportation and consumption in terms of efficiency and performance. In the following section, a brief review of the main options for hydrogen production are described.

1.2 Hydrogen production

Since the two main sources for hydrogen on Earth are hydrocarbons and water, all current methods used for hydrogen production involve extraction from one of them. There is an important difference in terms of energy content between them.

Typical hydrocarbons like petroleum or natural gas are substances relatively reduced with respect to the oxidising conditions in the Earth atmosphere, which is rich in O_2. Thus, it is possible to extract energy from hydrocarbons by oxidising them, to CO_2 and water as final products, which is the basis of

the use of fossil fuels as energy sources. The simplest hydrocarbon, methane, burns following the reaction:

$$CH_4 + 2\,O_2 \longrightarrow 2\,H_2O + CO_2, \quad \Delta H = -889\ kJ/\text{mol} \tag{1.1}$$

The general reaction for burning of hydrocarbons is:

$$C_nH_2n + \frac{3n+1}{2}O_2 \longrightarrow (n+1)H_2O + nCO_2, \quad \Delta H<0 \tag{1.2}$$

The main advantage of the use of hydrocarbons for hydrogen production is that they do not need an external energy source. The reforming of natural gas is a good example [24]:

$$CH_4 + H_2O \rightleftharpoons CO + 3\,H_2, \quad \Delta H = 206\ \ \text{kJ/mol} \tag{1.3}$$

$$CH_4 + 2\,H_2O \rightleftharpoons CO_2 + 4\,H_2, \quad \Delta H = 165\ \ \text{kJ}/\text{mol} \tag{1.4}$$

Even though these reactions are very endothermic, the process can be fuelled with the combustion of more methane or other fuel, making thus the whole process self-sustained in terms of energy. The absence of the external energy need makes this technology more competitive than the ones based on hydrogen production from water.

Water is, on the contrary, a substance that cannot be further oxidised to extract energy from it. In order to obtain hydrogen from water, energy needs to be spent, according the equation 1.5:

$$H_2O_{(g/l)} \longrightarrow H_{2(g)} + \frac{1}{2}O_{2(g)}, \quad \Delta H > 0 \tag{1.5}$$

Energy needed to split water from liquid or gas phase is different [15]:

For water steam:

$$H_2O_{(g)} \longrightarrow H_{2(g)} + \frac{1}{2}O_{2(g)}, \quad \Delta H = +242\,\text{kJ/mol} \quad \text{(LHV)} \tag{1.6}$$

For liquid water:

$$H_2O_{(l)} \longrightarrow H_{2(g)} + \frac{1}{2}O_{2(g)}, \quad \Delta H = +286\,\text{kJ/mol} \quad \text{(HHV)} \tag{1.7}$$

The difference in ΔH of 44 kJ/mol between the lower heating value (LHV) and the higher heating value (HHV) is the molar enthalpy of vaporisation of water.

1.3 Hydrogen and renewable energy

When Jules Verne wrote his famous novel about the Mysterious Island which was published in Paris between 1874 and 1875 (L'île mystéruse), and predicted "water replacing coal", he was aware of the technology of electrolysis, which was discovered by William Nicholson in 1800.

Electrolysis is a word coming from Greek, where "lysis' means "cutting" or "separating".

However, hydrogen production from water by electricity has the disadvantage of energy required for being produced. At the same time, compared fossil fuels as gasoline and diesel, an equivalent mass of hydrogen contains about three times more energy.

But one would ask then: "Why bother synthesising hydrogen from water, when it can be done from hydrocarbons?". The increasing fossil fuel prices can only worsen this disadvantage, as the more the energy costs, the less economical sense water splitting has.

The answer lies in the so-called renewable energy sources. Basically, these can be described as natural energy sources that have, in principle, an infinite supply. Most of these sources, like biomass or wind, come ultimately from natural sources. Others, like geothermal energy, are not particularly renewable, but their final depletion is so far in the future that, for all intents and purposes, they can be considered as renewable. A main issue with most of these sources is their availability in time.

Decentralized production of hydrogen by means of water electrolysis is favourable in this case. When renewable energy sources are considered, electrolysis is a practical way of converting the surplus electrical energy into chemical energy and to be used when the power is needed [25].

For example, considering sunlight as a source of energy, photovoltaics is a technology which is used for harvesting solar energy. It will collect as much energy as possible in the given amount of time. This means that the limiting factor for the energy throughput will be the energy source itself. Since the amount of sunlight reaching the Earth's surface depends on astronomic factors (which are predictable) and weather (which is not), it is easy to see that solar energy and its related technologies are inherently unsteady as energy suppliers.

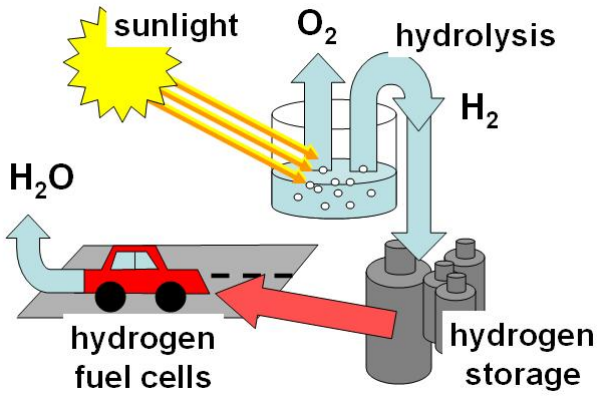

Figure 1.2: A possible application of hydrogen as an energy vector: the conversion of solar energy into fuel for transportation [4].

This problem is especially important when considering energy conversion to electricity. It is a known characteristic of electric energy that generation (supply) and consumption (demand) have to be carefully balanced to maintain the AC power grids working, as power lows and blackouts cause enormous economic losses or even equipment breakdown.

In this context, there is a great need of improving the availability of renewable energy sources. A way of achieving this is to store, at least temporarily, the generated energy, which is available for consumption during high-demand periods [26]. This is where the extensive use of hydrogen can be helpful.

Production of hydrogen from the energy of blowing wind attracts much attention. The wind power is stored in the form of produced hydrogen to even out the fluctuations in production due to natural variation of the wind. One of the proper wind–hydrogen systems has proven a valuable experience for the coming generations of wind-hydrogen systems. The station is located on the island of Utsira in the Atlantic Ocean, where Norsk Hydro and its partners have been running a wind generator-based hydrogen system since 2004 [25]. Two wind generators of 600kW each deliver electric energy to a small electrolyzer which stores its hydrogen under pressure. The hydrogen is used for powering a number of houses on this small island. A 12kW fuel cell from a Danish producer, IRD A/S, delivering the power in addition to 50kW of electric energy originating from an internal combustion-based generation unit. The combustion generator has an appreciably longer start up time than the fuel cell and the interplay of the two has proven a development challenge.

As an energy storage option, the hydrogen cycle can be very appropriate.

Therefore, most of long term visions about the use of hydrogen as an energy carrier include electrolysis. It requires an inexpensive reactant, water, and electricity to split it. From an environmental point of view, hydrogen has also the advantage of being a relatively clean energy carrier [23, 27]. The main drawbacks of hydrogen as compared to similar technologies are the lower round-trip efficiency, and the high dependency from electricity prices [28].

Polymer electrolyte membrane (PEM) water electrolysis systems offer several advantages over traditional technologies, including higher energy efficiency, higher production rates, and more compact design [29]. This method of hydrogen production is envisioned in a future society where hydrogen as the energy carrier is incorporated in an idealized "energy cycle". In this cycle, electricity from renewable energy sources is used to electrochemically split water into hydrogen and oxygen [30].

This technology is environmentally friendly and usually possess more compact size characteristics and power cost. Besides the high purity of produced gases, there is an opportunity of obtaining compressed gases directly in the installation [31].

1.4 Targets of the project

1.4.1 Corrosion tests

The first part of the project has been focused on selection and development of construction materials for porous gas diffusion layers and bipolar plates for high temperature electrolyzer stack. Intended corrosion studies, evaluating corrosion stability of materials in phosphoric acid and temperatures higher than 100 °C are scarce. The anodic part of the system was in the main focus in this work.

A series of austenitic steels (AISI 316L, AISI 321 and AISI 347) and Ni-based alloys (Hastelloy® C-276, Inconel® 625 and Incoloy® 825), as well as titanium and tantalum, were tested. In order to characterise the samples, anodic polarisation was performed on electrodes made of the selected materials under experimental conditions, simulating those of an electrolysis stack.

It was found that among tested candidates, the only capable of high resistance under these conditions was actually the CVD-tantalum coated stainless steel.

1.4.2 Supported catalysts

Another part of the project involved developing and testing of a catalyst support material for the oxygen evolution reaction (OER). The support was implemented in order to reduce high noble electrocatalyst loading.

Importance of use of a support for the catalyst and further research towards the development of more efficient and lasting oxygen evolution electrodes (OEEs) are discussed. Among promising candidates, a commercial SiC-Si composite material was finally selected and studied in this work.

One of the main goals was studying of influence of the selected support on the electrochemical behaviour of active IrO_2 catalyst. To accomplish this, supported catalysts with different compositions were prepared, in addition to pure samples of both IrO_2 and SiC-Si.

The electrochemical characterisation of the electrodes was performed using the CV technique in experimental conditions similar to those found in high temperature PEM electrolyzer cells (HTPEMECs). Physico-chemical characterisation of these materials was done by means of the X-Ray Diffraction, implementing the Scherrer equation for the crystal size calculations. BET surface area experiments were done for estimating the specific surface area of the materials, being an important factor in the electrode activity. Powder electric conductivity measurements were also performed for all samples in order to assess the effect of the support on conductivity of the electrodes.

1.5 List of publications

The research results have been reported in the following publications:

[32] A. Nikiforov, D. Aili, M.K. Hansen, I. Petrushina, E. Christensen, J.O. Jensen, Q. Li, and N.J. Bjerrum. Water electrolysis at elevated temperatures. In *Hydrogen + Fuel Cells 2009 conference, poster presentation*, Vancouver, Canada, May 31st - June 3rd 2009.

[33] I.M. Petrushina, A.V. Nikiforov, and N.J. Bjerrum. Corrosion behavior of highly austenitic stainless steels and ni-based alloys at elevated temperatures in concentrated phosphoric acid solutions. In *ICHMS'2009, 11th International Confrence, abstract, oral presentation*, pages 162–163, Yalta-Crimia-Ukraine, August 25th-31st 2009.

[34] N.J. Bjerrum, I.M. Petrushina, V. Bandur, and A.V. Nikiforov. Water electrolysis at elevated temperatures. In *ICHMS'2009, 11th In-*

ternational Confrence, abstract, oral presentation, pages 842–843, Yalta-Crimia-Ukraine, August 25th-31st 2009.

[35] A.V. Nikiforov, I.M. Petrushina, E. Christensen, N.J. Bjerrum, and A.L. Tomás-García. Corrosion behaviour of construction materials for high temperature water electrolysers. In *NMES'2010, 8th International Symposium, abstract, oral presentarion*, pages 16–17, Shanghai, China, July 1-15th 2010.

[36] A.V. Nikiforov, I.M. Petrushina, E. Christensen, A. L. Tomás-García, and N.J Bjerrum. Corrosion behaviour of construction materials for high temperature steam electrolysers. *International Journal of Hydrogen Energy*, 36(1):111–119, January 2011. ISSN 0360-3199. doi: 10.1016/j.ijhydene.2010.09.023.

[37] A.V. Nikiforov, I.M. Petrushina, E. Christensen, A.L. Tomás-García, and N.J. Bjerrum. Development of catalyst support for oxygen electrode for PEM steam electrolysers. In *2nd CARISMA international conference on progress in MEA materials for medium and high temperature polymer electrolyte fuel cells, abstract, poster presentation*, page 69, La Grande Motte, France, September 19th-22nd 2010.

[38] A. V. Nikiforov, A. L. Tomás-García, I. M. Petrushina, E. Christensen, and N. J. Bjerrum. Preparation and study of IrO_2/SiC-Si supported anode catalyst for high temperature PEM steam electrolysers. *International Journal of Hydrogen Energy*, 36(10):5797–5805, May 2011. ISSN 0360-3199. doi: 10.1016/j.ijhydene.2011.02.050.

[39] A. L. Tomás-García, A.V. Nikiforov, I.M. Petrushina, E. Christensen, and N.J Bjerrum. SiC-Si as a support material for oxygen evolution electrode in PEM steam electrolysers. In *Hydrogen + Fuel Cells 2011 conference, abstract contribution*, Vancouver, Canada, May, 15th - 18th 2011.

[40] A. V. Nikiforov, A. L. Tomás-García, I. M. Petrushina, E. Christensen, and N. J. Bjerrum. SiC-Si as a support material for oxygen evolution electrode in PEM steam electrolysers. In *9th European Symposium on Electrochemical Engineering (9th ESEE), abstract, oral presentation*, page 83, Chania, Crete, Greece, June 19th - 23rd 2011.

Chapter 2

Theory and Background

2.1 Principles of water electrolysis

The principles behind water electrolysis include the electrochemical splitting of water into hydrogen at the cathode and oxygen at the anode. From the energy point of view it is a conversion of an electrical energy to chemical energy in the form of hydrogen. The overall chemical reaction of water splitting process was presented in Section 1.2, equation 1.5.

Conventionally, 3 types of electrolyzers exist, defined by the type of electrolyte implemented. Those are alkaline, acidic, and solid oxide electrolyzer cell (SOEC). Depending on the type of electrolyzer, different half-reactions take place at anode and cathode compartments:

- Alkaline:

$$cathode : 2\,H_2O + 2\,e^- \rightarrow H_2 + 2\,OH^- \tag{2.1}$$

$$anode : 2\,OH^- \rightarrow \frac{1}{2}O_2 + 2\,H_2O + 2\,e^- \tag{2.2}$$

- Acidic:

$$cathode : 2\,H^+ + 2\,e^- \rightarrow H_2 \tag{2.3}$$

$$anode : H_2O \rightarrow \frac{1}{2}O_2 + 2\,H^+ + 2\,e^- \tag{2.4}$$

- SOEC:

$$cathode : \mathrm{H_2O} + 2\,\mathrm{e^-} \rightarrow H_2 + \mathrm{O^{2-}} \tag{2.5}$$

$$anode : \mathrm{O^{2-}} \rightarrow \frac{1}{2}\mathrm{O_2} + 2\,\mathrm{e^-} \tag{2.6}$$

The main commercial electrolysis technology used nowadays is the alkaline process (equations 2.1, 2.2). The electrolyte is an aqueous alkaline solution, with nickel-based alloys as electrodes. The working temperature is usually around 70-80 ℃. This method has the advantage of long-term performance and relatively low investment costs. On the other hand, it has the disadvantage of having high energy requirements, mainly because of high activation energies. Another problem is that, being the electrolyte alkaline, the system needs to be CO_2-free, in order to avoid the formation of carbonates in the cell. Current research on alkaline electrolysis focuses on new electrode materials, electrolyte additives and designs [41].

Being the only practical todays technology for producing hydrogen from water, the main advantage of electrolysis is the high gas purity achieved. However, the high production costs compared to hydrogen from fossil sources results to only around 0.1% of worldwide hydrogen production coming from water electrolysis [42].

2.2 Thermodynamics and kinetics

2.2.1 Thermodynamics

Both thermodynamics and reaction kinetics should be considered when electrochemically splitting water into hydrogen and oxygen. The Gibbs free energy (ΔG) for the net reaction for producing hydrogen and oxygen by water electrolysis is given by:

$$\Delta G = \mu\mathrm{H}_{2(g)} + \frac{1}{2}\mu\mathrm{O}_{2(g)} - \mu\mathrm{H_2O}_{(l)} = \Delta G^0 + RTln(p\mathrm{H_2}p\,\frac{1}{2}\,\mathrm{O_2}) \tag{2.7}$$

where $\mu\mathrm{H}_{2(g)}$, $\mu\mathrm{O}_{2(g)}$ and $\mu\mathrm{H_2O}_{(l)}$ are the chemical potentials of hydrogen, oxygen and water respectively, $p\mathrm{H_2}$ and $p\mathrm{O_2}$ are the partial pressures of hydrogen and oxygen respectively and ΔG^0 is the Gibbs free energy at standard conditions (1 atm, 25 °C).

The energy balance for the cell reaction may also be written, with the energy required to break and form molecular bonds and to bring the reactants to their reference states being the enthalpy (ΔH):

$$\Delta G = \Delta H - T\Delta S \tag{2.8}$$

giving (at standard conditions):

$$U_{\text{tn}} = -\frac{\Delta H}{nF} \tag{2.9}$$

where U_{tn} is the thermoneutral potential difference. If $E_{\text{cell}} > U_{\text{tn}}$, heat is lost from the cell (the cell produces surplus heat). When the cell potential $E_{\text{cell}} < U_{\text{tn}}$ the cell absorbs heat from the environment, the produced Joule heat does not meet the heat demand and the cell cools down if the heat is not provided by other means.

Efficiencies for the overall reaction 1.5 can also be written with the thermal energy efficiency defined as:

$$\eta_{\Delta H} = \frac{U_{\text{tn}}}{E_{\text{cell}}} \times 100\% \tag{2.10}$$

The energy efficiency, based on Gibbs free energy is defined as:

$$\eta_{\Delta G} = \frac{E_{\text{eq}}}{E_{\text{cell}}} \times 100\% \tag{2.11}$$

In an electrochemical process the energy efficiency is better expressed by $\eta_{\Delta G}$ which represents the efficiency in terms of the available work.

Since water electrolysis becomes increasingly heat consuming with temperature (Figure 2.1), larger portion of the total energy demand can be provided as heat at elevated temperatures. This provides an opportunity to utilize the Joule heat, that is inevitably produced due to the passage of electrical current through the cell. In this way, the overall electricity consumption and, thereby, the H_2 production price can be reduced.

2.2.2 Kinetics

The equilibrium potential (E_{eq}) is the theoretical electromotive force (EMF), calculated for the net reaction from the equation 2.12:

$$E_{\text{eq}} = -\frac{\Delta G}{nF} \tag{2.12}$$

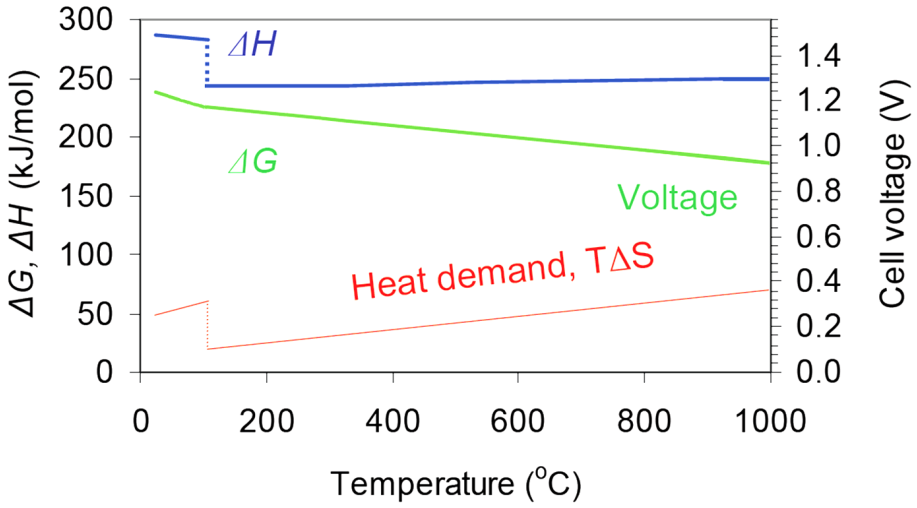

Figure 2.1: The theoretical cell voltage [5]

The equilibrium potential (E_{eq}) of electrochemical splitting of water can be found using the Nernst equation:

$$E_{\text{eq}} = E^0 - \frac{RT}{nF} ln(p_{H_2} p^{\frac{1}{2}}{}_{O_2}) \tag{2.13}$$

where n is the number of electrons involved, R is the gas constant, T is temperature (K), F is the Faraday constant, and E^0 is the standard potential. At standard conditions (298 K, 1 atm) $E_{\text{eq}} = 237349/2 \cdot 96487 = 1.230$ V. Although thermodynamics gives the minimum potential required to split water, due to the kinetics of the electrochemical reactions there will always be overpotentials decreasing the efficiency:

$$E_{\text{cell}} = E^{\text{eq}} + \eta_{\text{anode}} - \eta_{\text{cathode}} + IR \tag{2.14}$$

where E_{cell}, η_{anode}, η_{cathode}, and IR represent the actual cell potential, the anodic overpotential, the cathodic overpotential, and the voltage gain due to the cell ohmic resistance correspondingly. One of the main targets of the electrolytic industry is to achieve an applied cell potential difference, E_{cell}, as close as possible to the thermodynamic value E_{eq}.

Both two overpotentials and the ohmic resistance vary with current density. The resistance is given by the Ohm's law, whereas the overpotentials can be given by the Tafel equation (which is a simplification of the Butler-Volmer equation (see equation 2.29).

The overpotential terms for the anodic (η_a) and cathodic (η_c) reactions increase logarithmically with I, while the ohmic drop (IR) rises linearly.

This means that ohmic problems become more and more important as the electrolysis rate is increased.

Minimizing of η_a and η_c is a question of electrocatalysis and will be in details discussed in Section 2.6, while the ohmic drop is in principle a problem of cell engineering and electrolyte, although the two quantities are often interrelated.

A general electrode reaction in an electrochemical cell can be simplified to a simple charge transfer reaction between an oxidized and a reduced species:

$$\mathrm{O} + \mathrm{ne}^- \rightleftarrows \mathrm{R} \tag{2.15}$$

where O and R are oxidized and reduced species respectively and n accounts for the number of electrons transferred per reaction. With no current applied to the cell, potential of the electrode is given by the Nernst equation, introduced previously (2.13):

$$E^{\mathrm{eq}} = E^0 - \frac{RT}{nF} ln \left(\frac{C_r}{C_o} \right) \tag{2.16}$$

If current is applied to the cell, the net current i_{net} is expressed as a difference between cathodic and anodic currents:

$$i_{\mathrm{net}} = i_{\mathrm{a}} + i_{\mathrm{c}} \tag{2.17}$$

where i_c is cathodic current, which is negative and i_a is the anodic current which is positive. The forward reaction rate and the backward reaction rate for the electrode reaction 2.15 are linked to the current at the electrodes. Furthermore it is assumed that the electrode reaction is a first order reaction and the rate constants are named in a similar way, i.e. k_f and k_b. The concentrations of oxidised and reduced species are functions of distance from the electrode (x) and the time (t). The currents at the electrode surfaces are then given by:

$$i_{\mathrm{c}} = -nFAk_f C_O(0,t) \tag{2.18}$$

$$i_{\mathrm{a}} = nFAk_b C_R(0,t) \tag{2.19}$$

where A is the surface area of the electrode. The net reaction rate is the forward reaction rate plus the reaction rate of the backward reaction. This

results to the extended expression of the net current, which is given by:

$$i_{\text{net}} = i_{\text{a}} + i_{\text{c}} = nFA(k_b C_R(0,t) - k_f C_O(0,t)) \tag{2.20}$$

A general reference point for a potential at the electrode is $E^{0'}$. The potential reference point is defined as the potential where the forward and backward rate constants are equal. The cathodic and anodic activation energies are defined as $\Delta G^{\ddagger}_{0c}$ and $\Delta G^{\ddagger}_{0a}$. If the potential changes, so does the energy needed to reside an electron on the electrode. By introducing the transfer coefficient, α, the Gibbs free energy of the electrodes equals:

$$\Delta G^{\ddagger}_{c} = \Delta G^{\ddagger}_{0c} - \alpha nF(E - E^{0'}) \tag{2.21}$$

$$\Delta G^{\ddagger}_{a} = \Delta G^{\ddagger}_{0a} - (1-\alpha)nF(E - E^{0'}) \tag{2.22}$$

The transfer coefficient can range from zero to unity. It can be used to express the rate constants in case it is assumed that the rate constants can be described by the Arrhenius equation:

$$k_f = E_{A_f} exp\left(\frac{\Delta G^{\ddagger}_{c}}{RT}\right) \tag{2.23}$$

$$k_b = E_{A_b} exp\left(\frac{\Delta G^{\ddagger}_{a}}{RT}\right) \tag{2.24}$$

where E_{A_f} and E_{A_b} are the activation energies for the forward and backward reactions correspondingly. The Arrhenius expression and the equations for $\Delta G^{\ddagger}_{0c}$ and $\Delta G^{\ddagger}_{0a}$ can be combined, giving:

$$k_f = E_{A_f} exp\left(\frac{\Delta G^{\ddagger}_{0c}}{RT}\right) \cdot exp\left(\frac{-\alpha nF}{RT}\left(E - E^{0'}\right)\right) \tag{2.25}$$

$$k_b = E_{A_b} exp\left(\frac{\Delta G^{\ddagger}_{0a}}{RT}\right) \cdot exp\left(\frac{(1-\alpha)nF}{RT}\left(E - E^{0'}\right)\right) \tag{2.26}$$

Assuming that a solution has the same concentration of oxidant and reactant. Then $E = E^{0'}$ and the rate of the forward and the backward reaction are the same, $k_f C_O = k_b C_R$. Since the concentrations, the rate constants are equal and it is shown that the reference point $E^{0'}$ is the potential at which the rate constants have the same value.

The entire first part of the equations can be considered as a rate constant at the reference potential $E = E^{0'}$ and is called the standard rate constant k^0.

$$k_f = k^0 \cdot exp\left(\frac{-\alpha nF}{RT}\left(E - E^{0'}\right)\right) \tag{2.27}$$

$$k_b = k^0 \cdot exp\left(\frac{(1-\alpha)nF}{RT}\left(E - E^{0'}\right)\right) \tag{2.28}$$

This hides the temperature dependence of k^0. The values for the rate constants can now be inserted into the equation for the total current and this gives the Butler-Volmer formulation of the electrode kinetics, which is an important equation linking together electrode current and potential:

$$\begin{aligned} i &= i_a + i_c \\ &= nFAk^0\left(exp\left(\frac{(1-\alpha)nF}{RT}\left(E - E^{0'}\right)\right)C_R(0,t)\right. \\ &\qquad \left. - exp\left(\frac{-\alpha nF}{RT}\left(E - E^{0'}\right)\right)C_O(0,t)\right) \end{aligned} \tag{2.29}$$

Sometimes the Faraday's constant, the ideal gas constant and the temperature is combined to a single symbol "f" hiding the other temperature dependence:

$$f = \frac{nF}{RT} \tag{2.30}$$

The standard rate constant k^0 is a simple measure of the kinetics in the redox reaction. High values of the k^0 mean that the reaction reaches equilibrium fast. The reverse is true for low values of k^0. The highest measured values are 1-10 cm/s for very simple electron transfer reactions such as the reduction/oxidation of many aromatic compounds as it only requires electron transfer and resolvation.

It is important to remember that the reaction rate constants k_f and k_b can have relatively large values even though k^0 is small if an extreme potential relative to $E^{0'}$ is applied. The result is that the electrical energy is used to achieve the required activation energy.

When there is no net current at equilibrium there will still be a Faradaic activity at the electrode, but the anodic and cathodic currents are equal in this case. It can be interpreted as an exchange current, which can be

expressed in the terms of k^0. It will be shown below with the Butler-Volmer equation. With no net current the Butler-Volmer formulation gives:

$$\begin{aligned} 0 &= nFAk^0(exp((1-\alpha)f(E-E^{0'}))C_R(0,t) - exp(-\alpha f(E-E^{0'}))C_O(0,t)) \\ &\Leftrightarrow \\ &nFAk^0 exp(-\alpha f(E-E^{0'}))C_O(0,t) \\ &= nFAkexp((1-\alpha)f(E-E^{0'}))C_R(0,t) \end{aligned} \tag{2.31}$$

The concentration of oxidant and reactant at equilibrium is not a function of distance hence the concentrations are equal in bulk solution and at the surface. The equilibrium concentrations are called C_0^* and C_R^*:

$$nFAk^0 exp(-\alpha f(E-E^{0'}))C_0^* = nFAkexp((1-\alpha)f(E-E^{0'}))C_R^* \tag{2.32}$$

Either side of this equation can be interpreted as the exchange current i_0. If the left side of the equation is used then:

$$i_0 = nFAk^0 C_0^* exp(-\alpha f(E-E^{0'})) \tag{2.33}$$

The exchange current density (i_0) is a material dependent value and is often used for comparison of the electrocatalytic activity of different catalysts. The exchange current density is a fundamental property of an electrode's behaviour and it can be defined as the rate of reaction at an equilibrium electrode, expressed in terms of current density. A high exchange current density means that the rate of reaction is fast and this means that the catalyst is effective.

Instead of using the standard rate constant k^0 as a reference, the value of the exchange current i_0 can be used. The advantage of using the exchange current is that the current can be described as a deviation from the equilibrium potential which is called the overpotential (η). This eliminates the use of the formal potential $E^{0'}$.

Dividing by the expression for the exchange current and eliminating the formal potential $E^{0'}$, one of the approximations derives the so-called "current-overpotential" equation from the Butler-Volmer formulation [6]:

$$i = i_0(e^{(1-\alpha)f\eta} - e^{-\alpha f\eta}) \tag{2.34}$$

This approximation assumes that the solution is well stirred, or currents are kept so low that the surface concentrations do not differ appreciably from

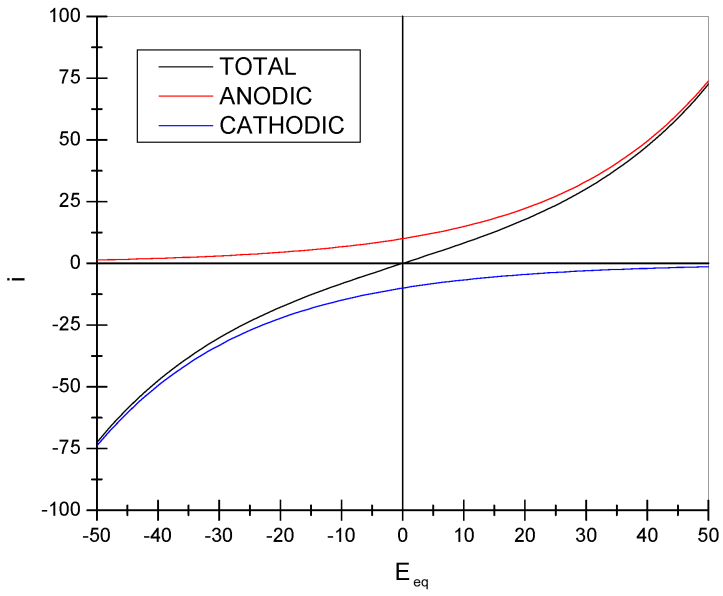

Figure 2.2: Plot of the electrode current according to the Butler-Volmer equation.

the bulk values, which means that the mass-transfer effect is completely excluded. This behaviour is depicted on picture 2.2. The black curve shows the total current, which is the sum of anodic and cathodic components i_c and i_a.

At low values of the overpotential the current-overpotential curves are linear. This is because of the limits of the natural exponential function at low values. For values of x, the exponential e^x can be approximated as $1 + x$. Applying this to the Butler-Volmer equation simplifies it significantly:

$$\frac{i}{i_0} = e^{(1-\alpha)f\eta} - e^{-\alpha f\eta} = (1 - (1-\alpha)f\eta) - (1 - \alpha f\eta) \quad \text{for } \eta \to 0 \tag{2.35}$$

$$\Rightarrow i = -i_0 f\eta \tag{2.36}$$

which shows that the net current is linearly related to overpotential in a narrow potential range close to E_{eq}. The ratio $-\eta/i$ has units of resistance

and is called the charge-transfer resistance and is given the symbol R_{ct}:

$$R_{\mathrm{ct}} = \frac{RT}{nFi_0} \tag{2.37}$$

This parameter is the negative reciprocal slope of the current-overpotential curve where it passes through the origin (η=0, i=0) and serves as an index for kinetic facility and can be evaluated directly in some experiments.

For large values of overpotentials (either negative or positive) the first part of the Butler-Volmer equation can be neglected and simplifies to:

$$\frac{i}{i_0} = e^{(1-\alpha)f\eta} - e^{-\alpha f\eta} = -e^{-\alpha f\eta} \quad \text{for } \eta \to \infty \tag{2.38}$$

If instead the overpotential is isolated it gives:

$$\begin{aligned} &\frac{i}{i_0} = -e^{-\alpha f\eta} \Leftrightarrow -ln\left(\frac{i}{i_0}\right) = -\alpha f\eta \Leftrightarrow \\ &\eta = \frac{1}{\alpha f} ln\left(\frac{i}{i_0}\right) \Leftrightarrow \eta = \frac{1}{\alpha f}(lni - lni_0) \Leftrightarrow \\ &\eta = \frac{RT}{nF\alpha}(lni - lni_0) = \alpha - (1-x)lni \end{aligned} \tag{2.39}$$

The last equation is called the Tafel equation and the associated Tafel plot (logarithm of current density vs. overpotential) is very useful for determining kinetic parameters. The exchange current density can be determined experimentally directly from the Tafel plot (Figure 2.3). The use of the above equation will be showed in details in Section 2.4.2.

The term $\frac{RT}{nF\alpha}$ is defined as the Tafel slope, which can be used to determine the reaction mechanism (see Section 2.3.2).

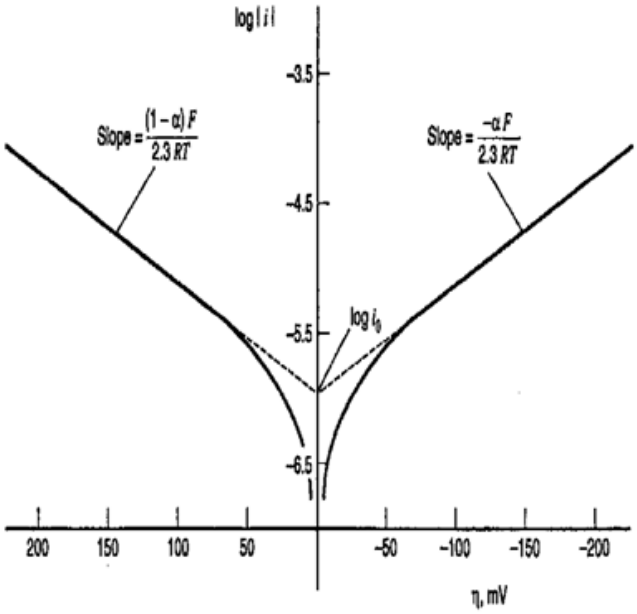

Figure 2.3: Tafel behaviour at large η [6].

2.3 Electrode reactions in PEM water electrolysis

2.3.1 Hydrogen evolution reaction (HER)

The electrochemical activity of hydrogen evolution reaction (HER) for different metals can be compared by a so-called "Volcano plot", where *log* of exchange current density is related to the bond energy of chemisorbed H to the metal [7]. As can be seen in Figure 2.4 the metals of intermediate bond-strength energy are the most active towards the HER. Those are represented by the noble metals. For the metals of low bond-strength the H desorption step becomes the rate determining, while for the metals with the high bond-strength the H desorption step becomes the rate determining [43]. Particularly, for the acidic type of electrolyzer (equations 2.4 and 2.3), the noble metals are of high interest due to their high corrosion resistance in such media.

Pt is known as the most active catalyst for the HER and is commonly used in PEMFCs both for the hydrogen oxidation and oxygen reduction [20, 44].

The HER on platinum catalyst occurs on a strongly bounded underpotential deposited (UPD) monolayer of H atoms. UPD hydrogen starts to cover the Pt surface at the potential ca. +0.35 V vs. standard hydrogen electrode

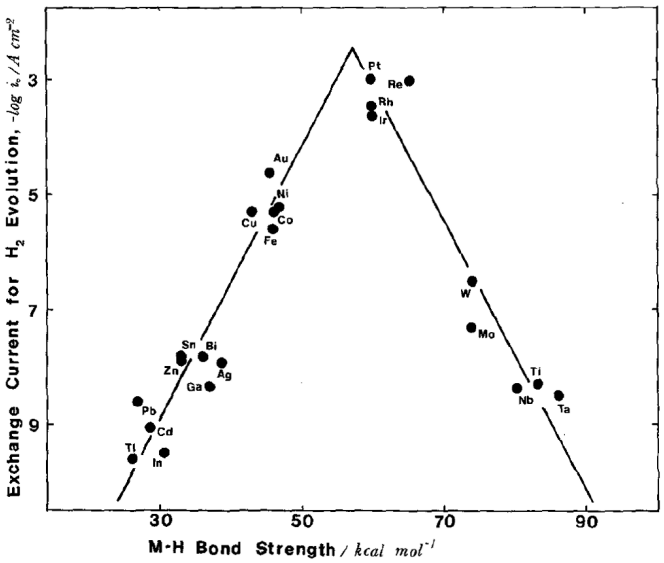

Figure 2.4: Volcano plot of the HER for dirrerent metals [7].

(SHE) and at 0 V vs. SHE the Pt metal surface is fully covered with H atoms [43].

Based on the thermodynamical considerations, it is not possible for UPD H to form H_2 when $E \geq 0$ (in this condition the M-to-H bond energy is higher than $\frac{1}{2}H_2$ bond. A typical voltammogram of Pt in 1.0 M H_2SO_4 solution is shown in Figure 2.5 and presents the peaks of weakly and strongly adsorbed hydrogen at ca. 0.12 and 0.25 V vs. SHE electrode respectively. This is a classic example of the adsorption process (more details in Section 2.4.1). The formation of an oxide film on the platinum surface can be noticed during the further anodic sweep. At the potential around 0.7 V vs. SHE the film is reduced back to metallic platinum.

The presence of adsorbed hydrogen atoms on the metallic surface can give rise to different reaction routes, while two mechanisms are generally considered important [9]:

$$\begin{aligned} \text{I}\cdot \quad & \mathrm{H^+ + e^- + M \rightarrow \mathit{M-H}} \\ & \mathrm{2\,M{-}H \rightarrow 2M + H_2 + e^-} \\ \text{II}\cdot \quad & \mathrm{H^+ + e^- + M \rightarrow \mathit{M-H}} \\ & \mathrm{M{-}H + H^+ + e^- \rightarrow \mathit{M} + H_2} \end{aligned} \tag{2.40}$$

Both of the presented mechanisms require the formation and then the cleavage of a M-H bond. Even for platinum different crystal phases on its surface provide different adsorption properties [45].

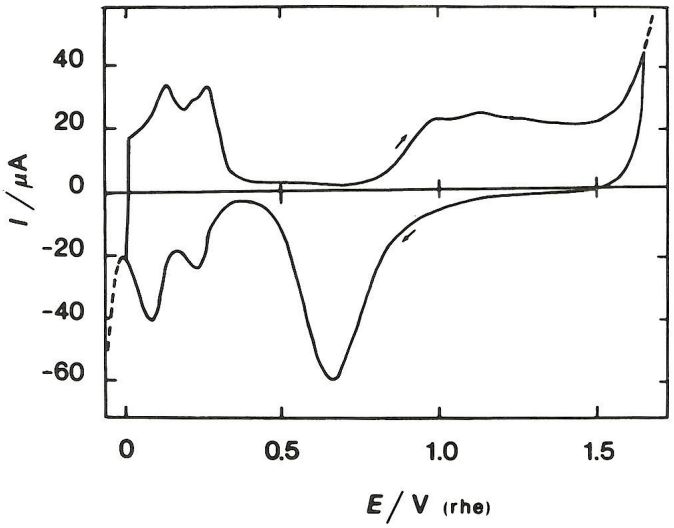

Figure 2.5: CV for Pt in 1.0 M H_2SO_4 solution [8].

Platinum is an example of a cathode material , for which two Tafel regions are observed. Close to E_{eq}, a Tafel slope of $(30\ mV)^{-1}$ is observed, while a higher overpotential region is characterised with a slope of $(120\ mV)^{-1}$ (Figure 2.46).

For the hydrogen cathode electrode, metallic nanodispersed platinum is the best today's solution in terms of balance between efficiency and cost. Different grades of Pt catalysts are available on the commercial market, mainly presented in the form of carbon supported metal catalyst. However, platinum is an expensive noble metal and lots of efforts have been made to substitute it. Nevertheless, until now nothing practical was found, while Pt catalyst for the HER remains one of the most widely investigated electrocatalysts in the field. For today, the focus in investigation is shifted to development of novel catalyst supports, thus optimising the use of noble metal, rather than finding new candidates, able to facilitate the HER. However, this study will not be focused on the HER and cathode catalyst materials.

2.3.2 Oxygen evolution reaction (OER)

As it was shown before, the anodic electrode reaction of oxygen evolution in acidic media involves the formation of four protons and four electrons (equation 2.4). The OER is a very complex reaction with the standard potential 1.23 V vs. SHE, which is higher than almost all the standard potentials of solid elements, which puts considerable limitations on the materials to be used as an oxygen electrode.

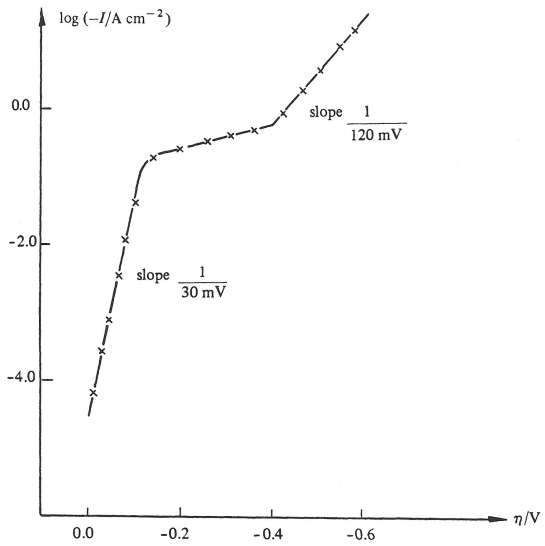

Figure 2.6: A Tafel plot for a Pt cathode in 5M H_2SO_4 [9].

The OER involves complex pathways of high activation energy and high energetic intermediates [46]. Oxygen species cover the metal surface by UPD by discharge of water before the liberation of O_2. Since the M-O bond strength is always stronger than the O-O bond strength in the gaseous molecule, the OER always takes place at oxide surface [47, 48]. This includes oxide phase formation on the metal surface by formation and breakage of new bonds between the oxygenated species and the surface metal ions during the anodic reaction [11]. Therefore, the OER catalysis is not a simple surface process, but also involves electrode material transformation processes.

A simplified mechanism with a bivalent oxide can be written [49]:

Electron transfer:

$$-\mathrm{M(OH)} \rightleftharpoons -\mathrm{M^+(OH)} + \mathrm{e^-} \tag{2.41}$$

Chemical reaction in acidic electrolyte:

$$-M^+(OH) + 2\,\mathrm{H_2O} \rightleftharpoons -M(OH)_2 + \mathrm{H_3O^+} \tag{2.42}$$

These electron transfer and chemical reaction are subsequently repeated until four adjacent hydroxyl groups can react:

$$4-\mathrm{M(OH)_2} \rightleftharpoons 4-\mathrm{M(OH)} + \mathrm{O_2} + 2\,\mathrm{H_2O} \tag{2.43}$$

Different Tafel plot slopes indicate other direct electron transfer reactions, e.g. a two-electron transfer:

$$-M(OH)_2 + -M(OH) + H_2O \rightleftharpoons [-M(OH)]_2O + H_3O^+ + e^- \quad (2.44)$$

Consequently the OER takes place from adjacent sites:

$$2\,[-M(OH)]_2O \rightleftharpoons 4\,-M(OH) + O_2 \quad (2.45)$$

As it was previously mentioned in Section 2.2.2 (equation 2.39), the reaction mechanism and rate determining step can be determined from analysis of the Tafel slope.

The experimental values of measured Tafel slopes for the OER are generally reported to be around 60 $mV \cdot dec^{-1}$ for the Ti/IrO_2-based dimensionally stable anode (DSA) electrodes in 1 M $HClO_4$ [10]. Another work reported the data for RuO_2-IrO_2 mixed oxide alloys prepared by radio frequency (RF) sputtering. The values were changing from 30 to 50 $mV \cdot dec^{-1}$ with growing RuO_2 content in the mixture [50]. For the mixed IrO_2-SnO_2 electrodes the values were reported around 40 $mV \cdot dec^{-1}$ [51]. At the same time, the slope was around 55-60 $mV \cdot dec^{-1}$ for similar DSA electrodes [52]. The symmetry factors α and $(1-\alpha)$, which are often assumed to be 0.5 were shown by several authors to be different from this value [53, 54].

The kinetic parameters of the OER differ with material, electrolyte, pH, etc. The Tafel plot will reflect these differences presented by its slope value. The OER data for some oxide electrodes is presented in Figure 2.7 [10]. However, there is always a problem of these results accurate reproducibility due to different physical properties of the active layer. Among them are roughness factor and porosity.

The complex combination of reactions involving surface species and material transformations, has lead to the formation of a Volcano plot (Figure 2.8). The figure shows the correlation of the electrocatalytic activity in terms of η, related to the enthalpy for the oxide formation from a lower to a higher oxidation state (ΔH_t°) [11]. As materials with intermediate values of ΔH_t°, Ru and Ir are the most active catalysts towards the OER. This was also confirmed by a number of publications [11, 55]. Materials whose ΔH_t° is high are too easily oxidised and therefore the intermediates bind too strongly, while those with low ΔH_t° are difficult to oxidise (e.g. PbO_2) and therefore the intermediates are absorbed too weakly [56]. Electrocatalytic activity of electrodes towards the OER have been also correlated with the redox potential of the metal present in the active oxide phase [57]. Therefore,

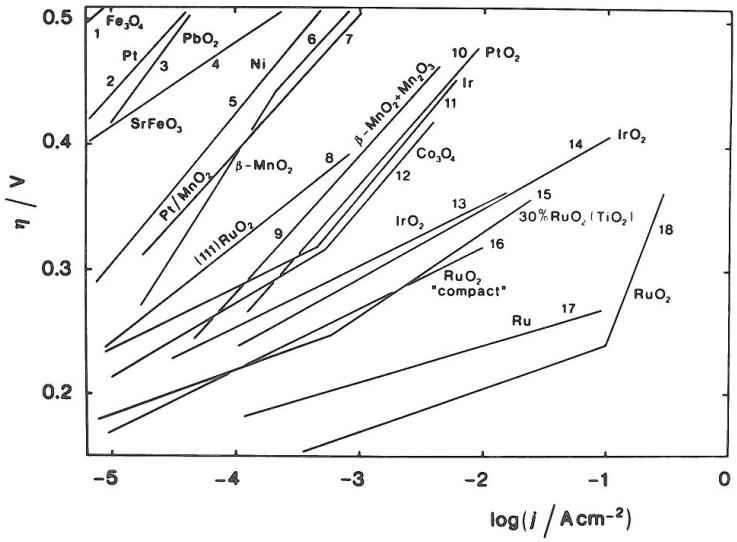

Figure 2.7: Schematic overpotential-*logi* curves for the OER on various oxides from acid solutions [10].

the ability of the oxide to undergo solid state redox transitions is important in respect to the materials electrocatalytic activity.

Since the OER is a complex system including the transfer of four electrons and four protons, it is in principle possible to propose a large number of reaction mechanisms.

Bockris has described a method for evaluating kinetic expression of electrode reactions, where several intermediate steps are involved. This method was applied to study different paths of the OER and many different possible paths and rate expressions for the OER have been listed within this reference. Among them, three common paths have been suggested to occur on iridium and ruthenium oxide coatings (equations 2.46,2.47,2.48). More detailed discussion on the oxygen evolution mechanism can be found in several publications [54, 56, 58–63].

The electochemical oxide path and the oxide path are both speculated to occur on RuO_2 and were proposed by J. Bockris in 1956 [53].

- The Electrochemical Oxide path [53].

$$\begin{aligned} \mathrm{S} + &\rightleftharpoons \mathrm{S{-}OH}(ads) + \mathrm{H^+} + \mathrm{e^-} \\ \mathrm{S{-}OH}(ads) &\rightleftharpoons \mathrm{S{-}O} + \mathrm{H^+} + \mathrm{e^-} \\ 2\,\mathrm{S{-}O} &\longrightarrow 2\,\mathrm{S} + \mathrm{O_2}(g) \end{aligned} \tag{2.46}$$

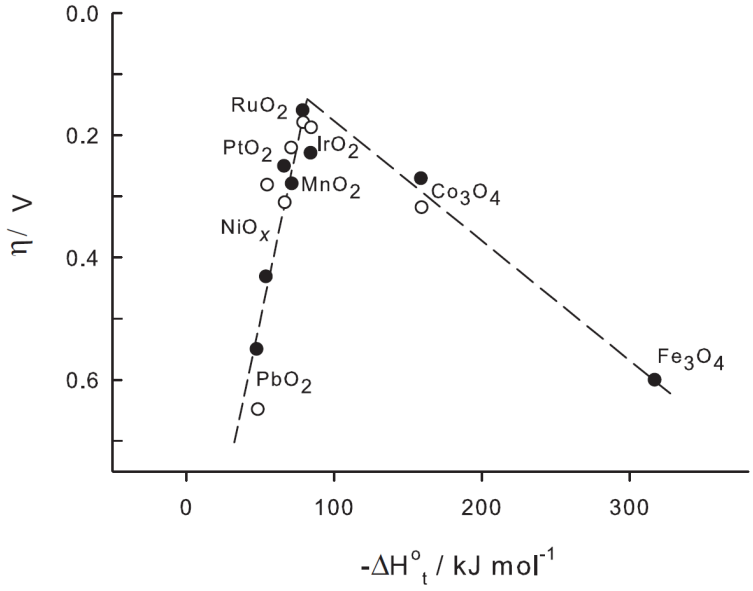

Figure 2.8: Electrocatalytic activity in O_2 evolution at various oxide electrodes as a function of the enthalpy of the lower to higher oxide transition. (∘) Alkaline and (•) acid solutions [11].

- The oxide path.

$$\begin{aligned} S + H_2O &\rightleftarrows S - OH_{(ads)} + H^+ + e^- \\ S - OH_{(ads)} &\rightleftarrows S - O + S + H_2O + e^- \\ 2S - O &\rightarrow 2S + O_{2_{(g)}} \end{aligned} \tag{2.47}$$

The Krasil'shikov path applies for both IrO_2 and RuO_2. It involves a negatively charged oxygen atom attached to the active site:

- The Krasil'shchikov Path [64]

$$\begin{aligned} S + H_2O &\rightleftarrows S - OH_{(ads)} + H^+ + e^- \\ S - OH_{(ads)} &\rightleftarrows S - O^- + H^+ \\ S - O^- &\rightleftarrows S - O + e^- \\ 2S - O &\rightarrow 2S + O_{2_{(g)}} \end{aligned} \tag{2.48}$$

where S is the active site.

In all proposed mechanisms the oxide surface is initially covered by a layer of OH-groups by discharge of water, which are further oxidized by ejection of H^+ and electrons along with an increase of the valence state of the metal

ion. This creates an unstable higher valence oxide which decomposes with liberation oxygen gas and may require rearrangement of the surface. Those oxides which are hardy oxidized further adsorb the intermediate too weakly and water discharge becomes the rate determining step. Oxides which are oxidized too easily absorb the intermediate too strongly and removal of oxygenated species becomes a limiting step [11]. As the affinity towards oxygenated species increase (increasing valence of the metal ion), the rate determining step moves further down the route and the Tafel slope decreases accordingly. Too high affinity towards oxygenated species will cause the release of oxygen gas to become rate determining and a limiting current density will be observed [65].

2.4 Electrochemical analysis techniques

2.4.1 Cyclic voltammetry

Cyclic voltammetry (CV) is one of the most used techniques in electrochemistry and covers a number of practical applications: studying of redox couples in the solution and on the electrode surface, investigating of adsorbed species, analytical applications in case of preceding/following chemical reactions, etc. Traditionally, CV is used for investigation of reversibility of redox processes occurring at the electrode. The mathematical background of the technique is sufficient to calculate the kinetic parameters of the mechanisms [9].

Usually, a standard 3-electrode electrochemical cell is used to perform CV experiments and consists of a working, counter and a reference electrode (Section 5.1.3.1). The potential of a working electrode is swept vs. reference electrode during the experiment between 3 values, which are initial potential, vertex potential and final potential. This creates the potential window of the experiment. The sweep rate v defines the speed of a potential change and in most experiment is varied from 10 mV/s to 10 V/s. In CV experiments v effects the parameters of the voltammetric curve, which are the cathodic (anodic) peak current $I_p^{c(a)}$, the peak potential $E_p^{c(a)}$ and half-peak potential $E_{p/2}$ (Figure 2.9). The relationship between these parameters and v is widely used for definition of mechanism of electrochemical reactions. Usually the reversible (controlled by electrode kinetics) behaviour of a system is observed at low v and irreversible at high values of v (Figures 2.10, 2.11).

However, during the interpretation of voltammograms the fact needs to be taken into account that cyclic voltammetry is a non-steady state technique. The current passing through the system is a sum of different processes, and some of them, like double layer charge-discharge, are transient processes that

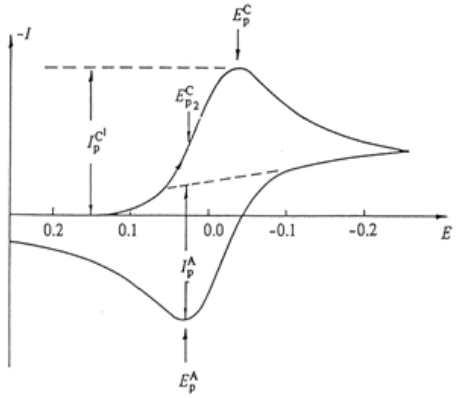

Figure 2.9: Typical cyclic voltammogramm and its basic parameters [9].

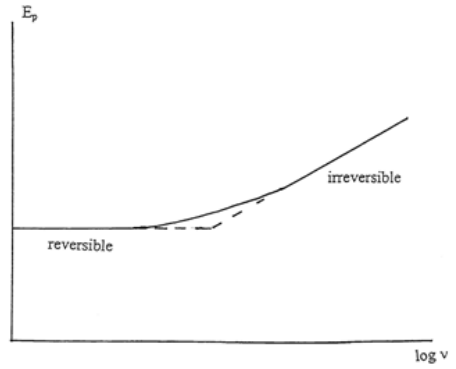

Figure 2.10: Dependence of the peak potential one the log of potential sweep rate.

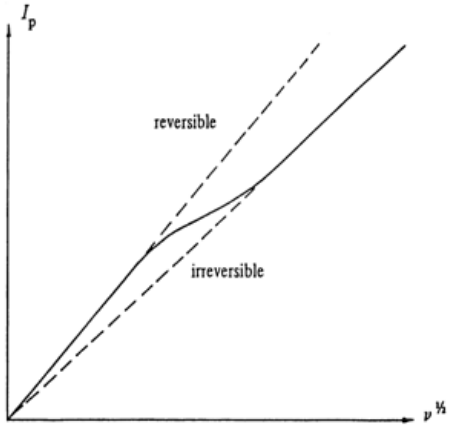

Figure 2.11: Dependence of the I_p on the v^2, showing the transition from reversible to irreversible regimes [9].

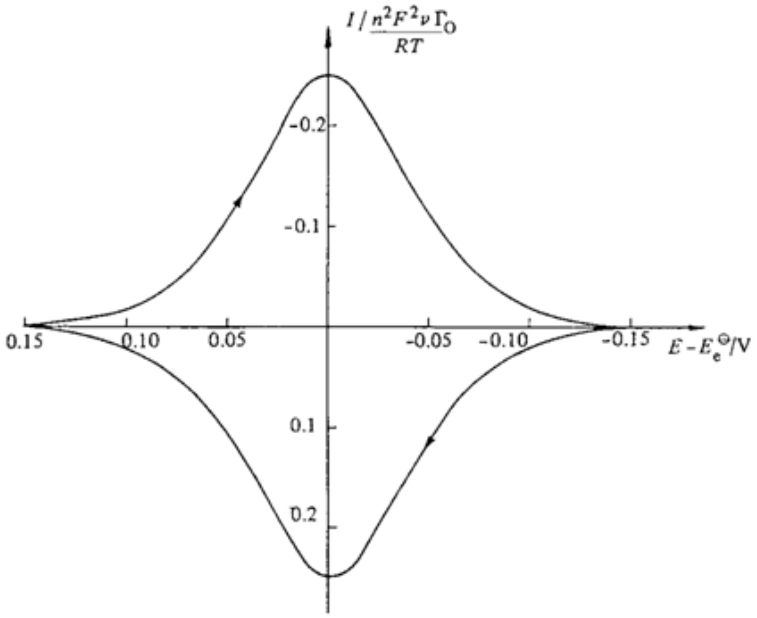

Figure 2.12: A CV curve of the reversible electrochemical adsorbtion reaction [9].

make difficult a straightforward interpretation of the results.

The most applicable techniques in electrocatalysis are the measurement of integrated charge and capacitance.

Integrated charge analysis One of the useful applications of CV is the quantitative studying of the adsorption mechanisms on the surface of electrocatalysts.

The active surface area of the electrocatalyst can be estimated by calculation of the charge, associated with adsorption of active species. Considering a simple case of the electron transfer (equation 2.15), where O and R are in the adsorbed form in this case and the mass transport effect is ignored (adsorbtion and desorbtion of reactants are the limiting steps). In the case of a reversible reaction, the peaks are sharp and symmetrical (Figure 2.12). If the adsorbed particles do not interact with each other (a case of the Langmuir adsorbtion isortherm), then:

$$i = \frac{n^2F^2}{RT}\frac{vA\Gamma_0^*(b_O/b_R)exp\left[(nF/RT)(E-E^{0'})\right]}{\{1+(b_O/b_R)exp\left[(nF/RT)(E-E^{0'})\right]\}^2} \tag{2.49}$$

where b_O and b_R are adsorption constants for O and R, Γ_O^* is the amount of O particles adsorbed on a monolayer (surface excess), and $E^{0'}$ is the Nernst

equilibrium potential of the redox couple O/R.

The peak current density is expressed by:

$$|i_p| = \frac{n^2 F^2 \Gamma_0}{4RT} vA \tag{2.50}$$

where

$$\Gamma_0 = |\frac{Q}{zF}| \tag{2.51}$$

The peak current in this case is proportional to the sweep rate, v, rather than to a square root of v. The peak current and the peak charge Q are proportional to the number of catalyst active sites. The charge of adsorbed species can be calculated using the area under polarisation curve:

$$\begin{aligned} Q &= \int I \cdot dt \\ v &= \frac{dV}{dt} \\ dt &= \frac{1}{v} \cdot dV \\ Q = \int I \cdot \frac{1}{v} \cdot dV &= \frac{1}{v} \cdot \int I \cdot dV \end{aligned}$$

In this case Q should be independent of v.

Capacitance In case if current is proportional to the scan speed, the behaviour of the electrode is capacitive. The total capacitance of an electrode can be expressed:

$$\begin{aligned} C = \frac{Q}{V} &= \frac{dQ}{dV} \\ dQ &= C \cdot dV \\ I = \frac{dQ}{dt} = C \cdot \frac{dV}{dt} &= C \cdot v \\ C &= \frac{I}{v} \end{aligned} \tag{2.52}$$

Considering a reversible process having the capacitance nature, no any peaks during CV are observed.

Considering the CV technique, at least two processes occur simultaneously due to the dynamic change of potential. The first is a reaction on the electrode surface, with kinetics described by the Butler-Volmer equation 2.29. Then, in parallel, the charge of an electrochemical capacitor formed by the interaction of the planar electrode surface with the electrolyte. Since the potential is continuously changing:

$$V(t) = V_0 + v \cdot t \tag{2.53}$$

the corresponding capacitive current can be calculated as:

$$i_{\text{cap}} = C \cdot \frac{dV}{dt} = C \cdot v \tag{2.54}$$

This contribution can be important depending on the relative magnitudes of the reaction rate and the electrode capacitance. In order to minimize the contribution of the capacitive current, pulse potential methods are normally used. Instead of a linear potential ramp (linear sweep voltammetry), a staircase potential ramp can be applied (linear staircase voltammetry). With this method, the current is measured at the end of each potential step. Since the capacitive current decreases exponentially with time, its contribution to the total current will be minimised.

2.4.2 Steady state polarisation and corrosion studies

Traditionally, the weight loss technique has been used to determine the corrosion rates of different materials [66–70]. It involves the periodic weight loss measurements after the defined time intervals having a sample immersed in an electrolyte. This technique is straightforward and does not require any knowledge of corrosion reactions that are occurring, however, prolonged test periods are needed (over 200h) for reasonable accuracy in this technique [71].

The electrochemical techniques potentially offer a faster way of determining corrosion rates, as nature of corrosion in electrolyte solutions is electrochemical. Therefore, generally considering corroding species of valence n, will give the following equation:

$$\mathrm{M} \rightarrow M^{n+} + \mathrm{ne}^- \tag{2.55}$$

As it was earlier shown in Section 2.2.2, the Tafel equation 2.39 describes the current density as a function of the electrode potential and can be used for the study of corrosion speed and mechanisms. The rate of the uniform

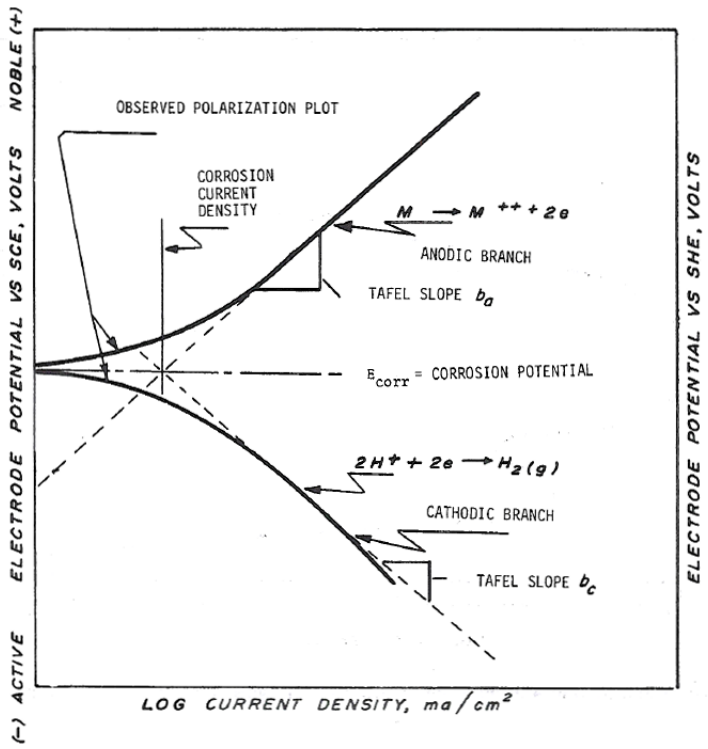

Figure 2.13: Hypothetical cathodic and anodic polarization diagram [12].

corrosion can be calculated through the exchange current density value directly to the mass loss rates or penetration rates (corrosion rate). It is made by means of the Tafel extrapolations [12].

The overpotential η is plotted against the *logi* value through the Tafel plot (Figure 2.13). The linear approximations intersection of two branches of the plot defines the corrosion current (corrosion current density i_{corr}), which is attributed to the main corrosion reaction taking place (equation 2.55). i_{corr} equals to i_0 at E_{corr} (equations 2.56-2.61). The values of the measured exchange current will show the maximum possible rate of corrosion in these conditions, as the effect of passivation is not taken into account.

$$for\ E >> E_{\text{cor}},\ i \simeq i_a = i_0 \cdot \exp\left\{\frac{(1-\alpha)\cdot n \cdot F}{RT} \cdot (E - E_{\text{cor}})\right\} \tag{2.56}$$

$$for\ E << E_{\text{cor}},\ i \simeq i_c = -i_0 \cdot \exp\left\{\frac{-\alpha \cdot n \cdot F}{RT} \cdot (E - E_{\text{cor}})\right\} \tag{2.57}$$

$$\ln i_a = \ln i_0 + \frac{(1-\alpha)\cdot n \cdot F}{RT} \cdot (E - E_{\text{cor}}) \tag{2.58}$$

$$\ln -i_c = \ln i_0 + \frac{-\alpha \cdot n \cdot F}{RT} \cdot (E - E_{\text{cor}}) \tag{2.59}$$

$$\ln i_a = \ln -i_c \rightarrow E = E_{\text{cor}} \tag{2.60}$$

$$i_a(E_{\text{cor}}) = i_0 \tag{2.61}$$

The corrosion potential (E_{corr}) (Figure 2.13) is another key parameter which gives an indication of how inclined to corrode an electrode material is, or what is the minimum potential at which it starts to undergo corrosion.

Another alternative is to use the so-called "Cyclic Tafel voltammetry" technique [36, 72]. In this case after the forward polarisation, the scanning direction is reversed and the corrosion potential and current are measured for the "passivated" material.

The corrosion current i_{corr} is found from the slope of the anodic polarisation curve, presented in the coordinates "electrode potential" vs. "log of the current density", as shown in Figure 2.13. The detailed ASTM technique description can be found elsewhere [12].

The assumption needs to be taken that the current distributes uniformly across the area of the electrode while using this technique. In this case, the current density equals:

$$i_{\text{cor}} = \frac{I_{\text{cor}}}{A} \tag{2.62}$$

where A is the exposed specimen area, cm^2

Further, the Faraday's Law is used for the calculation of the corrosion rate. For the penetration rate (corrosion rate (CR)) the derived from Faraday's Law equation is:

$$CR = K_1 \frac{i_{\text{cor}}}{\rho} EW \tag{2.63}$$

- CR is given is mm/year
- i_{cor} in μA/cm^2

- $K_1 = 3.27 \cdot 10^{-3}$, $\mathrm{mm} \cdot \mathrm{g}/\mu\mathrm{A} \cdot \mathrm{cm} \cdot \mathrm{year}$ [73]
- ρ is the density of material
- EW is considered dimensionless in these calculations

2.5 Physicochemical analysis techniques

2.5.1 X-Ray powder diffraction (XRD)

XRD is one of the oldest and most important analytical techniques used for characterisation of catalysts. The technique allows to define different crystalline phases in the sample, as well as, to a certain extent, to calculate the average crystalline size. The technique is based on the interaction of generated X-rays with atoms in regular structures.

If one put a single crystal in X-Ray beam, it will be hard to find any diffraction from it. Diffraction originates from the condition, where crystal has to be placed in the beam so as to fulfil the Bragg condition for diffraction (the Bragg's law). Another approach is to investigate a powder, which virtually has an infinite number of crystals. In this case, there will always be many crystals in the right position for diffraction from any of the lattice planes, which is the simple condition for powder diffraction. It is essential using this method to have enough crystals to fulfil the condition of always having enough crystals in position for diffraction for each lattice plane. This is why it is also important when a sample needs to be studied with the X-Ray Diffraction that a sample is grounded to a properly prepared fine powder (e.g. with mortar and pestle).

The Bragg's law defines the diffraction angle dependance on the lattice spacing and the wavelength (equation 2.64):

$$n\lambda = 2d \cdot \sin\theta \tag{2.64}$$

where n is an integer number, λ is the wavelength of incoming X-rays, d is the distance between crystal planes and θ is the diffraction angle between incoming X-ray and the lattice (Figure 2.14).

The interaction of an incoming front wave with each atom creates a secondary wave; the interference between different waves creates a diffraction pattern. This effect will be stronger if the wavelength of the radiation is comparable to the distance between elements of the crystal. Since these distances are usually in the order of 1Å, X-rays are used for crystallographic studies. The wavelength of Cu-Kα X-ray source, $\lambda = 1.5405981$ Å). Wavelengths of

this range can penetrate into the bulk of the sample under investigation, making it a bulk composition analysis, rather than a surface investigation.

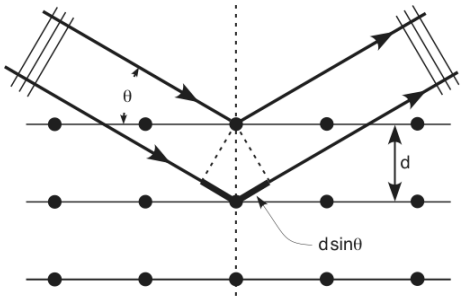

Figure 2.14: Illustration of Bragg's Law.

In crystalline substances, multiple diffraction planes are present. When X-rays interact with a crystal, they are interacting with every plane. Considering different orientations and distances, for a given incident angle only one plane may give a signal, according to the equation 2.64.

Starting from here, a rather complex systematic study can be made to assign each signal to a crystalline plane. This way, it is possible to identify a substance and its crystalline phase, and even mixtures, with this method. In practice, crystallography databases are used [74], usually with the aid of software, for identifying the different phases in a sample.

Usually the sample in the X-ray diffractometer rotates during the analysis, ensuring that all possible crystal orientations are tested, and thus no diffraction peaks are lost in the measurement.

The Scherrer equation can be used for the calculation of the mean crystal size [75]:

$$\tau = \frac{K\lambda}{\beta \cos\theta} \tag{2.65}$$

where K is a shape factor, usually taken as 0.9; λ is the X-ray wavelength; β is the peak width in radian; and θ is the Bragg angle of the peak. According to the equation 2.65, peaks broaden as crystal size decreases. In theory any diffraction peak can be used for calculating the crystal size. However, in practice, it is convenient to use peaks with a high signal-to-noise ratio. The calculation can involve some uncertainties. Apart from the crystal size, there are other parameters which contribute to the peak width. Among them are noise and particle strain. This makes τ a lower size limit and decreases the use of this method. Nevertheless, similar samples can be compared between each other.

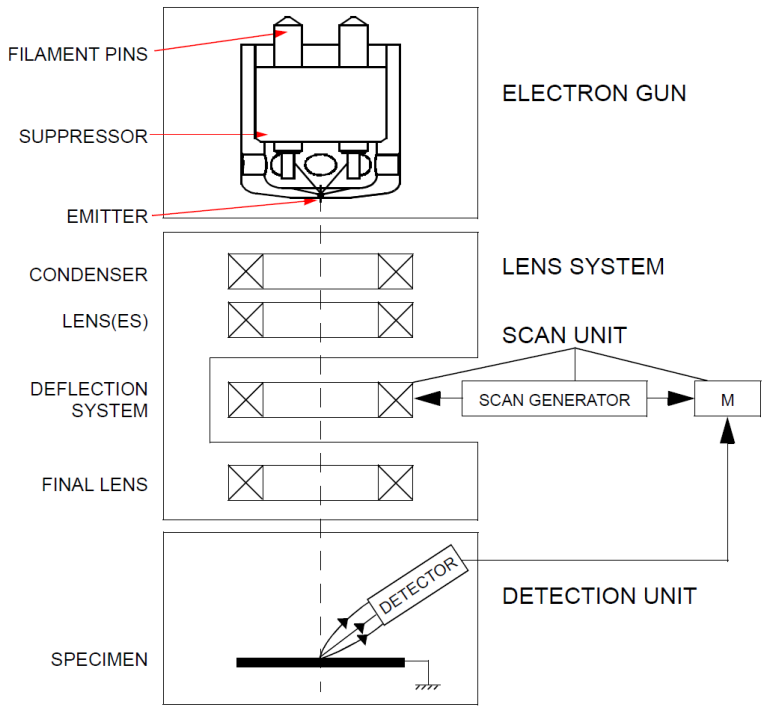

Figure 2.15: Scanning electron microscope schematic overview.

The Rietveld method was introduced by Hugo Rietveld in late 1960s and is used for analysing powder diffraction data and presents a method of structure refinement, where the whole point-to-point pattern fitting of the difference between experimental and calculated intensities is used [76]. The crystal structure is refined by fitting all the reflections to a calculated pattern using a least squares approach for refining a theoretical line profile. This method, unlike others, is able to deal accurately with strongly overlapping reflections.

As in a multiphase powder diffraction pattern the integrated intensity of reflections for a single compound is related to the phase abundance in the mixture, it can be used for the quantitative phase analysis of the mixed phase powders [77].

2.5.2 Scanning electron microscopy (SEM)

SEM is a powerful microscopy technique, which allows to investigate the texture and morphology of the samples (both of powder and bulk materials).

The schematic overview of the scanning electron microscope is presented in Figure 2.15 and it consists of the following components 2.1:

Table 2.1: Main components of scanning electron microscope and their functions.

Component name	Function
Electron gun (electron emitter)	Producing of a narrow beam of accelerated electrons, which have a defined kinetic energy
Lens system	Focusing of electrons into a beam by the electrostatic or electromagnetic apparatus.
Secondary electron detector	Reading the secondary electrons emitted by the sample
Backscattered electron detector	Reading electrons produced by the secondary electron emission
energy dispersive X-ray spectroscopy detector (optional, see Section 2.5.3)	Measuring of the emitted X-ray radiation

Two types of electron detectors can be used and both secondary and backscattered electron detectors read the emission of electrons from a solid object when it is bombarded by the primary electrons (emitted from the electron gun).

First type of electrons are those, mainly created by colliding of the primary electrons with the outer electrons in the sample and are called the secondary emitted electrons (Figure 2.16). Secondary electrons arise from the depth region of ca. 10 nm from the surface of the sample and therefore give the information about the surface morphology. The diffusion of incident electrons within the specimen has little influence on the image, thus allowing the best resolution to be obtained using the secondary electron detector.

Another type of electrons is called backscattered electrons. They appear if the acceleration voltage of the primary electrons is high enough and some of primary electrons can penetrate inside the sample, interact with the nucleus and be backscattered with virtually undiminished energy and emitted again from the specimen surface (Figure 2.16). Then the backscattered electron detector registers these electrons. The contrast of the backscattered electron image depends on the mean atomic number of the substances which constitute the specimen. Therefore, the backscattered electron image is commonly used to obtain the information on specimen composition.

The important parameters in SEM imaging can be listed as following:

- Magnification
- Depth of field
- Working distance
- Resolution
- Contrast
- Saturation
- Signal intensity
- Signal/noise ratio

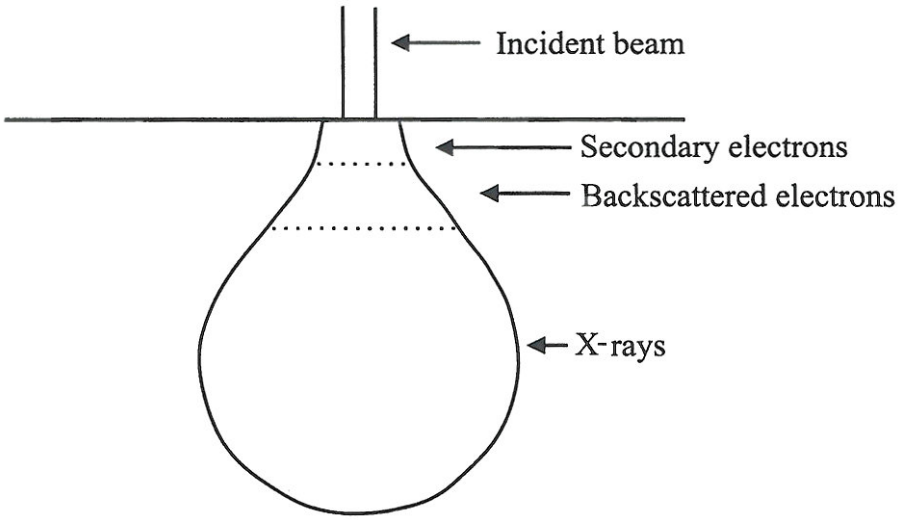

Figure 2.16: Interaction between an incident beam and a specimen [13].

2.5.3 Energy dispersive X-ray spectroscopy (EDX)

The impinging electron of high energy (usually more than 10 kV) in the primary beam can interact with the electron on the inner shells of the atom, ejecting an electron from its orbit and creating a positive hole. This ejected electron is called secondary. As the atom is in an excited state and has too much energy, it returns to its stable state by filling this created hole one of the electrons from an outer (high energy) level, restoring its status quo, releasing the excess energy in the form of an X-ray quantum of characteristic wavelength. The outermost missing electron is replaced by one form the free electrons always present in a material and the amount of released of X-ray radiation is further detected by the EDX detector . The amount of this surplus energy depends on the atom, since it is related on the energy of the initial and final levels. Then the analyses of the emitted readiation gives a possibility to analyse the chemical composition of the sample. The EDX spectrometer makes a spectrum of X-rays emitted by the specimen on the basis of their energy. Spectra show distinctive peaks for the elements present in the sample (corresponds to a wavelength of the emitted X-rays) and the peak height (intensity of the X-rays) indicates the element concentration. The principle scheme of EDX is shown in Figure 2.17.

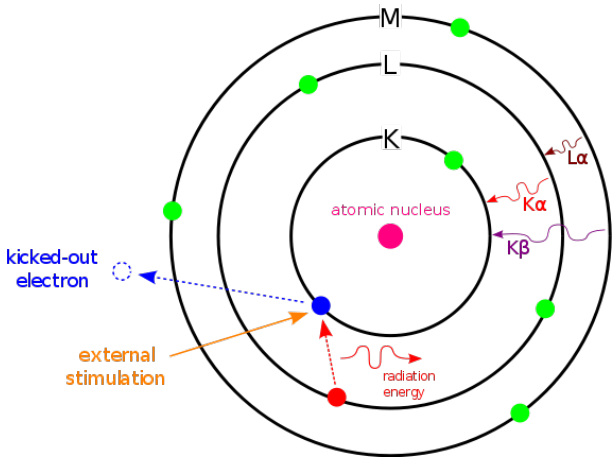

Figure 2.17: The principle scheme of EDX spectroscopy.

2.5.4 Sample preparation for scanning electron microscopy (SEM) and energy dispersive X-ray spectroscopy (EDX) for catalyst powder analysis.

The combination of SEM and EDX techniques is a very powerful micro-analysis instruments. Investigating the supported electrocatalysts it allows to detect the sites of catalyst location on the support matrix, morphology of the prepared powder and average particle size. This information is important for the estimation of possible decrease of electrocatalyst particle agglomeration.

However, the importance of the sample preparation procedure in microscopy is hard to overestimate. It differs depending on the observation technique used. Moreover, various sample preparation methods can be used within the same technique, which often gives different results. One or few would usually be chosen, depending on the subject of interest for the sample under investigation. For studying of powder electrocatalysts, there are several possibilities. One of the techniques is the same as in powder sample preparation for X-ray fluorescence (XRF) analysis, where powder pellets compressed under high pressure are commonly used [78]. This technique involves a risk of significant grain reorientation during pressing, which can give a wrong image on the original geometrical arrangement of the particles.

Another potential technique includes preparation of a ”catalyst ink” dispersion on the metallic support plate. This method is commonly implemented to characterize the electrocatalytic activity of powders [55]. In this case, the dissolved polymer is used as a ”binding agent” for a nano-sized catalyst particles. The usage of this ”catalyst ink” suspension can disturb SEM investigations. The polymer material can partially cover the active catalyst

surface, which will lead to the charging artefacts. It happens if polymer particles create a nonconductive surface layer on the powder. In this case, when it is illuminated with a negatively charged electron beam, the charge would be accumulated on the surface, preventing the emission of electrons.

More appropriate appears a technique, where the catalyst powder is dispersed in ethanol solution. Further, the prepared dispersion is applied on the backing plate and sent for SEM or EDX investigations.

2.5.5 SediGraph particle size analysis

The SediGraph method of particle sizing has been used since 1967. Although, the are more "modern" methods available, the SediGraph method still remains viable and satisfy the needs of certain applications.

The principles of this method lie in particle sizing by measurement of settling (sedimentation) velocity and mass fraction determination by relative absorption of low-energy X-ray. National Institute of Standards and Technology (NIST) in a guide to particle size characterisation defines the SediGraph as a robust technique, providing rapid analyses and having the capability to be used over a broad size range with minimal changes [79].

Sedimentation size analysis depends on the fact that the measured equilibrium velocity of a particle through a viscous medium, resulting from the action of the gravitation force, can be related to the size of the particle by the Stoke's law. For spherical particles, the Stoke's law is expressed by:

$$D = Kv^{1/2} \tag{2.66}$$

where D is the diameter of a spherical particle, v is its equilibrium sedimentation velocity and K is the constant of proportionality and accounts for density of the particle and physical properties of the liquid medium and is expressed by:

$$K = [(18\eta)/(\rho - \rho_0)g] \tag{2.67}$$

where ρ is particle density. Liquid is characterised by its density ρ_0, viscosity η. g is the gravitational acceleration.

Those equations apply rigorously provided that as the particle settles and displaces of the liquid, laminar flow around the particle is maintained. This condition is satisfied while the particle Reynolds number is less than 0.3:

$$Dv\rho_0 < 0\,3 \tag{2.68}$$

In practice, truly spherical particles are seldom encountered, and Stoke's law is not exact for any other shape. Since irregular shapes cannot in any case be described by a single linear dimension, it is accepted practice to specify the size of non-spherical particles in terms of the diameter of a sphere of the same material that should have the same material that would have the same sedimentation velocity. Thus, for non-spherical particles, the terms "Stoke's diameter" or "equivalent spherical diameter" are universally understood. The term equivalent spherical diameter (ESD) is some times used in a different context to mean the diameter of a sphere of the same material that would have the same mass as the particle in question. That is, the results of measurements of particle dimensions from electron micrographs are frequently reduced to size distribution curves in terms of mass ESD. In general, the relationship between these two measures of size is given by the inequality:

$$\frac{Sedimentation\ \text{ESD}}{Mass\ \text{ESD}} \leq 1 \tag{2.69}$$

The ratio expressed in the equation 2.69 is usually close to unity. Data concerning the sedimentation velocity of suspended particles may be obtained in two ways:

1) By measuring the concentration of particle remaining in suspension as a function of time.

2) By measuring the quantity of sediment produced as a function of time.

The letter approach is less desirable mathematically because of the graphical differentiation required to reduce the data to a size distribution curve.

Measurements based on the first approach are traditionally performed in the following way: a dilute, deflocculated dispersion of the fine particle material is stirred to render it homogeneous and then allowed to stand tranquilly while undergoing sedimentation. Time is measured from the beginning of the settling period. By Stoke's law, a particle of diameter D will settle a distance h in time t according to the expression:

$$D = K(h/t)^{1/2} \tag{2.70}$$

where K is defined by equation 2.67. Consequently, after a given time t, all particles larger than the corresponding diameter D_1 will have fallen below a given distance h from the surface of the suspension. If the initial (uniform) concentration of material was C_0 (g/cm^3) and the concentration after time

t, at distance h is C_1 (g/cm^3), then P_1, the weight percent of material finer than D_1, is given by:

$$P_1 = 100(C_1/C_0) \tag{2.71}$$

By obtaining values of C_1 after various times, the corresponding values of P_1 and D_1 may be calculated. Then the yield can be plotted in integral, or cumulative distribution of particle size in terms of Stoke's ESD.

The SediGraph uses a finely collimated X-ray beam to measure particle concentration in terms of the transmittance of the suspension relative to the suspending liquid. The transmittance to X-ray is a function of the weight concentration of suspended solids. Since X-ray beam can be made extremely small and because it does not disturb the suspension, it constitutes the ideal measuring technique. If a sample container or cell of rectangular cross section is irradiated from a direction perpendicular to one of its sides by a collimated X-ray beam, the fraction of the incident radiation transmitted by the cell when filled with the suspension under study is given by

$$I/I_0 = 1/exp[-(a_1\phi_1 + a_s\phi_s)L_1 - a_cL_2] \tag{2.72}$$

where I and I_0 are the transmitted and incident intensities, a_1, a_s and a_c are the X-ray absorption coefficients of the liquid, the particulate solids, and the cell walls, respectively. ϕ_1 and ϕ_s are the weight fractions of liquid and solid present in the suspension. L_1 is the internal cell thickness in the direction of irradiation and L_2 is the total thickness of the cell walls. Incident intensity I_0 is a measured baseline of a transmitted X-ray beam that has been projected through the liquid medium prior to the introduction of the sample.

By using the relation $\phi_1 = 1 - \phi_s$ and by defining a transmittance I as the ratio of the transmission of the cell when filled with a sample dispersion to its transmission with pure suspending liquid, there is obtained:

$$T = \frac{1}{exp[\phi_s(a_s - a_1)L_1]} \tag{2.73}$$

or

$$lnT = -A\phi_s \tag{2.74}$$

where A is a constant for particular apparatus and suspension components.

By collimating the X-ray beam through horizontal slits with a vertical dimension small compared to the sedimentation depth, h, the measured values

of T can be used in calculating the particle size distribution:

$$P = 100(lnT_1/lnT_0) \tag{2.75}$$

where T_0 refers to the transmittance of the initial suspension.

2.5.6 Brunauer-Emmett-Teller (BET) surface area

The surface morphology as well as the specific surface area of an electrode are related to its performance, as provide information about hypothetical amount of active surface sites. The method of physical gas adsorption on the surface of the solid sample can be used for calculation of different properties. One of them, the specific surface area of the powder can be measured by the nitrogen gas adsorption technique, known as BET and named after Brunauer, Emmett and Teller who derived it. The BET method is based on a physical adsorption model where the formation of multiple layers of adsorbate can be formed. The formation depends on the partial pressures of the adsorbed gas and the properties of the sample. By selecting an adequate range of data points from the adsorption isotherm, it is possible to calculate the surface area of the sample. The BET equation can be expressed as follows:

$$\frac{1}{V(P_0/P) - 1} = \frac{C - 1}{V_m \cdot C}\left(\frac{P}{P_0}\right) + \frac{1}{V_m \cdot C} \tag{2.76}$$

where V is the volume of gas adsorbed at pressure P, V_m is the gas monolayer adsorption capacity, P_0 is the vapour pressure of the gas at the experiment temperature (saturated vapour pressure) and C is a BET constant, depending on gas type and temperature.

The monolayer capacity V_m is defined as the quantity of adsorbate required to cover the adsorbent with a monolayer. Usually a second layer may be forming before the monolayer is complete, but V_m is determined from the isotherm equations irrespective of this. It is done by plotting so-called adsorption isotherm in terms of the volume of gas adsorbed as function of the equilibrium pressure. A plot of $P/V(P_0 - P)$ against P/P_0 yields a straight line having a slope $(C - 1)/V_m c$ and an intersect $1/V_m C$.

When $c >> 1$, equation 2.76 takes the form:

$$(P_0 - P)V = P_0 V_m \tag{2.77}$$

Therefore, it may be assumed that for high c - values the BET plot passes

through the origin and the slope is inreversely proportional to the monolayer capacity. Thus only one experimental point is required. This simplification is frequently applied for routine analysis.

2.6 Electrocatalysts and their properties

The general meaning, attached to the term "Electrocatalysis" is "The dependence of the electrode reaction rate on the nature of the electrode material". Electrocatalyst is a material that favours the kinetics and/or selectivity of an electrochemical reaction of interest. Fundamental research sees in it a link to applied problems, and therefore the need to establish a conceptual guide to selection and design of new materials. Industry looks at electrocatalysis with the hope to be able to improve electolyser performance, thus reducing operational costs. The horizons of application of electrocatalysts in the field of oxide electrodes were opened by Henry B. Beer in 1960's [80].

As it was earlier discussed in Section 2.2.2, the thermodynamical demand to split water is only 1.23 V. In the reality, there are several factors which make this potential to be higher. One of them is the kinetics of the electrode reactions, which require some extra energy in order the reaction to proceed at reasonable rate. This parameter is called the electrode overpotential (η) and its schematic contribution to the total cell voltage is shown in Figure 2.18.

The value of η_c and η_a depends directly on the type of material used as an electrode. Electrocatalyst reduces the activation energy reguired for the reaction to occur. Therefore, electrocatalysts are characterised by the value of overpotential they posses for the reaction to proceed at a fixed rate (current density). But the decreased half-reactions overpotential is not the only factor to consider developing an electrocatalyst. In one of his numerous works on electrocatalysts, Sergio Trasatti put together requirements for technological applications of electrodes or electrocatalysts (Table 2.2) [11].

Attributes, which define the performance of an electrocatalyst can be collected in the following Table 2.3 [11, 81].

2.6.1 Crystal structure of catalysts

As it was mentioned in Section 2.3.2, OER catalysts are limited to noble Ir and Ru metals and their oxides. In this work the most attention will be put on catalytic powders of IrO_2, which have greater stability and reasonable activity in comparison with Ru-based catalysts [55]. Both Ru and Ir oxides have the same lattice structure, which is identical to the mineral

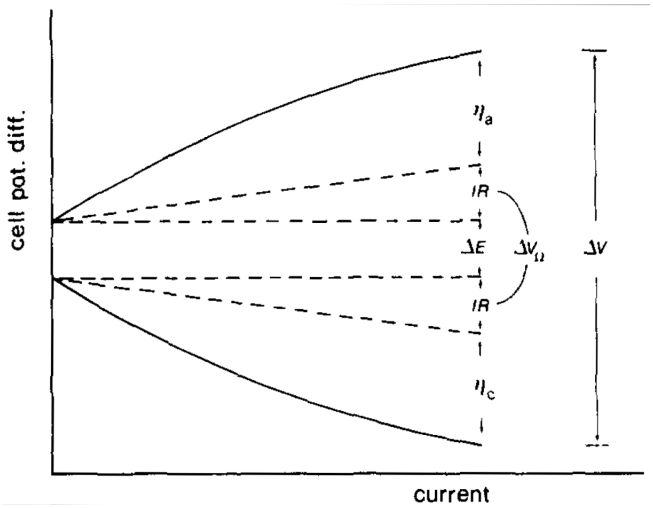

Figure 2.18: Dependence of the components of the potential difference applied to an electrolysis cell on current flow [14].

Table 2.2: Requisites for electrodes for technological applications

(1)	High surface area
(2)	High electrical conduction
(3)	Good electrocatalytic properties
(4)	Long-term mechanical and chemical stability at the support/active layer and at the active layer/solution interface
(5)	Minimized gas bubble problems
(6)	Enhanced selectivity
(7)	Availibility and low cost
(8)	Health safety

rutile. In virtue of this they have a metal-like electronic conductivity. The rutile crystal structure presents a tetragonal unit cell and consists of parallel chains of octahedrons, where a metal ion is coordinated by six oxygen atoms (Figure 2.19). Ruthenium oxide is slightly oxygen deficient while the iridium oxide has a slight access of oxygen compared to the stoichiometric value [14].

2.6.2 Electrical conductivity

The high electrical conductivity of electrodes is important in energy conversion devices. A sufficiently low resistance is necessary to avoid undesirable losses through the ohmic drop. It is also highly responsible for the overall

Table 2.3: Factors of electrocatalysis at oxides

(1)	Chemical nature of the catalyst
(2)	Morphology (dispersion, crystal size, crystallinity, lattice distortion, etc.)
(3)	Non-stoichiometry (ionic defects, electronic defects, solid-state redox etc.)
(4)	Magnetic properties
(5)	Band structure of the oxide
(6)	Bond strength of M-O
(7)	Number of d-electrons
(8)	Effective Bohr magnetron (electron magnetic dipole moment)
(9)	Surface electronic structure
(10)	Geometric factors
(11)	Crystal-field stabilization energy
(12)	Synergetic effects (effects of mixing and doping)

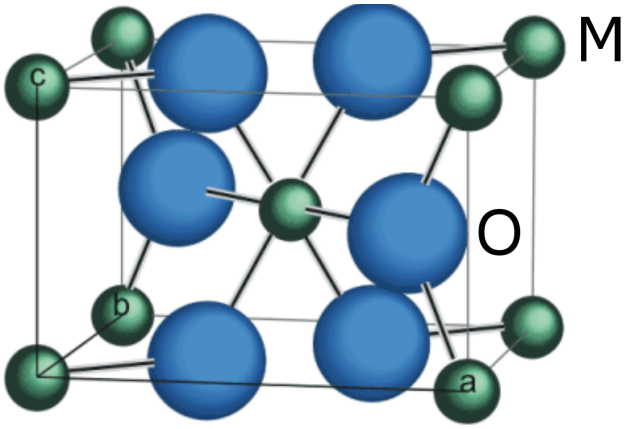

Figure 2.19: Rutile structure of IrO_2

performance of OER electrodes [14]. As it was mentioned in a previous section, high electrical conductivity is atributed to Ir and Ru oxides, while most of other inorganic oxides are insulators, having a covalent type of bond.

The phenomenon of rutile oxides metallic-type conductivity is explained by the spreaded electron orbitals, which facilitates the excitation of electrons from valence to conduction band [82]. Electrical resistivities of IrO_2 and RuO_2 are 6 and $5{\times}10^{-5}$ $\Omega \cdot cm$ respectively, measured at 300K [83]. It was suggested that for these two oxides, electrical resistivity is mainly located in the intergrain regions and conductivity has a "hopping" mechanism from grain to grain [14]. It means that electrical conductivity of these oxides depends on crystallite size and the gap between two grains. The larger the gap is, the lower is conductivity, as it provides the tunnelling of electrons through it, thus defining the apparent energy barrier.

The electrical properties of electrocatalytic oxides were summarised in several publications [81, 84]. As Matsumoto has outlined, the practical electrodes usually include the stabilising non-conductive agents, e.g. TiO_2, which creates a semiconducting interlayer. Even though the created space charge layer decreases the performance of electrocatalyst, the overall conductivity of the catalytic layer is tolerable. This artefact is explained by the insignificant potential drop for a p-type semiconductors under the conditions of anodic polarisation. Due to the mentioned property, they are under higher interest rather than semiconductors of a n-type [81].

In practice, metal oxide electrodes possess mixed amorphous-crystalline state conductivity properties, and these will depend on the degree of crystallinity. Nevertheless amorphous hydroxides of lower average valence present electronic conductivity of a semiconductor nature [65]. The electrical conductivity of amorphous oxides can be improved by introducing of defects in the crystal structure. By contrast, distortion of the crystalline oxides' lattice of metallic conductors such as RuO_2 and IrO_2 may change the band width, decreasing the electrical conductivity [14].

2.6.3 Catalyst support

Besides factors, such as composition and the atomic structure of electrocatalyst, geometrical particle structure and the specific surface area should be considered. The geometrical parameters of the catalytic powder eventually influences dispersion and utilisation of material, available surface area, layer morphology, mass transport parameters, electrical conductivity and mechanical stability of the layer.

As any catalytic reaction takes place on the atomic surface of the catalyst, the specific active surface (surface area per mass) is a crucial property that is to be maximized. The only one way of achieving this is minimizing the particle size of the catalyst. As it is known, the surface-to-volume ratio is higher, the smaller a particle is. For instance, for a spherical particle:

$$\frac{S}{V} = \frac{4\pi R^2}{\frac{4}{3}\pi R^3} = \frac{3}{R} \tag{2.78}$$

However, small particles tend to grow into bigger ones, agglomerating due to their higher surface energy. The lower surface area over the time means the loose of the catalyst activity. This phenomenon becomes more probable with higher working temperature. A way of stabilising the small particles is to use a support, to which the active catalyst is affixed. It lowers the particles' energy and thus slows their agglomeration. Most of the catalysts in the chemical industry are supported (e.g. hydrodesulfurization process) [85, 86].

A typical supported electrocatalyst structure implicates active nano particles of active material, being arranged on larger particles of a support (Figure 2.20). This increases the specific surface area of active component significantly due to larger macro pores of support material. If the electrical conductivity of the support is higher than that of the active component, it will decrease the ohmic resistance of the layer, and accordingly the overall IR drop, presented before (equation 2.14 and figure 2.18).

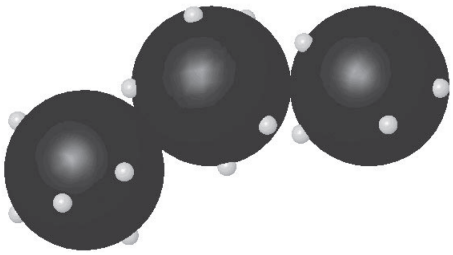

Figure 2.20: The idealised structure of carbon-supported platinum catalyst for PEMFC [15].

Another potential advantage of use of a catalyst support in the catalytic layer could be due to the increased pore size and following decreased mass transport limitations at high current densities [87]. Bigger particles of a catalyst support would provide additional surface area and bigger pores for the escape of produced gases.

Catalyst support can also affect the electronic structure of the catalyst, altering its reactivity and/or selectivity [88]. It was shown that supported catalyst shows different catalytic properties due to metal-support interactions [85]. Presence of a support can contribute to the electrochemical reaction itself. For example, in case of RuO_2 used as a support, it will possess partial ionic conductivity and transport protons in a way which carbon support doesn't [88, 89].

2.6.4 Electrochemical behaviour of IrO_2 and RuO_2

As it was mentioned in Section 2.4.1, CV is a useful technique for investigation of the surface properties of the metal oxides. Typical voltammograms for IrO_2, RuO_2 and their mixture are shown in figure 2.22 [17]. Electrodes, containing noble metal oxides in the active layer are often prepared by the DSA technology (see Section 3.6).

Redox reactions on the surface of electrocatalyst give rise to redox peaks during CV scanning. As the adsorbed species collect charge on the electrode surface, the type of behaviour can be designated as pseudo capacitance. It is important not to mix it with the double layer capacitance (charging of the

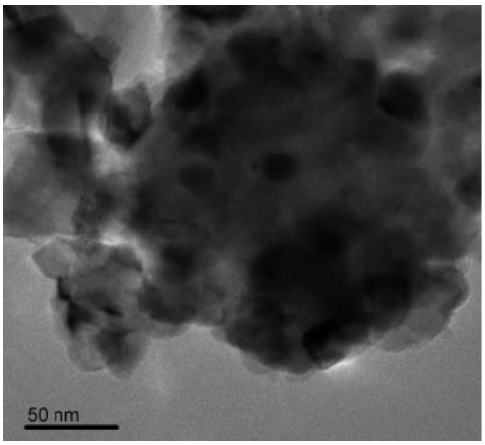

Figure 2.21: TEM image of a TiC-supported Ir catalyst [16]. The darkest zones are richer in Ir.

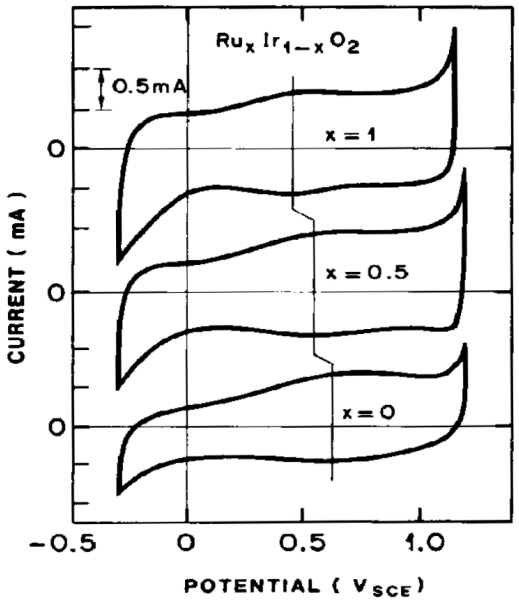

Figure 2.22: Cyclic voltammogram of $Ru_xIr_{1-x}O_2$ for x=1, 0.5 and 0 in 1 N H_2SO_4 [17].

double layer). Pseudo capacitance is a Faradaic process, including crossing of the double layer by electrons [90]. The surface electrochemistry of IrO_2 in acidic media is usually associated with with 2 redox processes of Ir^{3+}/Ir^{4+} and Ir^{4+}/Ir^{6+}, having the characteristic peaks on CV plot at ca. 0.8 and 1.25 V vs. SHE correspondingly [91]. However, some authors [92, 93] reported the broad peaks formation explained by formation of different iridium oxidation states on the electrode surface. Since the current and the charge corresponding to these peaks is proportional to the active catalyst area, the measurement of the charge is usually used for comparing the relative activity of different catalyst samples (see Section 2.4.1). The charging process for iridium oxide catalyst can be presented by the following reaction 2.79 [94]:

$$IrO_a(OH)_b \rightleftharpoons IrO_{(a+\delta)}(OH)_{(b-\delta)} + \delta H^+ + \delta e^- \tag{2.79}$$

Both IrO_2 and RuO_2 when placed in electrolyte are covered with the hydroxide layer, as it is shown in reactions 2.79,2.82. The reaction mechanism for the oxygen oxidation on the IrO_2 surface has been studied by several authors as well as several models for the OER were proposed. One of them, proposed by Kotz, includes the formation of IrO_3. According to this model, the mechanism includes four reversible reactions. The assumption is taken that iridium hydroxide is protonated in acidic media and with following loosing of a proton and an electron three times and further evolution of oxygen on the deprotonated IrO_3 [58]:

$$\begin{aligned} Ir(OH)_3 &\rightleftharpoons IrO(OH)_2 + H^+ + e^- \\ IrO(OH)_2 &\rightleftharpoons IrO_2(OH) + H^+ + e^- \\ IrO_2(OH) &\rightleftharpoons IrO_3 + H^+ + e^- \\ IrO_3 + H_2O &\rightleftharpoons \frac{1}{2}O_2 + IrO(OH)_2 \end{aligned} \tag{2.80}$$

From the proposed reaction mechanism follows that it requires two active adjoining iridium sites for realising of one molecule of O_2.

Recently, another oxygen formation mechanism on the surface of IrO_2 was described. It is speculated in the model that the two O atoms are most likely to split in the O_2 molecule simultaneously from the same active site of IrO_2 (Figure 2.23) [95] .

In this model, pure metal on the surface hydrates two times, accorded with splitting the water into a proton, an electron and a hydroxyl group. Further, two protons and electrons are released to form an unstable triagonal IrO_2 complex, which is assumed to release oxygen gas and reform the metal surface. More detailed discussion on the possible mechanisms of OER on oxide sites can be found in Section 2.3.2.

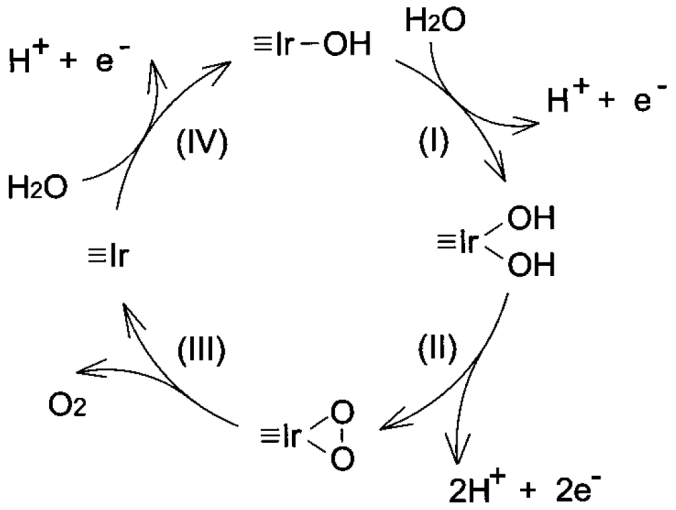

Figure 2.23: One-catalytic site model for the OER on Ir surface

According to Burke, corrosion of IrO_2 can proceed along with the OER, forming a soluble iridate [8, 58]:

$$IrO_3 + H_2O \longrightarrow IrO_4{}^{2-} + 2\,H^+ \tag{2.81}$$

The charging process of RuO_2 was assumed to have the similar mechanism as for IrO_2 [94]:

$$RuO_x(H_2O)_y \rightleftharpoons RuO_{(x+\delta)}(H_2O)_{(y-\delta)} + 2\,\delta\,H^+ + 2\,\delta\,e^- \tag{2.82}$$

As suggested by Wen, this process has three characteristic pair of redox transitions: Ru^{2+}/Ru^{3+}, Ru^{3+}/Ru^{4+} and Ru^{4+}/Ru^{6+}, showing 3 broad peaks on the CV [96]. A possible corrosion of RuO_2 to volatile RuO_4 was outlined by several authors (see Section 2.3.2). The potential of this transition is around 1.4 V, which is within the typical potential range of operating electrolyzer.

Chapter 3

High Temperature PEM Water Electrolysis

3.1 Principles of PEM water electrolysis

As it was mentioned in Section 2.1, there are mainly 3 types of electrolyzers: alkaline, acidic and SOEC. This study will be concentrated on acidic electrolyzers, where reactions follow the described pathes (reactions 2.3, 2.4).

The efficiency of water splitting by electrolysis is rather low for conventional electrolyzers and there is hence a large potential for improvement. One of the potential advantages of PEM cells over more abundant alkaline electrolyzers is that they were shown to be reversible [97–99]. The type of an electrochemical cell working both as a fuel cell and a water electrolyzer is called a unitized regenerative fuel cell (URFC) [100–103]. These devices produce hydrogen from water in the electrolysis mode, while electricity can be inversely produced in the fuel cell mode. This mode of working is beneficial when the lack of electricity changes with the excess energy available (periods of low consumption) [104].

PEM water electrolysis technology is frequently presented in literature as a potentially very effective alternative to more conventional alkaline water electrolysis [105–107]. Among advantages are higher production rates and energy efficiency [29]. In a future "hydrogen society" this method is envisioned as a part of the "energy cycle", where hydrogen acts as an energy carrier. In this cycle, electricity from renewable energy sources is used in electrolysis for electrochemical splitting of water [1]. A PEM electrolyzer

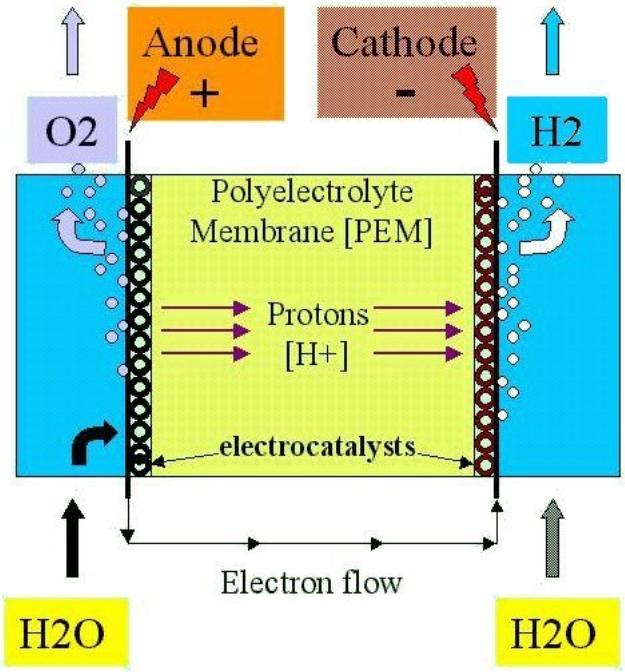

Figure 3.1: The schematic diagram of a PEM electrolyzer cell [18].

cell (PEMEC) is schematically presented in Figure 3.1. PEM cells usually use perfluorinated ion-exchange membranes as an electrolyte (known under the trademark Nafion®).

The first PEM electrolyzers were created in 1966 by General Electric Company. However, those systems were developed for special purposes, e.g. spacecraft and submarines.

In a PEM cell the electrolyte is a solid ion-exchange membrane, which does not involve compulsory circulation of electrolyte through it. Different types of ionic membranes will be discussed in Chapter 3.7. The electrodes are usually directly sprayed or pressed on the opposite sites of the solid polymer electrolyte (SPE), thus being the origin of a membrane electrode assembly (MEA)[102, 108–110]. Also, electrodes can be sprayed on the GDL, and then put together leaving the SPE between them [111, 112]. A PEM electrolyzer stack consists of a combination of several cells (as many as 100), electrically connected in series [113]. The cells are separated from each other by a metal plate (also called a bipolar plate), which serves both as a current collector and as an interconnect to the next cell in the stack. Flows of evolved hydrogen and oxygen are usually swept out through the bipolar plate by water flow and further separated from it outside the cell.

The main advantages attributed to PEM cells are:

Figure 3.2: Commercial Hogen® PEM water electrolyzer unit [19].

- electrolyte layer can be very thin, meaning lower ohmic loses and thus higher overall efficiency (see Section 2.2.2).
- smaller mass-volume characteristics and power costs [114].
- reversibility (one device can both work in electrolyzer and fuel cell mode) [115, 116].
- an opportunity of operating at differential pressure [117–119].

Among disadvantages referred to PEM cells are:

- the cost of electrolyte is high [120, 121].
- the electrolyte is corrosive which limits the choice of materials [122–124].
- variety of catalysts is still limited to noble metals.

Several commercial types of PEM electrolyzers are available today on the market [19, 125, 126] and one of the models is shown in Figure 3.2. Some units have power up to 44 kW and the claimed lifetime up to 40,000 hours. Still, the main drawbacks of such systems are the price of materials and complex system components, which ensures save and reliable function.

Several academic and industrial groups are nowadays involved in the PEM electrolyzer research. Among a number of them are: Norwegian University of Science and Technology (NTNU) [120, 127], Matsushita Electric Works, Ltd and Fuji Electric Co., Ltd. in Japan [128, 129], CNR-ITAE in Italy [130, 131], School of Materials and Metallurgy and Institute of Fuel Cell in China [16, 132], “Institut de Chimie Moléculaire et des Matériaux”

in France [133, 134], Hydrogen Energy and Plasma Technology Institute, Russian Research Center "Kurchatov Institute" [31, 87], etc.

3.2 High temperature PEM electrolysis. Advantages and drawbacks

At temperatures above the boiling point of water, the energy efficiency of water splitting can be significantly improved because of decreased thermodynamic energy requirements, which is one of the major advantages of these systems. The equilibrium potential decreases with higher operating temperatures (Section 2.2.1, Figure 2.1). Since the reaction of water splitting is not spontaneous and the Gibbs free energy is positive, a positive change of a factor $T \cdot \Delta S^{\ominus}$ in the equation 3.1 means less energy needs to be applied. As the reaction has a positive entropy, the equilibrium will be displaced towards the products for high temperatures. The term $T \cdot \Delta S^{\ominus}$ increases with increasing temperature, thus increasing the contribution of thermal energy to the total needs for the water splitting reaction [135]. Therefore, the part of heat, which can be used for the reaction is higher, meaning that the production costs of hydrogen are decreased [136]. It was noticed much earlier that econonomic reasons force to move towards high temperature electrolysis (120-150 °C) [47].

$$\begin{aligned} \Delta G^{\ominus} &= \Delta H^{\ominus} - T \cdot \Delta S^{\ominus} \\ \Delta G^{\ominus} &= -nF\Delta E^{\ominus} \\ \Delta S^{\ominus} > 0 \rightarrow \frac{dG^{\ominus}}{dT} &< 0 \\ \frac{d\Delta E^{\ominus}}{dT} = -\frac{d\Delta G^{\ominus}}{dT} &> 0 \end{aligned} \tag{3.1}$$

According to the Arrhenius' equation 2.23, the kinetics of the electrode reactions is enhanced at elevated temperatures. It is associated with lower overpotentials at the electrodes, giving higher efficiency for electrolysis.

Another positive opportunity provided while operating at temperatures above 100 °C is that water is not in a liquid phase (at ambient pressure) and this fact significantly simplifies water/gas management. In this case all the reactant/product flows are in a steam phase and the transport of them is easier, which provides simplified stack construction and operation [137].

The heat management is also easier for high temperature systems, as the heat flow out of the system is proportional to the temperature gradient between the cell and the ambient. This means that cooling is more effective

in elevated-temperature systems, as there are less efficiency losses associated with the forced cooling of the cell [44].

Another benefit of high temperature systems is attributed to the decreased sensibility of catalysts towards poisoning by adsorption of inhibiting agents. This effect is acknowledged to be a considerable advantage of high temperature PEM fuel cells (HTPEMFCs) [137]. The inhibition mechanism usually involves chemisorption of species on the catalyst surface, covering and screening it from interacting with the reactants. This adsorption is weaker at higher temperatures, giving higher tolerance to impurities [138].

However, with increasing temperature, the probability and rate of side processes, such as dissolution of the electrodes and components corrosion, is higher. This decreases the lifetime of the whole system and increases demands to all materials used with respect to corrosion and thermal stability [106, 139]. The corrosion issue for construction materials in such cells will be addressed in the following Section 3.3.

3.3 Construction materials for high temperature PEM water electrolysis (bipolar plates and current collectors)

Elevated working temperatures involve increased demands for corrosion resistance of catalysts and current collectors, while the contact resistance in the GDL should remain reasonable.

High temperature PEM cell cannot be build from the same materials as a cell working below 100 °C. Among new materials to be developed are polymer membranes, as commercial Nafion® membranes lose their conductivity at temperature above 100 °C due to membrane dehydration [108]. This means that different membranes should be used for this temperature range. It will be further discussed in Section 3.7. Elevated temperatures as well create more severe corrosion media for other components in the cell.

The anodic compartment of electrolyzer is expected to have stronger corrosive conditions than cathodic due to high positive polarization in combination with presence of evolving oxygen. This will be even more severe when the temperature is elevated. It is therefore an important task to choose materials which possess sufficient corrosion resistance. This demands further development of all materials from which electrolyzer cells are built.

One of the important components in PEM stack is a bipolar plate. Bipolar plate is a multifunctional and expensive part in a electrolysis stack as it collects and conduct current from cell to cell, permits an adequate gas flow, and

the flow channels in the plate carry off produced gases, as well as providing most of the mechanical strength of the stack. In a typical PEM electrolysis stack, bipolar plates comprise most of the mass, and almost all the volume. Usually they also facilitate heat management in the system. These complex requirements make a task of finding proper materials difficult [140]. The highly oxidising acidic conditions in the oxygen electrode compartment pose a serious challenge to the materials used in these systems [139].

The most crucial demands for bipolar plate materials are resistance to spalling, dimensional stability and resistance to corrosion in electrolyte media under anodic/cathodic polarization. Numerous research projects have been devoted to bipolar plate materials in fuel cells [122–124, 141–145]. However, the number of suitable materials for PEM electrolyzers is still limited because of high requirements for corrosion resistance at the oxygen electrode, where high overpotentials are combined with low pH media of electrolyte.

In Nafion®-based systems, titanium is the most widely used bipolar plate material, which is ideal in terms of corrosion resistance and conductivity [102, 146–148]. Porous sintered titanium powder commonly serves as a GDL material [87, 149].

The conductivity of Nafion® membranes decreases dramatically at temperatures above 100 °C (Section 3.7.3). Thus, PBI membranes doped with phosphoric acid are typically used in PEM fuel cells at elevated temperatures [148]. However, materials like steels corrode easily in phosphoric acid solutions and therefore it is important to study other alloys and materials for current collectors [67, 150]. Tantalum and nickel alloys show better corrosion resistance than stainless steels partly due to higher corrosion potentials and partly due to the formation of passive oxide layers on the metal surface [69, 151]. Titanium generally has rather limited resistance to phosphoric acid [152]. Previous studies showed that titanium current collectors would considerably suffer from corrosion at temperatures above 80 °C in concentrated phosphoric acid environments [36, 153].

Different types of stainless steels can be used as bipolar plates, and they have advantages of being good heat and electricity conductors, can be machined easily (e.g. by stamping), are non-porous, and consequently very thin pieces are able to keep the reactant gases apart.

A possible alternative to stainless steel bipolar plates can be the use of nickel-based alloys [151]. Ni-based alloys are widely applied in process industry and energy production in nuclear power plants. When compared to conventional stainless steels, generally a higher degree of resistance against corrosion is observed for these materials. This can be explained partly by more noble corrosion potential of Ni and by different properties of the oxide films formed on Ni-based alloys [151]. Also, it has been proposed recently that nickel and

stainless steel alloys can be used as a construction material in PEM water electolysers, but at temperatures no higher, than 100 °C [153].

In order to simulate corrosion conditions at the anodic compartment of a PEM water electrolysis cell during half-cell experiments, it is necessary to choose a proper electrolyte. Investigating systems including membranes based on perfluorinated sulfonic acid, e.g. Nafion®, 0.5M sulphuric acid is commonly used as an electrolyte, simulating the electrolyzer cell conditions [55, 120]. Similarly, H_3PO_4 can be used to model systems based on membranes doped with H_3PO_4. 85% solution of H_3PO_4 can be chosen to study the limiting case of corrosion, considering that in working electrolyzer systems the actual concentration of active acid at the electrode-electrolyte-water three-phase boundary would by much less than in this limiting case.

In a highly oxidizing media such as the anodic compartment of high temperature steam electrolysis stack, it is essential to characterize the effect of different parameters on the behaviour of the protective oxide films. To date, no works have been addressed to the study of Ni-based alloys for use as bipolar plates in high temperature PEM steam electrolyzers.

In this work, metal alloys, namely austenitic stainless steels AISI 316L, AISI 321, AISI 347 and Ni-based alloys Hastelloy®C-276, Inconel®625, Incoloy®825, as well as titanium and tantalum were tested in terms of corrosion resistance. Platinum and gold were also investigated for studying the potential window of concentrated H_3PO_4. All samples were subjected to anodic polarisation in 85% phosphoric acid electrolyte solution at 120 °C. The corrosion speed of metal alloys was investigated additionally for 30 °C and 80 °C to show the influence of temperature on corrosion resistance.

3.3.1 Metal coatings and a CVD technique

As the requirements to construction materials are quite severe and the price for materials which fulfil these requirements tends to be rather high, one of the approaches can be use of a coating on the less expensive and available material. If the technology is robust and affordable, the price of the materials can be significantly reduced, as expensive material use is restricted to the surface. Tantalum was shown to have superior resistance towards acidic solutions [154]. This is attributed to the formation of a thin Ta_2O_5 passivating film. As the cost of this material is rather high, its use is often limited to the coatings.

Cardarelli et. al showed that IrO_2 electrodes, prepared on copper base material, which is coated with tantalum by molten salt electroplating present much better corrosion stability than coatings, made on pure titanium [155].

Chemical vapour deposition (CVD) process can be used for tantalum coatings preparation, where product is deposited on the surface of a substrate inside the reaction chamber. The most common process of chemical vapour deposition (CVD) coating is hydrogen reduction of a metal chloride [156].

In this work a commercial CVD "Tantaline" coating on stainless steel AISI 316L, provided by Tantaline A/S (Denmark) was tested for corrosion in HTPEMEC environment [157].

3.4 Oxygen evolution electrodes (OEEs)

Present research attention in the field of electrolysis is concentrated on extending the lifetime, developing oxygen electrodes and stack design [134, 136, 158, 159]. The oxygen electrode is one of the main contributors to the loss of overall efficiency as it gives most of the activation losses due to slow kinetics of the OER. This problem arises from the complex mechanism of the oxygen/water reaction [100]. For a reaction involving 4 electrons per oxygen molecule, the activation energy is higher than that for hydrogen evolution. Several steps of this reaction are proposed, without agreement on a mechanism (see Section 2.3.2).

As electrodes have to be able to withstand strong corrosive acidic and oxidizing conditions at the anode compartment, noble metals and other substances, like their oxides and alloys were chosen at the dawn of research in this field as materials for the oxygen evolution electrodes [160]. The best catalyst seemed to be iridium-ruthenium metal based alloys [161]. On the contrary, platinum was found to have relatively high overpotential towards the OER due to the formation of a poorly conductive oxide layer on the surface of electrode. The electrical resistance of PtO_2 is about 10 orders of magnitude higher, than that for IrO_2 and RuO_2 [160].

Despite of attempts to replace iridium and ruthenium by cheaper manganese-based compounds [162], present applicable OER electrocatalysts are mainly based on iridium, ruthenium noble metals and their oxides [55].

As was shown in Figure 2.8 (Section 2.3.2), ruthenium oxide is known as the most active catalyst towards the OER [11] and has been widely studied [94, 163–167]. However, it is inclined to corrode. According to thermodynamical calculations, the oxidation of RuO_2 to RuO_4 occurs at potentials more positive than 1,387 V (vs. SHE) [168]. The proposed mechanism of corrosion can be found in Section 2.6.4. The instability of Ru-based anodes at high overpotentials in acidic media has been proved by several studies. The mechanism of corrosion is explained by the conversion of RuO_2 to soluble, non-conductive and volatile RuO_4 [58, 169]. This compound was reported

to have a boiling point of around 130 °C [170, 171]. It was confirmed experimentally that durability of ruthenium oxide anodes in the long-term test is poor [110], which limits its practical use. Elevated temperatures will aggravate corrosion of RuO_2, thus making impossible the use of Ru and its oxides as catalysts for the OER in high temperature PEM steam electrolyzers.

Several studies were intended to improve the stability of RuO_2 during anodic oxygen evolution by mixing it with IrO_2. This causes a decrease in the corrosion rate of RuO_2 depending on the IrO_2 content in the mixture [17, 172]. IrO_2 appears to have greater stability and a reasonable activity compared with Ru-based electrocatalysts for such systems [55]. Apparently, IrO_2 is the most stable OER electrocatalyst for PEM water electrolyzers studied until now.

However, other works showed that a binary catalyst mix of IrO_2 and RuO_2 gives quite promising results [96, 173]. Moreover, Kötz confirmed that catalytic properties of binary Ru-Ir alloys depend on a shift in a redox potential towards the OER and surface segregation effects, not attributed to individual compounds [50].

Unfortunately, high loadings of noble metals puts considerable commercial limitations on a wider application of PEM electrolyzers and a significant reduction of loadings should be achieved [134].

One of the present trends in applied PEM electrolyzer research includes replacement of materials containing precious metals with cheaper materials, based on non-precious metals. A great number of oxides have been investigated [10]. But unfortunately, gained by several last decades experience clearly shows, that still there are only few adequately active catalysts towards the OER, which are based on Ir, Ru and their oxides IrO_2 and RuO_2. Understanding this fact, it is safe to assume, that the serious attention should be put in the possible reducing of the precious catalyst loading. It can be done be increasing the active surface area of the available noble electrocatalysts.

The reaction rate is proportional to the number of active sites on the catalyst surface, which indicates that the specific surface area of the catalyst contributes to its performance [174]. Thus increasing of the catalyst surface area is one of the ways to decrease the catalyst loading. This can be done by two means.

The first includes doping of active oxides with other, more available materials, such as SnO_2, Sb_2O_3,TaO_x,Mo_xO_y, CeO_2, etc [51, 120, 175–178]. This approach involves introduction of a dopant precursor on the initial stage of catalyst synthesis and is mainly oriented towards increasing the specific performance of the catalyst or improving its stability. Following this method, composite binary or even ternary catalytic oxides are usually

obtained [95, 178].

Bertoncello et al. showed the possibility of preparing electrodeposited layer of composite RuO_2 and PbO_2 on the Ti support, presenting acceptable activity and long term performance stability [179].

Other approach involves maximizing of the activity of the catalyst by improving its texture and surface properties. It can be done by use of an adequate support material for the catalyst. The presence of a support can prevent particle agglomeration, thus improving the specific surface area of the electrode. This approach will be discussed in details in Section 2.6.3.

The OEE stability over time can be presented in the way, proposed by Trasatti [14]:

In Figure 2.18 it was shown the contributions of different components on the overall overpotential of an electrolyzer cell (equation 3.2) [14]:

$$\Delta V = \Delta E + \eta_a + \eta_c + \Delta V_\Omega + \Delta V_{(t)} \tag{3.2}$$

According this equation, the value ΔV will increase while operating the cell, as the term $\Delta V_{(t)}$ is attributed to the "electrode stability over time" factor. ΔV can be related to the degradation of the outer surface of the electrocatalyst and/or of the support/active layer interface in the case of coatings. However, electrode wear can happen without any changes in ΔV until the whole catalyst is consumed. In such a case an increase of ΔV is observed at the point of total electrode fail .

3.5 Preparation of powder electrocatalysts and films for the OER

A PEM electrolyzer concept includes using of the active catalyst in the form of powder. Therefore, it is essential to review different methods of catalyst powder preparation. As it was outlined in Section 3.4, most of practical electrocatalysts for the OER are limited to iridium and ruthenium metals and their oxides. This melals have similar properties and belong to the transition metal group, thus most of the preparation methods of any of it can be used for the synthesis of other.

3.5.1 Adams fusion technique

The Adams fusion method is based on an ion exchange reaction to obtain the metal oxide [180]. The starting compound is the complex $H_2IrCl_6 \cdot 4\,H_2O$,

which is dissolved in isopropanol and mixed with $NaNO_3$, providing the substitution of the chloride ligand by the nitrate ions according to the following equation [181]:

$$H_2IrCl_6 + 6\,NaNO_3 \rightarrow 6\,NaCl + Ir(NO_3)_4 + 2\,HNO_3 \tag{3.3}$$

The resulting solution is then heated until the solvent is evaporated. The remaining solid, consisting on a mixture of NaCl and $Ir(NO_3)_4$, is heated up to 500 °C in a furnace in order to decompose the nitrate ion, according to the following reaction:

$$Ir(NO_3)_4 \xrightarrow{\Delta} IrO_2 + 4\,NO_2\uparrow + O_2\uparrow \tag{3.4}$$

The final product is a mixture of IrO_2 and NaCl. The oxide is thus purified by washing with water until the chloride concentration is lower than 40 ppm.

As it was mentioned before, RuO_2 electrocatalyst can be prepared analogically by this synthesis [167].

3.5.2 Polyol method

This method belongs to the "low temperature" methods of catalyst preparation. Polyol method allows original synthesising of catalyst metal powders, while the metal oxide would be further formed directly at the anode in situ electrolysis (Section 2.3.2).

In this method a polyol such as ethylene glycol serves as a solvent and as a reducing agent. The glycol-metal precursor mixture is heated to reflux temperature and metal particles are precipitated out of solution. The metal-glycol mixture is usually cooled to room temperature, washed several times through centrifugation, filtered and then collected powder is dried in air.

The reducing temperature is usually around 100 °C. It was shown that iridium nanoparticles can be synthesized without any sintering during the process and the average size of particles can be lowered down to 3 nm [182].

Alternatively, a preparation of noble metal catalysts was reported at room temperature, using sodium borohydride or mixture of it with ethanol as a reducing agent [55, 112, 183].

3.5.3 Modified polyol method (colloid method)

Nanopowders of iridium oxide or mixed oxide powders can be prepared by so-called "Modified polyol method" [51, 181]. The precursor salt-ethylene

glycol mixture is heated in the nitrogen protected atmosphere until the reflux temperature and kept under stirring for 2 hours to form the colloid. This is followed by adjusting pH with alkaline solution (NaOH) and separation of the colloid from glycol by centrifugation. The obtained colloid metal hydroxide is washed repeatedly in deionised water, dispersed in acetone and dried in air at 60 °C. Further the metal oxide is obtained via thermal treatment at 500 °C.

3.5.4 Catalyst film preparation methods

The sol-gel methods Method is based on dissolving a metal precursor in the form of acetylacetonates $[CH_3COCH{=}C(O^-)CH_3]_3M$ in the solution of isopropanol and glacial acetic acid. The mixture is then exposed to ultrasonic radiation to produce more stable sol. Then the sol-gel film is applied on a base metal surface and dried on the furnace at temperature 400-600 °C. The procedure is repeated until the coating of desired amount of material is deposited on the electrode, followed by the final heat-treatment [92, 184]. This technique was reported to be used for synthesis of mixed oxides catalyst [172, 185].

Synthesis of metallic iridium catalyst through the sol-gel method is also possible by using iridium chloride as a precursor. In this case, methanol is used as a dispersion agent for the salt, followed by addition of the precipitation agent (tetramethylammonium hydroxide) and stirring at 60 °C. After obtaining of precipitated $Ir(OH)_3$, it is filtered, rinsed with methanol and dried at 60 °C. The obtained $Ir(OH)_3$ powder is further reduced with hydrogen or argon stream at 600 °C [186].

Other techniques A number of other methods can be used for preparation of noble oxide films on substrate metal, among them are electrodeposition [60, 187, 188] or magnetron sputtering [121, 147].

3.6 DSA-type electrodes, their preparation and properties

An abbreviation DSA stands for a dimensionally stable anode, which is the current type of anode used in industrial production of chlorine and oxygen by electrolysis. It is essentially a sheet of titanium metal, coated with a mixture of metal oxides. The electrode is called a “dimensionally stable” as the coating has a very long service life time (several years) under conditions of operating cell. This type of anode is a good contrast to traditionally used

carbon anodes for chlorine production, which are consumed considerably during the cell operation [189].

Even though dimensionally stable anodes can not be directly used in the PEM technology, the discovery of them by Henry B. Beer in the end of 1960-s provoked something of a technological revolution in the large electrolytic industry. The invention revealed that the performance of anodes made of thermally prepared noble metal oxides was better than of the corresponding noble metals. The use of these electrodes was described in several patents [80, 190, 191] and noble metal oxide electrocatalysts became established in many industrial electrochemical processes in the form of DSAs.

However, this fact was not instantly recorded by the open scientific literature and the first concrete fundamental investigation on the topic appeared in the early seventies when such electrodes had already accumulated long industrial use. Since then, intensive research have been done on different metal oxide coatings and preparation parameters of DSA electrodes [93, 192].

The technological impact of the so-called dimensionally stable anode based on mixed oxides whose active component is mainly RuO_2 has been decisive. Further developments are expected and pursued actively. Properties whose improvement is sought for are essentially electrical conduction, chemical stability and electrocatalytic activity [10]. Chemical stability is an important demand as the electrocatalyst layer contains precious metals and besides the cost of the lost material, maintenance costs rise due to the need for electrode replacement or re-coating. Also, the active coating layer should not be passivated, providing the acceptable electronic conductivity.

Massive electrodes are not any longer common in modern technology: as a rule industrial electrodes are now made by the coating of a inert base material (usually titanium) with a relatively thick layer (few microns) of the active oxide coating. The active electrocatalytic component (more often RuO_2) is usually prepared by the thermal decomposition of a suitable precursor (by pyrolysis). A stabilizing agent is often used along with the active material, composing a mixed oxide in the active layer [61]. Among mechanical stability promoters TiO_2,TaO_2, ZrO_2, CeO_2, SnO_2 or Nb_2O_5 can be used [59, 193].

Even though ruthenium oxide is the most active oxide towards the OER [11], it suffer instability and therefore is usually stabilized with another oxide, e.g. IrO_2 or SnO_2 [50, 194, 195]. Stannic oxide easily adopts the rutile crystal structure and therefore a solid solution, as ruthenium-tin oxide is commonly described in the open literature [52, 196].

While electrodes based on RuO_2 and TiO_2 mixture are industrially used in chlorine-alkali cells [197], tantalum is a well-known addition to ruthenium oxide based electrodes [198]. IrO_2–TaO_2 oxide mixture have been suggested

to be the most efficient electrocatalitic composition towards the OER in acidic electrolytes due to high activity and corrosion stability [199, 200].

As the substrate material affects properties of DSA-type oxide layers [201], is is important to choose optimal base metal. One of the demands to it is its cost as it should have reasonable price to make this material accessible for the mass-production. Titanium, having a low cost/performance ratio for this application, is the most commonly used base material and is utilized for almost all conventional DSAs [202].

A comprehensive study of electrodes with different base materials, coated with IrO_2–RuO_2–TaO_2 was performed by Vercesi et al. [203]. Four metals as titanium, zirconium, tantalum and niobium were tested along with 2 alloys, e.g. "niobium-1% zirconium" and "tantalum-40% niobium". The results showed that the most crucial step in preparation of the electrode, which later had great influence on the performance and service life, was the coating layer thermal treatment procedure. While iridium and tantalum in the coating reacted with oxygen to form oxides, the base material itself was oxidised, and thus resulted in formation of an oxide layer between the base material and the coating. This could lead to cracks in the coating and building of an insulating layer between the active catalyst and the base material, which would greatly decrease the activity of the electrode.

The corrosion stability investigation of prepared DSAs included polarisation of the electrodes in sulphuric acid of various concentrations under 2V of anodic overpotential (vs. SCE). Results showed that zirconium is not suitable as the base material, because its corrosion rate was a number of magnitudes greater than that for other studied materials.

Preparation procedure influences greatly the final electrode performance, stability and service life. The traditional preparation method of DSAs includes thermal decomposition (calcination) of a precursor salt (usually chloride) to the corresponding oxide. The first step includes preparation of a precursor salt solution. The corresponding metal salt is dissolved in alcohol or water. If the DSA should consist of several oxide compounds in the active layer, then solutions, containing corresponding metal salt precursors are mixed to obtain the desired ratio. The prepared precursor solution is applied on the base material and then fired at high temperature to form a compact metal oxide layer.

Use of different precursor solvents influences properties, such as wettability of the painting solution, which in turn varies the deposition yields. As well, solvent influences on the kinetics of thermal decomposition with further impact on the electrocatalytic properties [204]. The discussion addressed to the choice of an appropriate solvent was done by Comninellis at al. [205]. As high volatility of alcohols can cause a partial evaporation of a precursor,

solvent influences the final deposition yield. It may result in overestimation of the amount of deposited material, as precursor is applied in the form of a solution. The surface tension of the painting solution varies with different solvents and also influences the evaporation rate [205].

Before application of the precursor solution, the base material is pretreated in order to provide better adherence with the active oxide layer. Typically, the procedure includes the following steps: sandblasting, ultrasonic cleaning and final etching in the concentrated acid solution [155, 193, 206].

The precursor solution is applied on the base material either by dipping, brushing, or spraying. The electrode is then heated in oven for several minutes at low temperatures (60-100 °C) to evaporate the solvent, and then baked at high temperature for typically 5-10 minutes (at 300-500 °C). The procedure of treatment with precursor mixture is followed by drying and baking and is repeated as many times as desired in order to obtain a coherent and contiguous layer. Eventually, electrode is calcined at high temperature, ranging typically from 300 to 550 °C during a couple of hours in order to get a compact metal oxide layer [91, 205].

The influence of calcination temperature on electrode properties was investigated by Ma et al. [167]. The increase of the temperature increased particle size of RuO_2. This resulted in higher electronic conductivity, but lower electrochemical active surface area, which is undesirable. Catalysis does not happen on the plain surface of crystallite, but on the edges, where there are clefts and spikes. Thus, it is important during preparation of the electrodes to find the optimal temperature for achieving a good balance between crystallite size and layer conductivity.

The composition of the mixed precursor salts may not always correspond to the composition of the oxide coating layer. This is possible because of the metal salts, which are dissolved in e.g. alcohol, can evaporate during baking and annealing at high temperatures, if the boiling point or/and decomposition temperature are low enough [205]. It can be presented by taking into account the rates of oxide formation (r_f) and evaporation/sublimation (r_e), which can be expressed as:

$$\text{starting material} \xrightarrow{r_f} \text{oxide formation} \tag{3.5}$$

$$\text{starting material} \xrightarrow{r_e} \text{evaporation} \tag{3.6}$$

The rate of oxide formation is primarily dependent on the bond strength, concentrations and temperature. The rate of evaporation or sublimation depends on the physical properties of the metal salt, e.g. melting, boiling points and also sublimation temperature. These two reaction rates compete

with each other and when r_e predominates, most of the metal will be lost during thermal decomposition [205].

There are essentially two crucial steps in the preparation of DSA electrodes. The first is drying of the precursor solution, which is a necessary step for evaporation of the solvent. Here a part of the material may evaporate if its boiling point is too low. The second step is calcination, when the temperature is raised typically above 300 °C. In this state the two previously described reaction rates r_f and r_e compete and thus influence the final composition of the oxide layer. It has been shown that the catalytically active compounds, such as IrO_2 and RuO_2, along with Ta_2O_5 can be deposited with a yield close to 100 %, while losses of dispersants such as SnO_2 were very high. In fact, tin oxide layer formed by dissolving $SnCl_4$ in 20 % HCl and ethanol resulted in deposition yield of around 20 %, while when using $SnCl_2$ the deposition yields were around 60 %. This difference occurred because of different boiling points of the metal salt precursors, which are 114 °C for $SnCl_4$ and 652 °C for $SnCl_2$. However, when preparing mixed oxides, such as $SnO_2{-}Sb_2O_5$ from $SnCl_2$ and $SbCl_5$ precursors, the overall deposition yield was only 35 %, which means the tremendously large looses.

Although very comprehensive studies of the structural and electrochemical properties of DSA oxides have been carried out, less is still known regarding the structure and electrocatalytic properties of oxide powders. This is probably due to the fact that DSA electrodes are applied in real industrial processes compared with the same oxide compositions in powdered form. Therefore analysis of powder-based oxides gives an insight to the specific nature of noble metal oxides as electrocatalysts while providing a possible use in PEM water electrolysis applications. By using a multi-disciplined approach to develop and characterize electrocatalysts, Marshall [120] achieved significant improvements in studying of performance and efficiency of PEM water electrolysis cells.

3.7 Electrolytes for water electrolysis

Electrolyte is one of the main components of any type of electrolyzer. The importance of electrolyte is emphasized by the fact that the type of electrolyzer, as well as of fuel cell, is named after the type of electrolyte used. In the classical view it is traditionally a solution of acid, base or water soluble salt in the water. When added, those dissociate into ions in the solution, which increases conductivity of pure water. Other type of electrolytes are solid and can be based on a polymer (PEM) or a ceramic membrane(SOFC/SOEC).

3.7.1 Alkaline electrolyte

This type of electrolyte is the most industrialised for today. The electrolyte is based on highly caustic potassium or sodium hydroxide (around 30 wt.%) aqueous solutions. The operating conditions are usually 70-90 °C and pressures from ambient up to 35 bar [41, 207]. The main disadvantages of a system based on alkaline electrolytes are high energy consumption, frequent maintenance and safety issues with the electrolyte [41]. The research in alkaline water electrolysis is on the decline, more interest is put in improving of the acidic water electrolysis. In industrial perspective the development of a cheap acidic water electrolyzer cell would be a great improvement to the current alkaline electrolyzer cells. The reason is that with the acidic electrolysis higher operating current densities and higher pressures can be achieved together with lower energy consumption and use of less voluminous systems [149].

3.7.2 Solid oxide electrolyte

Use of ceramic membranes instead of polymer based membranes is also an option. Ceramics are more stable at higher temperatures than polymers. However, increased electric resistance might be an issue for ceramics. Solid oxide cells use yttria or scandia-stabilised zirconia membranes as an O^{2-} ion conductor and can operate at temperatures around 800-1000 °C. In the temperature interval between 600-800 °C a membrane consisting of $LaGaO_3$ doped with small amounts of Sr and Mg can be used efficiently. Sr and Mg will allow oxide ions to travel through the lattice structure, thus providing ion flow through the membrane. A cheaper electrolyte might be based on CeO_2. This ceramic is limited to temperatures less than 700 °C but the cheaper material is a major advantage [107]. Unfortunately, this technology is still not satisfactory for industry with respect to materials and fabrication process [208].

3.7.3 Acidic electrolyte and polymer electrolyte membranes

The acidic water electrolysis traditionally uses sulphuric or phosphoric acid as they are stable within the potential window of water. The acid increases the conductivity of water through the donating protons.

The polymer electrolyte membrane (PEM) is a membrane which acts as a proton conductor in electrolyzer cell. Usually, the ionic membrane consists of a solid polytetrafluoroethylene (PTFE) backbone, which is chemically altered and contains sulfonic ionic functional groups thus the pendant side chains terminated with $-SO^{3-}$. The acid dissociates and release protons by

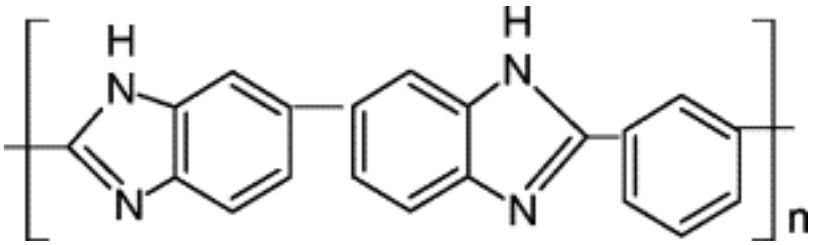

Figure 3.3: General structure of Poly[2,2'-(m-phenylene)-5,5'-bibenzimidazole (PBI) [20].

the following mechanism (3.7):

$$SO_3H^- => SO_3^- + H^+ \tag{3.7}$$

The membranes of this type allow water molecules to penetrate into its structure, while remaining not permeable to molecular H_2 and O_2. The sulfonic groups are responsible for the transfer of protons during electrolysis, where a hydrated proton H_3O^+ can freely move within the polymer matrix, while a sulfonate ion SO^{3-} is fixed to the side chain of polymer. When electric current flows across the membrane, the hydrated protons are attracted to the cathode, where they are combined into hydrogen. Nafion® is the most known trademark among ionic membranes and is patented by Du Pont Company in 1966 [209]. A typical membrane has a thickness in the range of 50-100 μmeters and this type of membrane is commonly used as an electrolyte for conventional PEM water electrolyzers [87, 111, 112]. These membranes have excellent chemical stability, high ionic conductivity and excellent mechanical strength [112]. Water electrolysis using Nafion® as an electrolyte is a promising technology for large-scale hydrogen production [28, 30].

The conductivity of such membranes decreases significantly at temperatures above 80 °C, which is associated with the ion of water content [20, 210]. Sufficient efficiency is achieved using PBI membranes doped with phosphoric acid in PEM fuel cells at temperatures up to 200 °C under ambient pressure [20, 44, 137]. The structure of PBI is shown in Figure 3.3. Doped PBI membranes are a potential electrolyte for use in PEM steam electrolyzer systems. The ionic conductivity of membranes increases with temperature [20], which means the higher the working temperature is, the lower ohmic losses through electrolyte are. In spite of that, the conditions of extremely low pH combined with high overpotentials at the anodic compartment of the OEE impose serious limitations on materials which can be used in these cells.

In the laboratory conditions commonly 0.5M sulphuric acid is used for screening electrode materials in a 3-electrode electrochemical cells, simulat-

ing conditions of the Nafion®-based systems, which work at temperatures below 100 °C [51, 120]. Since high temperature PEM cells are working at temperatures around 150 °C, H_2SO_4 cannot be used to simulate conditions in the 3-electrode cell, even at high concentration. Instead, concentrated H_3PO_4 can ben used, which permits to work at temperatures as high as 150-160 °C, depending on the composition [211].

However, it was noticed by Appleby and Van Drunen that the Tafel slopes for noble electrocatalysts are significantly higher in concentrated phosphoric acid than those for more diluted solutions, being the apparent cause of adsorption of electrolyte on the electrode surface [212].

Other membranes have been investigated. The polymers which seem to be showing potential besides PBI in high temperature water electrolysis are polyether ketones, polyether sulfones and sulfonated polyphenyl quinoxalines (SPPQs). These polymers have high thermal stability and can withstand temperatures up to 200 °C. A membrane consisting of sulfonated polyetheretherketone (SPEEK) has shown comparable performance with Nafion® [213], but thermal stability and mechanical properties are not as good [105].

Composites made of SPEEK and PBI have also been investigated. The conclusion was that the proton conductivity of the composite membranes depended on content of PBI and thermal stability of the SPEEK membranes is improved with the addition of PBI [214].

As it was fairly noticed by Miller in one of his latest publications, the cost of Nafion®-based polymers calls for alternative membrane materials along with higher operating temperatures closer to 150 °C. These membranes are required to improve kinetics and obtain higher conversion efficiencies in solid polymer electrolyte (SPE) electrolyzers and new solid electrolytes are needed [134].

Effective and affordable membranes are very important for the commercialisation of PEM water electrolyzers as it is both easier to manufacture and safer as neither acid nor electrolyte are in liquid phase.

This study will not focus on the electrolyte development and solutions of acid will be used in the experiments to simulate the conditions of PEM electrolyzer cell.

3.8 Catalyst supports in PEM systems and possibilities of use refractory ceramics

Design and synthesis of electrocatalysts with the "supported" structure could greatly improve utilisation of the expensive component, thus decreasing the noble metal loading and, eventually, cost of the catalytic layer. Even structures involving inert support materials could significantly develop morphology of electrocatalyst through geometrical interactions between active component and support (using of TiO_2 in DSA electrodes is a classic example, found the industrial application).

Titanium-based supports with IrO_2 as an active electrocatalyst have been investigated for the OER [92, 100, 215]. However, the experiment conditions were simulating those in low temperature PEM systems and were different from conditions, found in high-temperature PEM cells.

Although Ti-based supports show good performance in Nafion®-based systems [216], they most likely cannot be implemented in PBI-based membranes, using phosphoric acid as an electrolyte due to high rate of titanium corrosion at elevated temperatures in phosphoric acid [36, 153].

Advantages of a support use in the catalytic layer were discussed in Section 2.6.3. Among other parameters, support material can have influence on the electronic structure of catalyst and enhance its activity. This effect is often called the strong catalyst support interaction (SCSI) [88]. The interactions between Ebonex carbon support and Pt catalyst have been proposed to be due to the hypo-d-electron character interaction, changing the electronic structure of catalyst. A synergetic effect was suggested to be due to increase of 5d vacancy of Pt and decrease of Pt–Pt bond distances by interaction with Ebonex carbon, which inhibits the chemisorption of OH. Regarding the oxygen reduction reaction (ORR), a shift of PtOH formation due to this effect to more positive potentials facilitates the interaction of O_2 with Pt and increases the catalyst activity [217, 218].

Hence, carbon is a widely used catalyst support material for PEM fuel cells [219]. On the other hand, one of the main reasons for fuel cell catalyst degradation is corrosion of its support, which occurs at potentials higher than 0.207 V (vs. SHE) in oxidizing conditions [20, 220, 221]. In electrolysis mode the corrosion speed of carbon would be much higher than in fuel cell mode due to higher anodic overpotentials of the OER [111]. The corrosion media for carbon will be even more severe at elevated temperatures as 120-200 °C [88]. Thus, carbon cannot be considered as a potential durable support for anode electrocatalyst in PEM electrolyzers and other materials with considerably higher corrosion resistance need to be tested.

Presently, only few supports have been investigated for the oxygen evolution electrodes [222]. Main requirements to the OEE electrocatalyst support are: reasonable conductivity, durability and corrosion stability. However, if conductivity of a support is low and material has high porosity, considerable ohmic drops will be measured in the active layer.

As discussed by S.Trasatti, a catalytic layer of 5 μm thickness with the resistivity of $10^{-2}\ \Omega \cdot cm$ will present resistance of 5 μΩ per unit apparent surface area (1 cm^2). Having a current flow of 1 A/cm^2, the ohmic drop will only be 5 μV. It means that for measuring a meaning ohmic drop of 5 mV, the resistivity of the catalytic layer should be in the order of 100 $\Omega \cdot cm$ (1 $\Omega \cdot m$). A good example could be $TiO_2 + RuO_2$ mixtures in traditional DSA electrodes. As TiO_2 is a good insulator, the total conductivity of the layer takes place through RuO_2 clusters, and it drops significantly with decreasing of RuO_2 content. It happens due to the interruption in the conductive chains. That is the reason why the electrodes composition cannot be decreased below 15-20 % of RuO_2 [14]. This type of conduction mechanism is also attributed to ceramic resistors, where RuO_2 is embedded in isolating SiO_2 [223, 224].

Therefore, some of the materials, which possess modest electric conductivity can be used as an anode for acidic solutions [225]. In the mentioned study, p−Si with electrical resistance of 1-3 $m\Omega \cdot cm$ was employed as a substrate for the active IrO_2 and results showed that this material can be used for preparation of DSA-type electrodes. Description of the DSAs and their preparation was given in Section 3.6

Indeed, the choice of materials in the area is highly limited, which is directly connected with increased cell voltages applied in the electrolyzer mode.

Referring to an another experience, gained during long years of industry and research of aluminium electrolysis, it was recognised that the search for inert anode materials is one of the most difficult challenges for modern materials science. It was also noticed, that it can well be that there is no material, that can meet the requirements of an industrial cell [226]. Later, Kvande outlined that large efforts have been done in the area, but none of them led to any acceptable material. The work in this field may perhaps be described as a long and mostly unfruitful struggle [227].

Only a dimensionally and chemically stable, as well as readily available and reasonably conductive material should be used for this application. Among others, ceramic materials are promising candidates. Previous works showed that those have a potential application in the PEM fuel cell (PEMFC) systems [216]. Carbides present a class of high temperature stable refractory materials, among them are boron [228], titanium [16] and silicon carbide [229, 230].

As it was outlined before, raw materials for preparation of inert anode or/and its support should be preferably cheap and readily available. Therefore, silicon carbide, a potential catalyst support for heterogeneous catalysis, can be a promising candidate [86]. It is known as a hard, refractory and chemically inert material [231]. It has also notable corrosion resistance in acidic media [232].

Electronic conductivity of this material is quite poor, however doping with appropriate elements can significantly increase this property [233]. High stability of silicon carbide in phosphoric acid solutions is a considerable advantage of this material, giving a new horizon for its electrochemical applications [71]. However, it was also proposed that free Si containing in SiC is mainly responsible for its corrosion [71].

Several studies reported successful use of silicon carbide as a catalyst support for PEM fuel cells [229, 230]. However, at present there are almost no publications covering any catalyst support investigations for electrolyzers [222]. Indeed, this area of research is more challenging and the material choice is highly limited, which is directly connected with the increased cell voltages applied in the electrolyzer mode.

In this work the importance of supported catalysts in the development of more efficient and lasting OEEs is expressed. Therefore, the main goal of this work is to study influence of the selected support on the electrochemical behaviour of IrO_2 active catalyst. To fulfil this, a refractory silicon carbide-silicon material (free Si less than 22%) was used as a support material and supported catalysts with different compositions were prepared and tested, along with pure IrO_2 and SiC-Si sample powders.

The Adams fusion is known as an old and reproducible technique for synthesis of nano-sized catalyst particles (Section 3.5.1). As the last step of this procedure involves calcination of a precursor at rather high temperatures (350-500 °C), a limited number of materials can withstand these conditions without being oxidised. SiC is a refractory material, withstanding these temperatures. Therefore, it was interesting to study its behaviour as a potential OER catalyst support.

Chapter 4

Construction Materials for High Temperature PEM Electrolyzers

Parts of this chapter has been published in the International Journal of Hydrogen Energy 2011;36(1):111–119, as a "Corrosion behaviour of construction materials for high temperature steam electrolyzers." [36].

4.1 Experimental part

4.1.1 Materials and reactants

For preparation of the samples and the electrochemical experiments, the following substances were used:

- Demineralised water
- H_3PO_4 85%, Sigma Aldrich, puriss. p.a. (analytical purity)
- H_2SO_4 95-97%, Sigma Aldrich, puriss
- Nafion® suspension, 5-6% in 50% propanol-water solution, by DuPont
- Ta plate electrode, Good Fellow Cambridge Ltd.
- Austenitic stainless steel plate (AISI 316L, AISI 321, AISI 347, annealed type of temper), by Good Fellow Cambridge Limited, England
- and Ti foil, by Good Fellow Cambridge Limited (England)

- Hastelloy® C-276, Inconel® 625 and Incoloy® 825 plates, by T.GRAAE SpecialMetaller Aps (Denmark)
- CVD tantalum coated stainless steel AISI 316L was provided by Tantaline A/S, Denmark
- SiC abrasive paper, by Struers A/S (Denmark)
- Diamond powder polishing suspension, particle size less than 0.25 μm, by Struers A/S (Denmark)
- PolyFast phenolic hot mounting resin with carbon filler, provided by Struers A/S (Denmark)

4.1.2 Materials and sample preparation

Typical chemical compositions of stainless steels and nickel-based alloys investigated in this work are given in Table 4.1.

Chemical composition of alloys (elements, weight%)

Alloy type	Ni	Co	Cr	Mo	W	Fe	Si	Mn	C	Al	Ti	Other	Nb+Ta
AISI 347	9.0-13.0	-	17-19	-	-	Bal.	1.0	2.0	0.08	-	-	-	0.8
AISI 321	9.0-12.0	-	17-19	-	-	Bal.	1.0	2.0	0.08	-	0.4-0.7	-	-
AISI 316L	10.0-13.0	-	16.5-18.5	2.0-2.5	-	Bal.	1.0	2.0	0.03	-	-	N less 0.11	-
Hastelloy® C-276	57	2.5	15.5	16.0	3.75	5.5	0.08	1.0	0.02	-	- -	V 0.35	-
Inconel® 625	62	1.0	21.5	9.0	-	5.0	0.5	0.5	0.1	0.4	0.4	-	3.5
Incoloy® 825	44	-	21.5	3.0	-	27	0.3	1.0	0.05	0.1	1.0	Cu 2.0	-

Table 4.1: Alloys chemical composition.

All specimens were cut into round plates of 15 mm in diameter. Afterwards, surfaces of all samples, apart from CVD tantalum coated SS316L, were manually ground prior to testing to eliminate any mill finish effects. Abrasive paper was used, followed by polishing with diamond powder. Finally, surfaces were degreased with acetone.

4.1.3 Characterisation

A high temperature electrochemical cell (Figure 4.1) was specially designed for corrosion studies at elevated temperatures. The working electrode was designed to hold a disk sample, with a geometric area of opening ca 0.2 cm^2. A coil of platinum wire was used as a counter electrode to ensure good polarization distribution. A calomel electrode was used as a reference electrode, connected to the system through a Luggin capillary. 85% phosphoric acid (analytical purity) was used as an electrolyte. Tests were performed at 30, 80 and 120 °C at air atmosphere. In this work the electrochemical cyclic

Tafel voltammetry technique is employed [12, 72, 234]. The experimental apparatus used for the electrochemical studies was potentiostat model VersaSTAT 3 and VersaStudio software by Princeton Applied Research. After open-circuit potential was established, scanning was initiated with a scan rate of 1 mV/s. The potential window was 1.5 V, starting at a potential of 400 mV less than the reference electrode potential and going up to 1.1 V more than the reference electrode potential. Reversed polarization was performed afterwards.

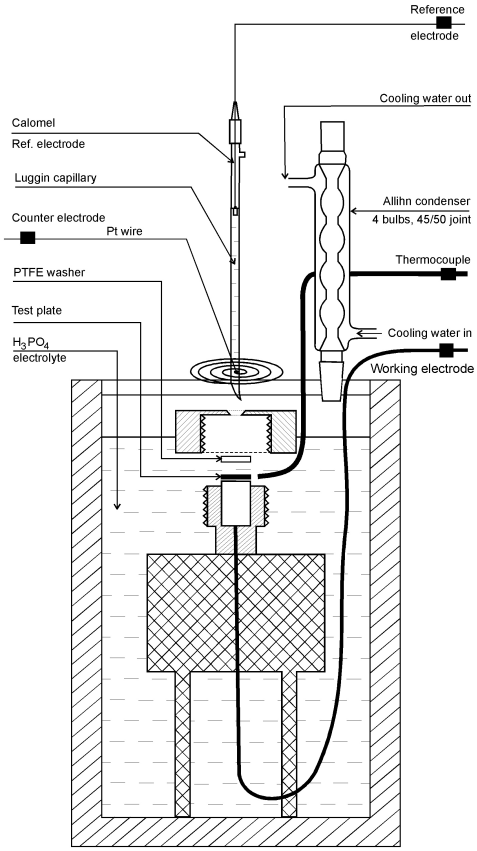

Figure 4.1: The electrochemical cell.

Cross-sections of the samples before and after voltametric measurements were studied using scanning electron microscopy (SEM) and energy dispersive X-ray spectroscopy (EDX). The cut was made for all the samples before and after immersion in 85% H_3PO_4 at 120 °C for the time of the electrochemical experiment. Duplicate plates were prepared for the cross-section investigation before the exposition. All samples were mounted in hot mounting resin. SEM measurements were made with the JEOL JSM 5910 scanning

electron microscope. The EDX-system used was INCA from Oxford Instrument (accelerating voltage 20.00 kV, working distance 10 mm).

4.2 Results and discussion

Figure 4.2 represents the polarisation curves for platinum and gold foil, which show the electrochemical stability window for these materials and electrolyte in concentrated phosphoric acid at 120 °C. It can be seen that platinum is a better catalyst for O^{2-} oxidation then gold (Figure 4.2).

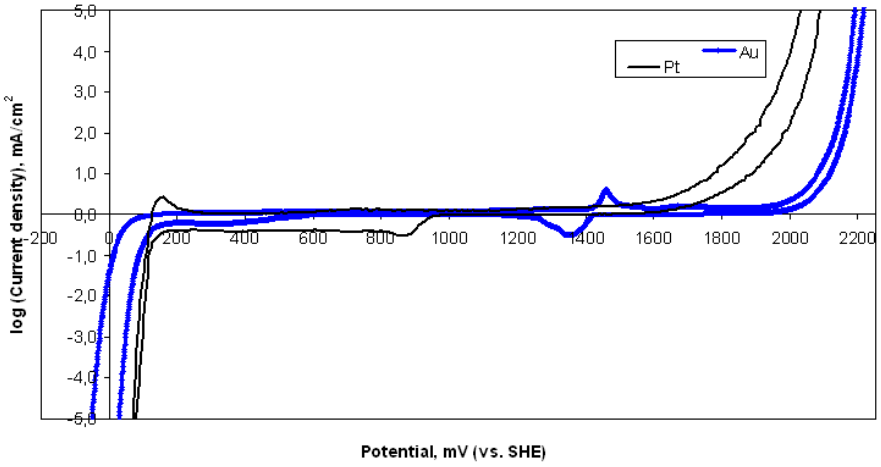

Figure 4.2: Potential window for Pt and Au in 85% H_3PO_4, 120 °C, 1 mV/s (vs. SHE).

The method of corrossion rate calculation, described in Section 2.4.2 was applied to all experiments. Figures 4.3-4.8 present Tafel plots for the materials tested, obtained at 80 °C and 120 °C. Anodic exchange current density values were obtained from cyclic Tafel plots [12]. Corresponding corrosion currents and approximate corrosion rates were calculated as described in Section 2.4.2 and are presented in Table 4.2. Approximate CRs were calculated in terms of penetration rate, using the Faraday's Law [73].

For all studied materials there is a dramatic influence of temperature on corrosion rate, which grows with increasing temperature.

It can be seen from cyclic Tafel behaviour, that for all of the studied alloys, corrosion is of a local type, i.e. pitting or intergranular (Figures 4.3-4.6).

The analysis of the shape of cyclic Tafel voltammograms can give useful information about possible corrosion mechanisms [72]. Particularly, data related to pitting behaviour can be obtained using a method, proposed by

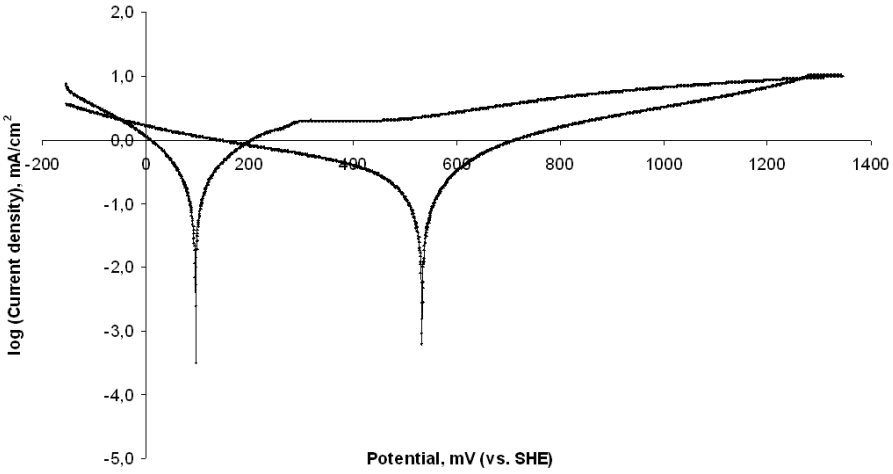

Figure 4.3: Tafel plot for AISI 316L in 85% H_3PO_4, 80 °C, 1 mV/s (vs. SHE).

Table 4.2: The comparison of corrosion currents (approximate CRs) of different materials at T=30, 80 and 120 °C.

	i_{corr}, mA/cm^2 (CR, mm/year)		
Sample	30 °C	80 °C	120 °C
Stainless steel AISI 316L	$3\,16 \times 10^{-3}(0,037)$	$6\,3 \times 10^{-2}(0\,73)$	$1\,3 \times 10^{-1}(1\,46)$
Stainless steel AISI 321	$1\,26 \times 10^{-4}(< 0\,01)$	$1\,0 \times 10^{-2}(0\,12)$	$4\,0 \times 10^{-2}(0\,46)$
Stainless steel AISI 347	$3\,02 \times 10^{-4}(< 0\,01)$	$2\,5 \times 10^{-2}(0\,29)$	$7\,9 \times 10^{-2}(0\,92)$
Inconel® 625	$1\,58 \times 10^{-4}(< 0\,01)$	$5\,3 \times 10^{-4}(< 0\,01)$	$2\,0 \times 10^{-2}(0\,23)$
Incoloy® 825	$1\,58 \times 10^{-4}(< 0\,01)$	$2\,0 \times 10^{-2}(0\,23)$	$3\,2 \times 10^{-2}(0\,37)$
Hastelloy® C-276	$1\,95 \times 10^{-4}(< 0\,01)$	$4\,0 \times 10^{-3}(0\,05)$	$2\,4 \times 10^{-2}(0\,28)$
Tantalum			$6\,3 \times 10^{-5}(< 0,001)$
Titanium			$6\,3(73,3)$

Pourbaix [235]. In this case, the anodic polarisation scan is not terminated at high positive potential, but is reduced at the same scan rate until reverse E_{corr} is reached. Usually, this kind of graph is called "The pitting scan". Using this technique, it can be assumed that if any pits arise during forward anodic polarisation, any further initiation or propagation then ceases and the surface is covered with an oxide film.

For all materials investigated, besides titanium, the repassivation occurs easily. After changing the direction of polarisation in the highly anodic region, the reverse scan shows more positive corrosion potentials, and lower currents are recorded for the same values of potential. After the reverse voltametric curve crosses the forward one (closing the hysteresis loop), current continues to drop. In most cases, the loop is very small or does not exist, which usually indicates high resistance to pitting type of corrosion. In other words, if any break in the passive layer occurs, it easily "heals" itself, preventing any further development of pits. Thus, it is expected that the pitting resistance is

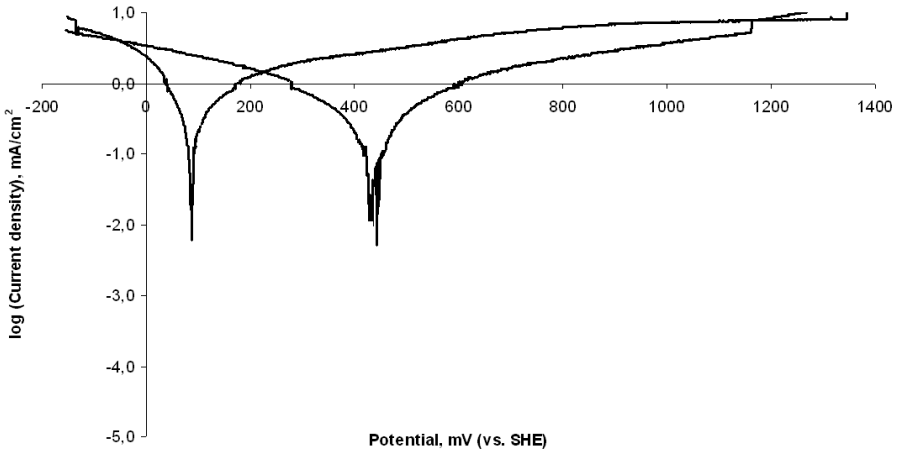

Figure 4.4: Tafel plot for AISI 316L in 85% H_3PO_4, 120 °C, 1 mV/s (vs. SHE).

excellent for all tested alloys, because surface protection eliminates local active sites. For titanium the hysteresis loop is very wide, and lasts for almost the whole anodic part of the polarisation curve. Reverse scanning repeats forward with higher values of currents, indicating the absence of "healing" passivation.

In Table 4.3 the comparison of corrosion potentials for forward and backward scans is given. In most cases, there is an obvious dependence between corrosion rate and E_{corr}. For example, more positive value of E_{corr} for AISI 321 stainless steel during reverse scan corresponds to the lowest corrosion speed of AISI 321 among other tested stainless steels.

Alloy AISI 321 exhibited the largest difference between forward (starting) and reverse corrosion potentials, as well as the most positive repassivation potential among the tested alloys at 120 °C. This corresponds to the lowest corrosion rate of AISI 321 among the stainless steels.

Titanium showed the poorest corrosion resistance. At 120 °C and open corrosion potential, the dissolution of titanium was observed visually, followed by intensive evolution of hydrogen gas. Under positive polarisation, it was partly passivated, but still the rates of dissolution were much higher than for austenitic stainless steels.

CVD tantalum coating on stainless steel showed an outstanding corrosion resistance, with the CRs being similar to earlier published data on this material [236]. The SEM image of the CVD-tantalum coated sample and the corresponding EDX spectra are shown in Figure 4.9 and Table 4.4 correspondingly. The coating appears to be homogeneous for the both sides of the plate, being around 5 and 50 µm on the contrary sides of the sample.

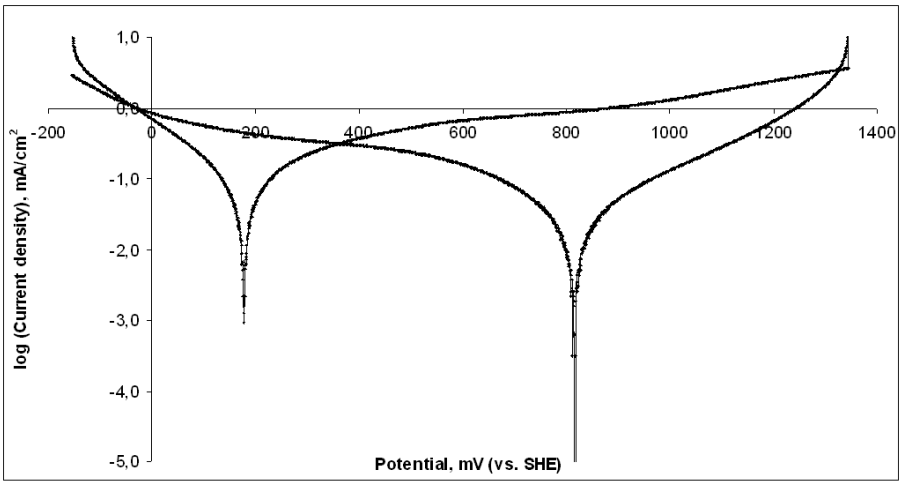

Figure 4.5: Tafel plot for AISI 321 in 85% H_3PO_4, 80 °C, 1 mV/s (vs. SHE).

The corrosion resistance at 120 °C increases in the following sequence in our series: Titanium < AISI 316L < AISI 347 < AISI 321 < Incoloy®825 < Hastelloy®C276 < Inconel® 625 < Tantalum

It can be clearly noticed, that for alloys the corrosion stability grows with the increasing content of nickel in this media, as shown in Table 4.5.

Generally, nickel based alloys show better corrosion stability than austenitic stainless steels in highly acidic media and elevated temperatures [237]. This tendency is also observed in our series.

Nickel's high degree of corrosion resistance is partly explained by higher positive standard potential among the studied alloy compounds. Comparing with less resistant iron, nickel has 250 mV more positive standard corrosion potential. Compared to pure nickel metal, nickel-chromium-iron-molybdenum alloys show considerably better resistance to corrosion in all inorganic acid solutions [151].

It can also be seen from Table 4.5, that titanium has a positive effect on the corrosion resistance of the alloys tested, even though its own resistance is much lower. This effect can be explained by the EDX data, obtained from AISI 321 and Inconel®625 before and after the electrochemical tests.

It is visible from Figures 4.10(a) (spectrum 3,4) and 4.10(b) (spectrum 2,4) and Tables 4.6(a) and 4.6(b) that before the corrosion test, Ti is not spread evenly on the surface of AISI 321, it is localized at definite points, unlike the other elements, distributed more homogeneously. It is safe to assume

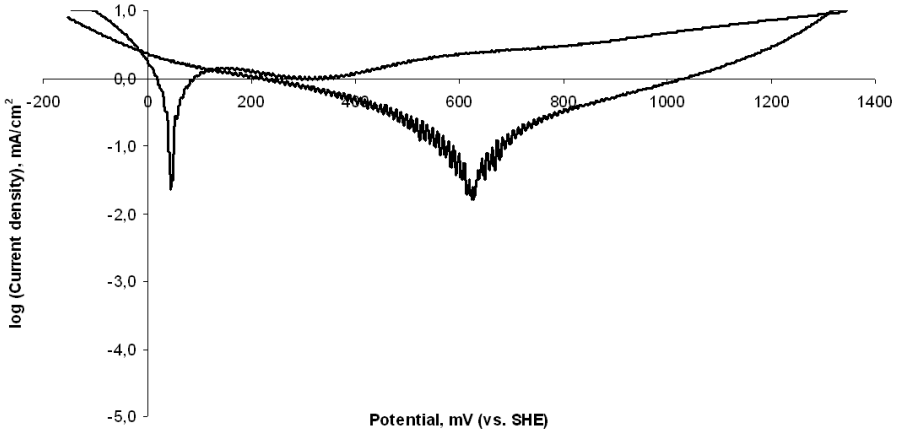

Figure 4.6: Tafel plot for AISI 321 in 85% H_3PO_4, 120 °C, 1 mV/s (vs. SHE).

that points of Ti location are situated on intergranular boundaries. It follows from the data that the content of titanium in the intergranular region dropped after the electrochemical experiment, indicating that corrosion in AISI 321 develops along the intergranular boundaries in this media. Titanium tends to be distributed along these boundaries during the severe anodic attack, thus preventing the formation of chromium carbides in these areas, which could promote chromium concentration drop resulting in a loss of passivity in these regions.

The same behaviour is observed for another alloy, containing titanium as an addition, protecting the material from intergranular corrosion. Figures 4.11(a) (spectrum 3,4), 4.11 (spectrum 1,3,5) and Tables 4.7(a), 4.7(b) show SEM and EDX data for Inconel®625. The same tendency is even more significant for this alloy. Titanium is distributed irregularly and its content decreases after the corrosion experiment.

The discussion above proves the extremely important role of doping the investigated alloys with titanium in this media, thus protecting them from the most apparent intergranular type of corrosion.

Molybdenum is more soluble in nickel than in austenitic stainless steels, and higher levels of alloying are possible with higher content of nickel. Therefore, the molybdenum content limit grows with nickel content and high contents of molybdenum are only possible in high nickel alloys [238].

Generally, the addition of molybdenum to stainless steels and alloys is used for enhanced corrosion resistance. For instance, addition of even one or two percents of molybdenum to ferritic stainless steels significantly increases the corrosion resistance of this material.

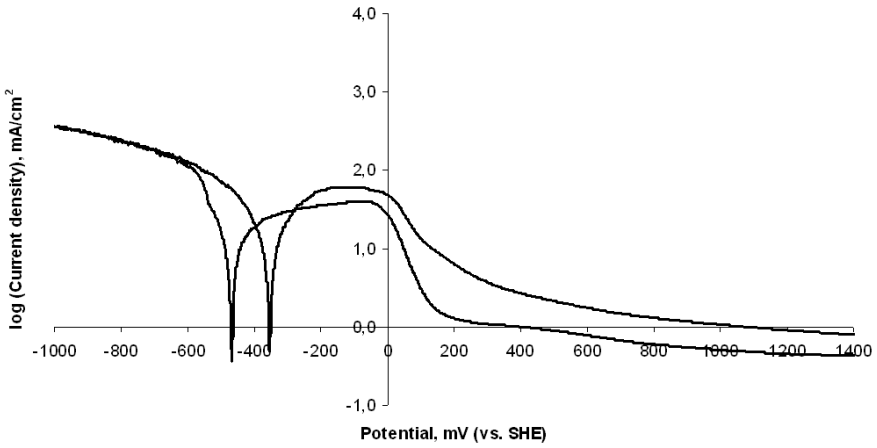

Figure 4.7: Tafel plot for titanium in 85% H_3PO_4, 120 °C, 1 mV/s (vs. SHE).

Pure nickel-molybdenum alloys, namely alloy B-2, contains approximately of 28% molybdenum and about 1,7% of iron. High molybdenum content in alloys gives excellent resistance to reducing acids, i.e. hydrochloric and sulphuric [239]. For sulphuric acid, this alloy shows good resistance, even at concentrations close to 90% and temperatures up to 120 °C. Non-oxidant conditions, however, must certainly exist in this case. Either the presence of oxygen or aeration will significantly accelerate the corrosion rate [237]. However, the role of molybdenum is not clearly noticed in our series.

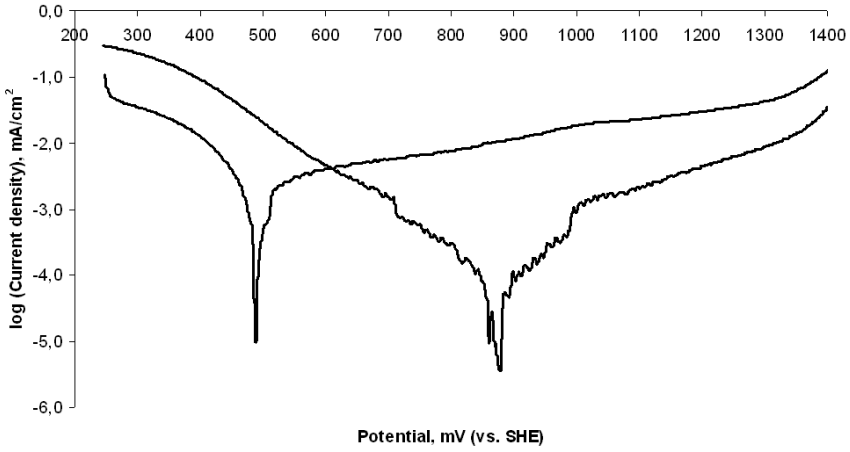

Figure 4.8: Tafel plot for tantalum in 85% H_3PO_4, 120 °C, 1 mV/s (vs. SHE).

Table 4.3: Measured corrosion potentials for forward and backward polarisation.

	E_{corr}, mV (vs. SHE)			
Material	80 °C		120 °C	
	forward	reverse	forward	reverse
Stainless steel AISI 316L	100	530	80	430
Stainless steel AISI 321	175	820	40	640
Stainless steel AISI 347	320	770	320	500
Inconel®625	125	635	90	490
Incoloy®825	105	540	60	595
Hastelloy®C-276	440	620	120	580
Tantalum			490	875
Titanium			−465	−357

Table 4.4: EDX data for the CVD-tantalum coated stainless steel sample, in wt.%.

	Composition, wt.%						
	O	Cr	Mn	Fe	Ni	Ta	Total
Spectrum							
1		19.2	1.0	70.7	9.1		100
2	4.8					95.2	100
3				1.3		98.7	100

Table 4.5: The content of Ni and Ti in the tested alloys.

Sample	AISI 347	AISI 316L	AISI 321	Inconel®625	Incoloy®825	Hastelloy®C-276
Ni content, wt.%	9-13	10-13	9-12	62	44	57
Ti content, wt.%	-	-	0.4-0.7	0.4	1.0	-

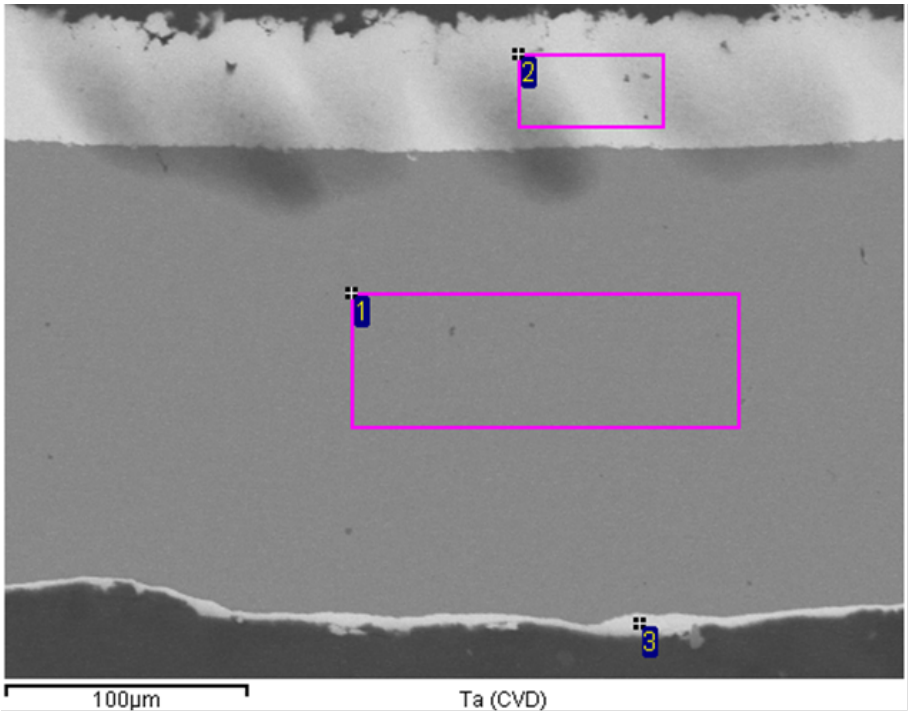

Figure 4.9: SEM image of the CVD-tantalum coated stainless steel sample. Numbers refer to EDX points and areas measured.

Table 4.6: EDX analysis data of AISI 321 before(a) and after(b) the electrochemical tests.

(a)

	Composition, wt.%, before the electrochemical tests							
	Si	Ti	Cr	Mn	Fe	Co	Ni	Total
Spectrum								
1	0.6	0.3	17.7	1.8	69.8	0.2	9.7	100
2	0.5	0.5	18.0	1.4	69.5	0.8	9.4	100
3	0.4	27.3	14.5	1.4	49.5	0.5	6.4	100
4	0.3	31.2	14.8	1.4	46.6		6.1	100

(b)

	Composition, wt.%, after the electrochemical tests							
	Si	Ti	Cr	Mn	Fe	Co	Ni	Total
Spectrum								
1	0.3	0.5	17.7	1.6	70.4	1.0	8.5	100
2	0.1	29.2	15.3	1.5	48.5	0.3	5.2	100
3	0.5	0.1	18.2	1.2	69.8	1.0	9.2	100
4	1.2	9.0	17.5	0.9	62.4	0.6	8.4	100

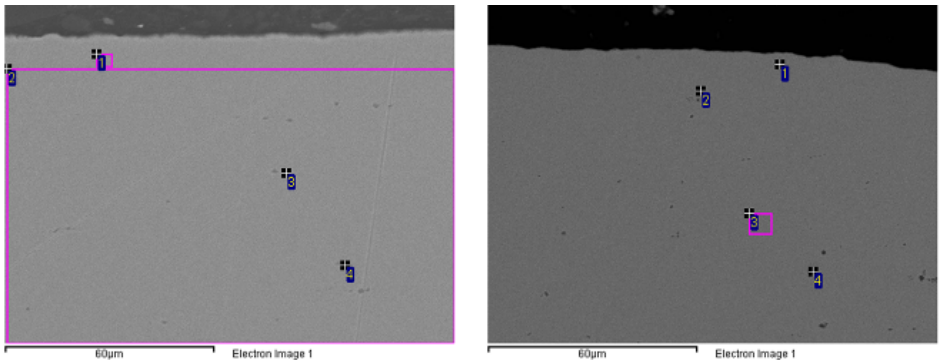

(a) (b)

Figure 4.10: SEM of AISI 321 before(a) and after(b) the electrochemical tests. Numbers refer to EDX points and areas measured.

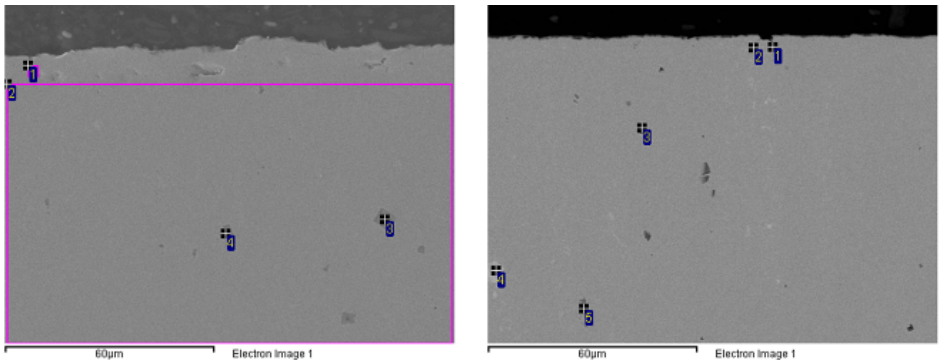

(a) (b)

Figure 4.11: SEM of Inconel®625 before(a) and after(b) the electrochemical tests. Numbers refer to EDX points and areas measured.

Table 4.7: EDX analysis data of Inconel®625 before(a) and after(b) the electrochemical tests.

(a)

	Composition, wt.%, before the electrochemical tests										
	Al	Si	Ti	Cr	Mn	Fe	Co	Ni	Nb	Mo	Total
Spectrum											
1	0.3	0.3		21.7		0.9		63.1	4.0	10.1	100
2	0.3	0.4	0.3	22.1		0.9	0.2	63.4	3.4	9.4	100
3		0.1	63.6	5.8		0.1		7.0	23.1	0.6	100
4	0.6	0.3	54.9	10.6	0.1	0.3	0.1	18.9	12.2	2.0	100

(b)

	Composition, wt.%, after the electrochemical tests										
	Al	Si	Ti	Cr	Mn	Fe	Co	Ni	Nb	Mo	Total
Spectrum											
1	0.5	0.8	20.5	13.7	0.3	0.4		34.9	21.4	7.9	100
2		2.2	0.1	15.8	0.5	0.5		40.1	14.0	27.0	100
3	0.2	0.1	48.6	12.3	0.0	0.8		24.4	10.0	3.9	100
4	0.3	2.1	0.1	13.7	0.7	0.1	0.1	29.4	26.1	27.5	100
5		0.1	43.4	11.1		0.4	0.3	21.2	19.8	4.0	100

4.3 Conclusions

It has been established that tantalum coated AISI 316L stainless steel and Inconel® 625 are the most suitable materials for bipolar plate in high temperature steam electrolyzers with H_3PO_4 doped membranes. It has also been found that small addition of titanium to the alloys increases the corrosion stability in this media. Among austenitic stainless steels, AISI 321 has the lowest corrosion rate.

Anodic passivation with decreased rate of dissolution was observed from the Tafel plots for all alloys and metals studied, indicating the formation of a protective oxide layer. The best corrosion resistance was found for tantalum. The titanium content was found to be an important parameter in the performance of the steels. The accumulation of titanium on the intergranular boundaries was assumed to inhibit the growth of chromium carbides in these regions, preventing intergranular corrosion of the samples. However, pure titanium showed the poorest resistance to corrosion, accompanied by the lowest corrosion potentials in the series and highest corrosion currents. Therefore, these facts exclude it as a possible material for use in bipolar plates in high temperature PEM steam electrolyzers.

Chapter 5

Preparation and Study of IrO_2/SiC–Si Supported Anode Catalyst for High Temperature PEM Steam Electrolyzers

Parts of this chapter has been published in the International Journal of Hydrogen Energy 2011;36(10):5797–5805, as a "Preparation and study of IrO_2/Si-Si supported anode catalyst for high temperature PEM steam electrolyzers." [38].

5.1 Experimental part

5.1.1 Materials and reactants

For preparation of the samples and the electrochemical experiments, the following substances were used:

- SiC-Si sintered composite plate (<22% free Si), supplied by the "State Powder Metallurgy Plant", Brovary, Ukraine
- $H_2IrCl_6 \cdot 4\,H_2O$, Alfa Aesar, 99 %
- $NaNO_3$, Sigma Aldrich, A.C.S. reagent
- Isopropanol, Fluka Analytical, pure

- Demineralised water
- H_3PO_4 85%, Sigma Aldrich, puriss. p.a. (analytical purity)
- Nafion® suspension, 5-6% in 50% propanol-water solution, by DuPont
- Ta rod electrode, Good Fellow Cambridge Ltd.
- Ag_2SO_4 99,9%, Chempur

5.1.2 SiC-Si/IrO_2 powder catalyst preparation

Catalyst support powder was prepared according to the following procedure: the as-received plate was cut with a diamond saw into squared samples with 1 cm side. The thickness of the plates was 2 mm. The prepared plates were cleaned in a ultrasonic bath, degreased with acetone, washed with demineralised water and finally dried at 80 °C. As it was described in Section 2.6.3, a support with a high specific area is needed in order to contribute to a good distribution of the active phase of the catalyst. Therefore, ball milling was employed for grinding the raw material. The ball milling ensures a moderate increase of specific area by particle size reduction. The silicon carbide-silicon plates were milled in a planetary ball mill (Fritsch, Pulverisette 7). Since SiC is a material with high hardness, a mill made of conventional steels could not be used for this procedure. This is due to the relative softness of steel, and associated risk of contamination of the sample by self abrasion of the steel balls and a possible tribochemical reaction. Therefore, two 45 ml steel vials, covered with tungsten carbide wear resistant lining were used. Milling was performed in a vial, which contained 6 WC balls, each 15 mm in diameter. The working vial contained 2 g of the starting material. The mill was operated at 730 r.p.m. from 5 to 35 minutes for different samples.

In order to deposit the active material directly on the support surface, iridium oxide was in-situ synthesised on the prepared SiC-Si support. As the support was added at the initial stage of the Adams fusion method, into the initial solution of catalyst precursor (see Section 3.5.1), it was expected that IrO_2 would adhere to the surface of the support. In order to determine the degree of chloride impurities in the final step of the synthesis, precipitation with Ag_2SO_4 was used as a qualitative test. The equilibrium chloride concentration is lower than the impurity degree required, thus ensuring that the oxide is pure enough. The iridium oxide content in the prepared catalyst was varied from 0 to 100 wt.% in steps of 10 wt.%. The calcinated products appeared to be fine powders, changing colour from black to more greyish with the increasing support content in composition.

5.1.3 The electrochemical characterization

5.1.3.1 Experimental conditions and the cell

Being the overall aim of the project searching for suitable materials for water electrolysis, it would in general case imply testing of these materials in-situ electrolysis cell. However, if the behaviour of the oxygen evolution electrode should be separated from the rest of the cell, a different approach is to be taken.

Therefore, the most suitable configuration for the study of single electrodes is a three-electrode setup (Figure 5.1). In this setup, the tested electrode is called working electrode, while the auxiliary electrode is called counter and provides the necessary connection for current to pass through the working electrode. This current is measured by a potentiostat. The third electrode used in this system is called the reference electrode, which provides a way of measuring potential on the working electrode. A typical thermostated model of a cell is presented in Figure 5.2. The working temperature in this cell is controlled by a circulating water, which limits its use up to 100 °C.

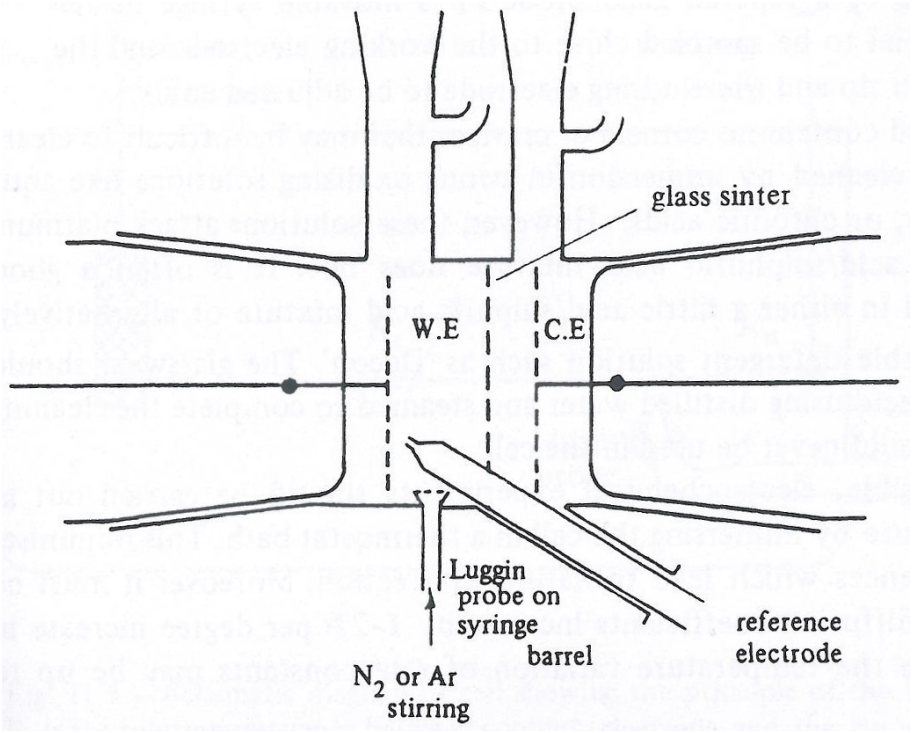

Figure 5.1: Three-electrode setup designed for controlled potential electrolysis study [9].

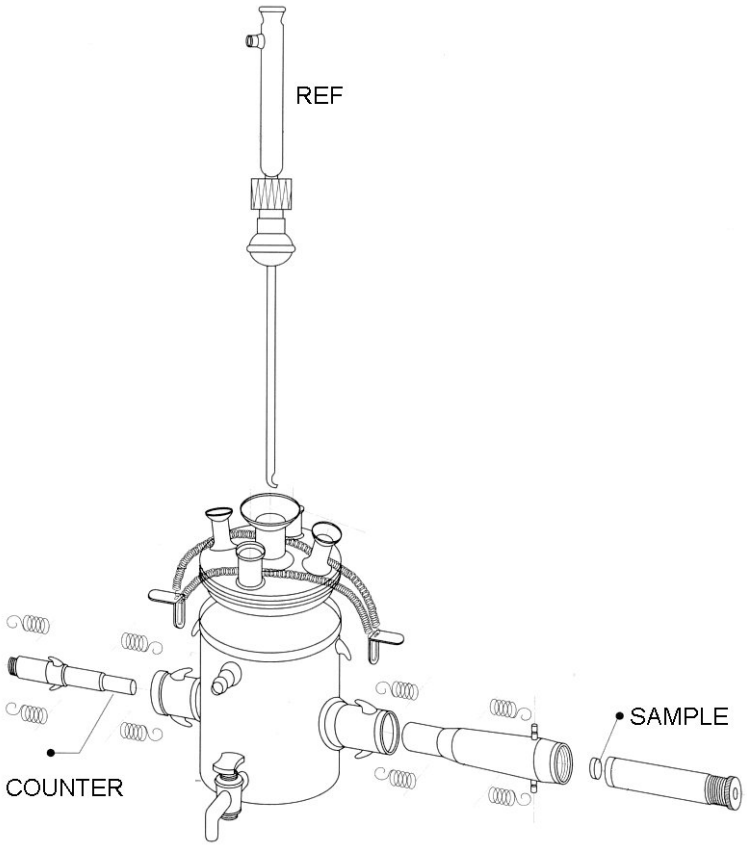

Figure 5.2: A typical three-electrode cell (provided by Radiometer analytical [21]).

This series of experiments required a cell able to work at least up to 150 °C. Therefore, a special three-electrode cell was designed for testing the performance of supported electrocatalysts. The heating of the cell was provided by an external heating plate (Figure 5.3).

This design affords good contact with a thermostatic heating plate below the cell, while avoiding excessive heating of the electric wired connections. Figure 5.4 shows a photograph of an assembled cell under operation.

In Chapter 3.7.3 it was noticed that in order to simulate the conditions of high temperature PEM cells it is needed to work in concentrated phosphoric acid media. In consequence, the electrochemical experiments were carried in 85% phosphoric acid and at temperatures up to 150 °C. Between samples, the cell was cooled down to room temperature, washed with demineralised water, then with acetone and the electrolyte was renewed for every next sample.

Cyclic voltammetry experiments were carried from room temperature (ca. 23 °C) to 80 °C, 120 °C and 150 °C, with the experiments performed from lower to higher temperatures. The temperature tolerance allowed during the experiments was ± 3 °C. Temperature was controlled by a k-type thermocouple, covered with Teflon® PTFE (by Omega Co.) and inserted into the working cell.

5.1.3.2 Cyclic voltammetry experiments

For each temperature, a series of CV experiments at different scan rates were carried out for all electrodes in the following sequence: 200, 100, 50, 20, 10 mV/s.

In all experiments a commercial platinum plate as a counter electrode and a KCl-saturated standard calomel reference electrode (SCE), connected to the system through a Luggin capillary were employed, provided by Radiometer Analytical SAS.

When studying the electrochemical behaviour of electrocatalysts, it is convenient to ensure that the electrode has a certain stability during the experiments performed. In addition, because of bubble formation during the OER, the catalyst layer can get easily detached from the working electrode, spoiling the experiment. However, the focus of this work was to investigate the support-catalyst interaction rather than to make a full characterization of the electrode. For a comparison of the different samples, it is not necessary to test them in an electrolysis cell, being sufficient to measure a specific catalyst activity at lower potentials [166, 195].

Therefore, the CV experiments were performed in the potential window starting at 0.0 V, going to the vertex potential of +1.2 V and reversing back to the initial value of 0.0 V (all potentials are vs. SCE). This allowed observation of the reversible redox behaviour of IrO_2 while avoiding formation of significant amounts of oxygen which could detach the catalyst layer from the working electrode. This permitted usage of the same sample for experiments at elevated temperatures.

Because of the need to minimise the transient double layer capacitance contributions (see Section 2.4.1), cyclic staircase voltammetry technique was chosen for electrochemical evaluation of electrocatalyst. An open circuit of 10 seconds was maintained between each experiment.

The experimental apparatus used for the electrochemical studies was a VersaSTAT 3 potentiostat and VersaStudio software by Princeton Applied Research.

5.1.3.3 Corrosion stability tests

For investigation of corrosion stability of the material, plates prepared as described in Section 5.1.2 were used. The testing of the material was performed in a specially designed cell, presented in Section 4.1.3 [36].

5.1.3.4 Preparation of Nafion®-bonded electrodes for CV investigation

In order to estimate the electrochemical performance of the prepared electrocatalyst powder, the following procedure was performed.

A tantalum cylinder, accurately embedded in a Teflon® PTFE body was used as a working electrode (Figure 5.5). The diameter of the cylinder was 7.5 mm which corresponded to the active surface area of 0.44 cm^2. Tantalum was chosen because of its superior corrosion resistance in hot phosphoric acid solutions, while having necessary conductivity and mechanical strength [36, 70].

However, the preliminary results showed that tantalum working electrode is passivated in the anodic conditions present during the cyclic voltammetry experiments. That led to difficulties of observing reasonable behaviour for each next catalyst powder sample deposited. Therefore, its surface was polished before every single experiment. Silicon carbide abrasive paper was used, followed by polishing with polycrystalline diamond powder (Struers A/S (Denmark)) with a particle size less than 0.25 μm. Finally, the surface was degreased with acetone and rinsed with demineralised water. The catalyst suspensions were prepared by adding of a 1 mg portion of prepared powder to 1 mL of demineralised water. The suspension was dispersed in an ultrasonic bath for 1 hour. Immediately after a 30 μL portion of the suspension was applied on the surface of the working electrode, following by drying of the catalyst layer under nitrogen protective atmosphere. A second suspension, consisting of 1% solution in water of 5 wt.% Nafion® was applied on top of the catalyst layer and dried in the same manner. This was done for improving the cohesion of the deposited catalyst layer. Therefore, each electrode contained 30 μg of sample powder. All 11 test electrodes were prepared in the same manner, using equal amount of applied sample, while ranging in its composition of active IrO_2 from 0 to 100 wt.% with a step of 10 wt.%.

The nominal composition of the prepared samples is shown in Table 5.1.

Table 5.1: Nominal composition of the samples

Sample	IrO_2 (mass %)	SiC-Si (mass %)
1	100	0
2	90,1	9,9
3	80,1	19,9
4	69,7	30,3
5	60,1	39,9
6	50.1	49,9
7	40,1	59,9
8	29,1	70,9
9	20,1	79,9
10	10,1	89,9
11	0	100

5.1.4 Physico-chemical characterization

The prepared at different milling time catalyst supports were first characterized by the SediGraph particle size analysis (the technique is described in Section 2.5.5) using the Sedigraph 5100 particle size analyser from Micrometrics ^{TM}. Prior to the analysis, the samples were dispersed in the suspending solution, which was a 0,002M Sodiumpyrofosphate solution in water.

The selected supported catalyst, containing 60% of IrO_2 and 40% of SiC-Si was studied using a combination of scanning electron microscopy (SEM) and energy dispersive X-ray spectroscopy (EDX) techniques. Samples for investigation were prepared in the following way (different sample preparation techniques are described in Section 2.5.4). The catalyst powder was dispersed in ethanol and the suspension was kept for 1 hour in an ultrasonic bath. Immediately after that, 20 μL portions of the prepared dispersion, containing 20 μg of the catalyst were applied both on a sticky carbon and polished gold backing plates, which were correspondingly used for SEM and EDX investigations. SEM measurements were made with an FEI Inspect S scanning electron microscope. The EDX system used was INCA from Oxford Instruments (accelerating voltage 5 kV, working distance 5.1 mm).

An additional series of experiments was performed to optimise the SEM and EDX sampling procedure. The results can be found in Appendix B.

The as-milled SiC-Si powder as well as other samples were characterized with XRD using a Huber D670 diffractometer (Cu-Kα X-ray source, α = 1.5405981 Å).

The BET method was used to evaluate the specific surface area of the catalysts. Automated Gemini 2375 surface area analyzer by Micromeritics, working at 77K was employed in our work.

5.1.4.1 Electrical conductivity of powders

As conductivity of powders depends strongly on their packing density [240], it is necessary to control the conditions at which measurements are done. The powder conductivity measurements were performed on a setup, especially designed for this purpose. A commercial micrometer was employed to measure the sample thickness with high precision, while controlling the pressure exerted with a torque wrench. The schematic and the photographic pictures of the working part of the cell are shown in Figures 5.6 and 5.7 correspondingly.

This setup conceptually consists of two copper pistons acting as contact electrodes. The micrometer presses together to pistons by means of a torque wrench key, connected directly to the micrometer axis, and applying in each case a fixed torque of 20 $cN \cdot m$, providing equal pressure for each sample. This permitted an accurate measurement of the powder thickness and conductivity simultaneously. The inner diameter of the cylinder is 3 mm, allowing use of small amounts of sample powder. This is also convenient from the economic point of view, given the high price of noble metal electrocatalysts.

The conductivities of all sample powders were measured using a technique, described previously by Marshall [181]. Measurements were conducted in air at room temperature.

The conductivity measurements were carried with a potentiostat model VersaSTAT 3 and VersaStudio software by Princeton Applied Research. In this experiment, a potentiostat needs to be connected to the cell in a 2-electrode arrangement. Since the potential to measure is the cell voltage, rather than the working electrode potential, the reference electrode was closed-looped with the counter electrode during the measurements. A linear staircase voltammetry experiment was run for each amount of powder in order to define a linear part of the polarisation curve for its further use for the calculation of resistance. A maximum potential of 10 mV was applied to the samples.

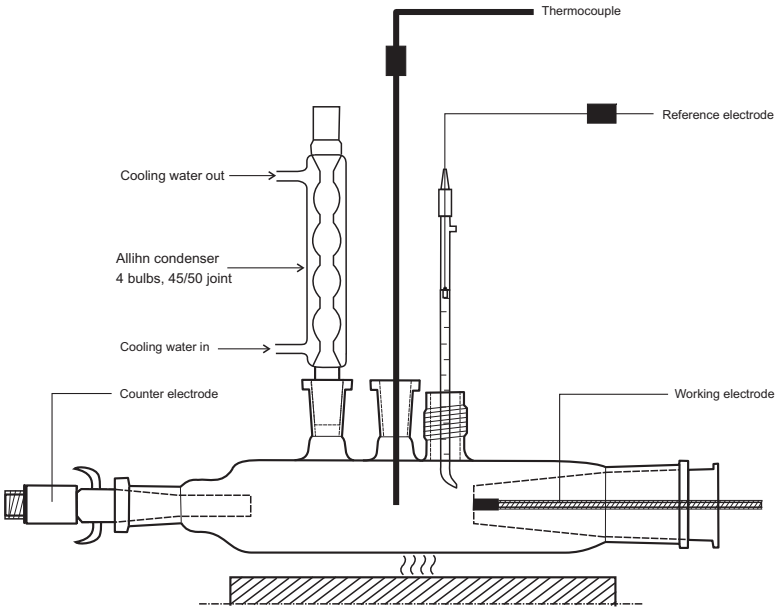

Figure 5.3: The electrochemical cell used in CV experiments

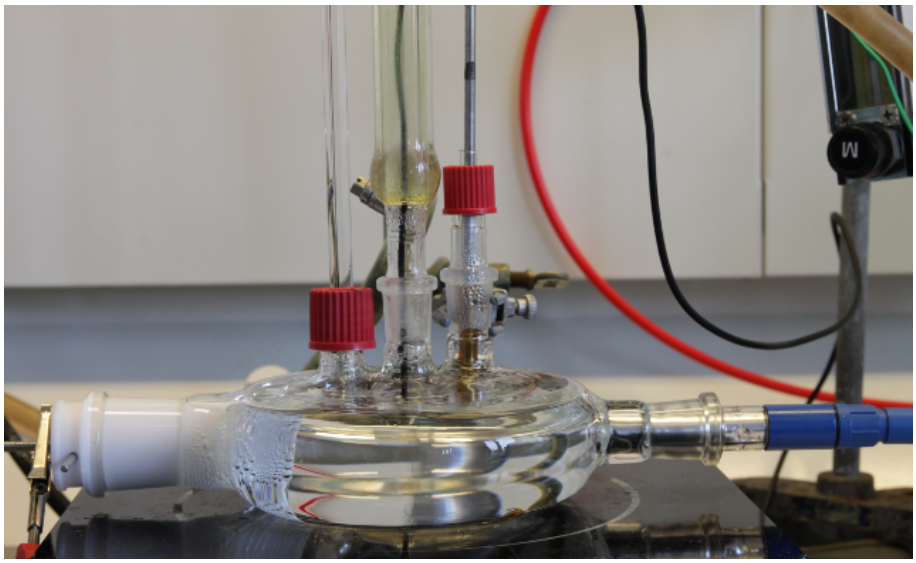

Figure 5.4: A photograph of the electrochemical cell used in CV experiments.

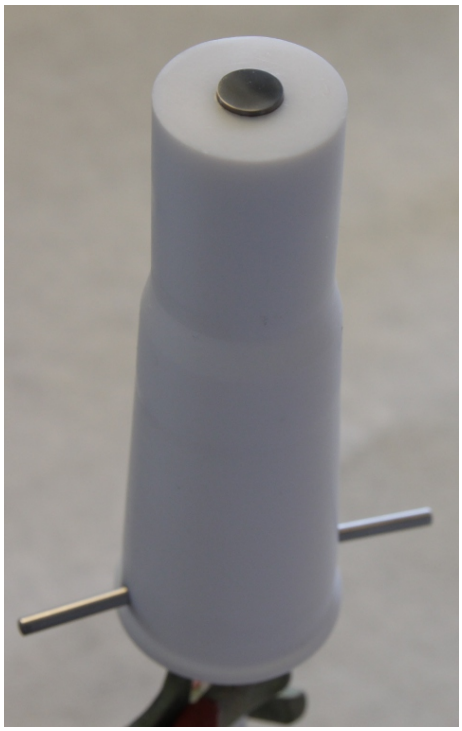

Figure 5.5: The working electrode, designed for the CV experiments.

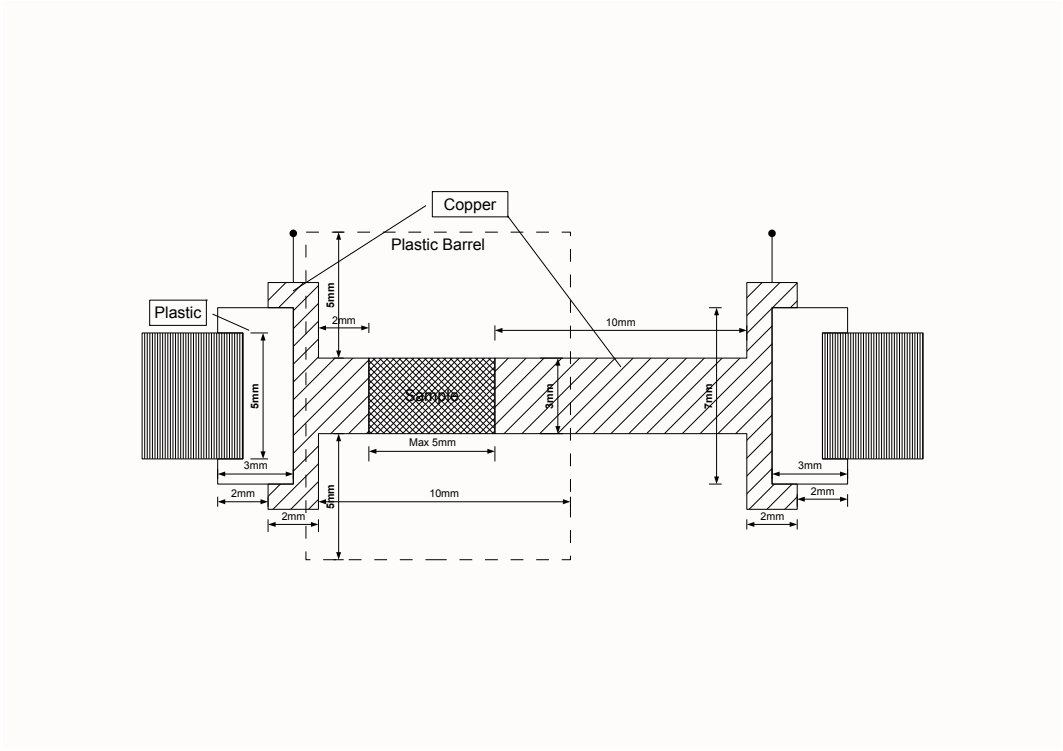

Figure 5.6: The electrical conductivity setup. The outermost rods are the anvil and spindle of a micrometer.

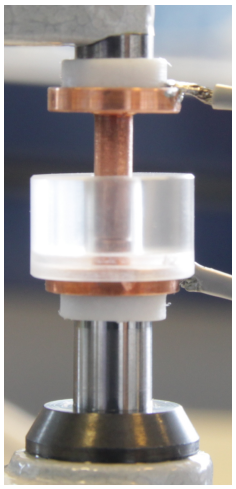

Figure 5.7: A photograph of the setup used for electrical conductivity measurements.

5.2 Results and discussion

5.2.1 Structural and electrical properties

5.2.1.1 Particle size distribution

The Sedigraph X-ray particle size distribution analysis was performed on ball milled for different time support material.

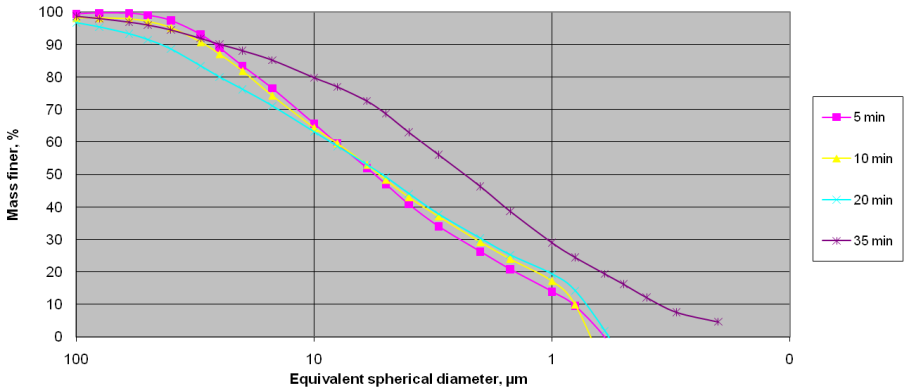

Figure 5.8: Cumulative mass percent finer vs. diameter of SiC-Si composite, ball milled during different time.

As it is presented in Figure 5.8, changing of the milling time from 5 to 35 minutes does not significantly affect the particle size distribution, as its values stay in the same order of magnitude. Therefore, the powder milled for 10 minutes was used in all samples for convenience and in order to avoid excessive contamination of the samples with WC impurities from the mill, as they accumulate in the working vial while the ball milling process, which will be shown in Section 5.2.1.2.

5.2.1.2 X-Ray Diffraction

The X-Ray diffractogram for pure IrO_2 prepared without presence of the support is shown in Figure 5.9. The diffraction peaks on this diagram are relatively broad and their position corresponds to IrO_2 sample data published in the literature [181].

In contrast to IrO_2, the peaks of the SiC-Si sample are much sharper, indicating bigger crystal size (Figure 5.11). Assignation of the peaks shows presence of both SiC and Si phases in the sample, which means that the support is a physical mixture of SiC and Si crystals, rather than a solid solution (Figure 5.10).

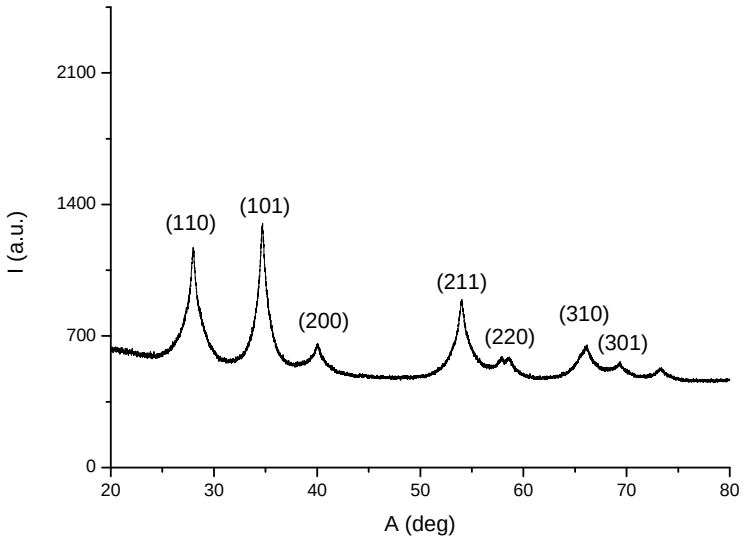

Figure 5.9: XRD spectrum for IrO_2.

The supported catalysts showed the characteristic signals of IrO_2, SiC and Si, e.g. the simultaneous presence of catalyst and support phases (Figure 5.11). Therefore, the produced catalyst consisted of a physical mixture of IrO_2 and support material without any other substances produced during the synthesis process due to reactants interaction, e.g. firing at 500 °C. This fact shows the chemical inertness of the support in conditions of the Adams fusion synthesis.

However, some weak peaks of WC were detected in the diffractogram of the support powder (Figure 5.12). This contamination apparently originates from the ball milling procedure. The Rietveld quantitative analysis of the support powder was performed with following calculation of the sample composition. Results are presented in Table 5.2:

Table 5.2: Quantitative analysis of the support by Rietveld treatment of the XRD data.

Phase	wt.%	vol.%
SiC	87.21	86.91
Si	8.95	12.3
WC	3.84	0.79

Additional data related to the performed Rietveld treatment can be found in Appendix A.

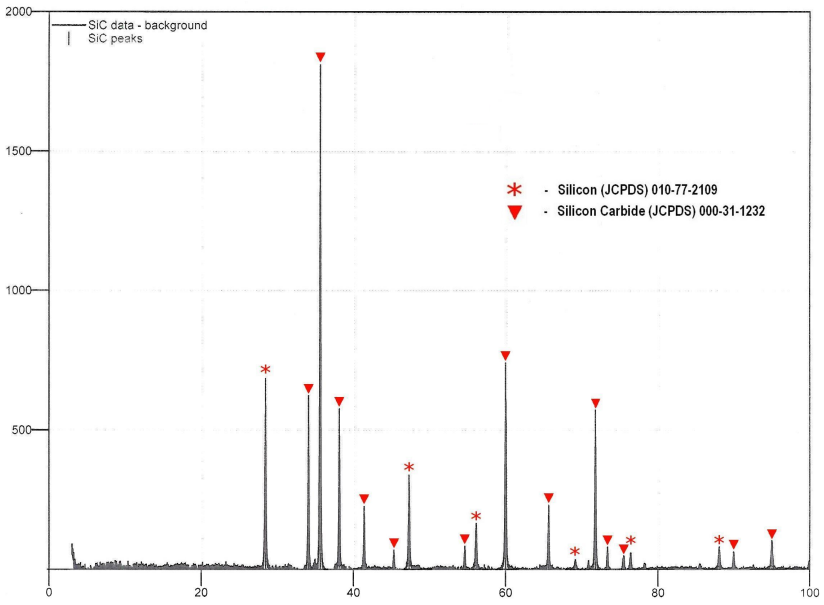

Figure 5.10: Diffractogram of a ball milled SiC-Si support, showing peak assignations for corresponding phases.

However, the amount of WC impurity was considered negligible (less than 1 vol. % percent for the clean support powder), and it will be shown in Section 5.2.2.2 that it does not influence on the CV results.

Since the XRD is a bulk technique with high penetration depth, the relative peak intensities should vary between samples following the bulk powder composition.

In order to assess this, the intensities of selected peaks were calculated for each sample. The peak at around 55 ° for IrO_2, the peak at around 30 ° for SiC, and the peak at around 35 ° for Si were chosen (see Figures 5.10 and 5.11). The given peak intensities were calculated by fitting them to Lorentz distributions.

The peak intensities were compared to the volume fractions according to the following calculations:

$$\chi_{\mathrm{IrO_2}} = \frac{I_{\mathrm{IrO_2}}}{I_{\mathrm{IrO_2}} + I_{SiC}} \tag{5.1}$$

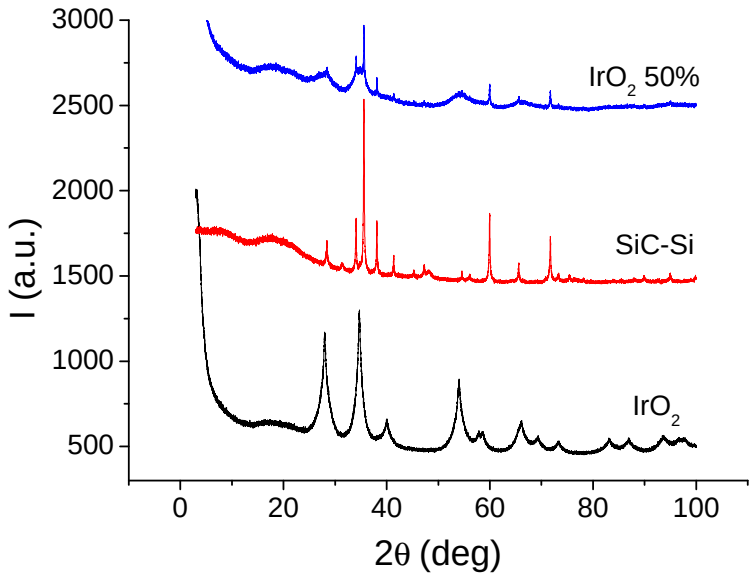

Figure 5.11: XRD spectra for IrO_2, SiC-Si support, and a 50% composite.

$$X^{vol}_{IrO_2} = \frac{\frac{X^{w}_{IrO_2}}{d_{IrO_2}}}{\frac{X^{w}_{IrO_2}}{d_{IrO_2}} + \frac{X^{w}_{SiC}}{d_{SiC}}} \tag{5.2}$$

where χ_{IrO_2} is the relative intensity of the IrO_2 peak and $X^{vol}_{IrO_2}$ is the volume fraction of IrO_2 in the mixture.

The results of these calculations are shown in Table 5.3 and Figure 5.13.

The general trend follows the sample composition with significant linearity (Figure 5.13). For the 90% IrO_2 sample, it was not possible to calculate this relation, since there were no significant SiC-Si peaks visible in the diffractogram, most likely because of the poor signal-to-noise ratio.

The peak of IrO_2 at around 55 ° for different samples was chosen in order to calculate the average crystal size, on the basis of the Scherrer equation 2.65.

The calculated crystal sizes of IrO_2 for the unsupported and the supported catalysts differ significantly (Figure 5.14). The supported catalysts showed smaller crystal size than for unsupported IrO_2. It can also be seen from the form of the XRD peaks. The support peaks (SiC, Si) in all samples are equally sharp and have similar width (Figure 5.11). In contrast, the peaks of the unsupported IrO_2 are significantly sharper than those of the supported

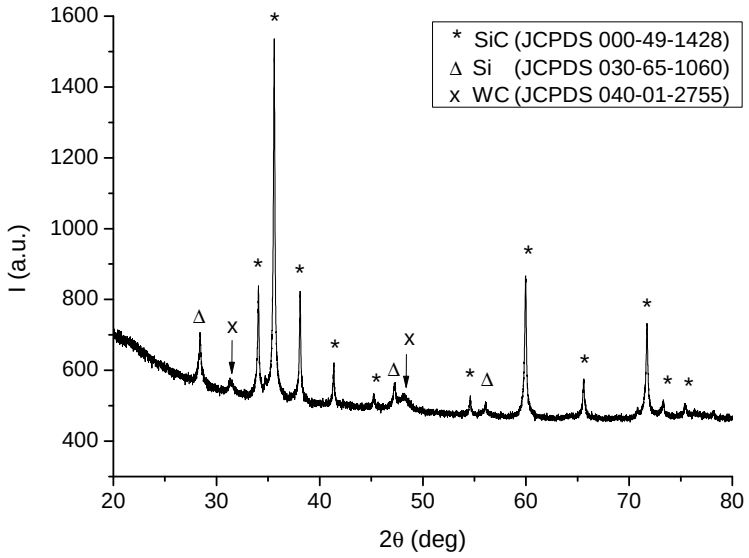

Figure 5.12: XRD spectra for the prepared support powder.

catalysts. Since the synthesis method and conditions were the same for all samples, and since the peak width is similar in all the supported catalyst samples, these results indicate that the presence of the support affects the IrO_2 synthesis step, influencing the crystal growth of the catalyst particles.

5.2.1.3 BET Surface Area

Physical adsorption of nitrogen was performed for all samples. The BET model was applied in order to calculate the corresponding surface area of the prepared powders. The BET area was calculated by using experimental points between 0.05 and 0.25 bar of nitrogen partial pressure. A resume of the calculated specific surface area is given in Table 5.5. The specific surface area of IrO_2 is considerably higher than that of the support. The IrO_2 powder has surface area of 121 m^2/g. In contrast, the support has only around 6 m^2/g. The BET area of the supported catalysts follows approximately the rule of mixtures and evolving of the specific area is approximately proportional to the mass fraction of IrO_2 (Figure 5.15). This is in accordance with the expected values, since the supported catalyst is, as it was shown in Section 5.2.1.2, a physical mixture of the support and the catalyst, with no reaction between the components. However, the BET area of pure IrO_2 is significantly lower than that of 80% and 90% IrO_2 samples. Therefore, the

Table 5.3: Relative intensity of XRD peaks for different powders with different composition.

Sample	IrO_2 (vol.%)	$\chi(IrO_2)$ (wt.%)	χ(SiC) (wt.%)
1	100	100	0
3	52.4	56.7	44.3
4	39.1	38.6	61.4
5	29.2	27.5	72.5
6	21.6	19.6	80.4
7	15.5	9.54	90.5
8	10.6	6.35	93.6
11	0	100	0

Table 5.4: Peak width and crystal size of selected peaks for the catalyst and the support.

Sample	IrO_2 wt.%	$\gamma(IrO_2)$ at 54.025°	$\tau(IrO_2)$ (Å)	γ(SiC) at 35.598°	τ(SiC) (Å)
1	100	1.64	0.951	-	-
2	90	3.19	0.487	-	-
3	80	3.76	0.413	0.202	7.22
4	70	4.21	0.370	0.173	8.39
5	60	3.82	0.407	0.147	9.89
6	50	5.00	0.311	0.168	8.65
7	40	4.58	0.339	0.148	9.81
8	30	5.08	0.306	0.152	9.56
9	20	-	-	0.150	9.71
11	0	-	-	0.188	7.76

pure IrO_2 catalyst seems to have different characteristics in comparison with the supported catalysts. This difference can be due to different conditions for the catalyst synthesis without and with presence of the support, where smaller IrO_2 particles are formed in the latter case (Section 5.2.1.2).

5.2.1.4 SEM and EDX analysis

The SEM image was obtained with an incident electron energy of 5 kV on the selected sample (Figure 5.16). In the SEM micrograph two groups of particles can be observed. The larger particles, between 5 and 10 µm in size are most likely the support particles. On these there are much smaller

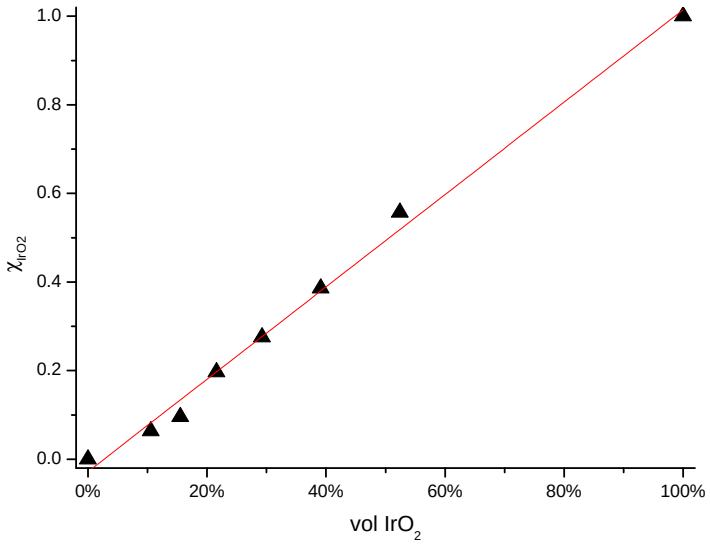

Figure 5.13: Correlation of XRD relative phase signals with nominal powder composition.

Table 5.5: BET area for all samples.

Sample	IrO_2 (wt.%)	BET area (m^2/g)
1	100	121
2	90	148
3	80	144
4	70	114
5	60	86.3
6	50	67.8
7	40	60.0
8	30	53.1
9	20	14.0
10	10	11.0
11	0	6.3

agglomerates of IrO_2. The active component seems to be distributed evenly over the surface of the support. This case suggests that the IrO_2 particles are formed on the support surface, which could provide nucleation sites for the formation of IrO_2. This could explain the results observed in the XRD and

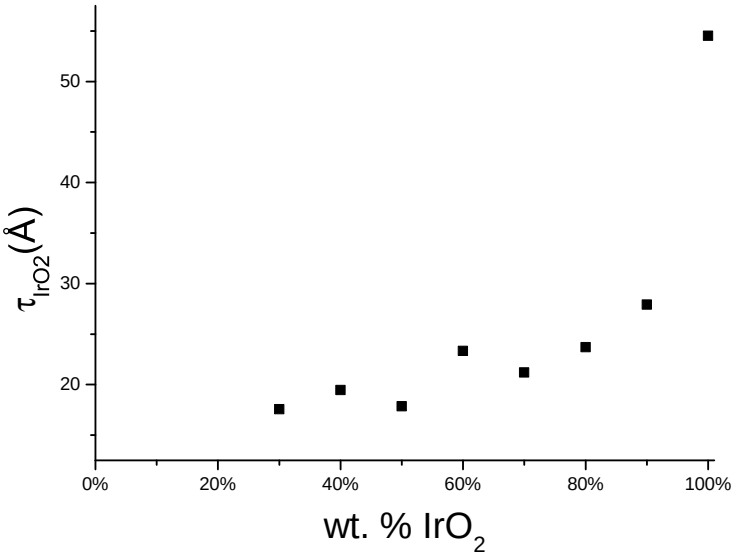

Figure 5.14: Calculated average crystal sizes for different samples.

BET experiments, where the IrO_2 particles in the supported samples tend to be smaller than in the pure IrO_2 sample (Figures 5.14, 5.15). In Figure 5.17 and Table 5.6 the results of the EDX quantitative analysis, performed at low voltage (5 kV) are presented. The content of IrO_2 in the chosen sample is close to the expected value.

Table 5.6: EDX data for SiC-Si/IrO_2 sample (SiC-Si:IrO_2 = 40:60).

	Composition, wt.%							
Spectrum	C	O	Na	Si	Fe	Mo	Ir	Total
1	7.0	20.4	3.1	13.3	2.6	0.9	52.8	100.0
2	6.5	19.6	2.3	15.5		2.0	57.0	100.0

5.2.1.5 Powder conductivity

The resistance of powders in this series was calculated by fitting the voltammogram to a straight line for each thickness of the same sample. The resistance was determined as the inverse of the polarisation slope (equations 5.3-5.5):

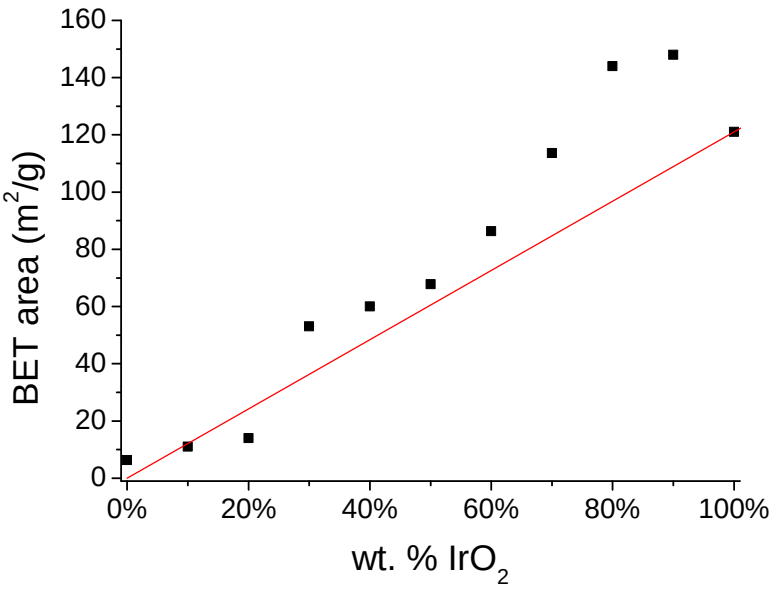

Figure 5.15: BET area trend with sample composition.

$$V = I \cdot R \tag{5.3}$$

$$dV = d(IR) = R \cdot dI \tag{5.4}$$

$$R = \frac{dV}{dI} \tag{5.5}$$

Consequently, for different thicknesses of the same sample, data presents a linear slope of the layer resistance vs. its thickness (Figure 5.18). The evolution of the resistance with the powder thickness is quite linear for all the samples.

A linear fitting of the resistances of different thicknesses can be performed to calculate the resistivity of powders using the Ohm's Law (equation 5.6):

$$R = \rho \cdot \frac{l}{a} \tag{5.6}$$

$$\rho = R \cdot \frac{a}{l} \tag{5.7}$$

Where ρ is the resistivity of the sample, measured in $\Omega \cdot cm$, l is the sample thickness, and a is the sample section area. Equations 5.6-5.7 are valid for any prismatic shape, such as a cylinder.

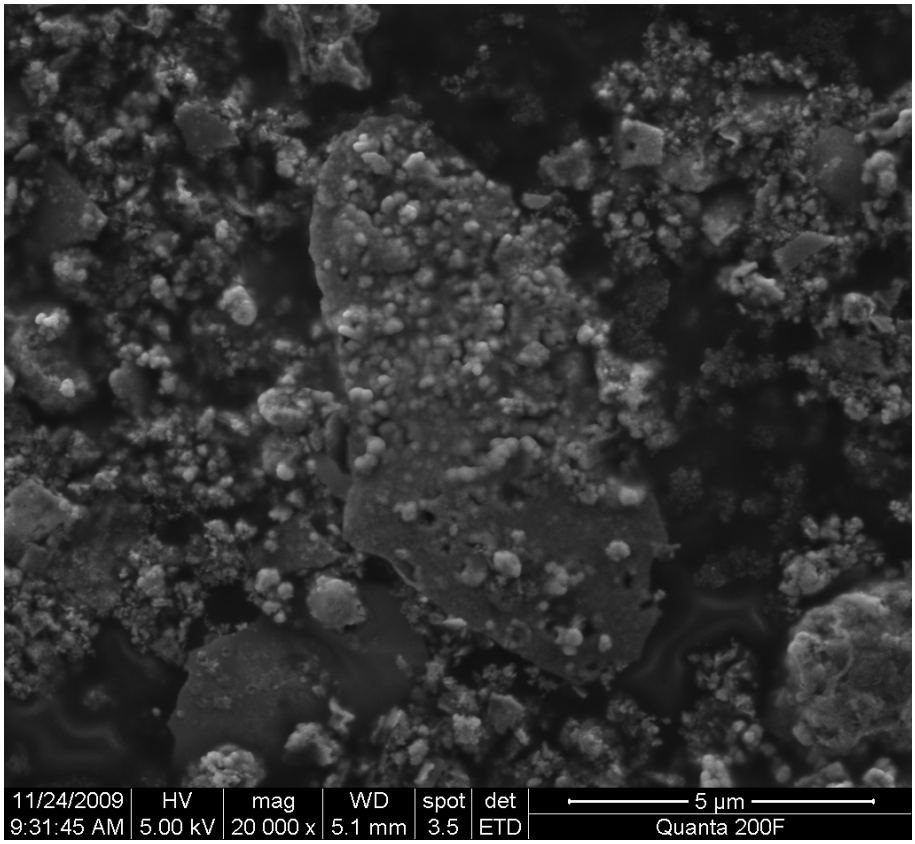

Figure 5.16: SEM micrograph of a sample with composition 60% IrO_2 and 40% SiC-Si support

The conductivity can be calculated from the resistivity value, being its reciprocal.

$$\sigma = \frac{1}{\rho} \tag{5.8}$$

It can be seen that this method provides good linear dependencies, with small experimental error. Thus, for every sample powder, resistivity and conductivity were determined. Figures 5.19 and 5.20 show the trends.

The dependency of conductivity on the sample composition is not linear, levelling off and increasing again with the mass fraction of IrO_2 (Figure 5.20). The effect of the support on conductivity of the catalyst powders is obviously negative. The catalyst is much more conductive than the support, being the difference of several orders of magnitude. The conductivities of pure IrO_2 catalyst and the support are 67 S/cm and $1.8 \cdot 10^{-5}$ S/cm correspondingly.

It has been proposed that a main aspect of electrical conductivity through

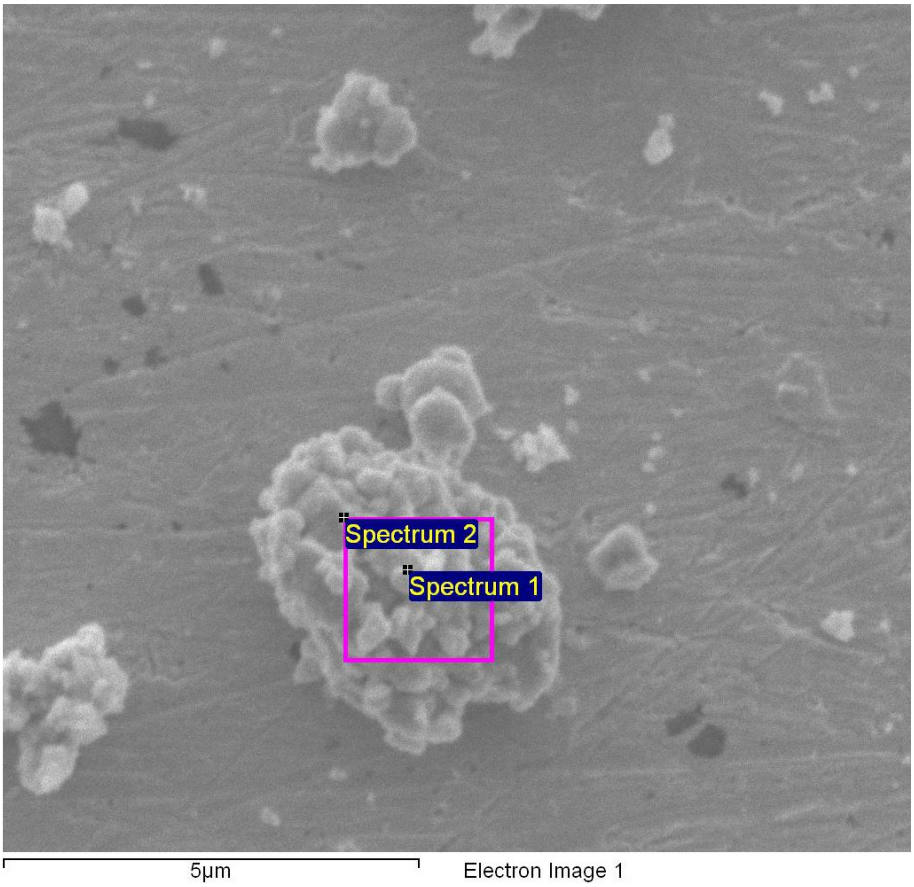

Figure 5.17: SEM micrograph for EDX analysis at 5 kV on a gold plate. Sample composition: 60 wt.% IrO_2 and 40 wt.% SiC-Si support

mixed powders is the contact resistance between the most conductive type of particles [116]. The presence of a step in conductivity around 60% of IrO_2 seems to support this hypotesis. It can be thus assumed that almost all current passes through the IrO_2 particles:

$$
\begin{aligned}
I_{total} &= I_{SiC} + I_{IrO_2} \\
V_{SiC} = V_{IrO_2} \Rightarrow I_{SiC} \cdot R_{SiC} &= I_{IrO_2} \cdot R_{IrO_2} \\
I_{total} &= V \cdot \left(\frac{1}{R_{SiC}} + \frac{1}{R_{IrO_2}} \right) \\
R_{SiC} \gg R_{IrO_2} \Rightarrow I_{total} &\simeq V \cdot \frac{1}{R_{IrO_2}} \\
I_{total} &\simeq I_{IrO_2}
\end{aligned}
$$

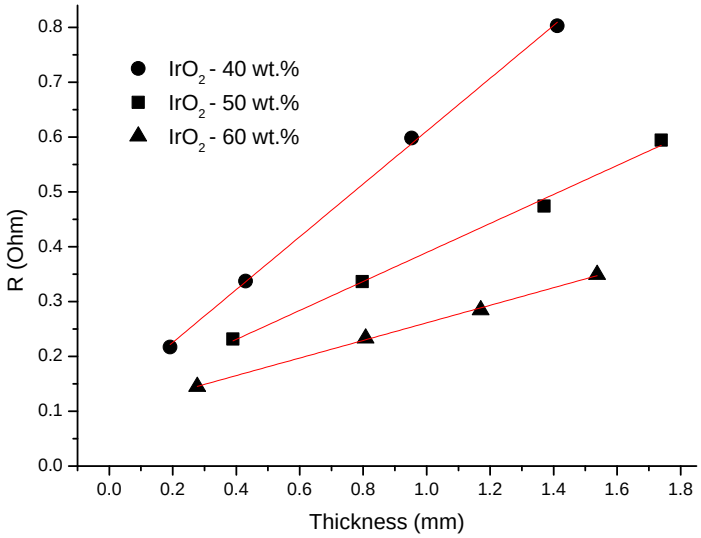

Figure 5.18: Evolution of resistance with powder thickness for some samples.

Therefore, the distribution of IrO_2 particles in the supported catalyst is very important for its resistance. Effectively, the way the oxide particles are packed together between the support particles determines the number of contacts between them, thus having an important effect on the total resistance of the material.

Although the dependency the of conductivity on the IrO_2 content is not linear, three regions can be identified in this series (Figure 5.20).

For high IrO_2 content in supported catalysts (above 60% of mass fraction), the conductivity does not change significantly with the composition. This can be explained by the existing "conductivity path" through IrO_2 particles.

For intermediate oxide content, there is a pronounced drop in conductivity, as the IrO_2 content decreases. It seems that there is an increasingly significant loss of paths for the current flow, with a decreasing number of oxide particles being able to transport current through them. In this interval, between 10% and 60% of mass fraction, the conductivity decreases in several orders of magnitude, effectively turning the conductivity to the original value of the support.

Below 10 wt.% IrO_2, it is evident that the contact between particles is so bad that the current has to flow through the support particles, which have high resistivity (around 500 $\Omega \cdot$m).

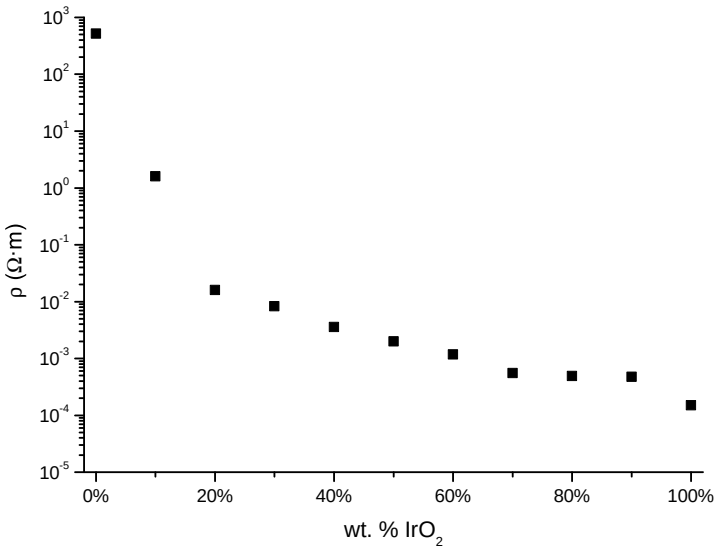

Figure 5.19: Resistivities of all samples, calculated from conductivity values (the latter are presented in Figure 5.20).

There is an important step in conductivity from pure IrO_2 to 90 wt.% IrO_2 powders. In principle, one could argue that the support particles create "holes" in the IrO_2 aggregate, decreasing the effective lateral section in the sample and thus increasing the resistance. However, the change in conductivity between 90 and 80 wt.% samples is much smaller. This suggests that there must be another factor in the observed conductivity step. For instance, the inclusion of the much bigger support particles, which have different size and shape, could alter the packing of the IrO_2 particles in the powder. Another factor can be different IrO_2 particle growth and consequently different size and/or shape of them in the presence of the support. The latter option is discussed in Sections 5.2.1.2,5.2.1.3, where the results indicate the smaller particles formed in the presence of the support at the synthesis step. The smaller particles of IrO_2 involve more contact resistance between the grains, therefore the overall resistance of powder is expected to increase with the particle size decreasing, being a consequence of the prevailing contact resistance to the overall conductivity, as it was proposed earlier [165, 240].

Taking above speculations into account, the upper limit for the loading of the SiC-Si support for IrO_2 electrodes can be recommended to be not more than 40 wt.%. Depending on the conductivity requirements, higher or lower limits could be considered.

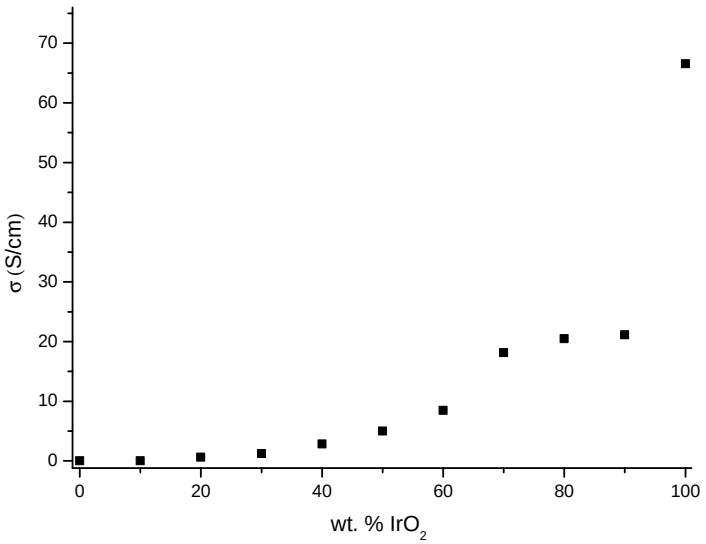

Figure 5.20: Powder conductivities of all samples.

A conventional lab-scale PEM electrolysis cell typically operates at 1 A/cm^2 with voltage of 1.8 V [112, 133], which gives an approximate value of the overpotential of the working electrolyzer 500-700 mV. Considering 10% of this value being an acceptable maximum for the anodic ohmic drop and taking the typical thickness of the anodic electrocatalytic layer of 10 µm [87], the resistivity of this layer can be up to 500-700 m$\Omega \cdot$ m and 50-70 m$\Omega \cdot$ m at the layer thickness of 100 µm.

The experimental resistivity values in our series range from above 500 $\Omega \cdot$ m to $1.5 \cdot 10^{-4} \Omega \cdot$ m. According to considerations exposed above, all compositions including and above 20 wt.% IrO_2 loading (the resistivity of this particular sample is 16 m$\Omega \cdot$ m) would have enough conductivity to be used as electrodes without big contribution to the total potential losses.

The similar discussion was provided in Section 3.8, where the resistance of a catalytic layer was proposed to be meaning for values at least of 1 $\Omega \cdot$ m, which likewise corresponds to all samples in our series with wt.% of IrO_2 equal or above 20 %.

Nevertheless, in a real MEA, the packing density and/or layer thickness can be different, so these conclusions are to be considered tentative, depending on the mentioned parameters.

5.2.2 Electrochemical characterization

5.2.2.1 The corrosion stability of the support at high temperatures

Corrosion stability of the support material was tested using the electrochemical cyclic Tafel voltammetry technique [36]. Figure 5.21 presents the Tafel plot for a SiC-Si plate. The potential shifts to more positive values after the anodic sweep, which shows the passivation of the material in the studied media. The corresponding corrosion current measured from the curve was 0,005 mA, dropping to 0,002 mA during the backward scan, which is at least one order of magnitude less than for all alloys, tested before in similar conditions (Chapter 4).

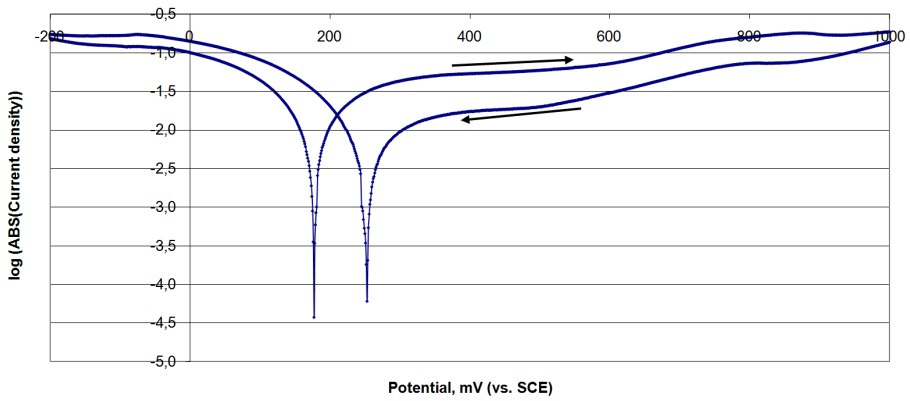

Figure 5.21: The Tafel plot for a SiC-Si plate. Scan rate 1 mV/s, electrolyte: 85% H_3PO_4, 120 °C.

5.2.2.2 Cyclic voltammetry experiments

Room temperature Even though the SiC-Si support is considered to be inert in chosen conditions, an additional experiment was performed for the support material on the tantalum working electrode in order to identify any considerable background current, which could also originate from WC impurities, detected earlier by the X-Ray diffraction (see Section 5.2.1.2).

Figure 5.22 shows that the signal of the support without active IrO_2 is few magnitudes lower than that of the supported catalysts, and therefore can be considered negligibly small. This means that in the supported catalysts almost all the signal comes from IrO_2. The figure also shows that WC impurities found before do not influence on the electrochemical results, being relatively inert.

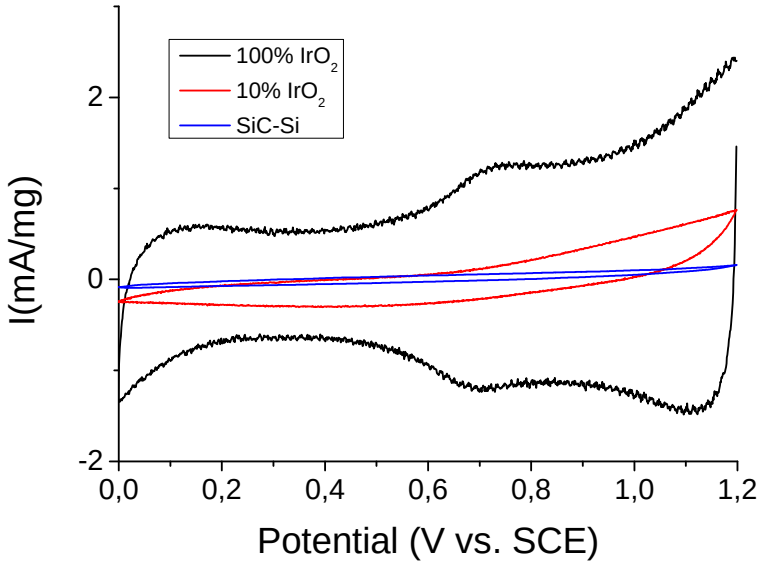

Figure 5.22: Comparison of the voltammograms of the support and some samples. Scan rate 20 mV/s.

The voltammogram of the SiC-Si support shows no peaks, having a pure capacitive behaviour (Figure 5.23). This indicates that the support is electrochemically inert, with no contribution to the faradaic processes, observed in the supported catalyst electrodes.

The potential scan rate of 20 mV/s is commonly used in literature for characterization of OER catalysts [51, 130]. The results for all samples at room temperature are shown at the scan speed of 20 mV/s in Figure 5.24.

The general shape of the curves is similar, with a common pseudo-capacitive behaviour as the hysteresis in the voltammogram indicates. The similar results has been previously published [55]. Figure 5.25 shows the evolution of the current for different potential scan rates. The current is roughly proportional to the speed, as would be expected from a capacitive behaviour. The total capacitance for unsupported IrO_2 was calculated by dividing the current at a fixed potential of 0.4 V vs. SCE over the speed (see equation 2.52) for different speeds. The resulting Figure 5.26 shows a relatively constant capacitance for the chosen speed interval. This means, that at the chosen potential the behaviour of the electrode is purely capacitive.

Figure 5.27 shows cyclic voltammograms, recorded with the prepared supported and unsupported iridium oxide on tantalum electrodes. There is an evident increase in associated voltammetric capacitance value corresponding

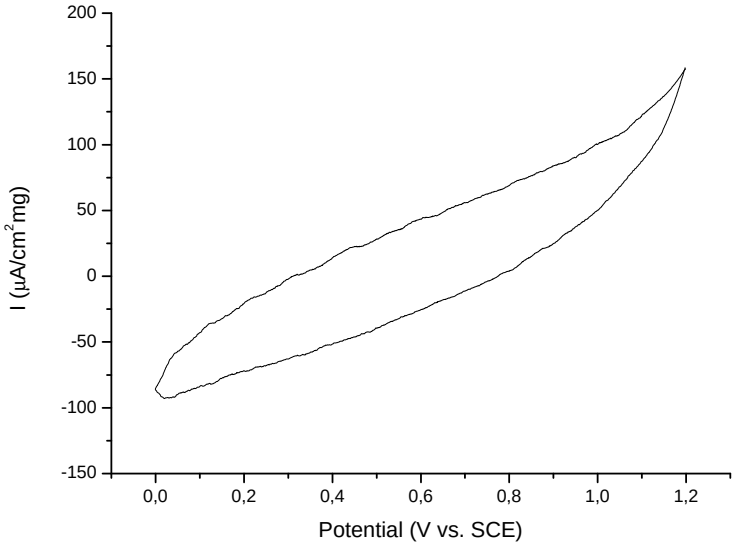

Figure 5.23: CV experiment of the SiC-Si support in H_3PO_4. Room temperature, 20 mV/s.

to the supported catalyst compared to the pure oxide catalyst material.

Integration of the charge over the whole potential range shows that the capacitance values obtained do change with the scan speed, although the difference is relatively small compared to the total value (Figure 5.28).

The presence of the broad redox peaks at around 0.7 V vs. SCE is likely to introduce the change of capacitance with speed. As was discussed in Section 2.6.4, these peaks are attributed to the reversible oxidation and reduction of IrO_2 on the electrode surface [93]. This feature allows integration of the charge under the anodic peak, separating the Faradaic process contribution from the double layer capacitance, which provides a convenient way of comparing the relative activity of different catalysts.

In order to determine the redox peaks contribution to the charge accumulation, the anodic peak current and charge were calculated for different speeds, using the same data as for Figures 5.26 and 5.28.

The charge was calculated from the area under the curves, shown in Figure 5.24, following these equations:

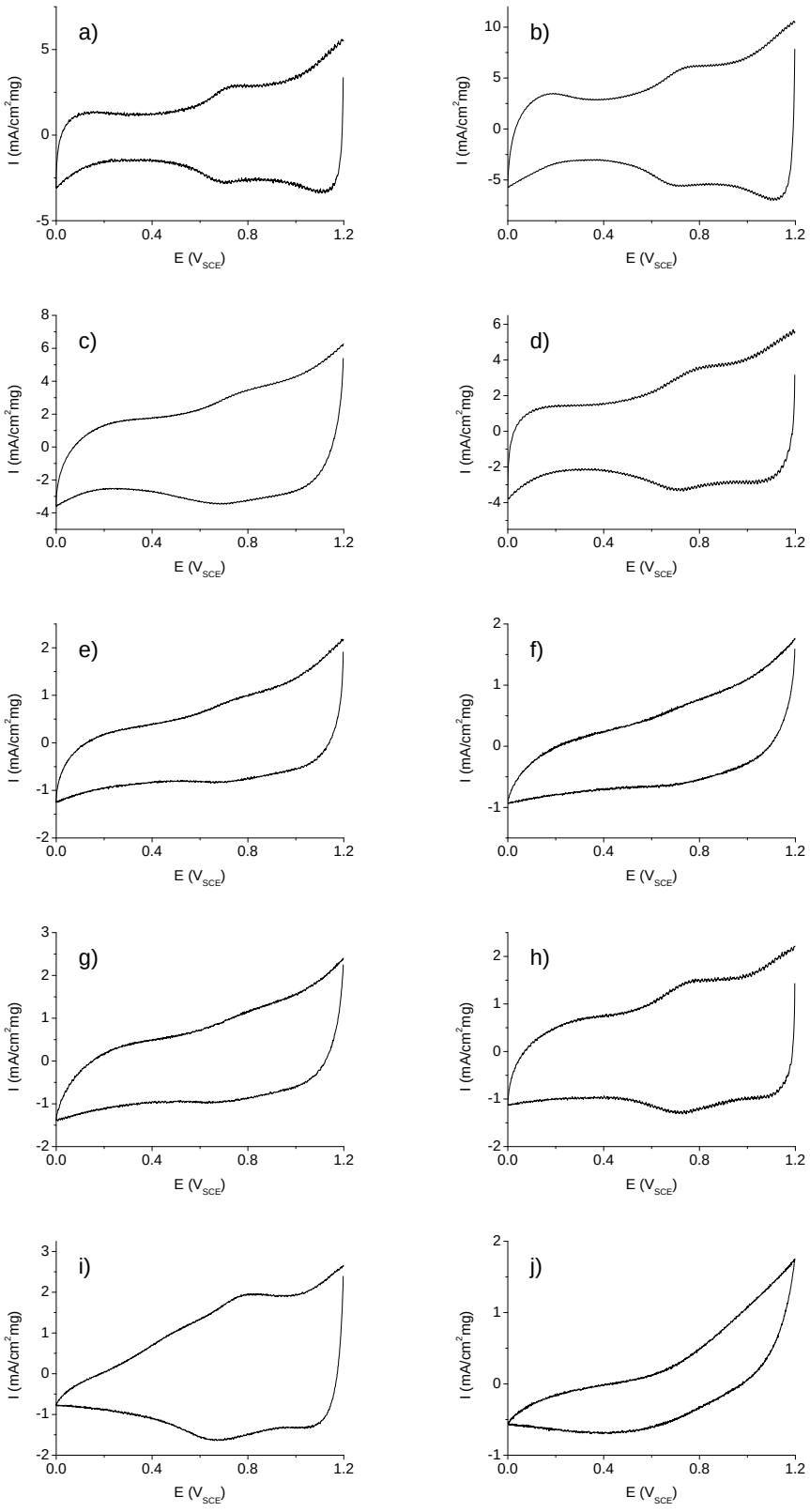

Figure 5.24: CV experiments in H_3PO_4 at room temperature. 20 mV/s. **a)** pure IrO_2. **b)** 90%. **c)** 80%. **d)** 70%. **e)** 60%. **f)** 50%. **g)** 40%. **h)** 30%. **i)** 20%. **j)** 10%.

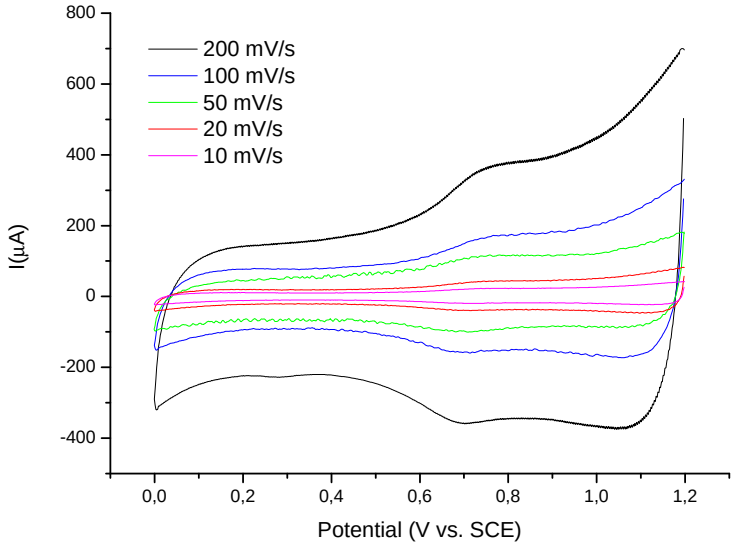

Figure 5.25: CV experiment of pure IrO_2 at different scan speeds. Room temperature.

$$Q = \int I \cdot dt$$
$$v = \frac{dV}{dt}$$
$$dt = \frac{1}{s} \cdot dV$$
$$Q = \int I \cdot \frac{1}{s} \cdot dV = \frac{1}{s} \cdot \int I \cdot dV$$

In Figure 5.29 it can be seen that the peak current is proportional to the scan speed. This result is in agreement with the capacitive behaviour, where the current is proportional to the rate of potential change:

$$C = \frac{Q}{V} = \frac{dQ}{dV}$$
$$dQ = C \cdot dV$$
$$I = \frac{dQ}{dt} = C \cdot \frac{dV}{dt} = C \cdot s$$

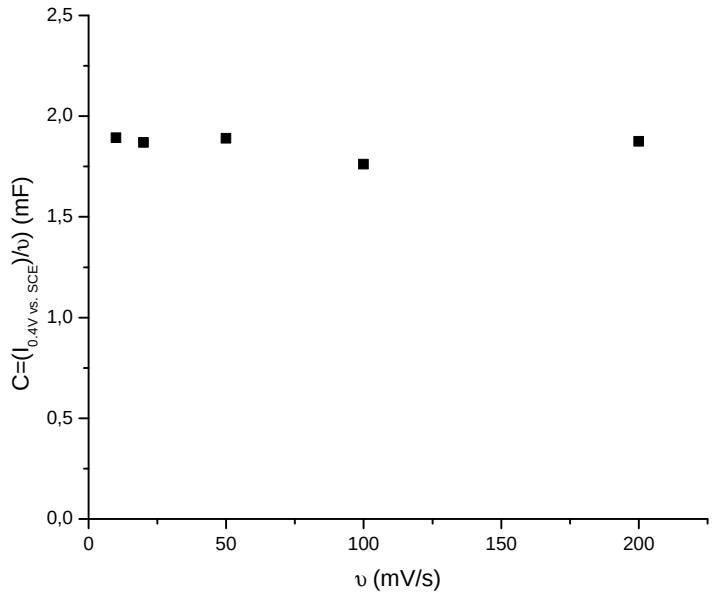

Figure 5.26: Calculated capacitance for different speeds. Pure IrO_2, room temperature.

However, if the electrode behaved as a pure capacitor, there would be no peaks. The evaluation of the charge under the peaks at different speeds (Figure 5.30) shows that the charge accumulated is quite constant, without significant variation with speed. This behaviour is indicative of an active surface layer on the electrode that is charged and discharged through fast faradaic processes.

This behaviour has been described for electrochemical reactions where only adsorbed species react significantly [22]. In this situation, the diffusion to and from the electrode is dismissed, as the rate-limiting step is the adsorption and desorption of reactants:

$$-\frac{\partial \Gamma_O(t)}{\partial t} = \frac{\partial \Gamma_R(t)}{\partial t} = \frac{i}{nFA} \tag{5.9}$$

Where Γ_O and Γ_R are the surface excesses of the oxidized and reduced species on the electrode.

If the reaction is electrochemically reversible, then it can be described by

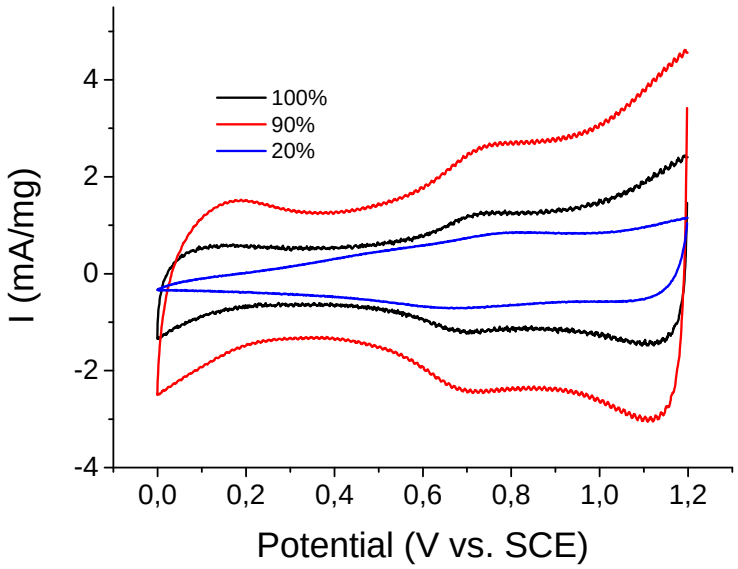

Figure 5.27: CV experiments of several supported catalysts in 85% H_3PO_4 at room temperature. Scan rate 20 mV/s.

previously introduced equation 2.49:

$$i = \frac{n^2F^2}{RT} \frac{vA\Gamma_0^*(b_O/b_R)exp\left[(nF/RT)(E-E^{0\prime})\right]}{\{1+(b_O/b_R)exp\left[(nF/RT)(E-E^{0\prime})\right]\}^2} \tag{5.10}$$

This equation yields a bell-shaped peak (Figure 5.31).

It is possible then to fit the peaks for all samples to this curve. According to this model, the peak current can be calculated as:

$$i_p = \frac{n^2F^2}{4RT} sA\Gamma_O^* \tag{5.11}$$

The peak current is thus proportional to the scan speed v, as was shown in Figure 5.29.

Since the total charge accumulated is proportional to the number of active sites on the catalyst, it can be calculated from the integration of the area, corresponding to the peak in the voltammogram. Thus, the peak charge of all samples is plotted against the IrO_2 loading in Figure 5.32. The background current under the corresponding anodic peaks was subtracted prior to integration.

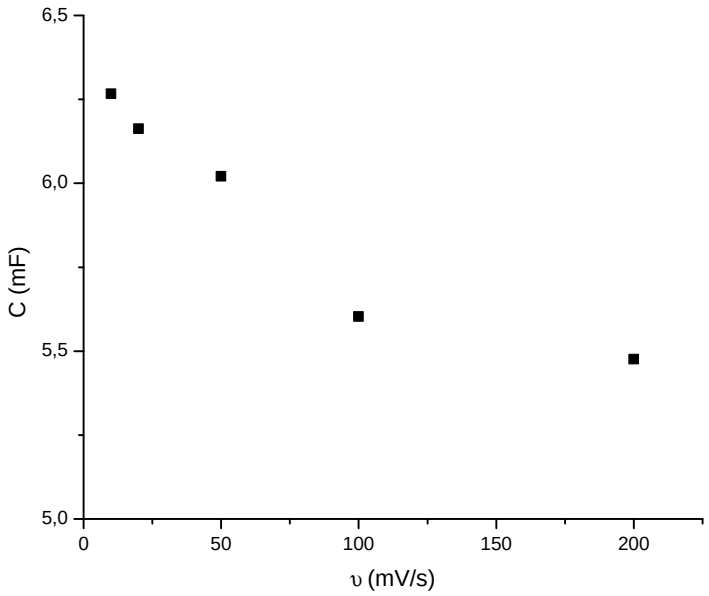

Figure 5.28: Capacitance calculated with charge integration. Same conditions as in Figure 5.26.

The total capacitance was also calculated for all samples. As is seen in Figure 5.33, it follows the same general trend as with the peak charge.

The activity of samples with higher IrO_2 loading tends to show greater values. Thus, for loadings above 60% the activity increases sharply, with a maximum for 90 wt.% IrO_2 loading. However, the activity of pure IrO_2 is lower than that of 70-90 IrO_2 wt.% samples, even though it contains the maximum amount of IrO_2. In theory, the activity should be proportional to the IrO_2 fraction. As found in the powder conductivity tests, the support has a very low conductivity compared to the active phase, so this cannot be the reason for the improvement in activity. Therefore, it can be assumed that the improvement of catalyst activity with the addition of the support must be related to particle formation during the synthesis of IrO_2. Taking into account the results of the XRD and BET experiments, a reason for the improvement could be smaller IrO_2 particle size for the supported catalysts. The smaller the IrO_2 particles are, the greater the specific surface area is, thus giving higher electrochemical activity.

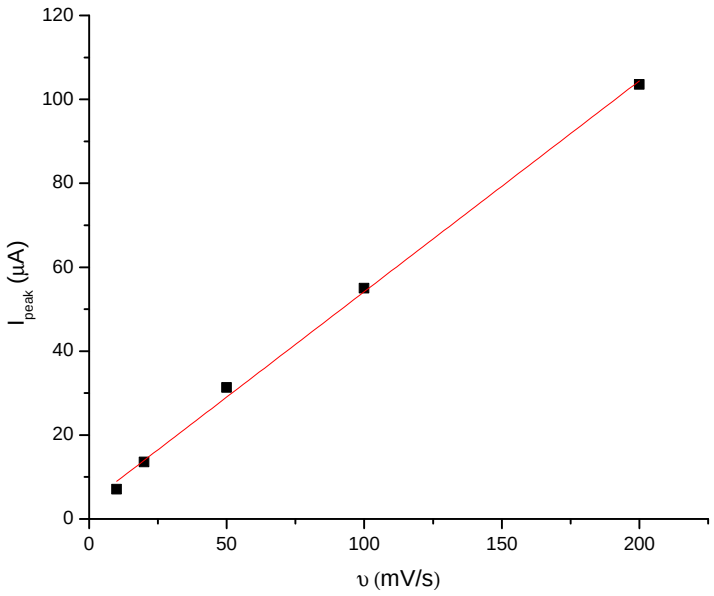

Figure 5.29: Peak current for the IrO_2 90% sample at different scan rates.

High temperature In Figure 5.34, the evolution of CV curves with temperature is shown for 90 wt.% IrO_2 electrode . The activity tends to decrease at higher temperatures, accompanied by the less pronounced redox peak at 0.7 V and smaller corresponding area under the voltammogram curve.

However, the activity of samples at high temperature follows the same trend as for experiments at room temperature (Figure 5.35). It is important, since the studied catalyst is expected to perform at temperatures around 150 °C.

As Figure 5.36 shows, there is a general trend of decreasing capacitance with temperature. However, the activity loss is more pronounced for samples with low IrO_2 loading. This trend has been observed for all samples, with quite sharp decreases in activity at high temperatures.

Considering the transition state theory of reaction kinetics applied to electrode reactions, the catalyst activity should increase with temperature (Section 2.2.2, equation 2.23). However, the evolution of activity with temperature is different for each sample in this series, with an apparent influence of the composition.

There can be several reasons for this behaviour. The first could be associated with a quick loss of active phase from the electrode. Because of the

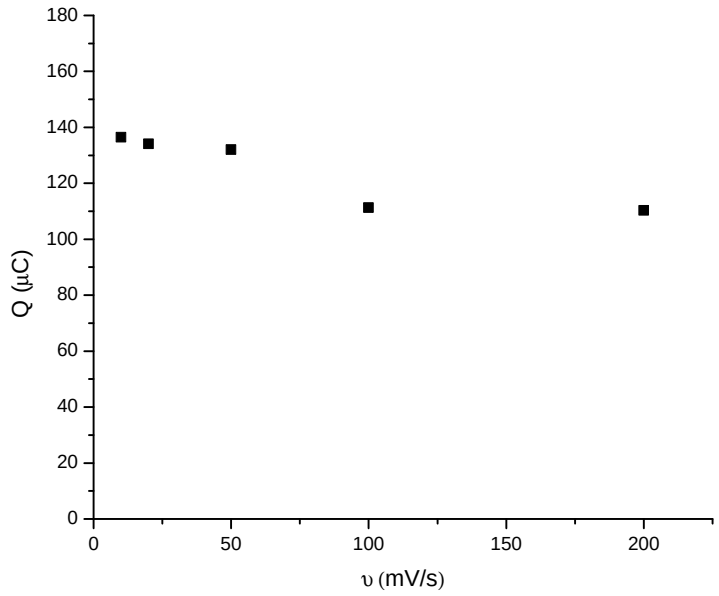

Figure 5.30: Integrated anodic peak charge for the IrO_2 90% sample at different speeds. H_3PO_4, room temperature.

way the catalyst was deposited on the electrode (drop casting and drying at room temperature), the powder is not strongly attached to the working electrode surface. This can make it easy to detach catalyst particles from the electrode by mechanical processes, like electrolyte convection during temperature increase between experiments. As evolution of activity with temperature depends on the composition, it confirms this speculation and can be explained by physical changing of the catalyst particles arrangement on the working electrode when introducing the bigger grains of SiC-Si support.

Another factor in loss of capacitance could be attributed to the adsorption of phosphoric acid on the electrode surface. Some authors [241] have suggested that there is a significant adsorption of acid on the surface of noble metal electrodes. This adsorption would be an exothermic process, which means that the adsorption of phosphoric acid should be weaker with higher temperatures, thus lowering the double-layer capacitance of the electrode. This, however, would increase the catalyst activity, and then the redox peaks should be more prominent. This factor does not explain the activity decrease.

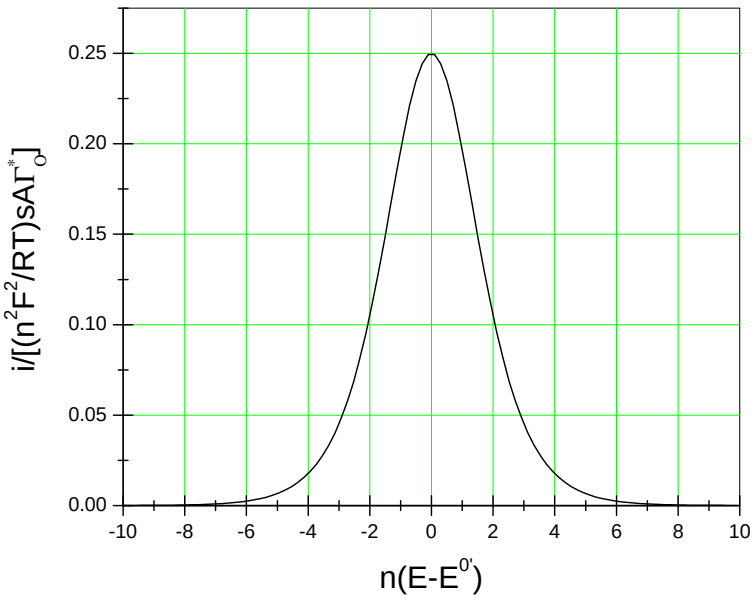

Figure 5.31: Characteristic i-E curve for the reaction of adsorbed species [22].

Therefore, it suggests an apparent problem of physical loss of catalyst powder from the working electrode, rather than a loss of activity of the catalyst itself. Apparently, the samples with higher support content have worse adhesion to the electrode, thus losing catalyst particles over time. This process could be accelerated by convection during heating between experiments at different temperatures.

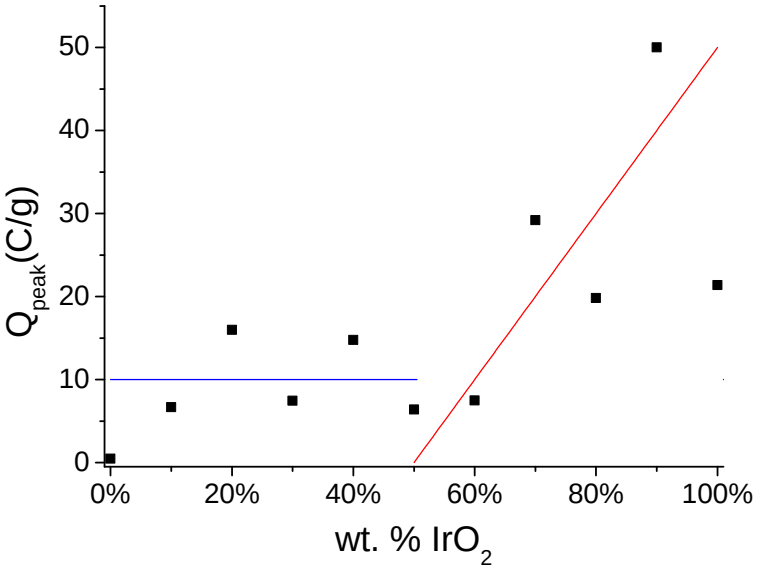

Figure 5.32: Integrated peak charge of all samples. 85% H_3PO_4, room temperature. Scan rate 20 mV/s.

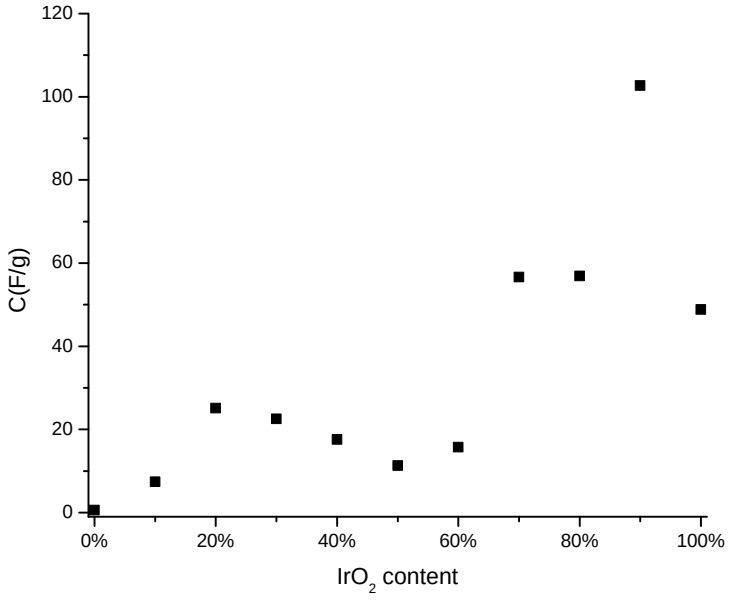

Figure 5.33: Total capacitance for all sample compositions. 85 % H_3PO_4, room temperature.

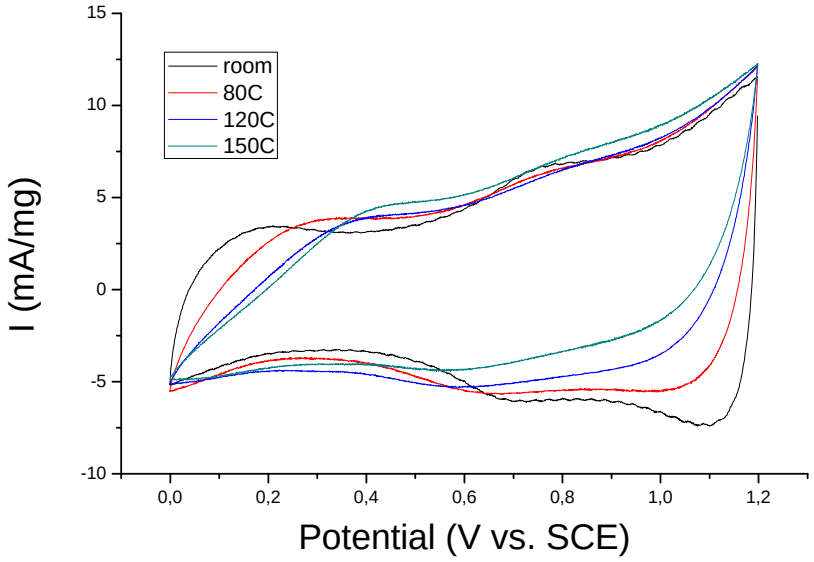

Figure 5.34: CV experiments for the 90% IrO_2 sample at different temperatures in 85% H_3PO_4. Scan rate 20 mV/s.

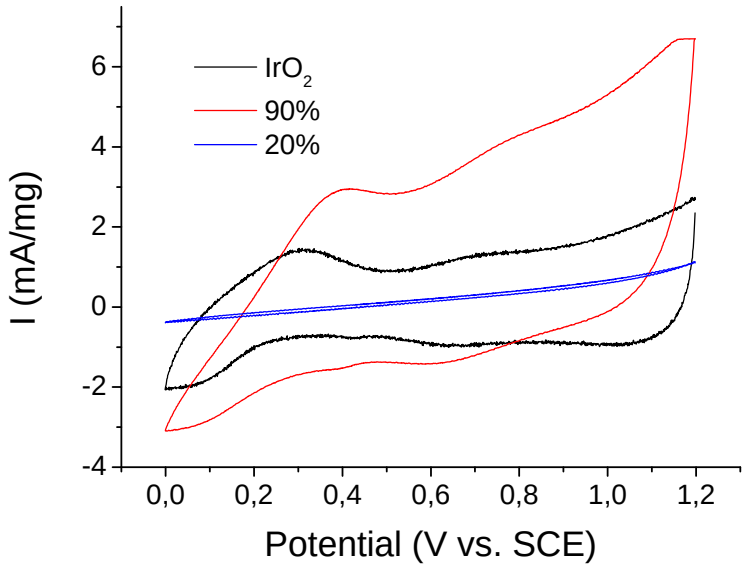

Figure 5.35: CV experiments for some samples at 150 °C in 85% H_3PO_4. Scan rate 20 mV/s.

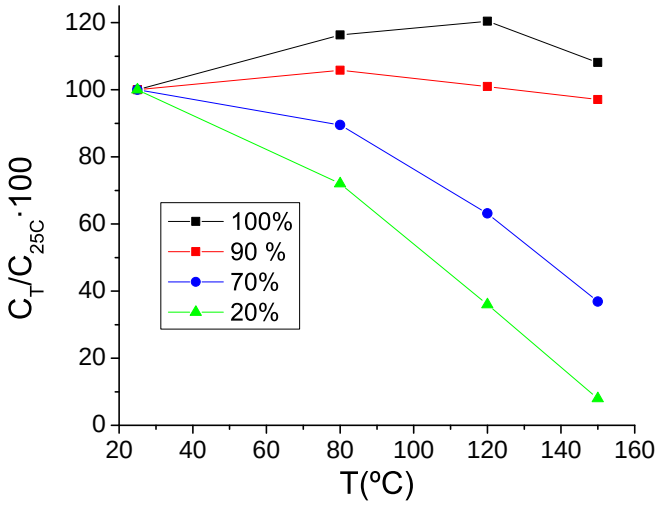

Figure 5.36: Evolution of capacitance with temperature for some samples in 85% H_3PO_4. Scan rate 20 mV/s.

5.3 Conclusions

Catalysts composed of IrO_2 on a SiC-Si support were prepared using the Adams fusion method. The bulk composition of the samples was successfully controlled, as shown in the XRD results.

The different techniques, employed for characterization of synthesized samples provide interesting results which allow to assess the influence of the addition of the support to the IrO_2 catalyst from different perspectives.

It was shown in Section 5.2.1.2 that there is a very good correlation of the relative signals of IrO_2 and SiC-Si with the nominal composition of the prepared powders. The average crystal size of IrO_2, as calculated from the analysis of the peak width, is noticeably smaller in the presence of the support particles. On the other hand, the support material was not modified during the preparation and no new phases formation were detected after the synthesis of supported catalyst (Figure 5.12). This means that any sample property directly related to its composition should follow the rule of mixtures and having the general agreement with equation 5.12:

$$S^{BET}_{sample} = X^{w}_{SiC} \cdot S^{BET}_{SiC} + X^{w}_{IrO_2} \cdot S^{BET}_{IrO_2} \tag{5.12}$$

where X^{w}_{SiC} and $X^{w}_{IrO_2}$ are the mass fractions of SiC and IrO_2, respectively.

This was shown by the BET results, where the specific surface area of each sample was approximately the result of weighting the contribution of specific surface areas of the support and the active phase (Figure 5.15). The support was found to have a rather small specific surface area, of around 6 m^2/g, while the active phase had 121 m^2/g.

However, the supported catalysts showed higher specific area than expected, especially for samples with 70-90 wt.% of IrO_2. The BET area for these samples is significantly higher than that of pure IrO_2 powder. The difference is explained neither by instrumental error, nor by a difference in composition, as has been shown. There must be other factor that is different for pure and supported IrO_2. This was attributed to different conditions during the catalyst synthesis, affecting the particle size.

The analysis of the XRD spectra and the evolution of the calculated crystal size with composition (Figure 5.14) confirms this speculation. While the particles of the support show homogeneous crystal size, the parameter changes for IrO_2 particles, increasing gradually with the oxide loading (Table 5.4). There is a significant step between 90% and pure IrO_2, with the particle size being particularly big for the pure oxide. Therefore, presence of the support apparently influences the crystal size.

Table 5.7 resumes the difference in properties between the support and the active phase.

Table 5.7: Comparison of properties of IrO_2 and SiC-Si compound.

Property	IrO_2	SiC-Si
Conductivity (S/cm)	66	$2 \cdot 10^{-5}$
BET area (m^2/g)	120	5
Particle size (µm)	0.3	5
Capacitance (F/g)	49	1

It is evident that none of the mentioned above properties of the SiC-Si composite are superior to those of IrO_2. It is especially noticeable that, even though the electric conductivity of the support is 6 orders of magnitude lower than that of IrO_2, the introduction of 10% of essentially insulating particles actually improves the performance of the catalyst, and also its surface texture.

The first phenomena that can affect the performance of the catalyst is the modified conditions during its synthesis. The IrO_2 particles are formed from a crystallized precursor. Known factors that can affect particle growth are temperature, ionic strength, saturation of the solution, etc. The presence of the support particles can affect the nucleation and/or growth of the precursor particles, for instance through the electrostatic interaction. Likewise, a support can provide a nucleation surface for the oxide and influence the particle growth, as the electronic microscopy images suggest, with the IrO_2 particles dispersed on the SiC-Si ones.

Another reason for the different performance could be different packing of catalyst particles during the electrode preparation procedure. The access of the electrolyte to the catalyst surface is obviously very important for its activity. In an electrode composed of aggregated particles, the spaces between particles provide room for the access of the electrolyte and thus adequate transport of reactants and current. The distribution of the catalyst particles is thus one of the key factors for the electrode performance. It can be affected by size and shape of the active phase particles, but also by the presence of a support material. It is possible that the support particles modify the access of the electrolyte, by changing the amount, length or diameter of the pores between particles.

The powder conductivity tests gave interesting results. The SiC-Si composite support had conductivity of 5-6 orders of magnitude lower, than the IrO_2 powder. This meant that the conductivity depended strongly on the IrO_2 loading.

However, this relationship was not linear, having a significant step in conductivity at middle loadings and following a model, where the contact between IrO_2 particles plays a key role in the current conduction through the sample. The step in conductivity around 60% in mass fraction of IrO_2 suggests the upper limit for the addition of a low-conducting support to the catalyst. A significant step in conductivity from the pure IrO_2 powder to the 90% sample was attributed to a difference in packing of the powder particles, with the presence of the support, decreasing the number of contacts between IrO_2 particles, which would be thus more loosely packed. However, a conducting support is usually chosen in order to guarantee good electric contact between the catalyst particles and the current collector, as for instance the carbon-supported Pt hydrogen electrode in PEMFCs. Therefore, in the case of a support, having high electrical conductivity, this question may not be of immediate interest.

At the same time, following a provided in Section 5.2.1.5 discussion on the general requirements for the catalytic layer maximum acceptable resistance value and its influence on the overall ohmic drop, all samples with a loading of IrO_2 20 wt.% and above inclusively have enough electronic conductivity for the catalytic layer application without significant contribution to the potential losses.

The CV experiments provided similar results. The behaviour of IrO_2 at room temperature was found to be similar to previously published results, having a pseudo-capacitive behaviour with broad redox peaks around 0.7 V vs. SCE. These peaks were attributed to the oxidation/reduction of adsorbed species on the electrode. The specific activity of 70-90 wt.% samples was found to be higher than that of pure unsupported catalyst. This was attributed to the improved surface properties of IrO_2 in the presence of the support, rather than to better conductivity or surface area of the support itself, which possesses rather poor properties, compared to IrO_2 (Table 5.7).

At high temperatures, all electrodes lost activity with respect to room temperature. This was contrary to the expected results, since the electrode kinetics should improve at elevated temperatures. The decreased activity was attributed to the loss of the catalyst material from the working electrode, perhaps due to electrolyte convection and poor interaction with the finely polished tantalum electrode surface. However, the activity trends with different composition were found to be the same as for room temperature.

The physicochemical characterization of the supported catalysts showed positive influence of the support in formation of IrO_2 particles. Some of the supported catalysts performed better than the pure catalyst, which suggests an influence of the support particles on the active phase through two possible mechanisms. The first is where presence of the support affects the formation of the IrO_2 particles with smaller particle sizes and thus higher surface area.

Second, when the IrO_2 particle packing can be affected by the SiC-Si particles, leaving more open spaces. This would explain both the lower electric conductivity of the supported catalysts with respect to the pure oxide, and higher activity and specific surface area of some of the samples.

Based on the above results, the SiC-Si compound can be recommended as a potential candidate for a catalyst support for oxygen evolution electrodes in phosphoric acid doped membrane steam electrolyzers.

Chapter 6

Concluding Remarks, Perspectives and Further Research

The corrosion stability of the chosen stainless steels and nickel-based alloys appeared to be insufficient for these materials to be used in HTPEMECs. However, CVD-tantalum coating showed outstanding stability in the selected media. Therefore, such coatings on the bipolar plates and gas diffusion layers are recommended for long term tests of working HTPEMECs.

Concerning materials for the oxygen evolution electrode, today, the oxygen evolution reaction catalysts are practically limited to only IrO_2. Moreover, RuO_2 appears to be unstable under the conditions of HTPEMEC. Alternatives must be found even if the working temperature of electrolyzers might be required to be higher for any valid non-noble catalyst material. Therefore, in this work a development towards oxygen evolution electrodes with lower active electrocatalyst loading was intended.

Even though the developed electrodes showed a promising activity, the long term stability investigations still need to be developed and performed.

In this work a commercial SiC-Si material was used, with a free Si part of ca 20%. Such semi-conducting materials are known to be highly sensitive even to minor doping, which can enhance conductivity of the material significantly. It is therefore proposed in the future to make investigation on synthesising SiC in the laboratory conditions with different portions of free silicon.

Even though the used catalyst support was poorly conductive itself, its addition to the active phase improved the specific activity of the catalyst. The most interesting compositions appear to be those with high loading of IrO_2. As discussed in Chapter 3.8, adequate supports should have good corrosion and thermal resistance in phosphoric acid at high temperatures and oxidizing conditions. The SiC-Si was found to be inert through the whole temperature range studied, which is a promising result regarding the possible study of related materials, such as titanium carbide and silicon nitride. This also suggests that a wide range of refractory materials might be found for oxygen evolution reaction electrodes in future investigation.

The decrease of performance of the prepared electrodes (Chapter 5) at high temperatures was attributed to the loss of the catalyst material from the surface of the electrode, rather than the loss of performance of the catalyst itself. Therefore, it is desirable to develop a conventional electrochemical characterisation technique for fast screening of powder OER catalysts at elevated temperatures.

Taking into account the results, the next step would be testing of the developed supported catalysts as anodes in assembled MEAs, and testing them in cell stacks. MEA testing presents a reliable option for assessing the activity of the catalyst under real working conditions.

Chapter 7

Papers

Paper 1

Corrosion behaviour of construction materials for high temperature steam electrolysers

A.V. Nikiforov, I.M. Petrushina, E. Christensen, A. L. Tomás-García, N.J Bjerrum.
International Journal of Hydrogen Energy, 36(1):111–119, January 2011

Available at www.sciencedirect.com

ScienceDirect

journal homepage: www.elsevier.com/locate/he

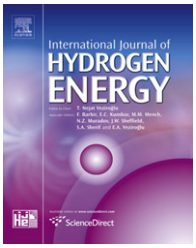

Corrosion behaviour of construction materials for high temperature steam electrolysers

A.V. Nikiforov, I.M. Petrushina, E. Christensen, A.L. Tomás-García, N.J. Bjerrum*

Energy and Materials Science Group, Department of Chemistry, Technical University of Denmark, Kemitorvet 207, DK-2800 Kgs. Lyngby, Denmark

ARTICLE INFO

Article history:
Received 14 July 2010
Received in revised form
6 September 2010
Accepted 8 September 2010

Keywords:
Water electrolysis
Polymer electrolyte membrane (PEM)
Metallic bipolar plate
Phosphoric acid
Corrosion resistance
Polarisation

ABSTRACT

Different types of commercially available stainless steels, Ni-based alloys as well as titanium and tantalum were evaluated as possible metallic bipolar plates and construction materials. The corrosion resistance was measured under simulated conditions corresponding to the conditions in high temperature proton exchange membrane (PEM) steam electrolysers. Steady-state voltammetry was used in combination with scanning electron microscopy and energy-dispersive X-ray spectroscopy to evaluate the stability of the mentioned materials. It was found that stainless steels were the least resistant to corrosion under strong anodic polarisation. Among alloys, Ni-based showed the highest corrosion resistance in the simulated PEM electrolyser medium. In particular, Inconel® 625 was the most promising among the tested corrosion-resistant alloys for the anodic compartment in high temperature steam electrolysis. Tantalum showed outstanding resistance to corrosion in selected media. On the contrary, passivation of titanium was weak, and the highest rate of corrosion among all tested materials was observed for titanium at 120 °C.

1. Introduction

Most of long term visions about the use of hydrogen as an energy carrier include electrolysis. Unfortunately, the efficiency of water splitting by electrolysis is rather low for conventional electrolysers and there is hence a large potential for improvement.

Decentralized production of hydrogen by means of water electrolysis is favourable in several ways. When renewable energy sources (hydropower, windmills, solar cells, etc.) are considered, electrolysis is a practical way of converting the surplus electrical energy into chemical energy to be used when the power is needed [1]. One way of doing this is by using high temperature water steam electrolysis (above 100 °C).

PEM water electrolysis technology is frequently presented in the literature as a potentially very effective alternative to more conventional alkaline water electrolysis [2–4].

PEM water electrolysis systems offer several advantages over traditional technologies, including higher energy efficiency, higher production rates, and more compact design [5]. This method of hydrogen production is envisioned in a future society where hydrogen as the energy carrier is incorporated in an idealized "energy cycle". In this cycle, electricity from renewable energy sources is used to electrochemically split water into hydrogen and oxygen [6].

This technology is environmentally friendly and usually has a considerably smaller mass–volume characteristic and power cost. Besides the high purity of produced gases, there is

* *Corresponding author.*
E-mail address: alnik@kemi.dtu.dk (A.V. Nikiforov).
0360-3199/$ – see front matter
doi:10.1016/j.ijhydene.2010.09.023

Table 1 – Alloy chemical composition.

Alloy type	Chemical composition of alloys (elements, weight%)												
	Ni	Co	Cr	Mo	W	Fe	Si	Mn	C	Al	Ti	Other	Nb+Ta
AISI 347	9.0–13.0	–	17-19	–	–	Bal.	1.0	2.0	0.08	–	–	–	0.8
AISI 321	9.0–12.0	–	17-19	–	–	Bal.	1.0	2.0	0.08	–	0.4-0.7	–	–
AISI 316L	10.0–13.0	–	16.5–18.5	2.0-2.5	–	Bal.	1.0	2.0	0.03	–	–	N Less 0.11	–
Hastelloy® C-276	57	2.5	15.5	16.0	3.75	5.5	0.08	1.0	0.02	–	– –	V 0.35	–
Inconel® 625	62	1.0	21.5	9.0	–	5.0	0.5	0.5	0.1	0.4	0.4	–	3.5
Incoloy® 825	44	–	21.5	3.0	–	27	0.3	1.0	0.05	0.1	1.0	Cu 2.0	–

an opportunity of obtaining compressed gases directly in the installation [7].

At temperatures above the boiling point of water, the energy efficiency of water splitting can be significantly improved because of decreased thermodynamic energy requirements, enhanced electrode kinetics and possible integration of the heat recovery. Other operating features, such as control of steam flow rate, cell temperature and cooling are easier for steam-based systems [8]. However, this increases the demands to all materials used with respect to corrosion stability and thermal stability [3,9].

At the anodic compartment of an electrolyser, strong corrosive conditions will generally exist due to high anodic polarisation in combination with the presence of oxygen. This will be even more severe when the temperature is elevated. It is therefore an important task to choose materials which besides their catalytic properties also possess sufficient corrosion resistance. This demands further development of all materials from which electrolyser cells are built.

Bipolar plates are a multifunctional and expensive part in high temperature steam electrolysis stacks, as they collect and conduct current from cell to cell, they separate gases, and the flow channels in these plates withdraw produced gases.

In a typical PEM electrolysis stack, bipolar plates comprises most of the mass, and almost all the volume. Usually they also facilitate heat management in the system.

The most crucial demands for bipolar plate materials are resistance to spalling and dimensional stability and resistance to corrosion in electrolyte media under anodic/cathodic polarisation. Numerous research projects have been devoted to bipolar plate materials in fuel cells [10–17]. However, the number of suitable materials for PEM electrolyser is still limited because of high requirements for corrosion resistance on oxygen electrode, where high overpotentials are combined with low pH media of electrolyte.

The most widely used bipolar plate material in Nafion® based systems is titanium, which is ideal in terms of corrosion resistance and conductivity [18–20]. The conductivity of Nafion® membranes decreases dramatically at temperatures above 100 °C. Thus, PBI membranes doped with phosphoric acid are typically used in fuel cells at elevated temperatures [21]. However titanium current collectors would considerably suffer from corrosion at temperatures above 80 °C in concentrated phosphoric acid environments [22].

Different types of stainless steels can be used as bipolar plates, and they have the advantages of being good heat and electricity conductors, can be machined easily (e.g. by stamping), are non-porous, and consequently very thin pieces are able to keep the reactant gases apart. The major disadvantage of these alloys is that they are prone to corrosion [13].

A possible alternative for stainless steel bipolar plates can be the use of nickel-based alloys [23]. Ni-based alloys are widely used in process industry and energy production in nuclear

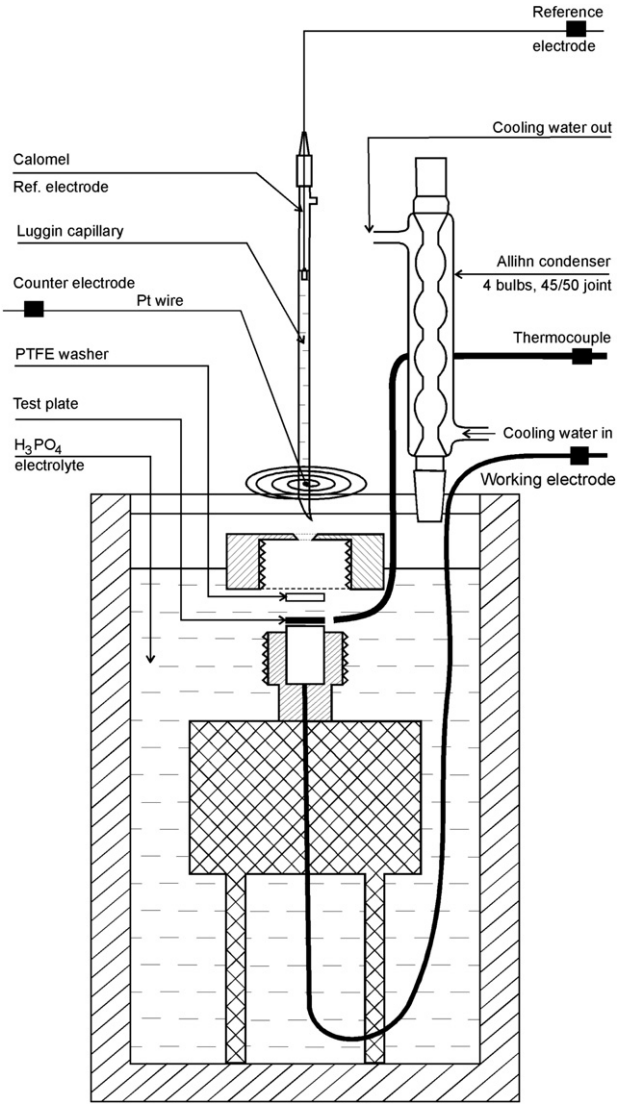

Fig. 1 – The electrochemical cell.

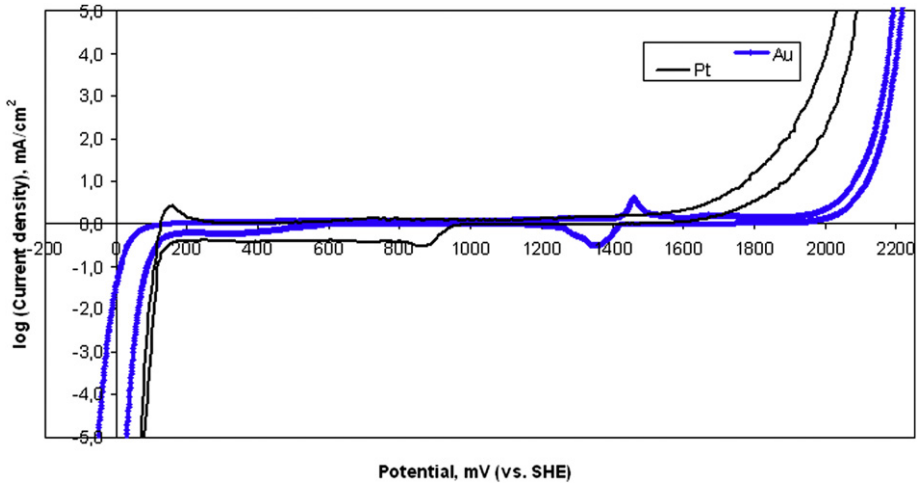

Fig. 2 – Potential window for Pt and Au in 85% H_3PO_4, 120 °C, 1 mV/s (vs. SHE).

power plants. When compared to conventional stainless steels generally a higher degree of resistance against corrosion is observed for these materials. This can be explained partly by the more noble corrosion potential of Ni and by the different properties of the oxide films formed on Ni-based alloys [23]. Also, it has been proposed recently that nickel and stainless steel alloys can be used as the construction material in PEM water electrolysers, but at temperatures no higher than 100 °C [22].

In order to simulate conditions at the anodic compartment of PEM water electrolysis cell during half-cell experiments, it was necessary to choose the proper electrolyte. Investigating systems including membranes based on perfluorinated sulphonic acid, e.g. Nafion®, 0.5 M sulphuric acid is commonly used as an electrolyte, simulating the electrolyser cell conditions [24, 25]. Similary, H_3PO_4 can be used to model systems based on membranes doped with H_3PO_4. 85% solution of H_3PO_4 was chosen to investigate the limiting case of corrosion, considering that in working electrolyser systems the actual concentration of active acid at the electrode-electrolyte-water three-phase boundary would by much less than in case of the approach taken here.

In a highly oxidizing media such as the anodic compartment of a high temperature steam electrolysis stack, it is essential to characterize the effect of different parameters on the behaviour of the protective oxide films. To date, no works have been addressed to the study of Ni-based alloys for use as bipolar plates in high temperature PEM steam electrolysers.

In this paper, the corrosion resistance of metal alloys, namely of austenitic stainless steels AISI 316L, AISI 321, AISI 347 and Ni-based alloys Hastelloy® C-276, Inconel® 625, Incoloy® 825, titanium and tantalum were tested in terms of corrosion resistance. Platinum and gold were also investigated for studying the potential window of concentrated H_3PO_4. All samples were subjected to anodic polarisation in 85% phosphoric acid electrolyte solution at 120 °C. The corrosion speed of metal alloys was investigated additionally for 30 °C and 80 °C to show the influence of temperature on corrosion resistance.

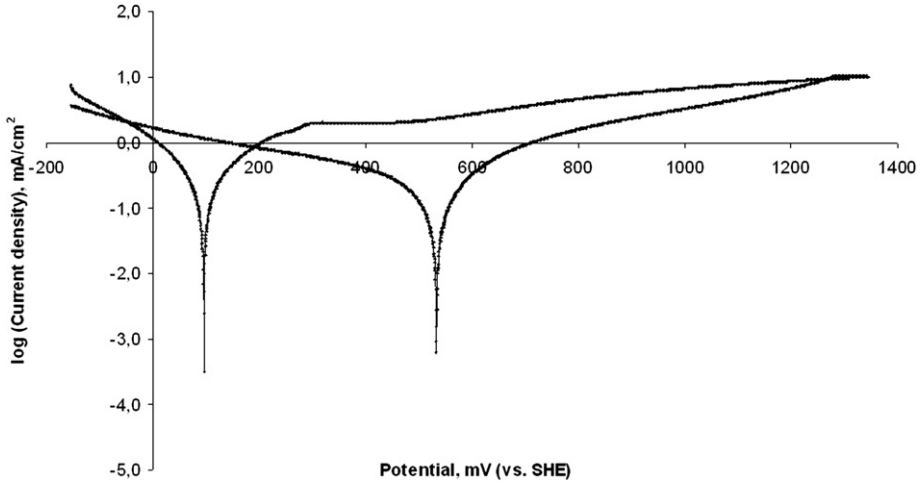

Fig. 3 – Tafel plot for AISI 316L in 85% H_3PO_4, 80 °C, 1 mV/s (vs. SHE).

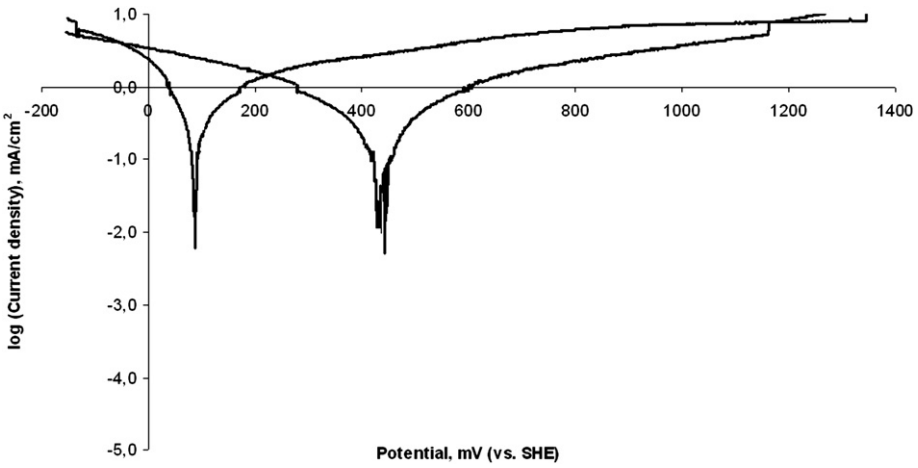

Fig. 4 – Tafel plot for AISI 316L in 85% H_3PO_4, 120 °C, 1 mV/s (vs. SHE).

In this work the electrochemical cyclic Tafel voltammetry technique is employed [26–28].

2. Experimental part

2.1. Materials and sample preparation

Specimens of austenitic stainless steels AISI 316L, AISI 321, AISI 347 (annealed type of temper) and Ti foil were provided by Good Fellow Cambridge Limited (England), Hastelloy® C-276, Inconel® and Incoloy® 825 were provided by T.GRAAE SpecialMetaller Aps (Denmark). Finally, CVD tantalum coated stainless steel AISI 316L was provided by Tantaline A/S (Denmark). Typical chemical compositions of stainless steels and nickel-based alloys investigated in this work are given in Table 1.

All specimens were cut into round plates of 15 mm in diameter. Afterwards the surfaces of all samples, apart from CVD tantalum coated SS316L, were manually ground prior to testing to eliminate any mill finish effects. SiC abrasive paper was used, followed by polishing with polycrystalline diamond powder (Struers A/S (Denmark)) with a particle size less than 0.25 μm. Finally, surfaces were degreased with acetone.

2.2. Characterisation

A high temperature electrochemical cell (Fig. 1) was specially designed for corrosion studies at elevated temperatures. A coil of platinum wire was used as a counter electrode to ensure a good polarisation distribution. A calomel electrode was used as a reference electrode, connected to the system through a Luggin capillary. The exposed specimen area was ca 0.2 cm^2. 85% phosphoric acid (analytical purity) was used as an electrolyte. Tests were performed at 30, 80 and 120 °C at air atmosphere. The experimental apparatus used for electrochemical studies was potentiostat model VersaSTAT 3 and VersaStudio software by Princeton Applied Research. After open-circuit potential was established, scanning was initiated with a scan rate of 1 mV/s. The potential window was 1.5 V, starting at a potential of 400 mV less than the reference electrode potential and going up to 1.1 V more than the reference electrode potential. Reversed polarisation was performed afterwards.

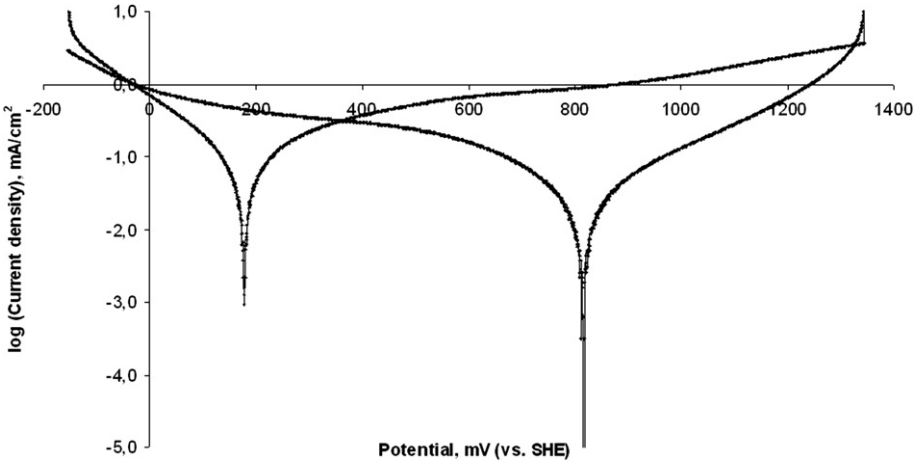

Fig. 5 – Tafel plot for AISI 321 in 85% H_3PO_4, 80 °C, 1 mV/s (vs. SHE).

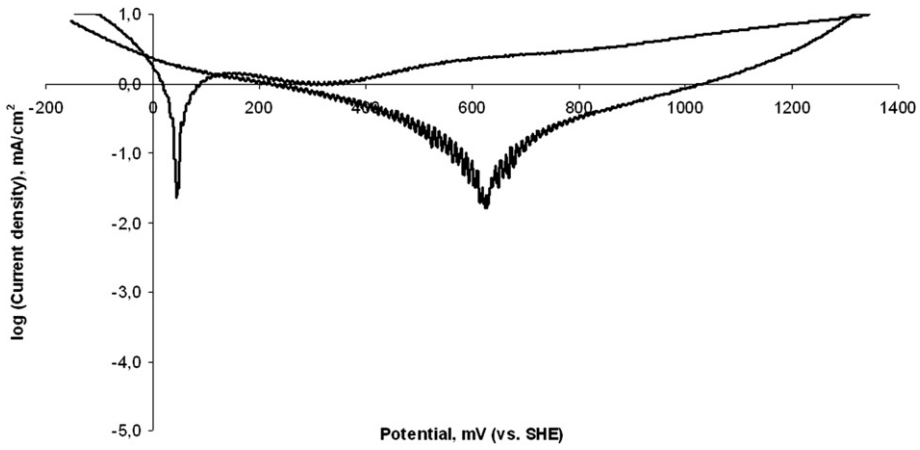

Fig. 6 – Tafel plot for AISI 321 in 85% H_3PO_4, 120 °C, 1 mV/s (vs. SHE).

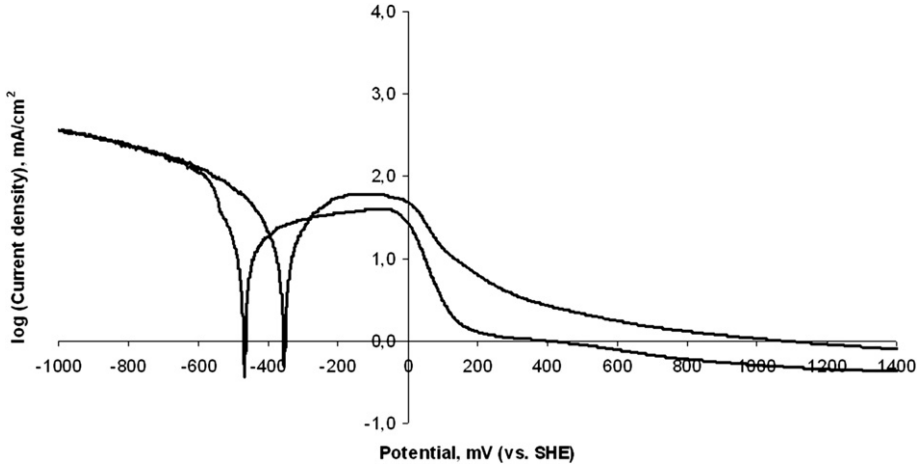

Fig. 7 – Tafel plot for titanium in 85% H_3PO_4, 120 °C, 1 mV/s (vs. SHE).

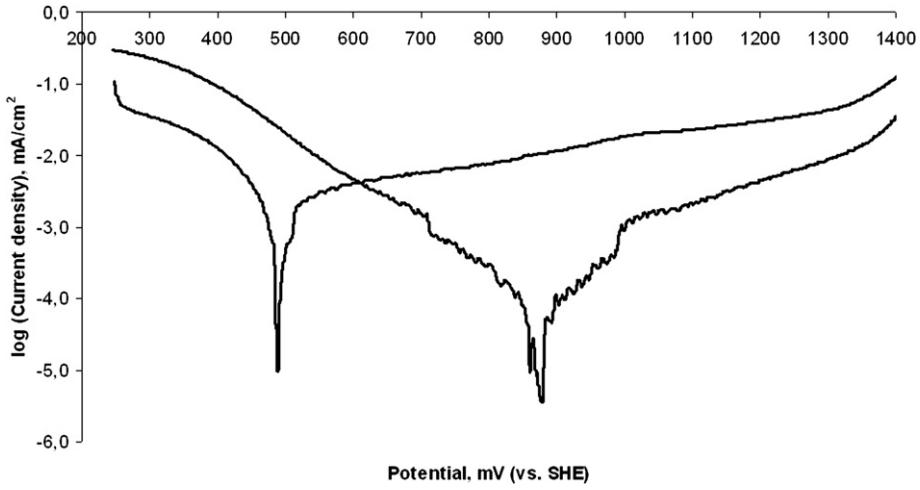

Fig. 8 – Tafel plot for tantalum in 85% H_3PO_4, 120 °C, 1 mV/s (vs. SHE).

Table 2 – The comparison of corrosion currents (approximate corrosion rates) of different materials at T = 30, 80 and 120 °C.

Sample	i_{corr}, mA (CR, mm/year)		
	30 °C	80 °	120 °
Stainless steel AISI 316L	$3.16\times10^{-3}(0,037)$	$6.3\times10^{-2}(0.73)$	$1.3\times10^{-1}(1.46)$
Stainless steel AISI 321	$1.26\times10^{-4}(<0.01)$	$1.0\times10^{-2}(0.12)$	$4.0\times10^{-2}(0.46)$
Stainless steel AISI 347	$3.02\times10^{-4}(<0.01)$	$2.5\times10^{-2}(0.29)$	$7.9\times10^{-2}(0.92)$
Inconel® 625	$1.58\times10^{-4}(<0.01)$	$5.3\times10^{-4}(<0.01)$	$2.0\times10^{-2}(0.23)$
Incoloy® 825	$1.58\times10^{-4}(<0.01)$	$2.0\times10^{-2}(0.23)$	$3.2\times10^{-2}(0.37)$
Hastelloy® C-276	$1.95\times10^{-4}(<0.01)$	$4.0\times10^{-3}(0.05)$	$2.4\times10^{-2}(0.28)$
Tantalum			$6.3\times10^{-5}(<0,001)$
Titanium			6.3(73,3)

Table 3 – Measured corrosion potentials for forward and back polarisation.

Material	E_{corr}, mV (vs. SHE)			
	80 °C		120 °C	
	Forward	Reverse	Forward	Reverse
Stainless steel AISI 316L	100	530	80	430
Stainless steel AISI 321	175	820	40	640
Stainless steel AISI 347	320	770	320	500
Inconel® 625	125	635	90	490
Incoloy® 825	105	540	60	595
Hastelloy® C-276	440	620	120	580
Tantalum			490	875
Titanium			−465	−357

Cross-sections of the samples before and after voltametric measurements were studied using scanning electron microscopy (SEM) and energy-dispersive X-ray spectroscopy (EDX). The cut was made for all the samples before and after immersion in 85% H_3PO_4 at 120 °C for the time of electrochemical experiment. Duplicate plates were prepared for the cross-section investigation before the exposition. All samples were mounted in PolyFast phenolic hot mounting resin with carbon filler, provided by Struers A/S (Denmark). SEM measurements were made with an JEOL JSM 5910 scanning electron microscope. The EDX-system used was INCA from Oxford Instrument (accelerating voltage 20.00 kV, working distance 10 mm).

3. Results and discussion

Fig. 2 represents the polarisation curves for platinum and gold foil, which show the electrochemical stability window for these materials in concentrated phosphoric acid at 120 C. It can be seen that platinum is a better catalyst for O^{2-} oxidation then gold (Fig. 2).

Figs. 3–8 present Tafel plots for the materials tested, obtained at 80 C and 120 C. Anodic exchange current density values were obtained from cyclic Tafel plots [28]. Corresponding corrosion currents and approximate corrosion rates are presented in Table 2. Approximate corrosion rates were calculated in terms of penetration rate (CR), using Faraday's Law [29].

For all studied materials there is a dramatic influence of temperature on corrosion rate, which grows with increasing temperature.

It can be seen from cyclic Tafel behaviour, that for all of the studied alloys corrosion is of a local type, i.e. pitting or intergranular Figs. 3–8.

The analysis of the shape of cyclic Tafel voltammograms can give useful information about possible corrosion mechanisms [26]. Particularly, data related to pitting behaviour can be obtained using a method, proposed by Pourbaix [30]. In this case, the anodic polarisation scan is not terminated at high anodic potential, but is reduced at the same scan rate until reverse E_{corr} is reached. Usually, this kind of graph is called "The pitting scan". Using this technique, it can be assumed that if any pits arise during forward anodic polarisation, any further initiation or propagation then ceases and the surface is covered with an oxide film.

For all materials investigated, besides titanium, the repassivation occurs easily. After changing the direction of polarisation in the highly anodic region, the reverse scan shows more positive corrosion potentials, and lower currents are recorded for the same values of potential. After the reverse voltametric curve crosses the forward one (closing the hysteresis loop), current continues to drop. In most cases, the loop is very small or does not exist, which usually indicates high resistance to pitting type of corrosion. In other words, if any break in the passive layer occurs, it easily "heals" itself, preventing any further development of pits. Thus, it is expected that the pitting resistance is excellent for all tested alloys, because surface protection eliminates local active sites. For titanium the hysteresis loop is very wide, and lasts for almost the whole anodic part of the polarisation curve. Reverse scanning repeats forward with higher values of currents, indicating the absence of "healing" passivation.

Table 4 – The content of Ni and Ti, in wt.% for the tested alloys.

Sample	AISI 347	AISI 316L	AISI 321	Inconel® 625	Incoloy® 825	Hastelloy® C-276
Ni content, wt.%	9–13	10–13	9–12	62	44	57
Ti content, wt.%	–	–	0.4–0.7	0.4	1.0	–

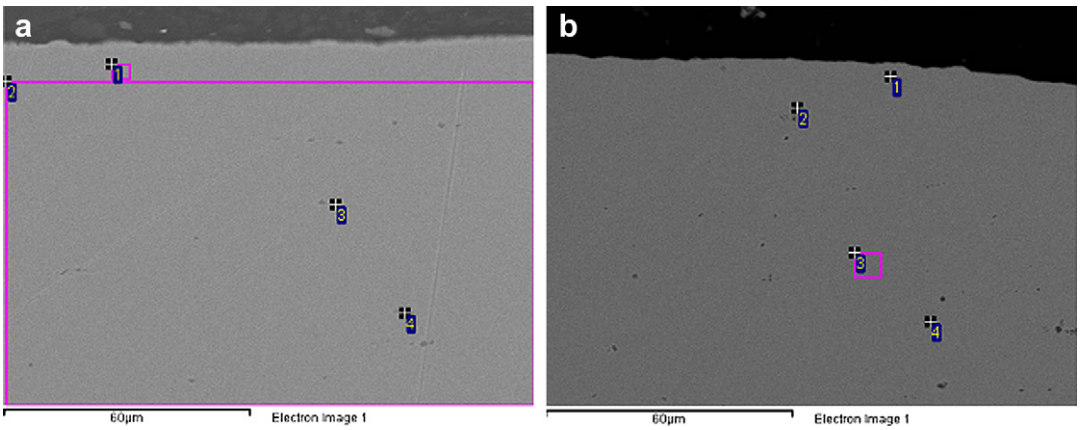

Fig. 9 – SEM of AISI 321 before (a) and after (b) the electrochemical tests. Numbers refer to EDX points and areas measured.

In Table 3 the comparison of corrosion potentials for forward and back scans is given. In most cases, there is an obvious dependence between corrosion rate and E_{corr}. For example, more positive value of E_{corr} for AISI 321 stainless steel during reverse scan corresponds to the lowest corrosion speed of AISI 321 among other tested stainless steels.

Alloy AISI 321 exhibited the largest difference between forward (starting) and reverse corrosion potentials, as well as the most positive repassivation potential among the tested alloys at 120 C. This corresponds to the lowest corrosion rate of AISI 321 among the stainless steels.

Titanium showed the poorest corrosion resistance. At 120 °C and open corrosion potential, the dissolution of titanium was observed visually, followed by intensive evolution of hydrogen gas. Under positive polarisation, it was partly passivated, but still the rates of dissolution were much higher than for austenitic stainless steels.

The corrosion resistance at 120 °C increases in the following sequence in our series:

Table 5 – EDX analysis data of AISI 321 before (a) and after (b) the electrochemical tests.

(a)

	Composition, wt.%, before the electrochemical tests							
Spectrum	Si	Ti	Cr	Mn	Fe	Co	Ni	Total
1	0.6	0.3	17.7	1.8	69.8	0.2	9.7	100
2	0.5	0.5	18.0	1.4	69.5	0.8	9.4	100
3	0.4	27.3	14.5	1.4	49.5	0.5	6.4	100
4	0.3	31.2	14.8	1.4	46.6		6.1	100

(b)

	Composition, wt.%, after the electrochemical tests							
Spectrum	Si	Ti	Cr	Mn	Fe	Co	Ni	Total
1	0.3	0.5	17.7	1.6	70.4	1.0	8.5	100
2	0.1	29.2	15.3	1.5	48.5	0.3	5.2	100
3	0.5	0.1	18.2	1.2	69.8	1.0	9.2	100
4	1.2	9.0	17.5	0.9	62.4	0.6	8.4	100

Titanium < AISI 316L < AISI 347 < AISI 321 < Incoloy® 825 < Hastelloy® c-276 < Inconel® 625 < TantalumIt can be clearly noticed, that for alloys the corrosion stability grows with the increasing content of nickel in this media, as shown in Table 4.

Generally, nickel-based alloys show better corrosion stability than austenitic stainless steels in highly acidic media and elevated temperatures [31]. This tendency is also observed in our series.

Nickel's high degree of corrosion resistance is partly explained by the higher positive standard potential among the studied alloy compounds. Comparing with less resistant iron, nickel has 250 mV more positive standard corrosion potential. But compared to pure nickel metal, nickel–chromium–iron –molybdenum alloys show considerably better resistance to corrosion in all inorganic acid solutions [23].

It can also be seen from Table 4, that titanium has a positive effect on the corrosion resistance of the alloys tested. This effect can be explained by the EDX data, obtained from AISI 321 and Inconel ®625 before and after the electrochemical tests.

It is visible from Fig. 9 (spectrum 3,4) and (spectrum 2,4) and Table 5a, b that before the corrosion test, Ti is not spread evenly on the surface of AISI 321, it is localized at definite points. It is safe to assume that these points are located on intergranular boundaries. It follows from the data that the content of titanium in the intergranular region dropped after the electrochemical experiment, indicating that corrosion in AISI 321 develops along the intergranular boundaries in this media. Titanium tends to be distributed along these boundaries during the severe anodic attack, thus preventing the formation of chromium carbides in these areas, which could promote chromium concentration drop resulting in a loss of passivity in these regions.

The same behaviour is observed for another alloy, containing titanium as an addition, protecting the material from intergranular corrosion. Fig. 10 (spectrum 3,4), (spectrum 1,3,5) and Table 6a, b show SEM and EDX data for Inconel ®625. The same tendency is even more significant for this alloy.

The discussion above proves the extremely important role of doping the investigated alloys with titanium in this media,

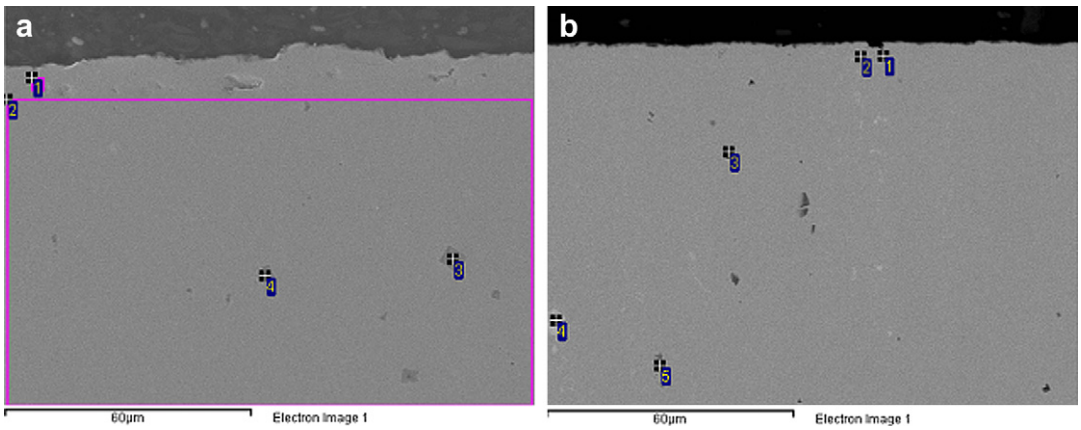

Fig. 10 – SEM of Inconel® 625 before (a) and after (b) the electrochemical tests. Numbers refer to EDX points and areas measured.

thus protecting them from the most apparent intergranular type of corrosion.

Molybdenum is more soluble in nickel than in austenitic stainless steels, and higher levels of alloying are possible with a higher content of nickel. Therefore, the molybdenum content limit grows with nickel content and high contents of molybdenum are only possible in high nickel alloys [32].

Generally, the addition of molybdenum to stainless steels and alloys is used for enhanced corrosion resistance. For instance, the addition of even one or two percent of molybdenum to ferritic stainless steels significantly increases the corrosion resistance of these material.

Pure nickel-molybdenum alloys, namely alloy B-2, contain approximately 28% molybdenum and about 1.7% iron. The very high molybdenum content gives excellent resistance to reducing acids, i.e. hydrochloric and sulphuric [33]. For sulphuric acid, this alloy shows good resistance, even at concentrations close to 90% and temperatures up to 120°. Non-oxidant conditions, however, must certainly exist in this case. Either the presence of oxygen or aeration will significantly accelerate corrosion rate [31]. However, the role of molybdenum is not clearly noticed in our series.

Table 6 – EDX analysis data of Inconel® 625 before (a) and after (b) the electrochemical tests.

(a)											
	Composition, wt.%, before the electrochemical tests										
Spectrum	Al	Si	Ti	Cr	Mn	Fe	Co	Ni	Nb	Mo	Total
1	0.3	0.3		21.7		0.9		63.1	4.0	10.1	100
2	0.3	0.4	0.3	22.1		0.9	0.2	63.4	3.4	9.4	100
3		0.1	63.6	5.8		0.1		7.0	23.1	0.6	100
4	0.6	0.3	54.9	10.6	0.1	0.3	0.1	18.9	12.2	2.0	100
(b)											
	Composition, wt.%, after the electrochemical tests										
Spectrum	Al	Si	Ti	Cr	Mn	Fe	Co	Ni	Nb	Mo	Total
1	0.5	0.8	20.5	13.7	0.3	0.4		34.9	21.4	7.9	100
2		2.2	0.1	15.8	0.5	0.5		40.1	14.0	27.0	100
3	0.2	0.1	48.6	12.3	0.0	0.8		24.4	10.0	3.9	100
4	0.3	2.1	0.1	13.7	0.7	0.1	0.1	29.4	26.1	27.5	100
5		0.1	43.4	11.1		0.4	0.3	21.2	19.8	4.0	100

4. Conclusions

It has been established that tantalum coated AISI 316L stainless steel and Inconel® 625 are the most suitable materials for bipolar plate in high temperature steam electrolysers with H_3PO_4 doped membranes. It has also been found that small addition of titanium to the alloys increases the corrosion stability in this media. Among austenitic stainless steels, AISI 321 has the lowest corrosion rate. Anodic passivation with decreased rate of dissolution was observed for all alloys and metals studied. The best corrosion resistance was found for tantalum, while titanium showed the poorest resistance to corrosion, thus excluding it as a possible material for use in bipolar plates in high temperature PEM steam electrolysers using H_3PO_4 doped membranes.

Acknowledgements

The work was supported by Center for renewable hydrogen cycling (HyCycle), Denmark, contract No. 2104-07-0041 and WELTEMP project under EU Seventh Framework Programme (FP7), grant agreement No. 212903.

REFERENCES

[1] Ulleberg O, Nakken T, Ete A. The wind/hydrogen demonstration system at utsira in norway: evaluation of system performance using operational data and updated hydrogen energy system modeling tools. International Journal of Hydrogen Energy 2010;35(5):1841–52.
[2] Linkous CA, Anderson HR, Kopitzke RW, Nelson GL. Development of new proton exchange membrane

electrolytes for water electrolysis at higher temperatures. International Journal of Hydrogen Energy 1998;23(7):525–9.
[3] Linkous C. Development of solid polymer electrolytes for water electrolysis at intermediate temperatures. International Journal of Hydrogen Energy 1993;18(8):641–6.
[4] Lessing PA. Materials for hydrogen generation via water electrolysis. Journal of Materials Science 2007;42(10):3477–87.
[5] Oberlin FMR. Status of the membral process for water electrolysis. In: Hydrogen energy progress VI, proceedings of the sixth world hydrogen energy conference. Oxford: Pergamon Press; 1986. p. 333–40.
[6] Barbir F. PEM electrolysis for production of hydrogen from renewable energy sources. Solar Energy 2005;78(5):661–9.
[7] Grigoriev S, Porembsky V, Fateev V. Pure hydrogen production by PEM electrolysis for hydrogen energy. International Journal of Hydrogen Energy 2006;31(2):171–5.
[8] Li Q, Jensen JO, Savinell RF, Bjerrum NJ. High temperature proton exchange membranes based on polybenzimidazoles for fuel cells. Progress in Polymer Science 2009;34(5):449–77.
[9] Dutta S. Technology assessment of advanced electrolytic hydrogen production. International Journal of Hydrogen Energy 1990;15(6):379–86.
[10] Hermann A, Chaudhuri T, Spagnol P. Bipolar plates for PEM fuel cells: a review. International Journal of Hydrogen Energy 2005;30(12):1297–302.
[11] Tawfik H, Hung Y, Mahajan D. Metal bipolar plates for PEM fuel cell-a review. Journal of Power Sources 2007;163(2):755–67.
[12] Hung Y, EL-Khatib KM, Tawfik H. Corrosion-resistant lightweight metallic bipolar plates for PEM fuel cells. Journal of Applied Electrochemistry 2005;35(5):445–7.
[13] Makkus RC, Janssen AH, de Bruijn FA, Mallant RK. Use of stainless steel for cost competitive bipolar plates in the SPFC. Journal of Power Sources 2000;86(1–2):274–82.
[14] Antunes RA, Oliveira MCL, Ett G, Ett V. Corrosion of metal bipolar plates for PEM fuel cells: a review. International Journal of Hydrogen Energy 2010;35(8):3632–47.
[15] Joseph S, McClure JC, Chianelli R, Pich P, Sebastian PJ. Conducting polymer-coated stainless steel bipolar plates for proton exchange membrane fuel cells (PEMFC). International Journal of Hydrogen Energy 2005;30(12):1339–44.
[16] Tian RJ, Sun JC, Wang L. Plasma-nitrided austenitic stainless steel 316L as bipolar plate for PEMFC. International Journal of Hydrogen Energy 2006;31(13):1874–8.
[17] Wang Y, Northwood DO. An investigation of the electrochemical properties of PVD TiN-coated SS410 in simulated PEM fuel cell environments. International Journal of Hydrogen Energy 2007;32(7):895–902.
[18] Di Blasi A, D'Urso C, Baglio V, Antonucci V, Arico' AS, Ornelas R, et al. Preparation and evaluation of RuO_2-IrO_2, IrO_2-Pt and IrO_2-Ta_2O_5 catalysts for the oxygen evolution reaction in an SPE electrolyzer. Journal of Applied Electrochemistry 2009;39(2):191–6.
[19] Labou D, Slavcheva E, Schnakenberg U, Neophytides S. Performance of laboratory polymer electrolyte membrane hydrogen generator with sputtered iridium oxide anode. Journal of Power Sources 2008;185(2):1073–8.
[20] Song SD, Zhang HM, Ma XP, Shao ZG, Zhang YN, Yi BL. Bifunctional oxygen electrode with corrosion-resistive gas diffusion layer for unitized regenerative fuel cell. Electrochemistry Communications 2006;8(3):399–405.
[21] He R, Li Q, Xiao G, Bjerrum NJ. Proton conductivity of phosphoric acid doped polybenzimidazole and its composites with inorganic proton conductors. Journal of Membrane Science 2003;226(1–2):169–84.
[22] International patent application, 03.01.2008, wo 2008/002150 a1, pct/no2007/000235 (03.01.2008).
[23] Rockel M. Corrosion behaviour of nickel alloys and high-alloy stainless steel. Nickel alloys. New York: Marcel Dekker Inc; 1998.
[24] Marshall A, Børresen B, Hagen G, Tsypkin M, Tunold R. Hydrogen production by advanced proton exchange membrane (PEM) water electrolysers-reduced energy consumption by improved electrocatalysis. Energy 2007;32: 431–6.
[25] Song S, Zhang H, Ma X, Shao Z, Baker RT, Yi B. Electrochemical investigation of electrocatalysts for the oxygen evolution reaction in PEM water electrolyzers. International Journal of Hydrogen Energy 2008;33:4955–61.
[26] Trethewey KR, Chamberlain J. Corrosion. Longman Group UK Limited; 1988.
[27] Annual book of ASTM standarts 10.05, g5-94, p. 60–70.
[28] Annual book of ASTM standarts 10.05, g3-89, p. 42–47.
[29] Annual book of ASTM standarts 10.05, g 102-89 (reapproved 1999), p. 446–452.
[30] Pourbaix M, Klimzack-Mathieiu L, Mertens C, Meunier J, Vanleugenhaghe C, de Munck L, et al. Potentiokinetic and corrosimetric investigations of the corrosion behaviour of alloy steels. Corrosion Science 1963;3(4):239–59.
[31] Friend WZ. Corrosion of nickel and nickel-base alloys. New York/Chichester/Brisbane.Toronto: J Wiley&Sons; 1980.
[32] Bil'chugov YI, Makarova NL, Nazarov AA. On limit of molybdenum content of pitting-corrosion-resistant austenitic steels. Protection of Metals 2001;37(6):597–601.
[33] Asphahani A, et al. United states patent 4846885 (1989).

Paper 2

Preparation and study of IrO_2/SiC-Si supported anode catalyst for high temperature PEM steam electrolysers

A. V. Nikiforov, A. L. Tomás-García, I. M. Petrushina, E. Christensen, N. J. Bjerrum

International Journal of Hydrogen Energy, 36(10):5797–5805, May 2011

INTERNATIONAL JOURNAL OF HYDROGEN ENERGY 36 (2011) 5797–5805

Available at www.sciencedirect.com

ScienceDirect

journal homepage: www.elsevier.com/locate/he

Preparation and study of IrO_2/SiC–Si supported anode catalyst for high temperature PEM steam electrolysers

A.V. Nikiforov, A.L. Tomás García, I.M. Petrushina, E. Christensen, N.J. Bjerrum*

Energy and Materials Science Group, Department of Chemistry, Technical University of Denmark, Kemitorvet 207, DK-2800 Kgs. Lyngby, Denmark

ARTICLE INFO

Article history:
Received 16 November 2010
Received in revised form
5 February 2011
Accepted 9 February 2011
Available online 12 March 2011

Keywords:
PEM water electrolysis
Catalyst support
Oxygen electrode
Corrosion resistance
Inert anode

ABSTRACT

A novel catalyst material for oxygen evolution electrodes was prepared and characterised by different techniques. IrO_2 supported on a SiC–Si composite was synthesised by the Adams fusion method. XRD and nitrogen adsorption experiments showed an influence of the support on the surface properties of the IrO_2 particles, affecting the IrO_2 particle size. The prepared catalysts were electrochemically characterised by cyclic voltammetry experiments at 25,80,120 and 150 °C. In accordance with the observed variation in particle size, a support loading of up to 20% improved the activity of the catalyst. Powder conductivity measurements were also performed, which showed the influence of the support particles in the packing of IrO_2 particles, perhaps favouring the formation of channels and pores between particles, thus increasing the catalyst utilisation.

1. Introduction

Some of the future aspirations of the "hydrogen energy cycle" involve the splitting of water by means of electrolysis and using the evolved hydrogen as a fuel. One way to do this would be by using a proton exchange membrane (PEM) electrolyser [1]. The electrolysis of steam instead of liquid water is favourable in several ways. The thermodynamic demands are lower at higher temperatures, waste heat can be utilised (effective cooling due to temperature gradient) and water management is simplified in such systems (avoiding two-phase operation).

Elevated working temperatures involve increased demands for corrosion resistance of catalysts and construction materials (bipolar plates and current collectors), while the contact resistance in gas diffusion layer (GDL) should remain reasonable.

For conventional PEM water electrolysers, Nafion® is commonly used as an electrolyte [2–4]. The conductivity of such membranes decreases significantly at temperatures above 80 °C, which is associated with the reduction of water content [5]. Sufficient efficiency is achieved using polybenzimidazole (PBI) membranes doped with phosphoric acid in PEM fuel cells at temperatures up to 200 °C under ambient pressure [5,6]. Doped membranes are a potential electrolyte for use in PEM steam electrolyser systems. Nevertheless, one of the main problems in such systems still remains the extremely low pH combined with elevated temperatures and high overpotentials at the anodic compartment. These conditions impose serious limitations on the materials which can be used.

The applicable electrocatalysts for the oxygen evolution reaction (OER) are still limited to Ir, Ru and their oxides [7]. The anodes used in research and in industry are mostly based on mixtures of an electrocatalyst and a stabilising agent, e.g.

* *Corresponding author.*
E-mail address: alnik@kemi.dtu.dk (A.V. Nikiforov).
0360-3199/$ – see front matter
doi:10.1016/j.ijhydene.2011.02.050

TiO_2. Such kinds of electrodes are known as dimensionally stable anodes (DSA) and were first developed by Beer [8–10].

For Nafion® based systems, porous *Ti* usually serves as an anode bipolar plate and GDL material [4,11]. Unfortunately, previous studies have shown that titanium can not be used in systems that involve phosphoric acid containing electrolytes [12,13].

Ruthenium oxide is known as the most active catalyst for the OER. Nevertheless, according to thermodynamical calculations, the oxidation of RuO_2 to RuO_4 occurs at potentials more positive than 1.387 V (vs. SHE) [14]. The instability of Ru-based anodes at high overpotentials in acidic conditions has been proved by several studies. The mechanism of corrosion is explained by the conversion of RuO_2 to soluble, non-conductive and volatile RuO_4, with a boiling point of 130 °C [15–17]. The facts mentioned above present *Ru* and its oxides as unsuitable catalysts for the OER in high temperature PEM steam electrolysers.

Several studies undertaken [18,19] devoted to improving the stability of RuO_2 during anodic oxygen evolution by mixing the catalyst with IrO_2. This causes a decrease in the corrosion rate of RuO_2 dependant on the IrO_2 content in the mixture. IrO_2 appears to have greater stability and a reasonable activity compared with Ru-based electrocatalysts for such systems [7]. Apparently, IrO_2 is the most stable OER electrocatalyst for PEM water electrolysers studied until now.

Unfortunately, high loadings of noble metals or their oxides puts considerable commercial limitations on a wider application of PEM electrolysers and a significant reduction of such metal loadings should be achieved [20]. In search for an electrode with lower loading requirement for the electrocatalyst, two main strategies can be followed:

The first includes doping of active oxides with other, more available materials, such as SnO_2, SbO_2, TaO_2, Mo_xO_y etc [1,21–23]. This approach involves introduction of a dopant precursor on the initial stage of catalyst synthesis. Following this method, composite binary or ternary catalytic oxides are usually obtained.

The second approach includes the use of a support material which would improve the specific surface area of the electrocatalyst and prevent particle agglomeration, thus increasing the specific surface area of the electrode.

Ideally, raw materials for the preparation of inert anode or/and its support should be cheap and readily available.

Carbon is a widely used catalyst support material for PBI fuel cells. On the other hand, one of the main reasons for fuel cell catalyst degradation is the corrosion of the carbon support, which occurs at potentials higher than 0.207 V (vs. SHE) [5,24]. In electrolysis mode the corrosion speed of carbon would be much higher than in fuel cell mode due to the higher anodic overpotentials of the OER. For this reason, carbon cannot be considered as a potential durable support for anode electrocatalyst in PEM electrolysers. The corrosion stability and durability of the OER electrocatalyst support appears to be one of the greatest challenges in the field.

In conclusion, only a dimensionally and chemically stable, as well as readily available and reasonably conductive material should be used for this application. Among others, ceramic materials are potentially promising candidates [25]. However, most ceramics have relatively low electrical conductivity while it is considered to be of high importance for the overall performance of electrodes. The value of the acceptable electrical conductivity of catalytic layers is discussed elsewhere [26].

Nevertheless, some of the materials with low electrical conductivity can be used as an anode for acidic systems [27]. In one study in particular, p–Si was employed as a substrate for thermal deposition of the active IrO_2 and results showed that this material can be used for the preparation of DSA-type electrodes.

Silicon carbide, produced by the Acheson process is known as a hard, refractory and chemically inert material [28]. Electrical conductivity of this material is quite poor, however doping with appropriate elements can significantly increase this property [29]. Considering a possible electrochemical application of silicon carbide, the main advantage among others is its high stability in phosphoric acid solutions [30].

Several studies have been published, reporting the successful use of silicon carbide as a catalyst support for PEM fuel cells [31,32]. However, at present there are almost no publications covering catalyst support investigations for electrolysers [33]. Indeed, this area of research is more challenging and the material choice is highly limited, which is directly connected with the increased cell voltages applied in the electrolyser mode.

In this study a refractory silicon carbide-silicon material (free *Si* less than 22%) was used as a support for the active OER catalyst IrO_2. The aim being to find a stable support and introduce it to the active catalyst.

2. Experimental part

2.1. *SiC–Si/IrO_2 powder catalyst preparation*

The sintered SiC–Si material was provided by the "State Powder Metallurgy Plant", Brovary, Ukraine. Catalyst support powder was prepared according to the following procedure: the as-received plate was cut with a diamond saw into squared samples with 1 *cm* side. The thickness of the plates was 2 mm. The prepared plates were cleaned in an ultrasonic bath, degreased with acetone, washed with demineralised water and finally dried at 80 °C. The silicon carbide-silicon plates were milled in a planetary ball mill (Fritsch, Pulverisette 7). Since SiC is a material with high hardness, a mill made of conventional steels could not be used for this procedure. This is due to the relative softness of the steel, and associated risk of contamination of the sample by self abrasion of the steel balls and a possible tribochemical reaction. Therefore, two 45 ml steel vials, covered with tungsten carbide wear resistant lining were used. Milling was performed in the vial, which contained 6 WC balls, each 15 mm in diameter. The working vial contained 2 g of the starting material. The mill was operated at 730 r.p.m. for 10 min.

The product of the milling was introduced at the initial stage of the Adams fusion method of IrO_2 synthesis [34]. The iridium oxide content in the prepared catalyst was varied from 0 to 100 wt.% in steps of 10 wt.%. As the support was added to the initial solution of the catalyst precursor, it was expected that the catalyst would adhere to the surface of the

support. Chemical inertness during synthesis was confirmed by XRD analysis. The calcinated products appeared to be fine powders, changing colour from black to more greyish with increasing content of silicon carbide in the composition.

2.2. The electrochemical characterisation

2.2.1. Corrosion stability tests

For investigation of the corrosion stability of material, plates prepared as described in section 2.1 were used. The corrosion stability test of the the material was performed in a specially designed cell, used in our previous work [12].

2.2.2. Preparation of Nafion bonded electrodes for CV investigation

In order to estimate the electrochemical performance of the prepared electrocatalyst powder, the following procedure was performed.

A tantalum cylinder, accurately embedded in a Teflon® PTFE body was used as a working electrode. The diameter of the cylinder was 7.5 mm which corresponded to an active surface area of 0.44 cm^2. Tantalum was chosen because of its superior corrosion resistance in hot phosphoric acid solutions, while having necessary conductivity and mechanical strength to support the electrocatalyst [12,35]. Silicon carbide abrasive paper was used for polishing, followed by polycrystalline diamond powder (Struers A/S (Denmark)) with a particle size less than 0.25 m. Finally, the surface was degreased with acetone and rinsed with demineralised water. The catalyst suspensions were prepared by adding of a 1 mg portion of prepared powder to 1 mL of demineralised water. The suspension was dispersed in an ultrasonic bath for 1 h. Immediately after a 30 μL portion of the suspension was applied on the surface of the working electrode, following by the drying of the catalyst layer under nitrogen protective atmosphere. A second suspension, consisting of a 1% solution in water of commercial 5 wt.% Nafion® (by DuPont) was applied on top of the catalyst layer and dried in the same manner. Therefore, each electrode contained 30 μg of sample powder. All 11 test electrodes were prepared in the same manner, using equal amount of applied test powder, while ranging in its composition of active IrO_2 from 0 to 100% with a step of 10%.

The performance investigations of the supported electrocatalyst were conducted in a specially designed three-electrode cell, which permitted use of the cell at temperatures up to at least 200 °C. The heating of the cell was provided by an external heating plate (Fig. 1).

A commercial platinum counter electrode and a KCl-saturated calomel reference electrode (SCE), connected to the system through a Luggin capillary were provided by Radiometer Analytical SAS.

The CV experiments were performed in the potential window between 0 and 1.2 V against the SCE. This allowed the observation of the reversible redox behaviour of IrO_2 while avoiding the formation of significant amounts of oxygen which could detach the catalyst layer from the working electrode. This permitted the use of the same sample for experiments at elevated temperatures. As it is necessary to evaluate the catalyst performance at the conditions close to those in a PEM cell, in our work the 85% phosphoric acid (analytical purity) was used as electrolyte. The range of temperatures was from room temperature (ca. 23 °C) to 80 °C, 120 °C and 150 °C, with the experiments performed from lower to higher temperatures. The temperature tolerance allowed during the cyclic voltammetry experiments was ±3 °C. Temperature was controlled by a k-type thermocouple, covered with Teflon® PTFE and inserted into the working cell (Omega Co.). For each temperature, a series of scans at different speeds were carried out in the following sequence: 200, 100, 50, 20, 10 mV/s. The CV scan started at 0.0 V, going to the vertex potential of +1.2 V and reversing back to the initial value of 0.0 V (all potentials vs. SCE). An open circuit of 10 s was maintained between each experiment. The experimental apparatus used for electrochemical studies was a VersaSTAT 3 potentiostat and VersaStudio software by Princeton Applied Research.

2.3. Physico-chemical Characterisation

The prepared powder samples were studied using scanning electron microscopy (SEM) and energy-dispersive X-ray spectroscopy (EDX). The catalyst powder was dispersed in ethanol and the suspension was kept for 1 h in an ultrasonic bath. 20 μL portions of this solution, containing 20 μg of the catalyst were afterwards applied to both a sticky carbon disk and a polished gold holders, which were correspondingly used for SEM and EDX investigations. SEM measurements were made with an FEI Quanta 200F scanning electron microscope. The EDX-system used was INCA from Oxford Instruments (accelerating voltage 5 kV, working distance 5.1 mm).

The as-milled SiC–Si powder as well as other samples were characterised with X-ray powder diffraction (XRD) using a Huber D670 diffractometer (Cu-K α x-ray source, $\alpha = 1.5405981$ Å).

The BET method was used to evaluate the specific surface area of the catalysts. Automated Gemini 2375 surface area analyser by Micromeritics was used in our work.

3. Results and discussion

3.1. Structural and electrical properties

3.1.1. X-Ray diffraction

The X-Ray diffractogram for the IrO_2 prepared without the support is shown in Fig. 2. The supported catalysts showed the characteristic signals of IrO_2, SiC and Si (Fig. 3). However, small peaks of WC were detected in the diffractogram of the support powder (Fig. 4). This contamination originates from the ball milling procedure. The produced catalyst consisted of a physical mixture of IrO_2 and support material with no any other substances produced during the synthesis process, e.g. firing at 500 °C. As other components were not detected in the samples (Fig. 3), the composite samples can be considered as physical mixtures of IrO_2 and support. The peak at around 55° and the width of IrO_2 peaks for different samples were chosen in order to calculate the average crystal size, on the basis of the Scherrer equation [36]:

$$T = \frac{K\lambda}{\beta\cos\theta} \quad (1)$$

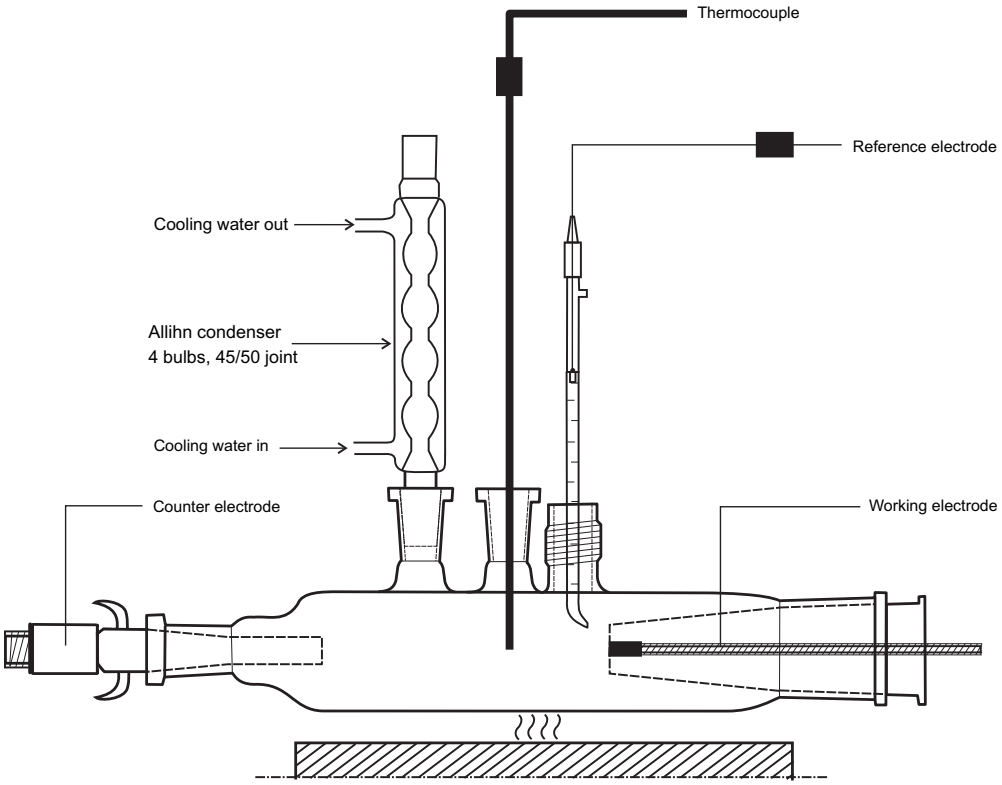

Fig. 1 – The electrochemical cell.

where *K* is a shape factor, usually taken as 0.9; λ is the X-ray wavelength; β is the peak width in radian; and θ is the Bragg angle of the peak.

The supported catalysts showed smaller crystal sizes than those for pure IrO_2, as can be seen in Fig. 5. Since the synthesis method and conditions were the same for all samples, these results indicate an influence of the support in the IrO_2 crystal growth during the catalyst synthesis.

3.1.2. *BET surface area*

The IrO_2 powder has a surface area of 121 m^2/g. In contrast, the support has only around 6 m^2/g. The BET area of the supported catalysts follows approximately the rule of mixtures. However, the BET area of pure IrO_2 is significantly lower than that of 80% and 90% IrO_2 samples (Fig. 6). As seen in the previous section, this difference can be due to different conditions in the catalyst synthesis, with smaller IrO_2 particles in the supported catalysts than in the pure sample.

3.1.3. *SEM and EDX analysis*

Scanning electron microscopy was performed on a selected sample containing 60% IrO_2 and 40% SiC–Si support. The images were obtained with an incident electron energy of 5 kV (Fig. 7). SEM results resolved that the active component was distributed evenly over the surface of the support. In the SEM

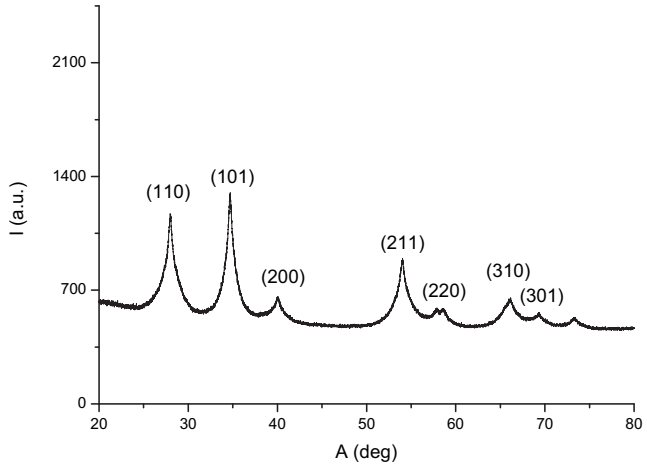

Fig. 2 – XRD spectrum for IrO_2.

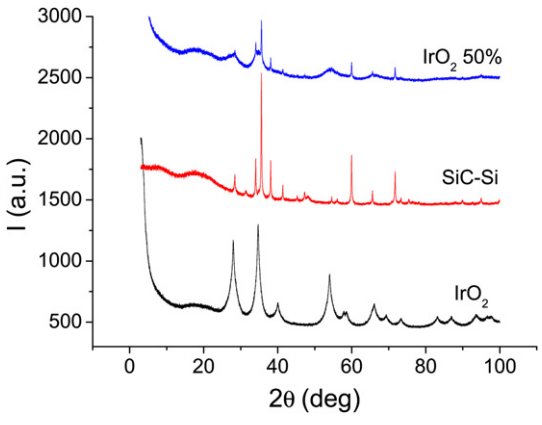

Fig. 3 – XRD spectra for IrO_2, SiC-Si support, and a 50% composite.

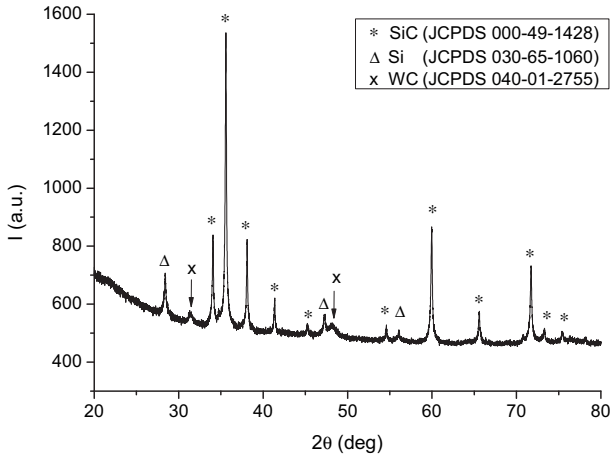

Fig. 4 – XRD spectra for the prepared support powder.

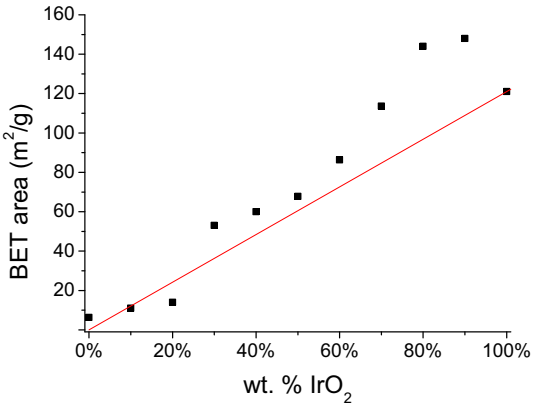

Fig. 6 – BET surface area of all samples.

micrograph two groups of particles can be seen. There are larger particles, between 5 and 10 μm in size which are most likely support particles. On these there are smaller agglomerate particles of IrO_2. The distribution of the IrO_2 particles on the support material seems to be quite homogeneous. This distribution suggests that the IrO_2 particles are formed on the support particles, which could provide nucleation sites for the formation of IrO_2. This could explain the results observed in the XRD and BET experiments, where the IrO_2 particles in the supported catalysts tend to be smaller than in the pure material (Figs. 5 and 6). On Fig. 8 and Table 1 the results of the EDX quantative analysis, performed at low voltage (5 kV) are presented.

3.1.4. *Powder conductivity*

The conductivities of all sample powders were measured using a technique, described previously by Marshall [37]. Measurements were conducted in air at room temperature. To this end, the resistance of powder samples with different thickness was measured (Fig. 9). It can be seen that the evolution of the resistance with the powder thickness is quite linear. The conductivity results are shown in Fig. 10.

The IrO_2 conductivity is 67 S/cm, i.e. much higher than for the support, which is $1.8 \cdot 10^{-5}$ S/cm. It can be thus assumed that almost all the current passes through the IrO_2 particles.

The dependency of conductivity on the sample composition is not linear, levelling off and increasing again with the mass fraction of IrO_2. The effect of the support on the conductivity of the composite powders is obviously negative. It has been proposed that the conduction of current through powders depends strongly on the contact resistance between particles [38]. The presence of a step in conductivity around 60% of IrO_2 seems to support this hypothesis. If we take into account the great difference in conductivity of support and IrO_2, it is clear that the contact between IrO_2 particles is very important for the conductivity of the material.

Although the conductivity changes regularly with composition, there is an increase from 90 wt.% to 100 wt.% IrO_2. This suggests that there must be another factor influencing particle

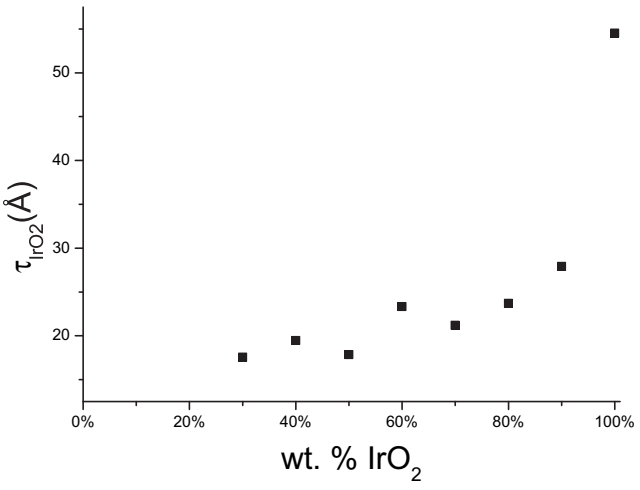

Fig. 5 – Calculated average crystal sizes for different samples.

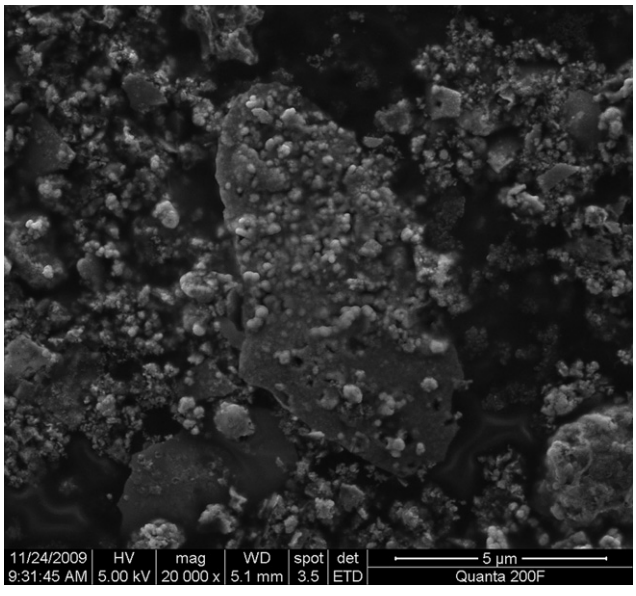

Fig. 7 – SEM micrograph of a sample with composition 60% IrO_2 and 40% SiC–Si support.

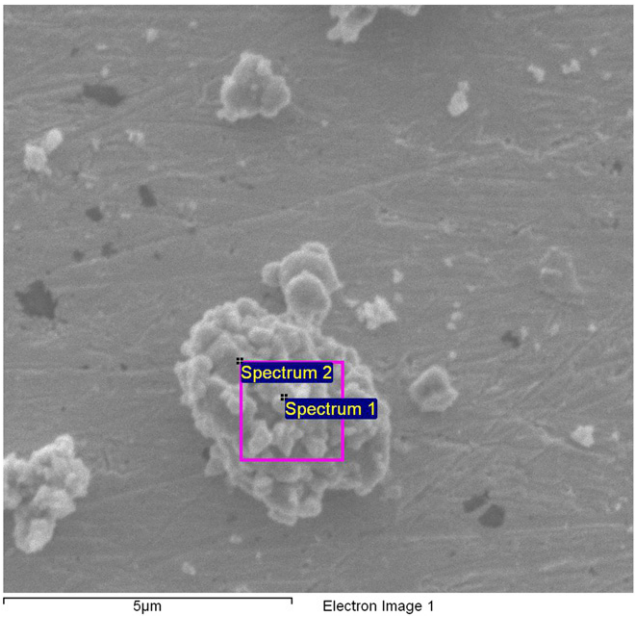

Fig. 8 – SEM micrograph for EDX analysis at 5 kV on a gold plate. Sample composition: 60% IrO_2 and 40% SiC–Si support.

contact. For instance, the inclusion of the support particles, with very different size and shape, could alter the packing of the IrO_2 particles in the powder. This could also be another effect of a different IrO_2 particle growth in the presence of the support, as mentioned above.

3.2. *Electrochemical characterisation*

3.2.1. *The corrosion stability of the support at high temperatures*

Corrosion stability of the support material was tested using the electrochemical cyclic Tafel voltammetry technique [12]. Fig. 11 presents the Tafel plot for a SiC–Si plate. The potential shifts to more positive values after the anodic sweep, which shows the passivation of the material in the studied media. The corresponding corrosion current measured from the curve was 0.005 mA, dropping to 0.002 mA during the backward scan, which is at least one order of magnitude less than for all alloy materials tested before in similar conditions [12].

3.2.2. *Cyclic voltammetry experiments*

3.2.2.1. *Room temperature*. Even though the SiC–Si support is considered to be inert under the chosen conditions, an additional experiment was performed for the tantalum working electrode and support material, in order to identify any considerable background current which could also originate from WC impurities, detected earlier by the X-Ray diffraction (see section 3.1.1).

Thus, in the supported catalysts, almost all the signal comes from the IrO_2 particles (Fig. 12). Catalysts with different loadings were characterised with cyclic voltammetry at potential scan rate of 20 mV/s. IrO_2 shows a pseudocapacitive behaviour, with a broad redox peak. This has been attributed to reversible oxidation and reduction of Ir [7] on the electrode surface. This feature allows integration of the charge under the anodic peak in order to compare the relative activity of the different catalysts. The background current under corresponding anodic peaks was subtracted prior to integration. Fig. 13 shows cyclic voltammograms, recorded with the prepared supported and unsupported iridium oxide on tantalum electrodes. There is an evident increase in associated voltammetric capacitance value corresponding to the

Table 1 – EDX data for SiC–Si/IrO_2 sample (SiC–Si: IrO_2 = 40:60).

Spectrum	Composition, wt.%							
	C	O	Na	Si	Fe	Mo	Ir	Total
1	7.0	20.4	3.1	13.3	2.6	0.9	52.8	100.0
2	6.5	19.6	2.3	15.5		2.0	57.0	100.0

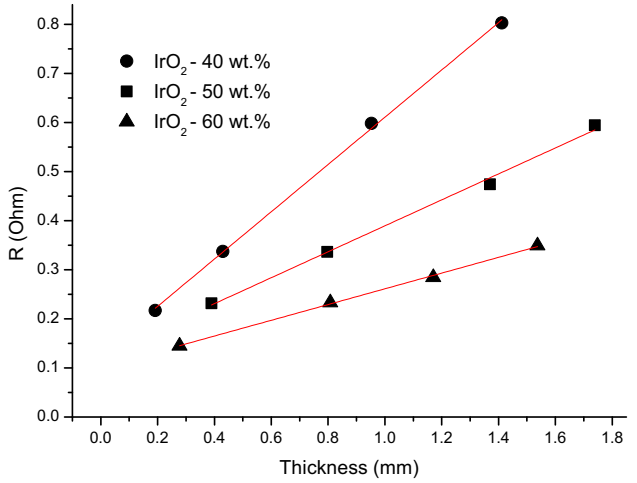

Fig. 9 – Evolution of resistance with powder thickness for some samples.

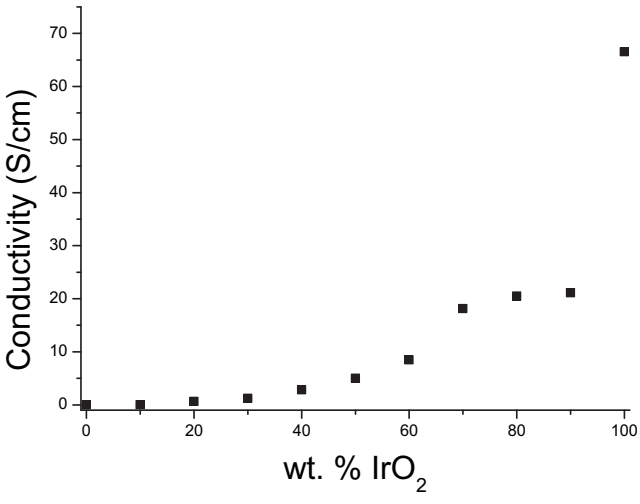

Fig. 10 – Powder conductivities of all samples.

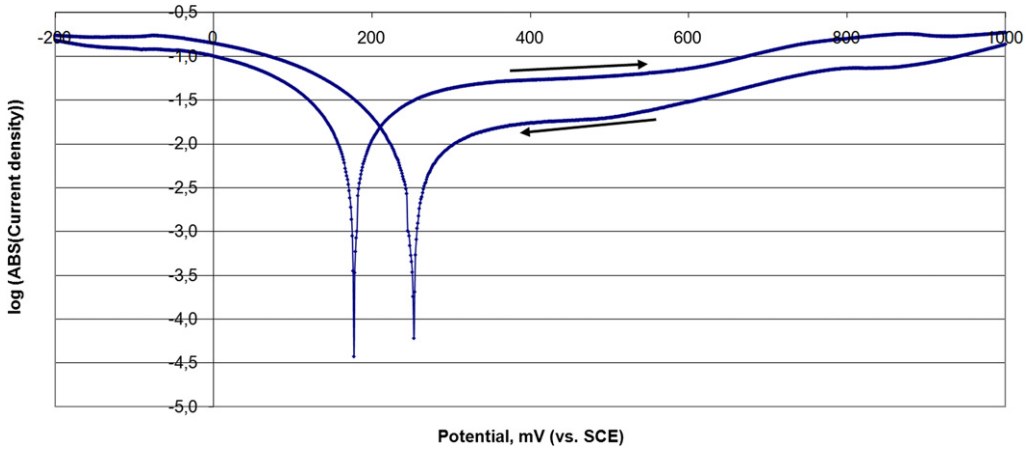

Fig. 11 – The Tafel plot for a SiC–Si plate. Scan rate 1 mV/s, electrolyte 85% H_3PO_4, 120 °C.

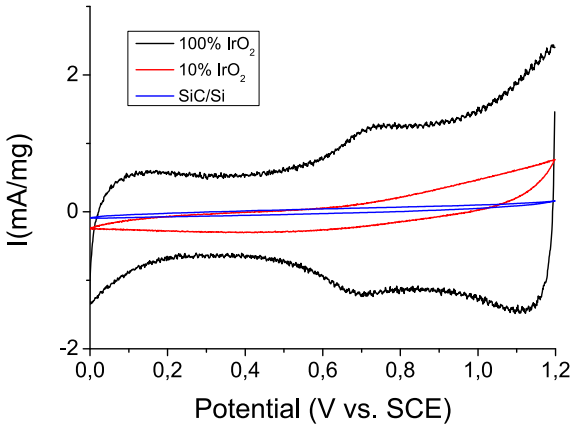

Fig. 12 – Comparison of the voltammograms of the support and some samples. Scan rate 20 mV/s.

supported catalyst compared to the pure oxide catalyst material. The peak charge of all samples is plotted against the IrO_2 loading in Fig. 14. The activity of samples with higher IrO_2 loading tend to show greater values. However, the activity of 80 wt.% and 90wt.% samples is higher than that of pure IrO_2. In theory, the activity should be proportional to the IrO_2 fraction. As shown by the powder conductivity tests, the support has a very low conductivity compared to the active phase, so this cannot be the reason for the improvement in activity. Therefore, it can be assumed that the improvement of catalyst activity with the addition of the support must be related to particle growth during the synthesis of IrO_2. Taking into account the results of the XRD and BET experiments, a reason for the improvement could be a smaller IrO_2 particle size for the supported catalysts, compared with the pure oxide. The smaller the IrO_2 particles are, the greater the specific surface area thus giving higher electrochemical activity.

3.2.2.2. High temperature. Cyclic voltammetry experiments were carried at 80, 120 and 150 °C. The rest of the experimental conditions were the same as for room temperature. In Fig. 15, the evolution of CV curves for 90 wt.% IrO_2 electrodes with temperature is shown. The activity tends to decrease at higher temperatures, with less pronounced peaks and smaller area under the voltammogram curve. This activity loss seems to be more pronounced for samples with low IrO_2 loading (Figs. 16 and 17).

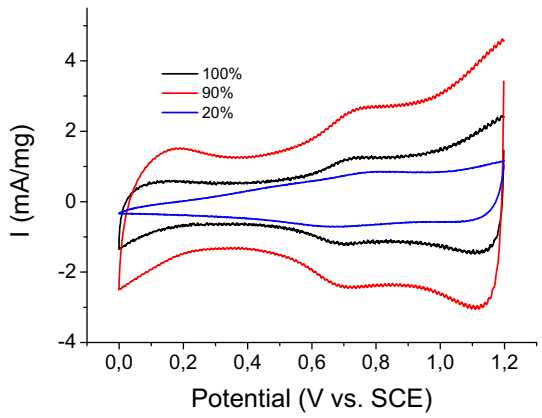

Fig. 13 – CV experiments of several supported catalysts, in 85% H_3PO_4 at room temperature. Scan rate 20 mV/s.

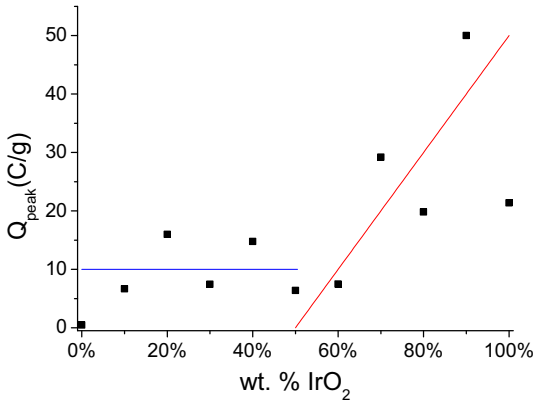

Fig. 14 – Integrated peak charge of all samples, in 85% H_3PO_4 at room temperature. Scan rate 20 mV/s.

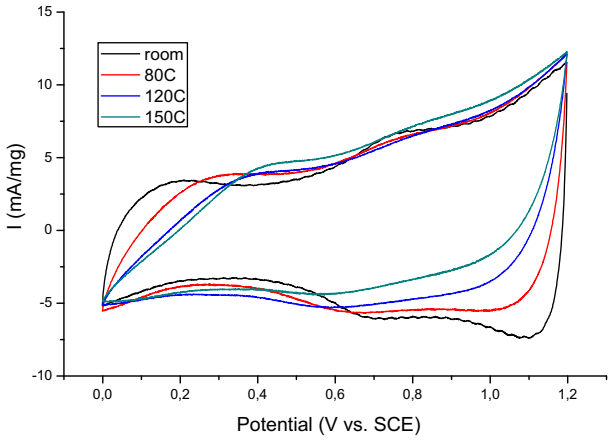

Fig. 15 – CV experiments for 90% IrO_2 at different temperatures, in 85% H_3PO_4. Scan rate 20 mV/s.

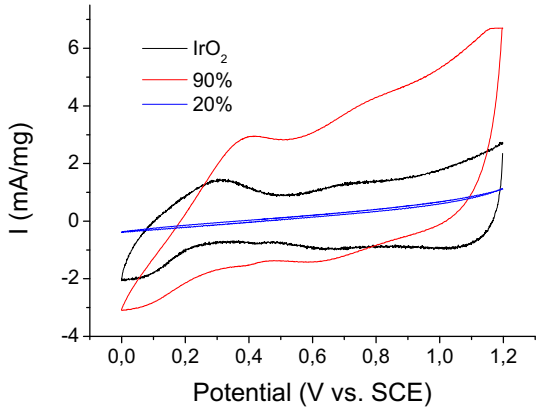

Fig. 16 – CV experiments for some samples at 150 °C, in 85% H_3PO_4. Scan rate 20 mV/s.

Considering the transition state theory of reaction kinetics applied to electrode reactions, the catalyst activity should increase with temperature. The evolution of activity with temperature is different for each sample, with an apparent influence of the composition. This suggests a problem of loss of catalyst, rather than an activity loss of the catalyst itself. Perhaps the samples with high support content have poor interaction with the electrode, thus losing catalyst particles over time. This process could be accelerated by convection during heating between experiments at different temperatures.

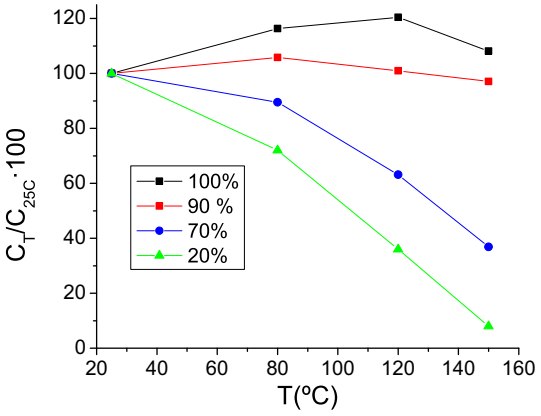

Fig. 17 – Evolution of capacitance with temperature for some samples, in 85% H_3PO_4. Scan rate 20 mV/s.

4. Conclusions

Catalysts composed of IrO_2 on a SiC–Si support were prepared using the Adams fusion method. The physicochemical characterisation of the obtained supported catalysts showed the influence of the support in the formation of the IrO_2 particles. Powder conductivity measurements indicate a very low conductivity of the support, with the contact between IrO_2 particles being an important factor in current conduction through the sample.

The electrochemical activity of IrO_2 was found to be improved in the presence of the support. The activity of 80 wt.% and 90 wt.% samples was found to be higher than that of unsupported catalyst. This was attributed to the improved surface properties of IrO_2 in the presence of the support, rather than to a better conductivity or surface area of the support itself, which possesses rather poor properties compared to IrO_2.

Based on the above results, the SiC–Si compound is a potential candidate as a support for an anode electrocatalyst for phosphoric acid doped membrane steam electrolysers.

Acknowledgements

The work was supported by Center for renewable hydrogen cycling (HyCycle), Denmark, contract No. 2104-07-0041 and WELTEMP project under EU Seventh Framework Programme (FP7), grant agreement No. 212903.

Appendix. Supplementary data

Supplementary data associated with this article can be found in online version at doi:10.1016/j.ijhydene.2011.02.050.

REFERENCES

[1] Marshall A, Børresen B, Hagen G, Tsypkin M, Tunold R. Hydrogen production by advanced proton exchange membrane (PEM) water electrolysers-reduced energy consumption by improved electrocatalysis. Energy 2007a;32:431–6.
[2] Zhang Y, Zhang H, Ma Y, Cheng J, Zhong H, Song S, et al. A novel bifunctional electrocatalyst for unitized regenerative fuel cell. Journal of Power Sources 2009;195:142–5.
[3] Millet P, Ngameni R, Grigoriev S. PEM water electrolyszers: from electrocatalysis to stack development. International Journal of Hydrogen Energy 2009;35:5043–52.
[4] Grigoriev S, Millet P, Volobuev S, Fateev V. Optimization of porous current collectors for PEM water electrolysers. International Journal of Hydrogen Energy 2009a;34(11): 4968–73.

[5] Li Q, Jensen JO, Savinell RF, Bjerrum NJ. High temperature proton exchange membranes based on polybenzimidazoles for fuel cells. Progress in Polymer Science 2009;34(5):449–77.
[6] Jensen JO, Li QF, Pan C, Vestbo AP, Mortensen K, Petersen HN, et al. High temperature PEMFC and the possible utilization of the excess heat for fuel processing. International Journal of Hydrogen Energy 2007;32(10–11):1567–71. doi:10.1016/j.ijhydene.2006.10.034.
[7] Song S, Zhang H, Ma X, Shao Z, Baker RT, Yi B. Electrochemical investigation of electrocatalysts for the oxygen evolution reaction in PEM water electrolyzers. International Journal of Hydrogen Energy 2008;33:4955–61. doi:10.1016/j.ijhydene.2008.06.039.
[8] Beer H. Electrode coated with a platinum-metal oxide and method of operating it. Patent NL 6606302 A. 1966.
[9] Beer H. Electrode and coating therefor. US Patent 3,632,498. 1972.
[10] Beer H. Electrode having platinum metal oxide coating thereon, and method of use thereof. US Patent 3,711,385. 1973.
[11] Grigoriev S, Millet P, Korobtsev S, Porembskiy V, Pepic M, Etievant C, et al. Hydrogen safety aspects related to high-pressure polymer electrolyte membrane water electrolysis. International Journal of Hydrogen Energy 2009b;34(14):5986–91.
[12] Nikiforov A, Petrushina I, Christensen E, Tomás-García A, Bjerrum N. Corrosion behaviour of construction materials for high temperature steam electrolysers. International Journal of Hydrogen Energy 2011;36(1):111–9. doi:10.1016/j.ijhydene.2010.09.023.
[13] International patent application, 03.01.2008, WO 2008/002150 A1, PCT/NO2007/000235. 03.01.2008.
[14] Pourbaix M. Atlas d'equilibres electrochimiques. Paris: Gauthier-Villars; 1963.
[15] Loucka T. Reason for the loss of activity of titanium anodes coated with a layer of RuO_2 and TiO_2. Journal of Applied Electrochemistry 1977;7:211–4.
[16] Kötz R, Neff H, Stucki S. Anodic iridium oxide films, XPS-studies of oxidation state changes and O_2-evolution. Journal of the Electrochemical Society 1984;131:72–7.
[17] Gatineau J, Yanagita K, Dussarrat C. A new RuO_4 solvent solution for pure ruthenium film depositions. Microelectronic Engineering 2006;83(11–12):2248–52. doi:10.1016/j.mee.2006.10.013.
[18] Kötz R, Stucki S. Stabilization of RuO_2 by IrO_2 for anodic oxygen evolution in acid media. Electrochimica Acta 1986;31(10):1311–6. doi:10.1016/0013-4686(86)80153-0.
[19] Mattos-Costa FI, de Lima-Neto P, Machado SAS, Avaca LA. Characterisation of surfaces modified by sol-gel derived $Ru_xIr_{(1-x)}O_2$ coatings for oxygen evolution in acid medium. Electrochimica Acta 1998;44:1515–23.
[20] Millet P., Mbemba N., Grigoriev S., Fateev V., Aukauloo A., Etiévant C. Electrochemical performances of PEM water electrolysis cells and perspectives. International Journal of Hydrogen Energy 2010;In Press, Corrected Proof. doi:10.1016/j.ijhydene.2010.06.105.
[21] Marshall AT, Sunde S, Tsypkin M, Tunold R. Performance of a PEM water electrolysis cell using $Ir_xRu_yTa_zO_2$ electrocatalysts for the oxygen evolution electrode. International Journal of Hydrogen Energy 2007b;32:2320–4.
[22] Marshall A, Børresen B, Hagen G, Tsypkin M, Tunold R. Electrochemical characterisation of $Ir_xSn_{1-x}O_2$ powders as oxygen evolution electrocatalysts. Electrochimica Acta 2006;51:3161–7.
[23] Cheng J, Zhang H, Ma H, Zhong H, Zou Y. Preparation of $Ir_{0.4}Ru_{0.6}Mo_xO_y$ for oxygen evolution by modified Adams' fusion method. International Journal of Hydrogen Energy 2009;34(16):6609–13. doi:10.1016/j.ijhydene.2009.06.061.
[24] Roen LM, Paik CH, Jarvic TD. Electrocatalytic corrosion of carbon support in PEMFC cathodes. Electrochemical and Solid State Letters 2004;7(1):A19–22. 10.1149/1.1630412.
[25] Antolini E, Gonzalez E. Ceramic materials as supports for low-temperature fuel cell catalysts. Solid State Ionics 2009;180(9–10):746–63. 10.1016/j.ssi.2009.03.007.
[26] Trasatti S. Physical electrochemistry of ceramic oxides. Electrochimica Acta 1991;36(2):225–41.
[27] Ouattara L, Diaco T, Duo I, Panizza M, Foti G, Comninellis C. Dimensionally stable anode-type anode based on conductive p-silicon substrate. Journal of the Electrochemical Society 2003;150(2):D41–5.
[28] Kumar PV, Gupta GS. Study of formation of silicon carbide in the Acheson process. Steel Research 2002;73(2):31–8.
[29] Richerson DW. Modern ceramic engineering. Properties, processing, and use in design. 3rd ed. Taylor & Francis Group, LLC; 2006.
[30] Divakar R, Seshadri SG, Srinivasan M. Electrochemical techniques for corrosion rate determination in ceramics. Journal of the American Ceramic Society 1989;72(5):780–4.
[31] Honji A, Mori T, Hishinuma Y, Kurita K. Platinum supported on silicon-carbide as fuel-cell electrocatalyst. Journal of the Electrochemical Society 1988;135(4):917–8.
[32] Rao CV, Singh SK, Viswanathan B. Electrochemical performance of nano-SiC prepared in thermal plasma. Indian Journal of Chemistry Section A-inorganic Bio-inorganic Physical Theoretical & Analytical Chemistry 2008;47(11):1619–25.
[33] Ma L, Sui S, Zhai Y. Preparation and characterization of Ir/TiC catalyst for oxygen evolution. Journal of Power Sources 2008;177(2):470–7. 10.1016/j.jpowsour.2007.11.106.
[34] Adams R, Shriner RL. Platinum oxide as a catalyst in the reduction of organic compounds. III. preparation and properties of the oxide of platinum obtained by the fusion of ceiloroplatinic acid with sodium nitrate. Journal of the American Chemical Society 1923;45:2171–9.
[35] Robin A, Rosa JL. Corrosion behavior of niobium, tantalum and their alloys in hot hydrochloric and phosphoric acid solutions. International Journal of Refractory Metals and Hard Materials 2000;18:13–21.
[36] Patterson AL. The Scherrer formula for X-ray particle size determination. Physical Review 1939;56(10):978–82. doi:10.1103/PhysRev.56.978.
[37] Marshall A, Børresen B, Hagen G, Tsypkin M, Tunold R. Preparation and characterisation of nanocrystalline $Ir_xSn_{1-x}O_2$ electrocatalytic powders. Materials Chemistry and Physics 2005;94:226–32.
[38] Celzard A, Mareche JF, Payot F, Furdin G. Electrical conductivity of carbonaceous powders. Carbon 2002;40(15):2801–15.

Bibliography

[1] http://hycycle.dk/. Hycycle. center for renewable hydrogen cycling, June 2009. URL http://hycycle.dk/.

[2] http://www.weltemp.eu/. Weltemp. URL http://www.weltemp.eu/.

[3] Smog over new york in 1988. source: Wikipedia.org. URL http://en.wikipedia.org/wiki/File:SmogNY.jpg.

[4] http://nanopedia.case.edu/. Hydrogen fuel economy. URL http://nanopedia.case.edu/NWPrint.php?page=nano.hydrogen.economy.

[5] J.O. Jensen, V. Bandur, N.J. Bjerrum, S.J. Højgaard, S.D. Ebbesen, and M. Mogensen. Pre-investigation of water electrolysis. Technical report, 2008. URL http://130.226.56.153/rispubl/NEI/NEI-DK-5057.pdf.

[6] Allen J. Bard and Faulkner Larry R. *Electrochemical methods Fundamentals and applications*. John Wiley & Sons Inc, 2nd edition, 2001.

[7] Sergio Trasatti. Work function, electronegativity, and electrochemical behaviour of metals: Iii. electrolytic hydrogen evolution in acid solutions. *Journal of Electroanalytical Chemistry and Interfacial Electrochemistry*, 39(1):163 – 184, 1972. ISSN 0022-0728. doi: 10.1016/S0022-0728(72)80485-6.

[8] L.D. Burke. *Oxide growth and oxygen evolution on noble metals*, volume Electrodes of conductive metallic oxides. Part A. Elsevier Scientific, 335 Jan van Galenstraat P.O. Box 211, 1000 AE Amsterdam, The Netherlands, 1980.

[9] D Pletcher, R. Greff, R. Peat, L. M. Peter, and J. Robinson. *Instrumental methods in electrochemistry*. Horwood Publishing, 1985.

[10] S. Trasatti. *Electrodes of conductive metallic oxides*. Studies in physical and theoretical chemistry. Elsevier, 335 Jan van Galenstraat P.O. Box 211, 1000 AE Amsterdam, The Netherlands, 1980.

[11] S. Trasatti. Electrocatalysis in the anodic evolution of oxygen and chlorine. *Electrochimica Acta*, 29(11):1503–1512, 1984. ISSN 0013-4686. doi: 10.1016/0013-4686(84)85004-5.

[12] Annual book of astm standarts 10.05, g3-89, p. 42-47.

[13] Peter J. Goodhew, John Humphreys, and Richard Beanland. *Electron Microscopy and analysis*. Taylor & Francis, third edition, 2001.

[14] S. Trasatti. Physical electrochemistry of ceramic oxides. *Electrochimica Acta*, 36(2):225–241, 1991. ISSN 0013-4686. doi: 10.1016/0013-4686(91)85244-2.

[15] James Larminie and Andrew Dicks. *Fuel Cell Systems Explained*. John Wiley & Sons Ltd, England, second edition, 2003. URL http://www.knovel.com.globalproxy.cvt.dk/web/portal/browse/display?_EXT_KNOVEL_DISPLAY_bookid=1109&VerticalID=0.

[16] Sheng Sui, Lirong Ma, and Yuchun Zhai. Investigation on the proton exchange membrane water electrolyzer using supported anode catalyst. *Asia-Pacific Journal of Chemical Engineering*, 4(1):8–11, 2009. ISSN 19322135. doi: 10.1002/apj.183.

[17] R. Kötz and S. Stucki. Stabilization of RuO_2 by IrO_2 for anodic oxygen evolution in acid media. *Electrochimica Acta*, 31(10):1311–1316, 1986. ISSN 0013-4686. doi: 10.1016/0013-4686(86)80153-0.

[18] Planetary engineering group earth. URL http://www.pege.org/. May 6, 2007.

[19] URL http://www.protonenergy.com.

[20] Qingfeng Li, Jens Oluf Jensen, Robert F. Savinell, and Niels J. Bjerrum. High temperature proton exchange membranes based on polybenzimidazoles for fuel cells. *Progress in Polymer Science*, 34(5):449–477, 2009. ISSN 00796700. doi: 10.1016/j.progpolymsci.2008.12.003.

[21] http://www.radiometer analytical.com/. URL http://www.radiometer-analytical.com/.

[22] Allen J. Bard and Larry R. Faulkner. *Electrochemical Methods. Fundamentals and Applications*. John Wiley & Sons Inc, 1980.

[23] Mustafa Balat. Potential importance of hydrogen as a future solution to environmental and transportation problems. *International Journal of Hydrogen Energy*, 33(15):4013–4029, 2008. ISSN 03603199. doi: 10.1016/j.ijhydene.2008.05.047.

[24] A. Heinzel, B. Vogel, and P. Hübner. Reforming of natural gas–hydrogen generation for small scale stationary fuel cell systems. *Journal of Power Sources*, 105(2):202 – 207, 2002. ISSN 0378-7753. doi: 10.1016/S0378-7753(01)00940-5.

[25] O. Ulleberg, T. Nakken, and A. Ete. The wind/hydrogen demonstration system at Utsira in Norway: Evaluation of system performance using operational data and updated hydrogen energy system modeling tools. *International Journal of Hydrogen Energy*, 35(5):1841–1852, March 2010. doi: 10.1016/j.ijhydene.2009.10.077.

[26] Z Yumurtaci. Hydrogen production from excess power in small hydroelectric installations. *International Journal of Hydrogen Energy*, 29(7): 687–693, 2004. ISSN 03603199. doi: 10.1016/j.ijhydene.2003.08.012.

[27] C Koroneos. Life cycle assessment of hydrogen fuel production processes. *International Journal of Hydrogen Energy*, 29(14):1443–1450, 2004. ISSN 03603199. doi: 10.1016/j.ijhydene.2004.01.016.

[28] John Turner, George Sverdrup, Margaret K. Mann, Pin-Ching Maness, Ben Kroposki, Maria Ghirardi, Robert J. Evans, and Dan Blake. Renewable hydrogen production. *International Journal of Energy Research*, 32(5):379–407, 2008. ISSN 0363907X. doi: 10.1002/er.1372.

[29] Fischer M. Oberlin R. Status of the membral process for water electrolysis. *Hydrogen energy progress VI, proceedings of the sixth world hydrogen energy conference, Oxford: Pergamon Press*, pages 333–40, 1986.

[30] Frano Barbir. PEM electrolysis for production of hydrogen from renewable energy sources. *Solar Energy*, 78(5):661–669, 2005. ISSN 0038092x. doi: 10.1016/j.solener.2004.09.003.

[31] S.A. Grigoriev, V.I. Porembsky, and V.N. Fateev. Pure hydrogen production by PEM electrolysis for hydrogen energy. *International Journal of Hydrogen Energy*, 31(2):171–175, 2006. ISSN 03603199. doi: 10.1016/j.ijhydene.2005.04.038.

[32] A. Nikiforov, D. Aili, M.K. Hansen, I. Petrushina, E. Christensen, J.O. Jensen, Q. Li, and N.J. Bjerrum. Water electrolysis at elevated temperatures. In *Hydrogen + Fuel Cells 2009 conference, poster presentation*, Vancouver, Canada, May 31st - June 3rd 2009.

[33] I.M. Petrushina, A.V. Nikiforov, and N.J. Bjerrum. Corrosion behavior of highly austenitic stainless steels and ni-based alloys at elevated temperatures in concentrated phosphoric acid solutions. In *ICHMS'2009, 11th International Confrence, abstract, oral presentation*, pages 162–163, Yalta-Crimia-Ukraine, August 25th-31st 2009.

[34] N.J. Bjerrum, I.M. Petrushina, V. Bandur, and A.V. Nikiforov. Water electrolysis at elevated temperatures. In *ICHMS'2009, 11th International Confrence, abstract, oral presentation*, pages 842–843, Yalta-Crimia-Ukraine, August 25th-31st 2009.

[35] A.V. Nikiforov, I.M. Petrushina, E. Christensen, N.J. Bjerrum, and A.L. Tomás-García. Corrosion behaviour of construction materials for high temperature water electrolysers. In *NMES'2010, 8th International Symposium, abstract, oral presentarion*, pages 16–17, Shanghai, China, July 11-15th 2010.

[36] A.V. Nikiforov, I.M. Petrushina, E. Christensen, A. L. Tomás-García, and N.J Bjerrum. Corrosion behaviour of construction materials for high temperature steam electrolysers. *International Journal of Hydrogen Energy*, 36(1):111–119, January 2011. ISSN 0360-3199. doi: 10.1016/j.ijhydene.2010.09.023.

[37] A.V. Nikiforov, I.M. Petrushina, E. Christensen, A.L. Tomás-García, and N.J. Bjerrum. Development of catalyst support for oxygen electrode for PEM steam electrolysers. In *2nd CARISMA international conference on progress in MEA materials for medium and high temperature polymer electrolyte fuel cells, abstract, poster presentation*, page 69, La Grande Motte, France, September 19th-22nd 2010.

[38] A. V. Nikiforov, A. L. Tomás-García, I. M. Petrushina, E. Christensen, and N. J. Bjerrum. Preparation and study of IrO_2/SiC-Si supported anode catalyst for high temperature PEM steam electrolysers. *International Journal of Hydrogen Energy*, 36(10):5797–5805, May 2011. ISSN 0360-3199. doi: 10.1016/j.ijhydene.2011.02.050.

[39] A. L. Tomás-García, A.V. Nikiforov, I.M. Petrushina, E. Christensen, and N.J Bjerrum. SiC-Si as a support material for oxygen evolution electrode in PEM steam electrolysers. In *Hydrogen + Fuel Cells 2011 conference, abstract contribution*, Vancouver, Canada, May, 15th - 18th 2011.

[40] A. V. Nikiforov, A. L. Tomás-García, I. M. Petrushina, E. Christensen, and N. J. Bjerrum. SiC-Si as a support material for oxygen evolution electrode in PEM steam electrolysers. In *9th European Symposium on Electrochemical Engineering (9th ESEE), abstract, oral presentation*, page 83, Chania, Crete, Greece, June 19th - 23rd 2011.

[41] Kai Zeng and Dongke Zhang. Recent progress in alkaline water electrolysis for hydrogen production and applications. *Progress in Energy and Combustion Science*, 36(3):307 – 326, 2010. ISSN 0360-1285. doi: 10.1016/j.pecs.2009.11.002.

[42] Risø National Laboratory. Risøenergy report 3. hydrogen and its competitors. Technical report, 2004. URL http://www.risoe.dtu.dk/Risoe_dk/Home/Knowledge_base/publications/Reports/ris-r-1469.aspx.

[43] B. E. Conway and G. Jerkiewicz. Relation of energies and coverages of underpotential and overpotential deposited h at pt and other metals to the [']volcano curve' for cathodic h2 evolution kinetics. *Electrochimica Acta*, 45(25-26):4075 – 4083, 2000. ISSN 0013-4686. doi: 10.1016/S0013-4686(00)00523-5.

[44] J. O. Jensen, Q. F. Li, C. Pan, A. P. Vestbo, K. Mortensen, H. N. Petersen, C. L. Sorensen, T. N. Clausen, J. Schramm, and N. J. Bjerrum. High temperature PEMFC and the possible utilization of the excess heat for fuel processing. *International Journal of Hydrogen Energy*, 32 (10-11):1567–1571, July 2007. doi: 10.1016/j.ijhydene.2006.10.034.

[45] Hideaki Kita, Shen Ye, Akiko Aramata, and Nagakazu Furuya. Adsorption of hydrogen on platinum single crystal electrodes in acid and alkali solutions. *Journal of Electroanalytical Chemistry and Interfacial Electrochemistry*, 295(1-2):317–331, 1990. ISSN 0022-0728. doi: 10.1016/0022-0728(90)85025-Z.

[46] S. Trasatti. *Electrochemical Hydrogen Technologies*, chapter Electrode kinetics and electrocatalysis of hydrogen and oxygen electrode reactions. Elsevier, Amsterdam, 1990.

[47] S. Trasatti. *Electrodes of conductive metallic oxides*. Studies in physical and theoretical chemistry. Elsevier, 335 Jan van Galenstraat P.O. Box 211, 1000 AE Amsterdam, The Netherlands, 1980.

[48] D.Ohms, V.Plzak, S.Trasatti, K.Wiesener, and H.Wendt. *Electrochemical hydrogen technologies*. Elsivier Amsterdam, p.1, 1990.

[49] G. Sanddstede. *Elektrochemische Stoffgewinnung-Grundlagen und Verfahrenstechnik*, volume 125 of *DECHEMA-Monographien*. DECHEMA, Frankfurt am Main, 1992.

[50] R. Kötz and S. Stucki. Oxygen evolution and corrosion on ruthenium-iridium alloys. *Journal of the Electrochemical Society*, 132:103–107, 1985. ISSN 00134651. doi: 10.1149/1.2113735.

[51] A. Marshall, B. Børresen, G. Hagen, M. Tsypkin, and R. Tunold. Electrochemical characterisation of $Ir_xSn_{1-x}O_2$ powders as oxygen evolution electrocatalysts. *Electrochimica Acta*, 51:3161–3167, 2006. ISSN 00134686. doi: 10.1016/j.electacta.2005.09.004.

[52] C.P. De Pauli and S. Trasatti. Composite materials for electrocatalysis of o2 evolution: IrO_2+SnO_2 in acid solution. *Journal of Electroanalytical Chemistry*, 538-539:145–151, 2002. ISSN 1572-6657. doi: 10.1016/S0022-0728(02)01055-0.

[53] J. O. Bockris. Kinetics of activation controlled consecutive electrochemical reactions - anodic evolution of oxygen. *Journal of Chemical Physics*, 24(4):817–827, 1956. doi: 10.1063/1.1742616.

[54] B. E. Conway and M. Salomon. Electrochemical reaction orders: Applications to the hydrogen- and oxygen-evolution reactions. *Electrochimica Acta*, 9(12):1599 – 1615, 1964. ISSN 0013-4686. doi: 10.1016/0013-4686(64)80088-8.

[55] Shidong Song, Huamin Zhang, Xiaoping Ma, Zhigang Shao, Richard T. Baker, and Baolian Yi. Electrochemical investigation of electrocatalysts for the oxygen evolution reaction in PEM water electrolyzers. *International Journal of Hydrogen Energy*, 33:4955–4961, 2008. ISSN 03603199. doi: 10.1016/j.ijhydene.2008.06.039.

[56] S. Trasatti. *Electrochemical Hydrogen technologies*, chapter The oxygen evolution reaction, pages 104–135. Elsevier, 1990.

[57] P. Rasiyah and A. C. C. Tseung. The role of the lower metal oxide/higher metal oxide couple in oxygen evolution reactions. *Journal of The Electrochemical Society*, 131(4):803–808, 1984. doi: 10.1149/1.2115703.

[58] R. Kötz, H. Neff, and S. Stucki. Anodic iridium oxide films, XPS-studies of oxidation state changes and O_2-evolution. *Journal of the Electrochemical Society*, 131:72–77, 1984. ISSN 00134651. doi: 10.1149/1.2115548.

[59] V.A. Alves, L.A. da Silva, J.F.C. Boodts, and S. Trasatti. Kinetics and mechanism of oxygen evolution on IrO_2-based electrodes containing ti and ce acidic solutions. *Electrochimica Acta*, 39(11-12):1585 – 1589, 1994. ISSN 0013-4686. doi: 10.1016/0013-4686(94)85139-5.

[60] D. CUKMAN, M. VUKOVIC, and M. MILUN. Enhanced oxygen evolution on an electrodeposited ruthenium+iridium coating on titanium. *Journal of Electroanalytical Chemistry*, 389(1-2):209–213, June 1995. doi: 10.1016/0022-0728(95)03873-F.

[61] S.Trasatti and G.Logi. *Electrodes of Conductive Metallic Oxides Part B*, chapter Oxygen and chlorine evolution reactions on conductive metallic oxide anodes, page 521. Elsevier, 335 Jan van Galenstraat P.O. Box 211, 1000 AE Amsterdam, The Netherlands, 1980.

[62] A.C. Riddiford. Mechanisms for the evolution and ionization of oxygen at platinum electrodes. *Electrochimica Acta*, 4(2-4):170 – 178, 1961. ISSN 0013-4686. doi: 10.1016/0013-4686(61)80015-7. An International Journal of Pure and Applied Electrochemistry published by Pergamon Press Ltd. under the auspices of the International Committee for Electrochemical Thermodynamics and Kinetics.

[63] A. Damjanovic, A. Dey, and J.O'M. Bockris. Kinetics of oxygen evolution and dissolution on platinum electrodes. *Electrochimica Acta*, 11(7):791 – 814, 1966. ISSN 0013-4686. doi: 10.1016/0013-4686(66)87056-1.

[64] Krasil'shchikov. *Zh. Fiz. Khim.*, 37:531, 1963.

[65] S. Gottesfeld and S. Srinivasan. Electrochemical and optical studies of thick oxide layers on iridium and their electrocatalytic activities for the oxygen evolution reaction. *Journal of Electroanalytical Chemistry and Interfacial Electrochemistry*, 86(1):89–104, 1978. ISSN 0022-0728. doi: 10.1016/S0022-0728(78)80358-1.

[66] Jian-shu Lu. Corrosion of titanium in phosphoric acid at 250 °C. *Transactions of Nonferrous Metals Society of China*, 19:552–556, 2009. ISSN 10036326. doi: 10.1016/S1003-6326(08)60311-8.

[67] M Benabdellah and B Hammouti. Corrosion behaviour of steel in concentrated phosphoric acid solutions. *Applied Surface Science*, 252 (5):1657–1661, 2005. ISSN 01694332. doi: 10.1016/j.apsusc.2005.03.191.

[68] T. A. Lukashenko and K. I. Tikhonov. Corrosion resistance of a series of group IV-VI transition metal carbides and nitrides in concentrated solutions of sulfuric and phosphoric acids. *Zhurnal Prikladnoi Khimii (Sankt-Peterburg)*, 71(12):2017–2020, 1998. ISSN 0044-4618.

[69] A Mitsuhashi, K Asami, A Kawashima, and K Hashimoto. The corrosion behavior of amorphous nickel base alloys in a hot concentrated phosphoric acid. *Corrosion Science*, 27(9):957–970, 1987. ISSN 0010938X. doi: 10.1016/0010-938X(87)90062-X.

[70] Alain Robin and Jorge Luiz Rosa. Corrosion behavior of niobium, tantalum and their alloys in hot hydrochloric and phosphoric acid solutions. *International Journal of Refractory Metals and Hard Materials*, 18:13–21, 2000. ISSN 02634368. doi: 10.1016/S0263-4368(99)00034-7.

[71] Ramesh Divakar, Srinvasa G. Seshadri, and Makuteswara Srinivasan. Electrochemical techniques for corrosion rate determination in ceramics. *Journal of the American Ceramic Society*, 72(5):780–784, 1989. ISSN 00027820. doi: 10.1111/j.1151-2916.1989.tb06217.x.

[72] Kenneth R Trethewey and John Chamberlain. *Corrosion*. Longman Group UK Limited, 1988.

[73] Annual book of astm standarts 10.05, g 102-89 (reapproved 1999), p. 446-452.

[74] www.crystallography.net. Crystallography open database. URL http://www.crystallography.net/.

[75] A. L. Patterson. The Scherrer formula for X-ray particle size determination. *Physical Review*, 56(10):978–982, Nov 1939. doi: 10.1103/PhysRev.56.978.

[76] H. M. Rietveld. Line profiles of neutron powder-diffraction peaks for structure refinement. *Acta Crystallographica*, 22(1):151–152, Jan 1967. doi: 10.1107/S0365110X67000234.

[77] H. P. Klug and L. E. Alexander. *X-ray Diffraction Procedures for Polycrystalline and Amorphous Materials*. Wiley, New York, 2nd edition, 1974.

[78] John S. Watson. Fast, simple method of powder pellet preparation for x-ray fluorescence analysis. *X-Ray Spectrometry*, 25(4): 173–174, 1996. doi: 10.1002/(SICI)1097-4539(199607)25:4<173::AID-XRS158>3.0.CO;2-Z.

[79] Ajit Jillavenkatesa, Stanley J. Dapkunas, and Lin-Sien H. Lum. Particle size characterisation, January 2001. The National Institute of Standards and Technology.

[80] H.B. Beer. Electrode coated with a platinum-metal oxide and method of operating it. Patent NL 6606302 A, 1966.

[81] Y. Matsumoto and E. Sato. Electrocatalytic properties of transition metal oxides for oxygen evolution reaction. *Materials Chemistry and Physics*, 14(5):397–426, 1986. ISSN 0254-0584. doi: 10.1016/0254-0584(86)90045-3.

[82] J. Honig. *Electrodes of conductive metallic oxides*, chapter Electronic band structure of oxides with metallic of semiconducting characteristics., pages 1–96. Elsevier s, 335 Jan van Galenstraat P.O. Box 211, 1000 AE Amsterdam, The Netherlands, 1980.

[83] Donald B. Rogers, Robert D. Shannon, Arthur W. Sleight, and Joseph L. Gillson. Crystal chemistry of metal dioxides with rutile-related structures. *Inorganic Chemistry*, 8(4):841–849, 1969. doi: 10.1021/ic50074a029.

[84] S. Trasatti and G. Logi. *Electrodes of conductive metallic oxides*, chapter Properties of conductive transition metal oxides with rutile-type structure., pages 301–358. Elsevier, 335 Jan van Galenstraat P.O. Box 211, 1000 AE Amsterdam, The Netherlands, 1980.

[85] George Blyholder. Metal-support interaction: A theoretical approach. *Journal of Molecular Catalysis A: Chemical*, 119(1-3):11 – 17, 1997. ISSN 1381-1169. doi: 10.1016/S1381-1169(96)00465-7. International Conference on Theoretical Aspects of Heterogeneous Catalysis.

[86] M. J. Ledoux and C. Pham-Huu. Silicon carbide - a novel catalyst support for heterogeneous catalysis. *Cattech*, 5(4):226–246, 2001. doi: 10.1023/A:1014092930183.

[87] S.A. Grigoriev, P. Millet, S.A. Volobuev, and V.N. Fateev. Optimization of porous current collectors for PEM water electrolysers. *International Journal of Hydrogen Energy*, 34(11):4968–4973, 2009. ISSN 03603199. doi: 10.1016/j.ijhydene.2008.11.056.

[88] O. E. Haas, S. T. Briskeby, O. E. Kongstein, M. Tsypkin, R. Tunold, and B. T. Borresen. Synthesis and characterisation of $Ru_xTi_{x-1}O_2$ as a catalyst support for polymer electrolyte fuel cell. *Journal of New Materials For Electrochemical Systems*, 11(1):9–14, January 2008.

[89] K. E. Swider, C. I. Merzbacher, P. L. Hagans, and D. R. Rolison. Synthesis of ruthenium dioxide titanium dioxide aerogels: Redistribution of electrical properties on the nanoscale. *Chemistry of Materials*, 9(5): 1248–1255, May 1997. doi: 10.1021/cm960622c.

[90] B.E. Conway. *Electrochemical supercapacitors*. Kluwer Academic, New York, USA, 1999.

[91] S. Ardizzone, A. Carugati, and S. Trasatti. Properties of thermally prepared iridium dioxide electrodes. *Journal of Electroanalitical chemistry*, 126:287–292, 1981. doi: 10.1016/S0022-0728(81)80437-8.

[92] A. Deoliveirasousa, M. Dasilva, S. Machado, L. Avaca, and P. Delimaneto. Influence of the preparation method on the morphological and electrochemical properties of Ti/IrO_2-coated electrodes. *Electrochimica Acta*, 45(27):4467–4473, 2000. ISSN 00134686. doi: 10.1016/S0013-4686(00)00508-9.

[93] L. A. Da Silva, V. A. Alves, S. Trasatti, and J. F. C. Boodts. Surface and electrocatalytic properties of ternary oxides $Ir_{0.3}Ti_{0.7-x}Pt_xO_2$ oxygen evolution from acidic solution. *Journal of Electroanalytical Chemistry*, 427:97–104, 1997. ISSN 00220728. doi: 10.1016/S0022-0728(97)83088-4.

[94] D. Michell, D.A.J. Rand, and R. Woods. A study of ruthenium electrodes by cyclic voltammetry and x-ray emission spectroscopy. *Journal of Electroanalytical Chemistry and Interfacial Electrochemistry*, 89(1): 11 – 27, 1978. ISSN 0022-0728. doi: 10.1016/S0022-0728(78)80027-8.

[95] Guohua Chen, Xueming Chen, and Po Lock Yue. Electrochemical behavior of novel Ti/IrO_x-Sb_2O_5-SnO_2 anodes. *The Journal of Physical Chemistry B*, 106(17):4364–4369, 2002. ISSN 1520-6106. doi: 10.1021/jp013547o.

[96] Ten-Chin Wen and Chi-Chang Hu. Hydrogen and oxygen evolutions on Ru-Ir binary oxides. *Journal of The Electrochemical Society*, 139 (8):2158–2163, 1992. doi: 10.1149/1.2221195.

[97] H. B. Suffredini, J. L. Cerne, F. C. Crnkovic, S. A. S. Machado, and L. A. Avaca. Recent developments in electrode materials for water electrolysis. *International Journal of Hydrogen Energy*, 25(5):415–423, May 2000. doi: 10.1016/S0360-3199(99)00049-X.

[98] Weikang Hu, Xuejun Cao, Fupeng Wang, and Yunshi Zhang. A novel cathode for alkaline water electrolysis. *International Journal of Hydrogen Energy*, 22(6):621 – 623, 1997. ISSN 0360-3199. doi: 10.1016/S0360-3199(96)00191-7.

[99] N. A. Abdel Ghany, N. Kumagai, S. Meguro, K. Asami, and K. Hashimoto. Oxygen evolution anodes composed of anodically deposited mn-mo-fe oxides for seawater electrolysis. *Electrochimica Acta*, 48(1):21 – 28, 2002. ISSN 0013-4686. doi: 10.1016/S0013-4686(02)00539-X.

[100] Guoying Chen, Simon R. Bare, and Thomas E. Mallouk. Development of supported bifunctional electrocatalysts for unitized regenerative fuel cells. *Journal of The Electrochemical Society*, 149(8):A1092–A1099, 2002. ISSN 00134651. doi: 10.1149/1.1491237.

[101] H. Y. Jung, S. Park, P. Ganesan, and B. N. Popov. Electrochemical studies of unsupported PtIr electrocatalyst as bifunctional oxygen electrode in unitized regenerative fuel cell (urfc). *Proton Exchange Membrane Fuel Cells 8, Pts 1 and 2*, 16(2):1117–1121, 2008. doi: 10.1016/j.jpowsour.2009.02.060.

[102] S. D. Song, H. M. Zhang, X. P. Ma, Z. G. Shao, Y. N. Zhang, and B. L. Yi. Bifunctional oxygen electrode with corrosion-resistive gas diffusion layer for unitized regenerative fuel cell. *Electrochemistry Communications*, 8(3):399–405, Mar 2006. ISSN 1388-2481. Electrochemistry Communications.

[103] Larry L. Swette, Anthony B. LaConti, and Stephen A. McCatty. Proton-exchange membrane regenerative fuel cells. *Journal of Power Sources*, 47(3):343–351, 1994. ISSN 03787753. doi: 10.1016/0378-7753(94)87013-6.

[104] Tsutomu Oi and Yoshinori Sakaki. Optimum hydrogen generation capacity and current density of the pem-type water electrolyzer operated only during the off-peak period of electricity demand. *Journal of Power Sources*, 129(2):229 – 237, 2004. ISSN 0378-7753. doi: 10.1016/j.jpowsour.2003.11.050.

[105] C. A. Linkous, H. R. Anderson, R. W. Kopitzke, and G. L. Nelson. Development of new proton exchange membrane electrolytes for water electrolysis at higher temperatures. *International Journal of Hydrogen Energy*, 23(7):525–529, 1998. ISSN 03603199. doi: 10.1016/S0360-3199(97)00113-4.

[106] C.A. Linkous. Development of solid polymer electrolytes for water electrolysis at intermediate temperatures. *International Journal of Hydrogen Energy*, 18(8):641–646, 1993. ISSN 03603199. doi: 10.1016/0360-3199(93)90116-R.

[107] Paul A. Lessing. Materials for hydrogen generation via water electrolysis. *Journal of Materials Science*, 42(10):3477–3487, 2007. ISSN 00222461. doi: 10.1007/s10853-006-0398-8.

[108] V. Antonucci, A. Di Blasi, V. Baglio, R. Ornelas, F. Matteucci, J. Ledesma-Garcia, L. G. Arriaga, and A. S. Arico. High temperature operation of a composite membrane-based solid polymer electrolyte water electrolyser. *Electrochimica Acta*, 53(24):7350–7356, October 2008. doi: 10.1016/j.electacta.2008.04.009.

[109] F. Andolfatto, R. Durand, A. Michas, P. Millet, and P. Stevens. Solid polymer electrolyte water electrolysis: electrocatalysis and long-term stability. *International Journal of Hydrogen Energy*, 19(5):421 – 427, 1994. ISSN 0360-3199. doi: 10.1016/0360-3199(94)90018-3.

[110] Mikimasa Yamaguchi, Kayoko Okisawa, and Takahiro Nakanori. Development of high performance solid polymer electrolyte water electrolyzer in WE-NET. *Proceedings of the Intersociety Energy Conver-*

sion Engineering Conference, 3-4:1958–1961, 1997. ISSN 0146955x. doi: 10.1109/IECEC.1997.656726.

[111] Yining Zhang, Huamin Zhang, Yuanwei Ma, Jinbin Cheng, Hexiang Zhong, Shidong Song, and Haipeng Ma. A novel bifunctional electrocatalyst for unitized regenerative fuel cell. *Journal of Power Sources*, 195:142–145, 2009. ISSN 03787753. doi: 10.1016/j.jpowsour.2009.07.018.

[112] P Millet, R Ngameni, and S.A. Grigoriev. PEM water electrolyszers: From electrocatalysis to stack development. *International Journal of Hydrogen Energy*, 35:5043 – 5052, 2009. doi: 10.1016/j.ijhydene.2009.09.015.

[113] James F. McElroy. Recent advances in SPE® water electrolyzer. *Journal of Power Sources*, 47(3):369–375, 1994. ISSN 0378-7753. doi: 10.1016/0378-7753(94)87015-2. Proceedings of the Fourth Space Electrochemical Research and Technology Conference.

[114] Fateev VN. Pahomov, VP. Electrolysis of water with solid polymer electrolyte. Technical report, RRC "Kurchatov Institute", 1990.

[115] J. Pettersson, B. Ramsey, and D. Harrison. A review of the latest developments in electrodes for unitised regenerative polymer electrolyte fuel cells. *Journal of Power Sources*, 157(1):28–34, 2006. ISSN 03787753. doi: 10.1016/j.jpowsour.2006.01.059.

[116] T. Ioroi, N. Kitazawa, K. Yasuda, Y. Yamamoto, and H. Takenaka. Iro2-deposited pt electrocatalysts for unitized regenerative polymer electrolyte fuel cells. *Journal of Applied Electrochemistry*, 31:1179–1183, 2001. ISSN 0021-891X. doi: 10.1023/A:1012755809488.

[117] Monjid Hamdan. Low cost, high pressure hydrogen generator, June 2008. URL http://www.hydrogen.energy.gov/pdfs/review08/pd_10_hamden.pdf.

[118] Cecelia Cropley and Timothy Norman. A low-cost high-pressure hydrogen generator, April 2008. URL http://www.osti.gov/bridge/servlets/purl/926321-lTUJnC/926321.pdf.

[119] Monjid Hamdan. PEM electrolyzer incorporating an advanced low-cost membrane, 2010. URL http://www.hydrogen.energy.gov/pdfs/progress10/ii_e_2_hamdan.pdf.

[120] A Marshall, B Børresen, G Hagen, M Tsypkin, and R Tunold. Hydrogen production by advanced proton exchange membrane (PEM) water

electrolysers-reduced energy consumption by improved electrocatalysis. *Energy*, 32:431–436, 2007. ISSN 03605442. doi: 10.1016/j.energy.2006.07.014.

[121] E. Slavcheva, I. Radev, S. Bliznakov, G. Topalov, P. Andreev, and E. Budevski. Sputtered iridium oxide films as electrocatalysts for water splitting via PEM electrolysis. *Electrochimica Acta*, 52(12):3889–3894, March 2007. doi: 10.1016/j.electacta.2006.11.005.

[122] R. A. Antunes, M. C. L. Oliveira, G. Ett, and V. Ett. Corrosion of metal bipolar plates for PEM fuel cells: A review. *International Journal of Hydrogen Energy*, 35(8):3632–3647, April 2010. doi: 10.1016/j.ijhydene.2010.01.059.

[123] H. Tawfik, Y. Hung, and D. Mahajan. Metal bipolar plates for PEM fuel cell-A review. *Journal of Power Sources*, 163(2):755–767, 2007. ISSN 03787753. doi: 10.1016/j.jpowsour.2006.09.088.

[124] Allen Hermann, Tapas Chaudhuri, and Priscila Spagnol. Bipolar plates for PEM fuel cells: A review. *International Journal of Hydrogen Energy*, 30(12):1297–1302, 2005. ISSN 03603199. doi: 10.1016/j.ijhydene.2005.04.016.

[125] URL http://www.ginerinc.com/.

[126] URL http://www.hydrogenics.com/.

[127] Egil Rasten, Georg Hagen, and Reidar Tunold. Electrocatalysis in water electrolysis with solid polymer electrolyte. *Electrochimica Acta*, 48:3945–3952, 2003. ISSN 00134686. doi: 10.1016/j.electacta.2003.04.001.

[128] Y. Tanaka, S. Uchinashi, Y. Saihara, K. Kikuchi, T. Okaya, and Z. Ogumi. Dissolution of hydrogen and the ratio of the dissolved hydrogen content to the produced hydrogen in electrolyzed water using spe water electrolyzer. *Electrochimica Acta*, 48(27):4013–4019, 2003. doi: 10.1016/S0013-4686(03)00541-3.

[129] C. Mitsugi, A. Harumi, and F. Kenzo. WE-NET: Japanese hydrogen program. *International Journal of Hydrogen Energy*, 23(3):159–165, 1998. doi: 10.1016/S0360-3199(97)00042-6.

[130] S. Siracusano, V. Baglio, C. D'Urso, V. Antonucci, and A.S. Aricà. Preparation and characterization of titanium suboxides as conductive supports of IrO_2 electrocatalysts for application in spe electrolysers. *Electrochimica Acta*, 54(26):6292–6299, 2009. ISSN 00134686. doi: 10.1016/j.electacta.2009.05.094.

[131] S. Siracusano, V. Baglio, A. Di Blasi, N. Briguglio, A. Stassi, R. Ornelas, E. Trifoni, V. Antonucci, and A.S. Aricò. Electrochemical characterization of single cell and short stack PEM electrolyzers based on a nanosized IrO_2 anode electrocatalyst. *International Journal of Hydrogen Energy*, 35(11):5558 – 5568, 2010. ISSN 0360-3199. doi: 10.1016/j.ijhydene.2010.03.102. 3rd Argentinean and 2nd Latin American Congress inHydrogen and Sustainable Energy Sources, 3rd Argentinean and 2nd Latin American Congress in Hydrogen and Sustainable Energy Sources.

[132] Lirong Ma, Sheng Sui, and Yuchun Zhai. Investigations on high performance proton exchange membrane water electrolyzer. *International Journal of Hydrogen Energy*, 34:678–684, 2009. ISSN 03603199. doi: 10.1016/j.ijhydene.2008.11.022.

[133] Pierre Millet, Diana Dragoe, Serguey Grigoriev, Vladimir Fateev, and Claude Etievant. GenHyPEM: A research program on PEM water electrolysis supported by the european commission. *International Journal of Hydrogen Energy*, 34(11):4974–4982, 2009. ISSN 03603199. doi: 10.1016/j.ijhydene.2008.11.114.

[134] P. Millet, N. Mbemba, S.A. Grigoriev, V.N. Fateev, A. Aukauloo, and C. Etiévant. Electrochemical performances of PEM water electrolysis cells and perspectives. *International Journal of Hydrogen Energy*, In Press, Corrected Proof, 2010. ISSN 0360-3199. doi: 10.1016/j.ijhydene.2010.06.105.

[135] Y Shin, W Park, J Chang, and J Park. Evaluation of the high temperature electrolysis of steam to produce hydrogen. *International Journal of Hydrogen Energy*, 32(10-11):1486–1491, 2007. ISSN 03603199. doi: 10.1016/j.ijhydene.2006.10.028.

[136] M Ni, M Leung, and D Leung. Energy and exergy analysis of hydrogen production by solid oxide steam electrolyzer plant. *International Journal of Hydrogen Energy*, 32(18):4648–4660, 2007. ISSN 03603199. doi: 10.1016/j.ijhydene.2007.08.005.

[137] Q. F. Li, R. H. He, J. O. Jensen, and N. J. Bjerrum. Approaches and recent development of polymer electrolyte membranes for fuel cells operating above 100 degrees C. *Chemistry of Materials*, 15(26):4896–4915, December 2003. doi: 10.1021/cm0310519.

[138] A. Daghetti, G. Lodi, and S. Trasatti. Interfacial properties of oxides used as anodes in the electrochemical technology. *Materials Chemistry and Physics*, 8:1–90, 1983. ISSN 02540584. doi: 10.1016/0254-0584(83)90020-2.

[139] S. Dutta. Technology assessment of advanced electrolytic hydrogen production. *International Journal of Hydrogen Energy*, 15(6):379–386, 1990. ISSN 03603199. doi: 10.1016/0360-3199(90)90194-4.

[140] Wolf Vielstich Carl W. Hamann, Andrew Hamnelt. *Electrochemistry*. Wiley-VHC, second edition, 1997.

[141] Yue Hung, K. M. EL-Khatib, and Hazem Tawfik. Corrosion-resistant lightweight metallic bipolar plates for PEM fuel cells. *Journal of Applied Electrochemistry*, 35(5):445–447, 2005. ISSN 0021891x. doi: 10.1007/s10800-004-8350-6.

[142] Robert C. Makkus, Arno H.H. Janssen, Frank A. de Bruijn, and Ronald K.A.M. Mallant. Use of stainless steel for cost competitive bipolar plates in the SPFC. *Journal of Power Sources*, 86(1-2):274–282, 2000. ISSN 03787753. doi: 10.1016/S0378-7753(99)00460-7.

[143] S. Joseph, J. C. McClure, R. Chianelli, P. Pich, and P. J. Sebastian. Conducting polymer-coated stainless steel bipolar plates for proton exchange membrane fuel cells (PEMFC). *International Journal of Hydrogen Energy*, 30(12):1339–1344, September 2005. doi: 10.1016/j.ijhydene.2005.04.011.

[144] R. J. Tian, J. C. Sun, and L. Wang. Plasma-nitrided austenitic stainless steel 316L as bipolar plate for PEMFC. *International Journal of Hydrogen Energy*, 31(13):1874–1878, October 2006. doi: 10.1016/j.ijhydene.2006.03.003.

[145] Y. Wang and D. O. Northwood. An investigation of the electrochemical properties of PVD TiN-coated SS410 in simulated PEM fuel cell environments. *International Journal of Hydrogen Energy*, 32(7):895–902, May 2007. doi: 10.1016/j.ijhydene.2007.02.006.

[146] A. Di Blasi, C. D'Urso, V. Baglio, V. Antonucci, A. S. Arico', R. Ornelas, F. Matteucci, G. Orozco, D. Beltran, Y. Meas, and L. G. Arriaga. Preparation and evaluation of RuO_2 -IrO_2, IrO_2-Pt and IrO_2-Ta_2O_5 catalysts for the oxygen evolution reaction in an SPE electrolyzer. *Journal of Applied Electrochemistry*, 39(2):191–196, 2009. ISSN 0021891x. doi: 10.1007/s10800-008-9651-y.

[147] D. Labou, E. Slavcheva, U. Schnakenberg, and S. Neophytides. Performance of laboratory polymer electrolyte membrane hydrogen generator with sputtered iridium oxide anode. *Journal of Power Sources*, 185 (2):1073–1078, 2008. ISSN 03787753. doi: 10.1016/j.jpowsour.2008.08.013.

[148] Ronghuan He, Qingfeng Li, Gang Xiao, and Niels J. Bjerrum. Proton conductivity of phosphoric acid doped polybenzimidazole and its composites with inorganic proton conductors. *Journal of Membrane Science*, 226(1-2):169–184, 2003. ISSN 03767388. doi: 10.1016/j.memsci.2003.09.002.

[149] S.A. Grigoriev, P. Millet, S.V. Korobtsev, V.I. Porembskiy, M. Pepic, C. Etievant, C. Puyenchet, and V.N. Fateev. Hydrogen safety aspects related to high-pressure polymer electrolyte membrane water electrolysis. *International Journal of Hydrogen Energy*, 34(14):5986–5991, 2009. ISSN 03603199. doi: 10.1016/j.ijhydene.2009.01.047.

[150] J. Onoro. Corrosion fatigue behaviour of 317LN austenitic stainless steel in phosphoric acid. *International Journal of Pressure Vessels and Piping*, 86(10):656–660, 2009. ISSN 03080161. doi: 10.1016/j.ijpvp.2009.06.001.

[151] M. Rockel. *Corrosion behaviour of nickel alloys and high-alloy stainless steel*. Nickel Alloys. Marcel Dekker Inc, New York, 1998.

[152] Gerhard I.Kreysa and Reiner Eckermann. *DECHEMA corrosion handbook: corrosive agents and their interaction with materials*, volume 12. Chlorinated hydrocarbons-chloroethanes, phosphoric acid. VCH Verlagsgesellschaft, Weinheim (Germany) and VCH Publishers, New York, NY (USA), 1993.

[153] International patent application, 03.01.2008, WO 2008/002150 A1, PCT/NO2007/000235, 03.01.2008.

[154] M. Keijzer, K. Hemmes, P. J. J. M. VanDerPut, J. H. W. DeWit, and J. Schoonman. A search for suitable coating materials on separator plates for molten carbonate fuel cells. *Corrosion Science*, 39(3):483–494, March 1997. doi: 10.1016/S0010-938X(96)00137-0.

[155] F. Cardarelli, P. Taxil, A. Savall, Ch. Comninellis, G. Manoli, and O. Leclerc. Preparation of oxygen evolving electrodes with long service life under extreme conditions. *Journal of Applied Electrochemistry*, 28 (3):245–250, 1998. ISSN 0021891x. doi: 10.1023/A:1003251329958.

[156] M.Bengisu. *Engineering Ceramics*. Springer-Verlag Berlin Heidelberg 2001, 1963.

[157] URL http://www.tantaline.com/.

[158] M Ni, M Leung, and D Leung. Technological development of hydrogen production by solid oxide electrolyzer cell (SOEC). *International Journal of Hydrogen Energy*, 33(9):2337–2354, 2008. ISSN 03603199. doi: 10.1016/j.ijhydene.2008.02.048.

[159] Anne Hauch, Sune Dalgaard Ebbesen, Søren Højgaard Jensen, and Mogens Mogensen. Highly efficient high temperature electrolysis. *Journal of Materials Chemistry*, 18(20):2331, 2008. ISSN 0959-9428. doi: 10.1039/b718822f.

[160] M. H. Miles, E. A. Klaus, B. P. Gunn, J. R. Locker, W. E. Serafin, and S. Srinivasan. The oxygen evolution reaction on platinum, iridium, ruthenium and their alloys at 80 °C in acid solutions. *Electrochimica Acta*, 23(6):521 – 526, 1978. ISSN 0013-4686. doi: 10.1016/0013-4686(78)85030-0.

[161] R. Hutchings, K. Mueller, R. Koetz, and S. Stucki. Structural investigation of stabilized oxygen evolution catalysts. *Journal of Materials Science*, 19:3987–3994, 1984. ISSN 00222461. doi: 10.1007/BF00980762.

[162] T. Medhoui, E. Anxolabehere, and A. Aukauloo P. Millet P. Biomimetic approaches for the development of non-noble metal electrocatalysts. application to pem water electrolysis. In *Proceedings of the 16th World Hydrogen Energy conference*, number 390, pages 1–9, Lyon, 13–16, june 2006 .

[163] Chiaki Iwakura, Kazuhiro Hirao, and Hideo Tamura. Anodic evolution of oxygen on ruthenium in acidic solutions. *Electrochimica Acta*, 22(4):329–334, 1977. ISSN 0013-4686. doi: 10.1016/0013-4686(77)85082-2.

[164] Ailton J. Terezo and Ernesto C. Pereira. Preparation and characterisation of Ti/RuO_2 anodes obtained by sol-gel and conventional routes. *Materials Letters*, 53(4-5):339–345, 2002. ISSN 0167-577X. doi: 10.1016/S0167-577X(01)00504-3.

[165] G. Lodi, C. Deasmundis, S. Ardizzone, E. Sivieri, and S. Trasatti. Resistivity and temperature-coefficient of resistivity of ruthenium oxide layers influence of morphology. *Surface Technology*, 14(4):335–343, 1981. ISSN 0376-4583. doi: 10.1016/0376-4583(81)90039-X.

[166] M. Vukovic. Oxygen evolution on an electrodeposited ruthenium electrode in acid solution–the effect of thermal treatment. *Electrochimica Acta*, 34(2):287 – 291, 1989. ISSN 0013-4686. doi: 10.1016/0013-4686(89)87099-9.

[167] Hongchao Ma, Changpeng Liu, Jianhui Liao, Yi Su, Xingzhong Xue, and Wei Xing. Study of ruthenium oxide catalyst for electrocatalytic performance in oxygen evolution. *Journal of Molecular Catalysis A: Chemical*, 247(1-2):7–13, 2006. ISSN 1381-1169. doi: 10.1016/j.molcata.2005.11.013.

[168] M.Pourbaix. *Atlas d'equilibres electrochimiques*. Gauthier-Villars, Paris, 1963.

[169] T. Loucka. The reason for the loss of activity of titanium anodes coated with a layer of RuO_2 and TiO_2. *Journal of Applied Electrochemistry*, 7:211–214, 1977. ISSN 0021891x. doi: 10.1007/BF00618987.

[170] Y. Koda. Boiling points and ideal solutions of ruthenium and osmium tetraoxides. *Journal of the Chemical Society-chemical Communications*, (17):1347–1348, September 1986. doi: 10.1039/C39860001347.

[171] Julien Gatineau, Kazutaka Yanagita, and Christian Dussarrat. A new RuO_4 solvent solution for pure ruthenium film depositions. *Microelectronic Engineering*, 83(11-12):2248 – 2252, 2006. ISSN 0167-9317. doi: 10.1016/j.mee.2006.10.013.

[172] F. I. Mattos-Costa, P. de Lima-Neto, S. A. S. Machado, and L. A. Avaca. Characterisation of surfaces modified by sol-gel derived $Ru_xIr_{(1-x)}O_2$ coatings for oxygen evolution in acid medium. *Electrochimica Acta*, 44:1515–1523, 1998. ISSN 00134686. doi: 10.1016/S0013-4686(98)00275-8.

[173] Y. Zhang, C. Wang, N. Wan, and Z. Mao. Deposited RuO2-IrO2/Pt electrocatalyst for the regenerative fuel cell. *International Journal of Hydrogen Energy*, 32(3):400–404, 2007. ISSN 03603199. doi: 10.1016/j.ijhydene.2006.06.047.

[174] Gabriele Centi and Siglinda Perathoner. The role of nanostructure in improving the performance of electrodes for energy storage and conversion. *European Journal of Inorganic Chemistry*, 2009(26):3851–3878, 2009. ISSN 14341948. doi: 10.1002/ejic.200900275.

[175] A. Marshall, B. Børresen, G. Hagen, S. Sunde, M. Tsypkin, and R. Tunold. Iridium oxide-based nanocrystalline particles as oxygen evolution electrocatalysts. *Russian Journal of Electrochemistry*, 42: 1134–1140, 2006. ISSN 10231935. doi: 10.1134/S1023193506100223.

[176] A. T. Marshall, S. Sunde, M. Tsypkin, and R. Tunold. Performance of a PEM water electrolysis cell using $Ir_xRu_yTa_zO_2$ electrocatalysts for the oxygen evolution electrode. *International Journal of Hydrogen Energy*, 32:2320–2324, 2007. ISSN 03603199. doi: 10.1016/j.ijhydene.2007.02.013.

[177] Aaron T. Marshall and Richard G. Haverkamp. Electrocatalytic activity of IrO_2–RuO_2 supported on Sb-doped SnO_2 nanoparticles. *Electrochimica Acta*, 55(6):1978–1984, 2010. ISSN 00134686. doi: 10.1016/j.electacta.2009.11.018.

[178] Jinbin Cheng, Huamin Zhang, Haipeng Ma, Hexiang Zhong, and Yi Zou. Preparation of $Ir_{0.4}Ru_{0.6}Mo_xO_y$ for oxygen evolution by modified Adams' fusion method. *International Journal of Hydrogen Energy*, 34(16):6609 – 6613, 2009. ISSN 0360-3199. doi: 10.1016/j.ijhydene.2009.06.061.

[179] R. Bertoncello. Preparation of anodes for oxygen evolution by electrodeposition of composite oxides of Pb and Ru on Ti. *Journal of Electroanalytical Chemistry*, 492(2):145–149, 2000. ISSN 00220728. doi: 10.1016/S0022-0728(00)00300-4.

[180] R. Adams and R. L. Shriner. Platinum oxide as a catalyst in the reduction of organic compounds. III. Preparation and properties of the oxide of platinum obtained by the fusion of ceiloroplatinic acid with sodium nitrate. *Journal of the American Chemical Society*, 45: 2171–2179, Jul 1923. ISSN 0002-7863. doi: 10.1021/ja01662a022.

[181] A. Marshall, B. Børresen, G. Hagen, M. Tsypkin, and R. Tunold. Preparation and characterisation of nanocrystalline $Ir_xSn_{1-x}O_2$ electrocatalytic powders. *Materials Chemistry and Physics*, 94:226–232, 2005. ISSN 02540584. doi: 10.1016/j.matchemphys.2005.04.039.

[182] F. Bonet, V. Delmas, S. Grugeon, R. Herrera Urbina, P. Y. Silvert, and K. Tekaia-Elhsissen. Synthesis of monodisperse Au, Pt, Pd, Ru and Ir nanoparticles in ethylene glycol. *Nanostructured Materials*, 11:1277–1284, 1999. ISSN 09659773. doi: 10.1016/S0965-9773(99)00419-5.

[183] H. C. BROWN and C. A. BROWN. A new convenient technique for hydrogenation of unsaturated compounds. *Journal of the American Chemical Society*, 84(8):1495, 1962. doi: 10.1021/ja00867a036.

[184] Silvia Ardizzone, Giuseppe Cappelletti, Mariana Ionita, Alessandro Minguzzi, Sandra Rondinini, and Alberto Vertova. Low-temperature sol-gel nanocrystalline tin oxide. *Electrochimica Acta*, 50:4419–4425, 2005. ISSN 00134686. doi: 10.1016/j.electacta.2005.02.005.

[185] S. Ardizzone, C. L. Bianchi, L. Borgese, G. Cappelletti, C. Locatelli, A. Minguzzi, S. Rondinini, A. Vertova, P. C. Ricci, C. Cannas, and A. Musinu. Physico-chemical characterization of IrO_2-SnO_2 sol-gel nanopowders for electrochemical applications. *Journal of Applied Electrochemistry*, 39(11):2093–2105, November 2009. doi: 10.1007/s10800-009-9895-1.

[186] R. Cote, G. Lalande, D. Guay, J. P. Dodelet, and G. Denes. Iridium and ruthenium based electrocatalysts for oxygen reduction in polymer electrolyte fuel cells. In *2nd International Symposium on New Materials for Fuel Cell and Modern Battery Systems*, pages 743–755,

MONTREAL CANADA, July 06–10 1997. Ecole Polytechnique Montreal.

[187] M Yagi, E Tomita, and T Kuwabara. Remarkably high activity of electrodeposited IrO_2 film for electrocatalytic water oxidation. *Journal of Electroanalytical Chemistry*, 579(1):83–88, 2005. ISSN 00220728. doi: 10.1016/j.jelechem.2005.01.030.

[188] E. N. El Sawy and V. I. Birss. Nano-porous iridium and iridium oxide thin films formed by high efficiency electrodeposition. *Journal of Materials Chemistry*, 19(43):8244–8252, 2009. doi: 10.1039/b914662h.

[189] Kim Kinoshita. Electrochemical uses of carbon. Electrochemistry Encyclopedia. URL http://electrochem.cwru.edu/encycl/art-c01-carbon.htm.

[190] H.B. Beer. Electrode and coating therefor. US Patent 3,632,498, 1972.

[191] H.B. Beer. Electrode having platinum metal oxide coating thereon, and method of use thereof. US Patent 3,711,385, 1973.

[192] F. Hine, M.Yasuda, and T.Yoshida. Studies on oxide-coated metal anodes for chlor-alkali cells. *Journal of the Electrochemical Society*, 124(4):500–505, 1977. doi: 10.1149/1.2133337.

[193] X. M. Chen and G. H. Chen. Investigation of Ti/IrO_2-Sb_2O_5-SnO_2 electrodes for O_2 evolution. *Journal of the Electrochemical Society*, 152(7):J59–J64, 2005. doi: 10.1149/1.1922890.

[194] Chiaki Iwakura. Effect of active layer composition on the service life of (SnO_2 and RuO_2)-coated Ti electrodes in sulfuric acid solution. *Journal of The Electrochemical Society*, 132(10):2420, 1985. ISSN 00134651. doi: 10.1149/1.2113590.

[195] R. S. Yeo, J.Orehotsky, W. Visscher, and S. Srinivasan. Ruthenium-based mixed oxides as electrocatalysts for oxygen evolution in acid electrolytes. *Journal of the Electrochemical Society*, 128(9):1900–1904, 1981. doi: 10.1149/1.2127761.

[196] E. N. Balko and P. H. Nguyen. Iridium-tin mixed oxide anode coatings. *Journal of Applied Electrochemistry*, 21:678–682, 1991. ISSN 0021-891X. doi: 10.1007/BF01034045.

[197] B. Correa-Lozano, Ch. Comninellis, and A. De Battisti. Service life of Ti/SnO_2-Sb_2O_5 anodes. *Journal of Applied Electrochemistry*, 27: 970–974, 1997. ISSN 0021-891X. doi: 10.1023/A:1018414005000.

[198] Josimar Ribeiro and Adalgisa R. de Andrade. Investigation of the electrical properties, charging process, and passivation of RuO_2–Ta_2O_5 oxide films. *Journal of Electroanalytical Chemistry*, 592:153–162, 2006. ISSN 00220728. doi: 10.1016/j.jelechem.2006.05.004.

[199] Y. E. Roginskaya, O. V. Morozova, E.N. Loubnin, A.V. Popov, Y.I. Ulitina, V. V.Zhurov, S.A. Ivanov, and S. Trasatti. X-ray diffraction, transmission electron-microscopy and x-ray photoelectron spectroscopic characterization of IrO_2+Ta_2O_5 films. *Journal of the Chemical Society-faraday Transactions*, 89(11):1707–1715, June 1993. doi: 10.1039/FT9938901707.

[200] J Hu. Oxygen evolution reaction on IrO_2-based DSA® type electrodes: kinetics analysis of tafel lines and EIS. *International Journal of Hydrogen Energy*, 29(8):791–797, 2004. ISSN 03603199. doi: 10.1016/j.ijhydene.2003.09.007.

[201] A De Battisti, R. Brina, G. Gavelli, A. Benedetti, and G. Fagherazzi. Influence of the valve metal oxide on the properties of ruthenium based mixed oxide electrodes: Part I. Titanium supported RuO_2/Ta_2O_5 layers. *Journal of Electroanalytical Chemistry and Interfacial Electrochemistry*, 200(1-2):93 – 104, 1986. ISSN 0022-0728. doi: 10.1016/0022-0728(86)90048-3.

[202] Ch. Comninellis and G. P. Vercesi. Characterization of DSA®-type oxygen evolving electrodes: Choice of a coating. *Journal of Applied Electrochemistry*, 21:136–142, 1991. ISSN 0021-891X. doi: 10.1007/BF01020219.

[203] G.P. Vercesi, J. Rolewicz, Ch. Comninellis, and J. Hinder. Characterization of DSA-type oxygen evolving electrodes. choice of base metal. *Thermochimica Acta*, 176:31 – 47, 1991. ISSN 0040-6031. doi: 10.1016/0040-6031(91)80257-J.

[204] C Angelinetta, S Trasatti, L Atanasoska, Z Minevski, and R Atanasoski. Effect of preparation on the surface and electrocatalytic properties of RuO_2 + IrO_2 mixed oxide electrodes. *Materials Chemistry and Physics*, 22:231–247, 1989. ISSN 02540584. doi: 10.1016/0254-0584(89)90039-4.

[205] C. Comninnellis and G.P. Vercesi. Problems in DSA coating deposition by thermal-decomposition. *Journal of Applied Electrochemistry*, 21(2): 136–142, February 1991. doi: 10.1007/BF01464294.

[206] A. J. Terezo and E. C. Pereira. Preparation and characterization of Ti/RuO_2-Nb_2O_5 electrodes obtained by polymeric precur-

sor method. *Electrochimica Acta*, 44(25):4507–4513, 1999. doi: 10.1016/S0013-4686(99)00182-6.

[207] Alfredo Ursúa, Luis Marroyo, Eugenio Gubía, Luis M. Gandía, Pedro M. Diéguez, and Pablo Sanchis. Influence of the power supply on the energy efficiency of an alkaline water electrolyser. *International Journal of Hydrogen Energy*, 34(8):3221–3233, 2009. ISSN 0360-3199. doi: 10.1016/j.ijhydene.2009.02.017.

[208] J. D. Holladay, J. Hu, D. L. King, and Y. Wang. An overview of hydrogen production technologies. *Catalysis Today*, 139(4):244–260, January 2009. doi: 10.1016/j.cattod.2008.08.039.

[209] D.J. Connolly, Longwood, and W.F. Gresham. Fluorocarbon vinyl ether polymers, 1966.

[210] L. G. Lage, P. G. Delgado, and Y. Kawano. Thermal stability and decomposition of Nafion® membranes with different cations using high-resolution thermogravimetry. *Journal of Thermal Analysis and Calorimetry*, 75(2):521–530, 2004. doi: 10.1023/B:JTAN.0000027142.21928.c7.

[211] Der-Tau Chin and Howard H. Chang. On the conductivity of phosphoric acid electrolyte. *Journal of Applied Electrochemistry*, 19(1):95–99, 1989. ISSN 0021-891X. doi: 10.1007/BF01039396.

[212] A. Appleby and C. Vandrunen. The oxygen evolution reaction on rhodium and iridium electrodes in 85% orthophosphoric acid. *Journal of Electroanalytical Chemistry*, 60(1):101–108, 1975. ISSN 00220728. doi: 10.1016/S0022-0728(75)80207-5.

[213] Guoqiang Wei, Li Xu, Chengde Huang, and Yuxin Wang. SPE water electrolysis with SPEEK/PES blend membrane. *International Journal of Hydrogen Energy*, 35(15):7778 – 7783, 2010. ISSN 0360-3199. doi: 10.1016/j.ijhydene.2010.05.041. The 10th Chinese Hydrogen Energy Conference.

[214] Haiqiu Zhang, Xianfeng Li, Chengji Zhao, Tiezhu Fu, Yuhua Shi, and Hui Na. Composite membranes based on highly sulfonated PEEK and PBI: Morphology characteristics and performance. *Journal of Membrane Science*, 308(1-2):66–74, 2008. ISSN 0376-7388. doi: DOI: 10.1016/j.memsci.2007.09.045.

[215] B. Li, A. Lin, and F. Gan. Preparation and electrocatalytic properties of $Ti/IrO_2-Ta_2O_5$ anodes for oxygen evolution. *Transactions of Nonferrous Metals Society of China*, 16(5):1193–1199, 2006. ISSN 10036326. doi: 10.1016/S1003-6326(06)60400-7.

[216] E. Antolini and E.R. Gonzalez. Ceramic materials as supports for low-temperature fuel cell catalysts. *Solid State Ionics*, 180(9-10):746 – 763, 2009. ISSN 0167-2738. doi: 10.1016/j.ssi.2009.03.007.

[217] Milan M. Jaksic. Hypo-hyper-d-electronic interactive nature of synergism in catalysis and electrocatalysis for hydrogen reactions. *Electrochimica Acta*, 45(25-26):4085 – 4099, 2000. ISSN 0013-4686. doi: 10.1016/S0013-4686(00)00525-9.

[218] L. Vracar, N. Krstajic, V. Radmilovic, and M. Jaksic. Electrocatalysis by nanoparticles – oxygen reduction on Ebonex/Pt electrode. *Journal of Electroanalytical Chemistry*, 587(1):99–107, 2006. ISSN 00220728. doi: 10.1016/j.jelechem.2005.10.021.

[219] H. R. Colon-Mercado and B. N. Popov. Stability of platinum based alloy cathode catalysts in PEM fuel cells. *Journal of Power Sources*, 155(2):253–263, April 2006. doi: 10.1016/j.jpowsour.2005.05.011.

[220] L. M. Roen, C. H. Paik, and T. D. Jarvic. Electrocatalytic corrosion of carbon support in PEMFC cathodes. *Electrochemical and Solid State Letters*, 7(1):A19–A22, January 2004. doi: 10.1149/1.1630412.

[221] Kazuaki Yasuda, Akira Taniguchi, Tomoki Akita, Tsutomu Ioroi, and Zyun Siroma. Platinum dissolution and deposition in the polymer electrolyte membrane of a PEM fuel cell as studied by potential cycling. *Physical Chemistry Chemical Physics*, 8(6):746, 2006. ISSN 1463-9076. doi: 10.1039/b514342j.

[222] Lirong Ma, Sheng Sui, and Yuchun Zhai. Preparation and characterization of Ir/TiC catalyst for oxygen evolution. *Journal of Power Sources*, 177(2):470–477, 2008. ISSN 03787753. doi: 10.1016/j.jpowsour.2007.11.106.

[223] N. C. Halder. Electron-tunneling and hopping possibilites in RuO_2 thick-films. *Electrocomponent Science and Technology*, 11(1):21–34, 1983. doi: 10.1155/APEC.11.21.

[224] A. Szpytma and A. Kusy. On the segregation of the conductive phase in RuO_2-based thick resistive films. *Thin Solid Films*, 121(4):263–270, 1984. doi: 10.1016/0040-6090(84)90054-3.

[225] L. Ouattara, T. Diaco, I. Duo, M. Panizza, G. Foti, and C. Comninellis. Dimensionally stable anode-type anode based on conductive p-silicon substrate. *Journal of the Electrochemical Society*, 150(2):D41–5, 2003. ISSN 00134651. doi: 10.1149/1.1537756.

[226] Alan D. McLeod, Jean-Marc Lihrmann, John S. Haggerty, and Donald R. Sadoway. Selection and testing of inert anode materials for hall cells. *Light Metals: Proceedings of Sessions, AIME Annual Meeting (Warrendale, Pennsylvania)*, pages 357–365, 1987. ISSN 0873390601.

[227] Halvor Kvande. Inert electrodes in aluminum electrolysis cells. *Light Metals: Proceedings of Sessions, TMS Annual Meeting (Warrendale, Pennsylvania)*, pages 369–376, 1999. ISSN 10969586.

[228] W. T. Grubb and D. W. Mckee. Boron carbide, a new substrate for fuel cell electrocatalysts. *Nature*, 210(5032):192–194, 1966. ISSN 0028-0836. doi: 10.1038/210192b0.

[229] A. Honji, T. Mori, Y. Hishinuma, and K. Kurita. Platinum supported on silicon-carbide as fuel-cell electrocatalysts. *Journal of the Electrochemical Society*, 135(4):917–918, April 1988. doi: 10.1149/1.2095831.

[230] C. V. Rao, S. K. Singh, and B. Viswanathan. Electrochemical performance of nano-SiC prepared in thermal plasma. *Indian Journal of Chemistry Section A-inorganic Bio-inorganic Physical Theoretical & Analytical Chemistry*, 47(11):1619–1625, November 2008.

[231] P. V. Kumar and G. S. Gupta. Study of formation of silicon carbide in the Acheson process. *Steel Research*, 73(2):31–38, February 2002.

[232] J Riviere, J Delafond, P Misaelides, and F Noli. Corrosion protection of an AISI 321 stainless steel by SiC coatings. *Surface and Coatings Technology*, 100-101:243–246, 1998. ISSN 02578972. doi: 10.1016/S0257-8972(97)00622-1.

[233] David W. Richerson. *Modern ceramic engineering. Properties, processing, and use in design.* Taylor & Francis Group, LLC, third edition, 2006.

[234] Annual book of astm standarts 10.05, g5-94, p. 60-70.

[235] M. Pourbaix, L. Klimzack-Mathieiu, Ch. Mertens, J. Meunier, Cl. Vanleugenhaghe, L. de Munck, J. Laureys, L. Neelemans, and M. Warzee. Potentiokinetic and corrosimetric investigations of the corrosion behaviour of alloy steels. *Corrosion Science*, 3(4):239–259, 1963. ISSN 0010-938X. doi: 10.1016/S0010-938X(63)80030-X.

[236] M. Kouřil, E. Christensen, S. Eriksen, and B. Gillesberg. Corrosion rate of construction materials in hot phosphoric acid with the contribution of anodic polarization. *Materials and Corrosion*, 2011. ISSN 1521-4176. doi: 10.1002/maco.201006021.

[237] W.Z.Friend. *Corrosion of Nickel and Nickel-Base Alloys*. J.Wiley&Sons, New York-Chichester-Brisbane-Toronto, 1980.

[238] Yu. I. Bil'chugov, N. L. Makarova, and A. A. Nazarov. On limit of molybdenum content of pitting-corrosion-resistant austenitic steels. *Protection of Metals*, 37(6):597–601, 2001. ISSN 00331732. doi: 10.1023/A:1012879916686.

[239] Asphahani et. al. United states patent 4846885, 1989.

[240] A. Celzard, J. F. Mareche, F. Payot, and G. Furdin. Electrical conductivity of carbonaceous powders. *Carbon*, 40(15):2801–2815, 2002. doi: 10.1016/S0008-6223(02)00196-3.

[241] J. Kim, H. Kim, T. Lim, and H. Lee. Dependence of the performance of a high-temperature polymer electrolyte fuel cell on phosphoric acid-doped polybenzimidazole ionomer content in cathode catalyst layer. *Journal of Power Sources*, 170(2):275–280, 2007. ISSN 03787753. doi: 10.1016/j.jpowsour.2007.03.082.

Appendix A

Rietveld Treatment of the XRD Data for the SiC-Si Powder Catalyst Support

The Rietveld refinement of the XRD data of the SiC-Si support is presented in Figure A.1 and detailed parameters of the data treatment can be found below:

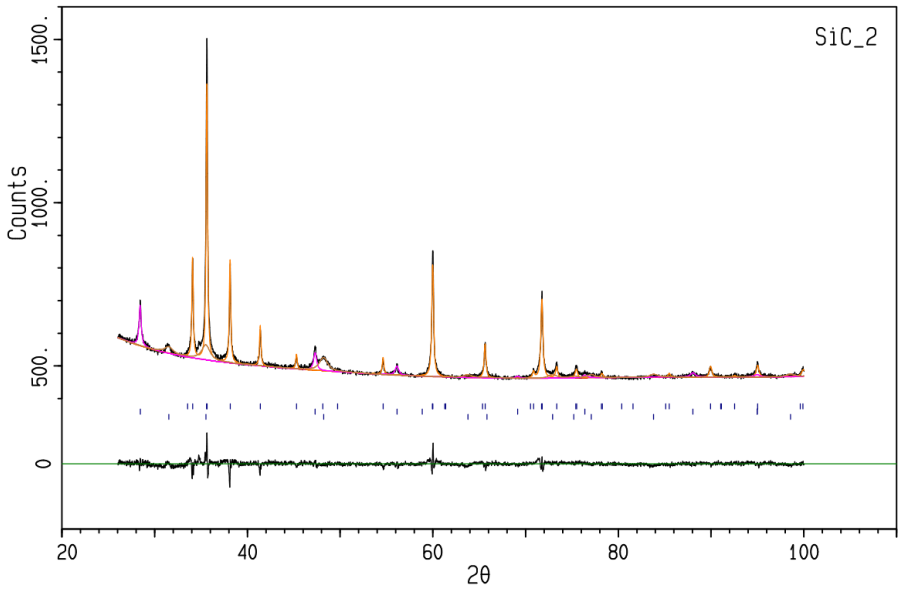

Figure A.1: Rietveld fitting for the XRD data for SiC-Si support.

Rp = 0.81 Rwp = 1.17 GOF = 0.27 22 parameters, 3700 observations

Parameter file : SiC_2.par
Raw data file : SiC_2.gdf

Wavelength(s) : 1.540510 A
Monochromator polarisation factor : 0.900000
Guinier tangent angle : 45.000000
Profile function : pseudo-Voigt
No. of halfwidths in peak : 50.000000
Two-theta range : 26.039690 - 100.019700 deg.
in steps of : 0.020000 deg.

Anomalous dispersion corrections :

C	0.018100	0.009100
Si	0.254100	0.330200
W	-5.473300	5.577400

Phase no. 1: SiC

RB = 1.22 37 Bragg reflections

Space group : P 63 M C

Unit cell:
3.080703(0.000208) 3.080703(.000208) 15.114550(.000663) A
90.00000(0.00000) 90.00000(0.00000) 120.00000(0.00000) deg.
Volume:
124.230(0.022) A**3

Scale factor : 0.00143530(.00000569)
Overall temp. fact. coeff. : 0.0000(0.0000) A**2
Absorption coefficient : 142.276 /cm
Density : 3.215 g/cm**3
Halfwidth parameters : 0.06150(.02288) 0.01769(.02285) 0.01920(0.00508)
Asymmetry parameter : 0.03000(0.00000)
Lorentzian parameters : 0.90000(0.00000) 0.00000(0.00000) 0.00000(.00000)

*10**4	x/a	y/b	z/c	SOF	B(A**2)
Si1	0(0)	0(0)	0(0)	1.000(0)	1.0(0)
Si2	3333(0)	6667(0)	1664(0)	1.000(0)	1.0(0)
Si3	6667(0)	3333(0)	3329(0)	1.000(0)	1.0(0)
C1	3333(0)	6667(0)	412(0)	1.000(0)	1.0(0)
C2	6667(0)	3333(0)	2080(0)	1.000(0)	1.0(0)
C3	0(0)	0(0)	3746(0)	1.000(0)	1.0(0)

Phase no. 2: Si

RB = 0.19 9 Bragg reflections.

Space group: F D 3 M

Unit cell:
5.430216(.000467) 5.430216(.000467) 5.430216(.000467) A
90.00000(0.00000) 90.00000(0.00000) 90.00000(0.00000) deg.
Volume:
160.122(0.041) A**3

Scale factor : 0.00012232(0.00000255)
Overall temp. fact. coeff. : 0.0000(0.0000) A**2
Absorption coefficient : 143.231 /cm
Density : 2.330 g/cm**3
Halfwidth parameters : 0.00000(0.00000) 0.43992(0.05455)-
0.03472(0.01460)
Asymmetry parameter : 0.03000(0.00000)
Lorentzian parameters : 0.90000(0.00000) 0.00000(0.00000)
0.00000(0.00000)

*10**4	x/a	y/b	z/c	SOF	B(A**2)
Si1	1250(0)	1250(0)	1250(0)	1.000(0)	1.0(0)

Phase no. 3: WC

RB = 0.51 10 Bragg reflections.

Space group: P -6 M 2

Unit cell:
2.915525(0.001723) 2.915525(0.001723) 2.835165(0.001496) A
90.00000(0.00000) 90.00000(0.00000) 120.00000(0.00000) deg.
Volume:
20.871(0.036) A**3

Scale factor : 0.00046236(.00001243)
Overall temp. fact. coeff. : 0.0000(0.0000) A**2
Absorption coefficient : 2323.940 /cm
Density : 15.581 g/cm**3
Halfwidth parameters : 0.00000(0.00000) 0.00000(0.00000)
1.12593(.07373)
Asymmetry parameter : 0.03000(0.00000)
Lorentzian parameters : 0.90000(0.00000) 0.00000(0.00000)
0.00000(0.00000)

*10**4	x/a	y/b	z/c	SOF	B(A**2)
W1	0(0)	0(0)	0(0)	1.000(0)	1.0(0)
C1	6667(0)	3333(0)	5000(0)	1.000(0)	1.0(0)

Quantitative analysis:
Phase 1: 87.21(0.49) wgt%; 86.91(0.51) vol%
Phase 2: 8.95 (0.19) wgt%; 12.30(0.26) vol%
Phase 3: 3.84 (0.10) wgt%; 0.79 (0.02) vol%

Combined absorption coefficient: 159.63 /cm

Two-theta zero: -0.0272(0.0015)

Background parameters (Chebyshev type i):

493(0) -46(0) 29(0) -11(0) 3(0)
 -2(0) 2(0)

Appendix B

Optimisation of the SEM and EDX Sampling for Supported IrO_2/SiC-Si Catalyst

An additional series of experiments was performed for optimisation the sampling of the selected powder catalyst, containing 60% of IrO_2 and 40% of SiC-Si. The main purpose of this series was to determine the effect of the backing plate material on the EDX powder composition results.

B.1 Sample preparation

The samples for investigation were prepared in a way, described previously in Section 5.1.4 with the difference that bother carbon tape and gold backing plates were used for SEM and EDX investigations. All experiments in this series were made on a FEI Inspect S microscope. The EDX-system used was INCA from Oxford Instruments. The EDX quantitative analysis was performed at 5,15 and 20 kV voltages in order to define the difference in composition data, depending on the penetration volume at different voltages.

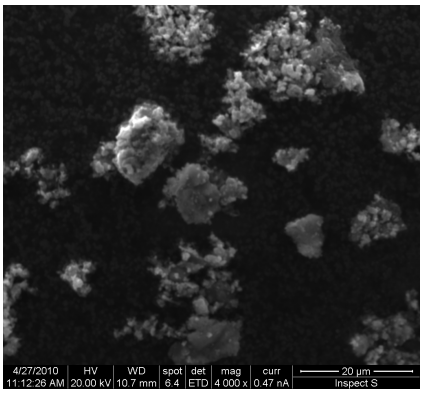

(a) ETD detector

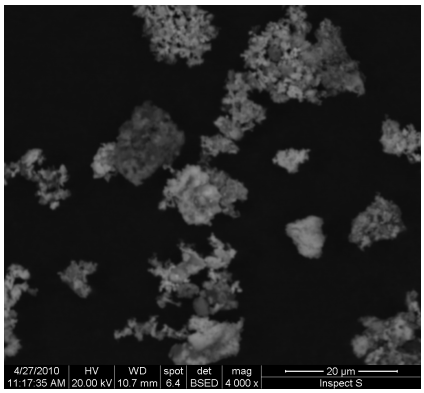

(b) BSED detector

Figure B.1: SEM images on carbon tape support, observed from two different detectors

B.2 Results and discussion

B.2.1 SEM analysis

SEM images of the IrO_2 catalyst on SiC-Si support are presented in Figures B.1(a) and B.1(b). Two images of the same area were taken, using 2 different detectors, while all other parameters of imaging were kept the same (voltage 20 kV, spot size 6.4). It is clear from the pictures that different information is provided. Secondary electrons are emitted from the area located closer to the surface area. Thus, using the secondary electron detector, the most important feature to be seen is the surface topography. Oppositely, backscattered electrons are emitted from deeper regions. The brightness gradient over the image in Figure B.1(b) can be correlated to the composition gradients along the sample surface (taking into account the penetration volume).

B.2.2 EDX analysis

SEM does not give direct information about sample composition, so the combination with the X-ray spectroscopy is usually used to make elemental analysis.

In Table B.1 are presented the corresponding X-ray line energies for the main elements expected. It is important to outline that there are no peak overlaps between these elements, which could disturb the analysis.

For the quantitative analysis it is commonly recommended to use the inci-

Table B.1: X-ray line energies for C, Si and Ir

	Composition, wt.%										
El.(At No.)	Mα	Mβ	L_l	Lα	Lβ_1	Lβ_2	Lγ_1	L_*abs*	K$\alpha_{1,2}$	Kβ	K_*abs*
C(6)									0,277		0,284
Si(14)									1,74		1,84
Ir(77)	1.980	2.053	8.041	9.175	10.708	10.920	12.512	13.424			

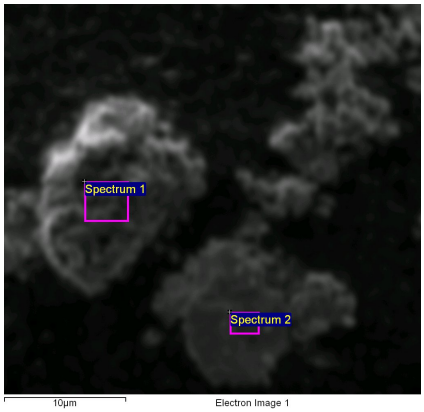

(a) SEM on carbon support, 5 kV

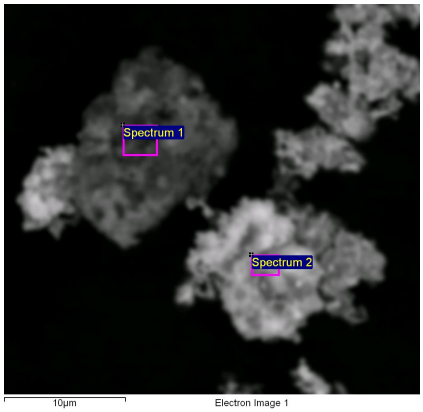

(b) SEM on carbon support, 20 kV

Figure B.2: SEM images on carbon support at two different voltages

dent beam with energy at least 2 times higher than the highest energy peak for exciting a line of interest.

During the EDX analysis on carbon tape support there is a noticeable disadvantage of this backing. Carbon content in the analysed signal reaches quite high values, which might be not reasonable for this material (figures B.2(a), B.2(b) and tables B.2(a), B.2(b). Comparing the composition of spectrums 1,2 in Tables B.2(a), B.2(b) it is clear that with increasing of voltage (and penetration volume of the beam) the content of carbon and silicon increases, while the content of iridium decreases, which means that most of the catalyst is located on the surface of the support, and none or a little fraction of it goes into the pores of the support. It can also be noticed, that at elevated voltage the charging effect is more evident (Fugure B.2(b)). It was decided to use an acceleration voltage of 5 kV in the following investigation of the sample.

Increasing content of carbon with increasing voltage could be also explained by possible partial penetration of the beam into the backing carbon tape plate. But because carbon was also expected in the material, it became important to divide these signals. It is possible by choosing the right support plate, which should not contain any elements expected in the sample. Thus, a polished gold plate was chosen for another session of EDX analysis.

Table B.2: EDX on carbon support

(a) EDX on carbon support, 5 kV

Spectrum	C	O	Na	Al	Si	Fe	Mo	Ir	Total
1	10.12	14.79	1.48	0.56	49.14		2.08	23.14	100.00
2	4.76	16.66	1.57		4.13		2.70	71.94	100.00

(b) EDX on carbon support, 20 kV

Spectrum	C	O	Na	Al	Si	Fe	Mo	Ir	Total
1	18.25	11.59	0.56	0.33	60.32	0.65	0.97	7.32	100.00
2	24.17	18.90	1.20	1	11.39	0.05	2.06	42.25	100.00

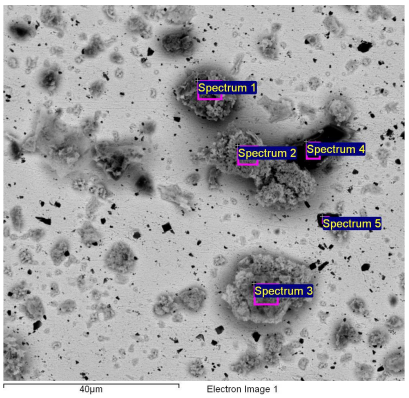

(a) SEM image at low magnification, 15 kV

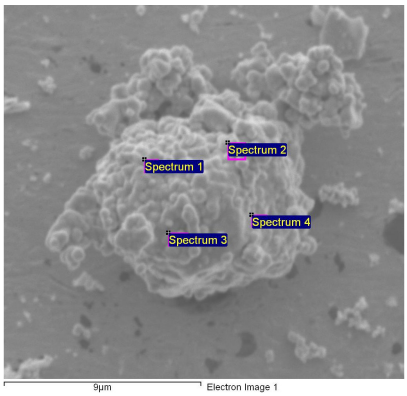

(b) SEM image at high magnification, 5 kV, spot size 4.5

Figure B.3: SEM images at low and high magnifications

Gold plate support On Figure B.3(a) is presented the overall low magnification SEM picture of the catalyst, distributed over the gold backing plate. Most of the spectrums of EDX analysis (Table B.3(a)) show that there is still signal from the backing gold plate.

Decrease of the acceleration voltage to 5 kV (Figure B.3(b)) does not help to eliminate the signal from the backing (spots 1,3 in Table B.3(b)). It means that while using carbon tape plate, not all the counts corresponding to carbon were obtained from the sample, even at low voltage of 5 kV.

On figures B.4(a), B.4(b) and tables B.4(a),B.4(b) are shown the results of the EDX quantitative analysis, performed at low voltage (5 kV) but with different spot size (3.0 and 4.5). It is noticeable that better resolution can be achieved at lower spot size. Even more, using the spot size 4.5 it was still possible to see the signal from the gold backing, which is not preferable

Table B.3: EDX data analysis at low and high magnifications

(a) EDX data for low magnification image, 15 kV

	Composition, wt.%								
Spectrum	C	O	Na	Si	Fe	Mo	Ir	Au	Total
1	6.67	16.63	1.95	23.22	0.05	1.99	43.14	6.34	100.00
2	3.12	14.86	2.94	5.62	0.10	2.33	64.58	6.46	100.00
3	5.51	21.34	3.89	6.57	0.11	3.16	50.39	9.02	100.00
4	27.51	6.99	0.41	55.09	0.10	0.24	7.95	1.72	100.00
5	21.72	0.70	0.07	54.17	0.10	0.05	0.38	22.83	100.00

(b) EDX data, 5 kV, spot size 4.5

	Composition, wt.%								
Spectrum	C	O	Na	Si	Fe	Mo	Ir	Au	Total
1	2.24	19.44	2.79	5.28		4.69	60.39	5.57	100.00
2	2.98	21.41	3.09	4.30			69.33	0.45	100.00
3	1.11	12.48	2.54	3.99		4.66	70.39	5.58	100.00
4	3.47	21.91	2.81	4.14	0.24	0.53	66.12	0.79	100.00

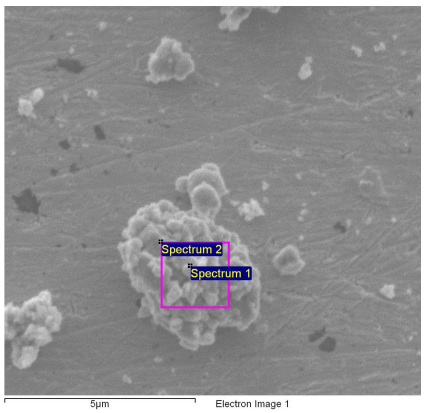

(a) SEM image at 5 kV, spot size 3.0

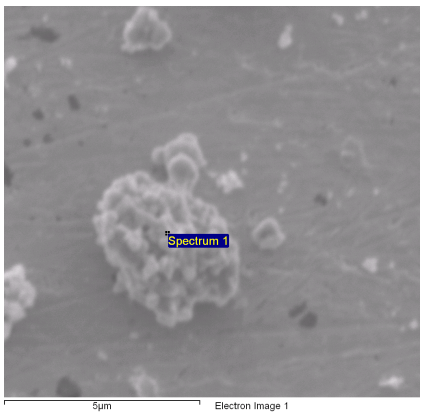

(b) SEM image at 5 kV, spot size 4.5

Figure B.4: SEM images at low voltage for different spot sizes

Table B.4: EDX data at low voltage and different spot sizes

(a) Spot size 3.0

	Composition, wt.%								
Spectrum	C	O	Na	Si	Fe	Mo	Ir	Au	Total
1	7.75	22.75	3.48	14.91	2.95		56.89		-6.91 100.00
2	6.62	19.86	2.36	15.69		1.67	57.60		-0.83 100.00

(b) EDX data for 5 kV image, spot size 4.5

	Composition, wt.%								
Spectrum	C	O	Na	Si	Fe	Mo	Ir	Au	Total
1	5.66	16.94	2.34	12.48		3.40	53.25	5.99	100

Table B.5: EDX analysis of supported catalyst powder, dispersed in ethanol and applied on gold plate, 5 kV

	Composition, wt.%				
Spectrum	C	O	Si	Au	Total
1	18.99	0.23	38.67	42.12	100.00
2	7.34	0.19	0.08	92.40	100.00

(table B.4(b)).

Another interesting feature which was found during the analysis is the quality of micro-level finishing of the backing plate. Some of the spectrums (4,5) in figure B.3(a) and table B.3(a) showed an elevated amount of carbon. It was decided to make EDX analysis of the clean polished gold plate to see any defects of the plate surface finishing.

Figure B.5 and table B.5 shows SEM and EDX analysis results of the clean polished gold plate, polished with SiC paper and finally grounded with diamond paste. Defects on the surface of the plate is possible to see with the unarmed eye. The analysis of the dark spot in spectrum 1 shows that they probably belong to the residues of the polishing SiC paper grains, which were left in the plate structure due to its relative softness. Spectrum 2 shows the composition of the "Clean gold plate surface", which still contains around 7 % of carbon, which could come from various sources (the vacuum pump could be one of them). This shows the importance of the micro level support plate surface finishing, when doing the EDX analysis.

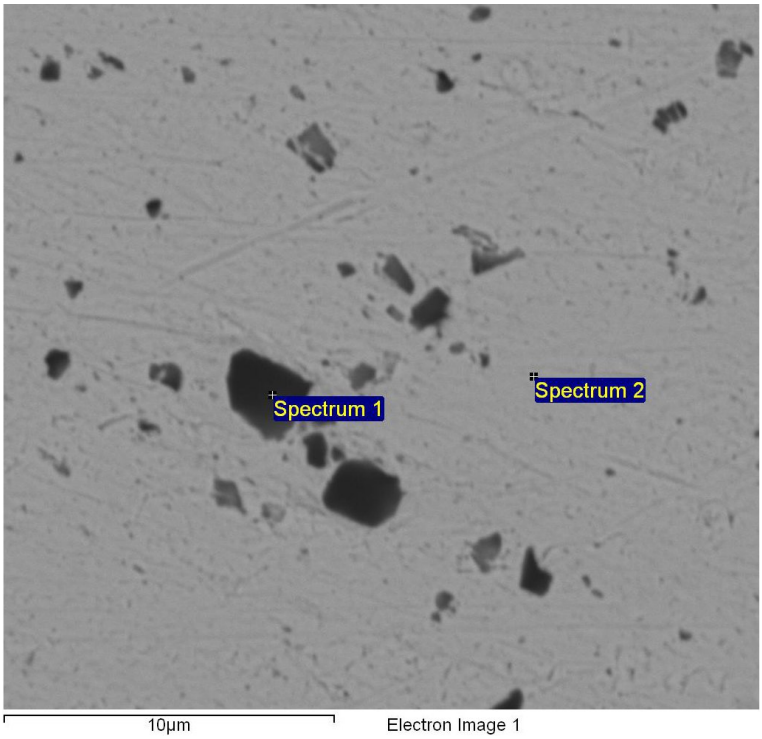

Figure B.5: EDX analysis of the polished gold plate

B.3 Conclusion

Investigation of iridium oxide electrocatalyst, supported of silicon carbide-silicon matrix was done by means of SEM and EDX analysis. Because of relatively low conductivity of the studied powder it is recommended to make such investigations at reduced voltages to prevent surface charging artefacts. It is also recommended to use decreased spot size for obtaining of high resolution image.

It is important to be aware of possible electron scattering from the backing metal plate. In this case the use of low voltage is a way to decrease the interaction volume. For the reasonable EDX data the spot size usually needs to be increased in order to get enough counts. But as it was outlined before, increasing of the spot size leads to poorer resolution. So optimum configuration can always be found depending only on the specific sample properties.

Apparently, the resolving power of SEM is not enough to see and analyse individual catalyst particles of IrO_2, which are the smallest in this system. Transmission electron microscopy can be recommended to fulfil this requirement.

It was found that the catalyst is distributed evenly over its surface of the catalyst support. In the case of using a gold plate as a sample holder, it was found that the surface of it was not analytically clean and contained particles of the grinding material, which apparently also had an influence on the quality of the quantitative EDX analysis.

www.energi.kemi.dtu.dk

Department of Chemistry
Energy and Materials Science group
Technical University of Denmark
Kemitorvet
Building 207
DK-2800 Kgs. Lyngby
Denmark
Tel: (+45) 45 25 24 19
Email: alnik@kemi.dtu.dk